Model and design of low-resolution digital/analog converters for metropolitan optical networks

Sylvain Almonacil

université PARIS-SACLAY

INSTITUT d'OPTIQUE GRADUATE SCHOOL ParisTech

NNT : 2019SACLO017

Model and Design of Low-Resolution Digital-to-Analog Converters for Metropolitan Optical Networks

Thèse de doctorat de l'Université Paris-Saclay
préparée à l'Institut d'Optique Graduate School

École doctorale n°572 Ondes et Matière (EDOM)
Spécialité de doctorat: Physique

Thèse soutenue à Palaiseau, le 13 décembre 2019, par

Sylvain ALMONACIL

CONFIDENTIEL jusqu'au 12 décembre 2024

Composition du Jury :

Christelle AUPETIT-BERTHELEMOT Professeur des Universités, Université de Limoges	Présidente
Antonella BOGONI Professeur associé, CNIT/Scuola Superiore Sant'Anna	Rapporteure
Chigo OKONKWO Professeur associé, Eindhoven University of Technology	Rapporteur
François GOUDAIL Professeur des Universités, Institut d'Optique Graduate School	Examinateur
Nicolas DUBREUIL Professeur des Universités, Institut d'Optique Graduate School	Directeur de thèse
Patricia LAYEC Ingénieur de Recherche, Nokia Bell Labs France	Co-Directrice de thèse

Thèse de doctorat

Résumé

Modélisation et Conception de Convertisseurs Numérique/Analogique pour les Réseaux Optiques Métropolitains

par Sylvain Almonacil

Le présent manuscrit de thèse traite de la modélisation et de l'optimisation des convertisseurs numérique/analogique (CNA) pour les réseaux optiques métropolitains. Plus particulièrement, la possibilité d'utiliser des CNA de faible résolution, typiquement 4 bits au lieu de leurs versions actuelles sur 8 bits, est étudiée. En effet, réduire la résolution des CNA permettrait de réduire leur consommation, leur complexité et donc leur coût, ce qui est particulièrement intéressant dans le contexte des réseaux optiques dits métropolitains (à l'échelle d'une région ou d'un pays) où ces caractéristiques doivent être minimisées.

Ce manuscrit est divisé en quatre chapitres précédés d'une introduction et suivis par une conclusion. L'introduction présente les évolutions sociétales qui engrangent une augmentation toujours plus rapide du nombre de données transportées, majoritairement par fibres optiques. Dans ce contexte général, le rôle grandissant des réseaux optiques métropolitains est mis en avant. Également, les implications techniques de ces évolutions sont présentées, notamment pour les transmetteurs optiques et plus particulièrement le CNA.

Le chapitre premier introduit l'architecture générale d'un lien optique fibré. Les développements technologiques les plus récents qui répondent à l'évolution continue de la demande en débits d'information sont résumés, permettant ainsi d'expliquer le rôle incontournable du CNA pour exploiter tout le potentiel des liaisons optiques fibrées. Une description détaillée du transmetteur et plus particulièrement du CNA est proposée. Les limitations physiques du CNA sont expliquées et détaillées plus particulièrement dans le cas d'une résolution physique réduite. A cause de ces limitations, les signaux émis souffrent de distorsions dont la modélisation et la compensation avec les méthodes les plus récentes sont décrites. Finalement, ce chapitre décrit un modèle de performance déjà existant (état de l'art) pour un lien optique de bout en bout. Il est expliqué comment les distorsions dues au CNA de faible résolution peuvent être intégrées dans ce modèle en les traitant séparément des distorsions propres au CNA de haute résolution, au lieu d'utiliser une mesure agrégée de toutes les distorsions comme il est d'usage de faire avec la résolution effective.

Le second chapitre propose une description détaillée des distorsions propres au CNA de faible résolution : l'erreur de quantification et l'erreur de clipping (dépassement). Ces deux bruits sont traités séparément puisqu'ils ont différentes origines et ont une influence différence sur le signal transmis. Le but est ici d'établir un modèle de prédiction du rapport signal sur bruit lorsqu'un CNA (ou un convertisseur analogique/numérique, CAN) de faible résolution est employé. Concernant l'erreur de quantification, l'état de l'art de sa modélisation est rappelé ainsi que les hypothèses permettant de la traiter comme une distorsion décorrélée du signal. Ces hypothèses sont discutées dans le cas des signaux employés en télécommunication optique. Concernant l'erreur de clipping, bien qu'elle soit toujours corrélée au signal, il est démontré que cette corrélation peut être suffisamment faible pour être négligée lorsque le taux d'échantillons "clippés" du signal est optimum. Le modèle proposé de prédiction du rapport signal sur bruit est vérifié à la fois par des simulations et des expériences et sa précision est discutée. Ce modèle permet d'expliquer les gains en performance obtenus par la suite.

Le troisième chapitre présente trois méthodes qui permettent de maximiser la performance des CNA faible résolution. Tout d'abord la méthode de la rotation de phase de la constellation est proposée pour les systèmes employant une pré-compensation de la dispersion chromatique. Les gains en performance obtenus sont vérifiés expérimentalement. Les deux autres méthodes sont empruntées aux domaines audio et radio. En exploitant la nature déterministe de l'erreur de quantification, il est possible de la filtrer numériquement au niveau du transmetteur afin de minimiser sa densité spectrale de puissance dans la bande fréquentielle du signal. Une stratégie pour intégrer cette technique dans un transmetteur optique est proposée et les gains en performance sont démontrés expérimentalement. La troisième technique, connue comme la quantification non uniforme, consiste à modifier la distribution en amplitude des niveaux de quantification du CNA. Les gains en performances attendus sont déterminés par des simulations numériques.

Le quatrième chapitre présente deux nouvelles architectures de transpondeur (couple émetteur/récepteur) adaptée au réseau très courte distance ou métropolitain. Premièrement, une nouvelle architecture de transmission à un débit symbole supérieur à la fréquence d'échantillonnage du CNA et du CAN est présentée. La possibilité de transporter des signaux au débit symbole de 125GBaud (125 Giga symboles par seconde) avec des CNA/CAN ayant une fréquence d'échantillonnage de seulement 92 Giga échantillons par seconde. Cela est fait sans pré-codage des données émises, contrairement aux autres méthodes existantes. Deuxièmement,

une architecture permettant de transmettre des signaux qui requièrent des rapports signal sur bruit très élevés (par exemple des signaux radio) dans une fibre optique. Cette architecture combine la modulation Sigma-Delta (CNA avec 1 bit de résolution physique) avec une nouvelle technique de modulation. Au lieu de filtrer le bruit de quantification du modulateur Sigma-Delta, ce dernier est reconstruit au récepteur, permettant ainsi de retrouver le signal perturbé seulement par le bruit de quantification, indépendamment des autres sources de bruit, permettant ainsi d'atteindre des rapports signal sur bruit de l'ordre de 60 décibel.

Remerciements

Je tiens ici à remercier toutes les personnes qui, chacune à leur manière, ont contribué à cette thèse. Ayant réalisé mon doctorat en collaboration avec Nokia Bell Labs, le Laboratoire Charles Fabry et l'Université Paris-Saclay dans le cadre d'une convention CIFRE, c'est l'occasion pour moi de souligner la chance exceptionnelle que j'ai eue de bénéficier de cette passerelle entre les milieux industriel et académique.

Tout d'abord, mes remerciements vont à Nicolas Dubreuil qui a été à l'origine de mon entrée dans le milieux des télécoms au travers du Projet Système effectué à l'Institut d'Optique. Plus qu'un directeur de thèse, il est également devenu un ami avec qui les kilomètres parcourus à vélo en vallée de Chevreuse resteront de très bons souvenirs. Je remercie aussi très chaleuresement Philippe Jennevé, qui était mon encadrant de stage chez Alcatel-Lucent à l'été 2015 et qui a aussi contribué intensément à mon travail de thèse. En retour, j'ai fait de mon mieux pour l'accompagner dans ses premières expériences en tant qu'aviateur.

Je tiens aussi à remercier Sébastien Bigo, Alberto Bononi et Paolo Serena qui m'ont offert l'opportunité, en préparation à cette thèse, de réaliser un stage de six mois à l'Université de Parme en Italie. Au delà de l'excellence de cet encadrement, je retiendrai aussi une très belle expérience humaine dont Matteo, Simone et les nombreux amis italiens sont les témoins.

Aussi, je remercie Patricia Layec qui a accepté de m'encadrer chez Nokia et qui m'a donné l'opportunité d'intégrer les Bell Labs en tant que membre permanent, et ce avant la fin de mon doctorat. C'est une marque de confiance dont je suis très reconnaissant et qui me permet de prolonger l'aventure avec mes collègues: Fabien, Emmanuel, Eric, Arnaud, Nihel, Nicola, Jelena, Petros, Haïk et bien d'autres.

Au quotidien, je ne saurais oublier mes amis qui ont fait que ces trois années sont passées très vite. Je pense particulièrement au "Midi-Pile" avec Julien mais aussi à Jeanne, Jean-Eloi, Léo, Joséphine pour ne citer qu'eux. J'ai une pensée particulière pour José Manuel Estaran qui a su apporter sa pierre à l'édifice aux moments opportuns.

Je termine par une pensée émue pour mes parents, ma sœur et ma compagne Alix qui ont été un soutien indéfectible et une source permanente de motivation durant toutes ces années. Qu'ils soient certains de ma profonde reconnaissance.

Bures-sur-Yvette, le 13/03/2020

Contents

Introduction

With no end in sight for the skyrocketing growth in data traffic since the beginning of the Internet era, back in the 80's, optical transmissions remain the unchallenged way of transporting information. This is why any data has more than 99.999% likelihood of transiting through an optical fiber. The key to this worldwide success lies in the physical properties of silica. Indeed, the propagation of light in optical fibers benefits from a low attenuation of the order of 0.2 dB/km (signal power divided by 2 every 15 km), compared to attenuation values ranging from 8 to 15 dB/km for copper cables. Associated with optical amplifiers, a low attenuation paves the way for long-haul transmissions (>1000 km). Underseas and transcontinental optical links (up to 10000 km) have been deployed all over the world. The optical network spider is also composed of smaller-scale links

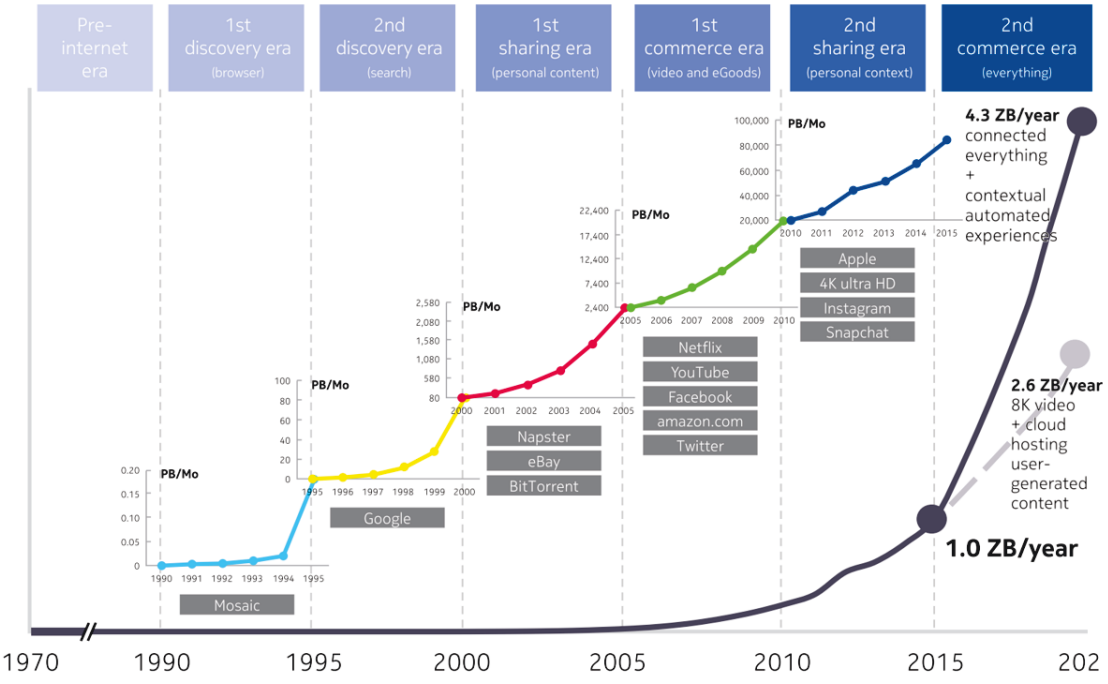

FIGURE 1: Global IP traffic since the dawn of the internet era [1].

that provide data transport in a metropolitan or country area (<600 km) and lastly to the access networks (fiber to the building) that connect the end-user applications (houses, companies, data centers...). Today, we estimate that 4 billion kilometers of optical fibers have been deployed all around the Earth. This has prevented the world from facing the dreaded capacity crunch. In light of this, we successfully entered the so-called *Zettabyte era* in 2015, for which the amount of information exchanged per year overpassed 1 zettabyte (ZB), as illustrated in Fig. 1. Cisco estimates that the annual global IP traffic will reach 4.8 ZB in 2022 [2] which corresponds to an instantaneous traffic of ≈1.2 Petabits (Pbits) per second (1 byte = 8 bits). This corresponds to 50 Gigabytes (GB) per month and per capita of the global population, while it was 16 GB per month in 2017 and only 10 Megabytes (MB) per month when we entered the third millennium, back in 2000.

This constant increase is supported by several trends. First, the most important fraction of the data traffic results from video over IP applications such as internet video (video chat, streaming), Video on Demand (VoD), video conferencing or

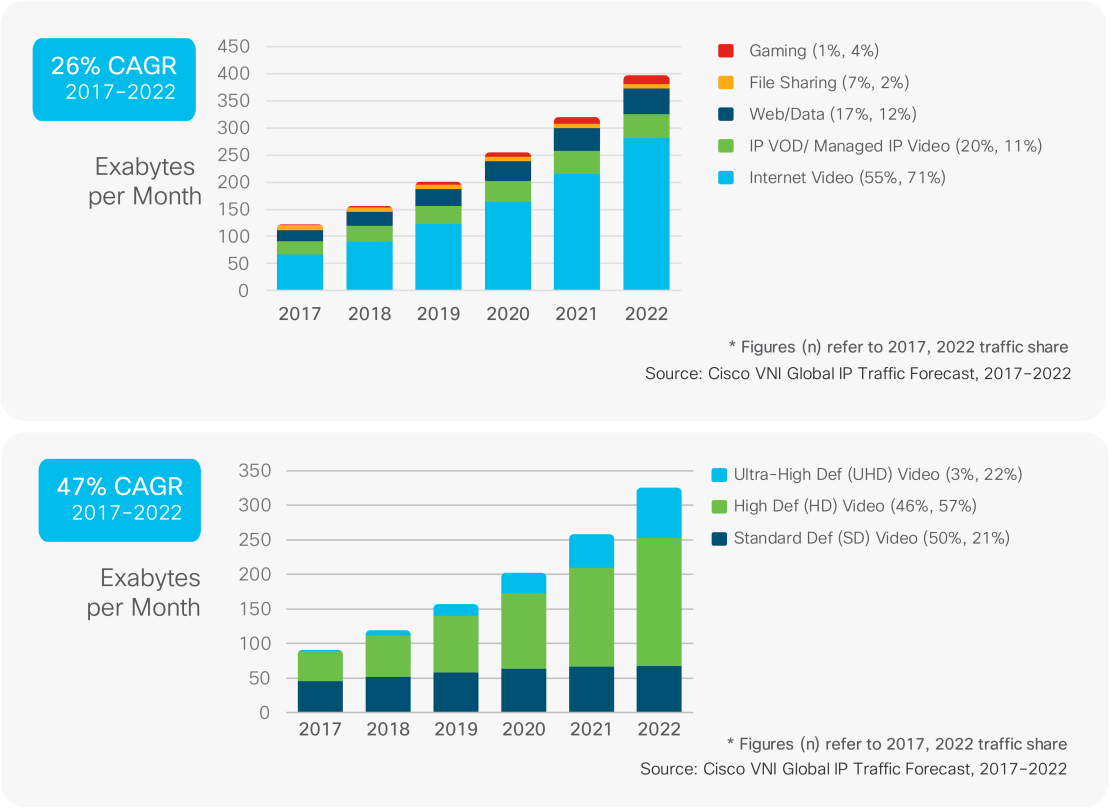

FIGURE 2: Up: Global IP traffic by application category. Bottom: Video over IP traffic by definition [2].

video surveillance, as revealed by the compiled data shown in the upper graph of Fig. 2. Altogether, they account for 80 to 90% of the overall global IP traffic. The effect of video applications, of 26% CAGR[1], on the global IP traffic, is more pronounced because of the introduction of the ultra-high definition (UHD, or 4K/8K) video streaming which requires a bit rate nine times higher than for Standard-Definition videos. The preeminence of UHD videos, with a CAGR of 47% for 2017-2022, is clearly visible on the bottom graph of Fig. 2. Second, the emergence of new digital consumers in the Middle East and Africa as well as in Asia Pacific will continuously fill the pipe. Third, another emerging application that implies the transfer of a large amount of data is video-gaming traffic. Newer consoles such as the Xbox One and the Playstation 4 have enough on board storage capacity to enable gamers to download new games rather than buying them on disc. The gaming traffic is expected to reach 4% of the overall IP traffic by 2022 [2], as shown in the upper graph of Fig. 2, because of the increasing files sizes of the graphically intense games.

However, this unrelenting growth in video services cannot explain by itself the deep mutation that optical fiber networks are facing today. Indeed, one can remark that the total instantaneous IP traffic of 1.2 Pbit/s is only ≈10x the bit rate that can be transported into one single optical fiber[2], of the order of 100 Terabits per second (Tbit/s) [3], so that only ten optical fibers can support the whole IP traffic. This thinking is obviously simplistic because communications do not occur from one single point to another. However, it reveals that optical links must be considered as a network whose meshing is increasing day after day, to match with the new applications arising from the societal mutation we are living today.

Why? Because an industrial revolution is ongoing, known as the fourth industrial revolution. The 4$^{\text{th}}$ industrial revolution consists in the digitization of everything, resulting from the leveraging of the Internet of Things (IoT), the augmented intelligence (AI), the cobots (collaborative robots) and the huge amount of available data (Big Data). Through this concept, known as Industry 4.0, every factory or industrial plant will benefit from faster, more flexible and more efficient processes thanks to the use of a massive number of augmented and connected devices. A first successful example of Industry 4.0 is the mining industry in which a deep automation and a collaboration between devices and humans increase safety

[1]The Compound Annual Growth Rate (CAGR) is the average annual growth rate (per year) over a given period. It is given by the formula $CAGR(t_n, t_0) = (V(t_n)/V(t_0))^{(1/((t_n - t_0)))} - 1$ with $V(t_0)$ the initial value, $V(t_n)$ the final value at year n and $t_n - t_0$ the number of years. One remarks that for a unique year, the CAGR corresponds to the geometric growth rate, hence making this measure adapted to the geometric progression of the IP traffic.

[2]We consider here the case of the most popular single-core single-mode fiber.

for operators, boost productivity, and enable a wide environmental monitoring [5]. In autonomous mining plants, both underground drilling and haulage of the ore is performed by (big) connected devices such as autonomous drilling systems or dump trucks, which are shown in Fig. 3. In 2018, the world leading mining company Rio Tinto was the first one to achieve a fully autonomous hole-pattern drilling without any human in-situ intervention in its iron ore mine in Pilbara, Western Australia [4]. Its autonomous drilling system enables the operator to use a single console at a remote location to control four autonomous drill rigs from multiple manufacturers simultaneously, thereby improving both precision and operational efficiency.

More generally, digitization creates a prevalent system in which people, processes, data, and things are connected to the Internet and to one another. Examples range from the connected car with autonomous driving to the connected house with advanced monitoring and functionalities. This revolution has a straight consequence: it hugely increases the number of connected devices and the

FIGURE 3: Example of machine-to-machine connection: Rio Tinto autonomous drilling system (left), haulage (center) and supervision room (right) [4].

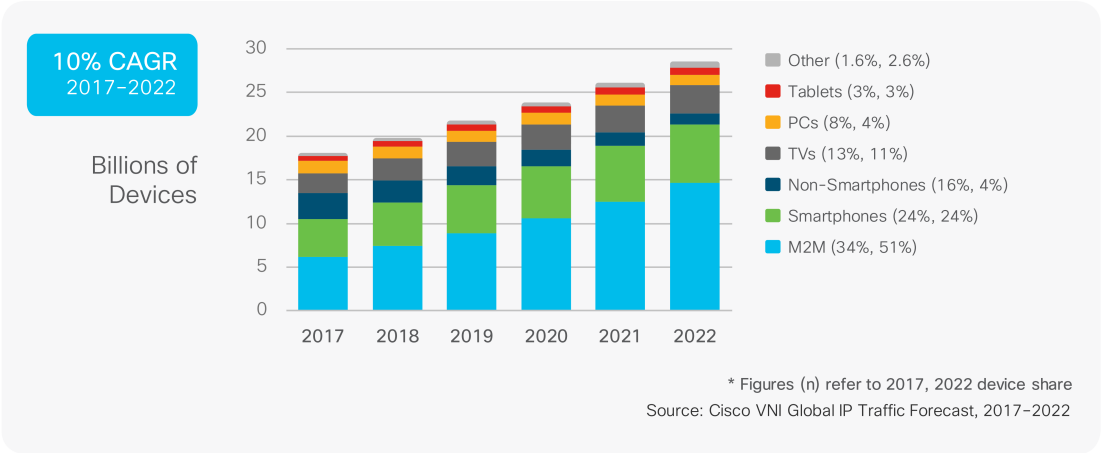

FIGURE 4: Global devices and connection growth [2].

associated data centers (DC) for data storage. Since the potential of these devices resides in the collaboration between one another in addition to the ones with humans, we also observe a strong increase in the number of connections between machines (machine to machine, M2M) as shown in the graph of Fig. 4.

This new type of connections is at the origin of the in-depth change of the optical network architecture. Indeed, M2M connections and related applications will require much less latency than human-to-machine or human-to-human connections. For instance, cobots or mining trucks interact in a time scale much smaller than the human latency, which is of the order of 100 ms. Consequently, data centers are located closer and closer to the user, firstly to minimize the round-trip-time of light, as illustrated in Fig. 5, and secondly to limit the number of optical and electro-optical components such as transponders or muxponders that introduce the majority of the latency[3].

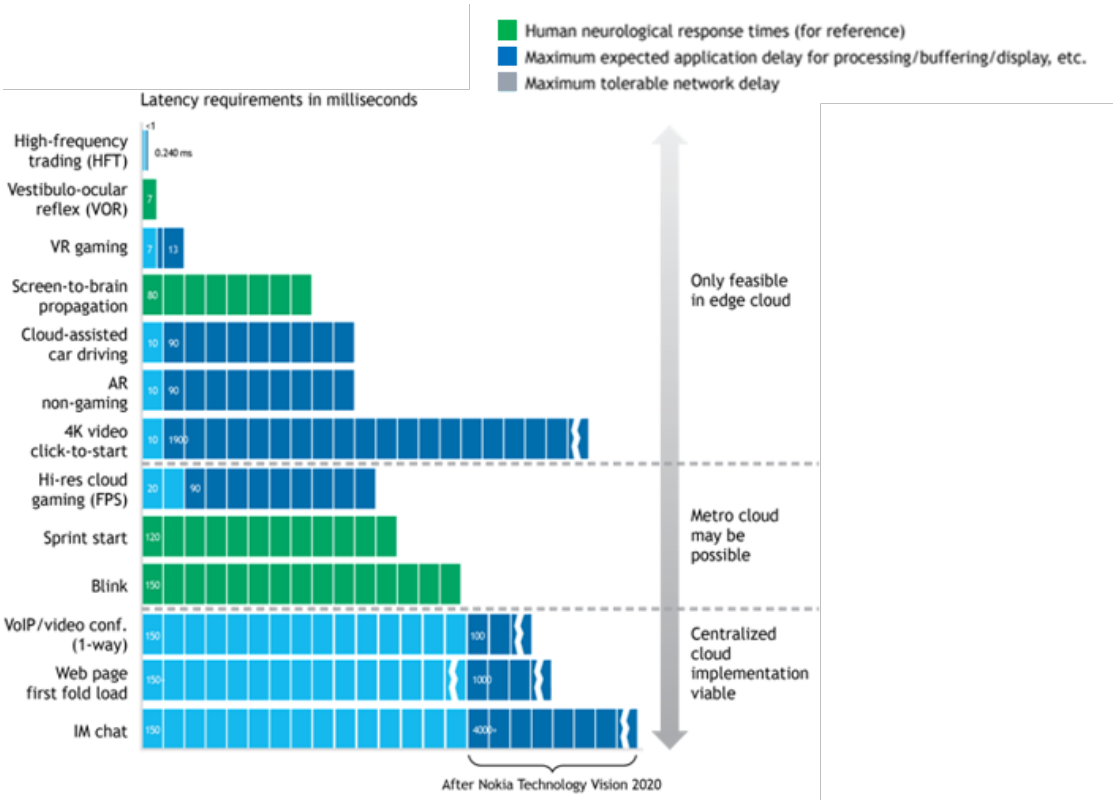

FIGURE 5: Application latency requirements compared to neurological response time (Chioka 2013, Berman 2014, Duffy 2002, Human Benchmark 2014, Microsoft 2015) [1].

[3]For a given required latency, one remarks that the speed of light theoretically enables a much higher propagation distance than the one effectively used. This is because the round-trip-time of light is much smaller than the latency introduced by the network switching elements, which number increases with distance.

Consequently, IP traffic in short-haul (intra and inter data centers) and hence in metropolitan and regional optical networks is growing about 2x times faster than in the core network, as reported in Fig. 6 for the last decade [6], a trend which is not expected to decline. Whereas short-haul and metropolitan links (metro network) refer to optical links with propagation distances of the order of several hundreds of kilometers (<600 km), the core network (backbone) connects different countries and continents which can be separated by thousands of kilometers. In 2017, 75% of the IP traffic ended or transited in the metro network while it was only 57% in 2012, as shown in Fig. 6.

This new balance in terms of traffic distribution, considering that data centers are centralized within the metro networks[4] (metro centralized scenario), is the consequence of the huge increase in IP traffic and of the general trend to bring data storage closer to the user in order to cope with the latency requirements of new digital applications and Industry 4.0. Academic and industrial actors are urged to propose disruptive hardware solutions dedicated to metro networks, not only to cope with the increasing data rates resulting from traffic booming, but also to do it in an efficient manner regarding cost, complexity and power consumption.

Indeed, metro optical links are fundamentally different from long-haul systems because of a smaller propagation distance, even if they are composed of the same three elements: the transmitter, the propagation channel and the receiver. When propagating over continental or inter-continental distances, the propagation channel is comprised of a concatenation of optical fibers separated by optical amplifiers to mitigate the silica attenuation. However, to minimize the number of amplifiers along the link, the distance between them is maximized and can reach up to 80 or 100 km such that the accumulated attenuation per fiber is of the order of 20 dB. Moreover, a high-input optical power is necessary at the entrance of each fiber span. Both effects, high input power and amplification, lead to nonlinear distortions experienced by the optical field along the span as well as noise accumulation. Nonlinear distortions come from the third order nonlinear response of silica, induced by the high optical power density while noise addition comes from the spontaneous emission of the Erbium doped fiber amplifier (EDFA),

[4]Another strategy will be to bring data centers even closer to the users, resulting in a metro decentralized architecture. Compared to the metro centralized architecture, decentralization favorites uni-cast traffic, i.e. traffic dedicated to a few numbers of users (video on demand, time-shift TV for instance) while the centralized scenario favorites broadcasting i.e. transmission for many users (traditional TV). Each architecture depends on the targeted application and tolerable latency. In the metro decentralized scenario, the growth in IP traffic within the metro will be 41% less than in the centralized scenario but still higher than in the core.

the amplification technology for optical networks. On the other hand, for short propagation distances, only a few numbers of amplifiers is necessary and the span length can be reduced because of the increasing density of data centers. Thus, in metro optical links, the nonlinear distortions and the EDFA-induced noise can be negligible or not predominant, such that the optical link performance is limited by the transmitter and the receiver impairments. Moreover, for long-haul optical systems, the power consumption of the whole system is mainly due the amplifiers while, for metro optical links, the couple transmitter/receiver contributes mainly to the power consumption.

It should also be noted that with the digitization era a specific kind of data traffic distribution, highly variable both in time and space, is booming. Long-haul networks are almost constantly loaded in data traffic because they carry aggregated data, that generally travel across several time zones, hence smoothing the variations even at a daily time scale. At the opposite, metro networks are more subject to hourly data traffic variations because they directly provide data for the end-user applications. For instance, television and internet video will be preeminent in the evening while positioning applications are more used during the working hours. An example of data traffic variation in a metropolitan network is shown in Fig. 7, considering the Amsterdam-exchanger for 21th June 2018 [7]. We clearly observe the traffic peaks corresponding to the FIFA world cup matches Portugal/Morocco and Iran/Spain. If we have a closer look we can also see the slight decrease in data traffic during the half-time.

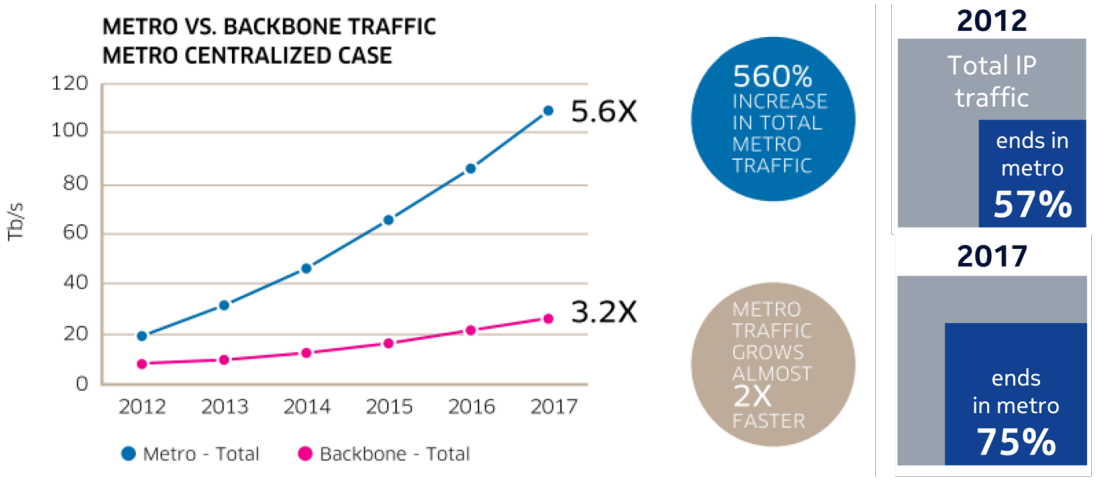

FIGURE 6: Left: Traffic growth in metro and backbone network with metro centralized video catching and DC deployment. Right: The changing distribution of traffic between metro and backbone [6].

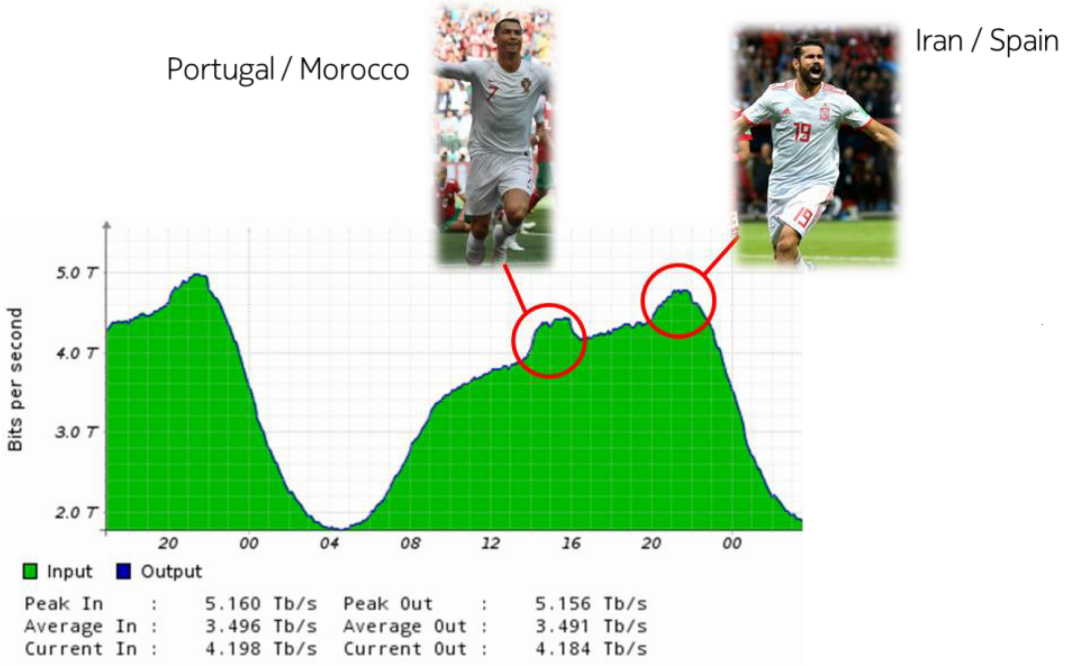

FIGURE 7: Aggregated traffic on all networks connected to the Amsterdam exchanger during FIFA World Cup (21th June 2018) [7].

DAC and ADC in optical networks

To sustain the constantly increasing demand in data traffic and to cope with its strong variability, high-speed digital-to-analog converter (DAC), analog-to-digital converter (ADC) and the associated digital signal processing (DSP) are the essential blocks of any modern metropolitan optical networks. Indeed, DAC and ADC convert multilevel signals between the digital and the analog domains and hence enable the heavy use of DSP at the transmitter and the receiver such that, for instance, the data rate can be easily adapted to the demand by tuning the modulation format. Originally, DAC and ADC were introduced into optical networks together with the commercialization of 10 Gbit/s intensity modulation (IM) and direct detection (DD) optical systems with pre-compensation of the chromatic dispersion [8] (2005). The pre-compensation consists in applying the inverse of the chromatic dispersion operator to the emitted optical field with a dedicated processing circuitry in the digital domain. Given the large chromatic dispersion pre-compensation, the digital signal is 2-dimensional Gaussian distributed, hence requiring a DAC at the transmitter. In this example, the DAC was operating at 20 Giga samples per second (GS/s). Afterwards, the ADC was introduced at the receiver side in the first coherent receivers [9]

(2008). In a coherent receiver, four identical ADC operate in parallel to convert the electrical voltages corresponding to the real and imaginary parts of the dual-polarization optical field, which are continuous-amplitude signals. Thus, the optical phase and the state of polarization can be retrieved at the receiver, enabling the digital compensation of linear effects such as the chromatic dispersion (post-compensation) or polarization effects (polarization mode dispersion for instance). This led to a first class of 40 Gbit/s coherent optical systems which were using 20 GS/s ADC. From this date and up to now, DAC and ADC are the spine of all major advances in coherent communications both for long-haul and metropolitan optical networks. The increase in electronic speed associated with the development of advanced DSP techniques such as Nyquist filtering enable a dense wavelength division multiplexing of high-order modulation formats at the data rates of 100 Gbit/s (2010), 200 Gbit/s (2012) and 400 Gbit/s (2014) with DAC and ADC pairs operating at 56 GS/s, 65 GS/s and now 92 GS/s (for more details on signal generation techniques, see Chapter 1) [10, 11]. Next generation of DAC and ADC (2020) will enable 800 Gbit/s and higher data rate. In addition to this, DAC and ADC enable an on-demand generation of multilevel signals and a real time tuning of the modulation format, the symbol rate or the spectral shape for instance, such that any signal can be generated according to the characteristics of the optical link (length, required capacity, characteristics of the fiber). This way of operating is known as the optical elastic networking [12]. In that context, manufacturers developed coherent optical transponders able to generate different modulation formats to meet with the data rate demand. For instance, in 2015, Nokia released its *Photonic Service Engine 2* which can generates six different modulation formats, hence producing data rates ranging from 50 to 250 Gbit/s [13]. More recently, the *Photonic Service Engine 3*, released in 2018, enables a quasi-continuous data rate flexibility through a specific modulation scheme of the optical field, called Probabilistic Shaping [14].

Optical transmitter power consumption

Using high-speed DAC significantly increases the power consumption and the cost of the transmitter/receiver pair. This is particularly detrimental for short-reach or metropolitan optical links because the power consumption and the cost of the entire optical link are mainly due to the transmitter and the receiver, as the propagation distance is small. In that context, authors in [15] highlighted that

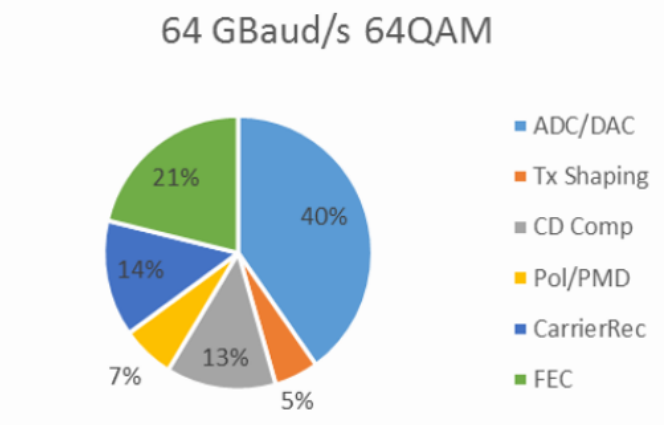

FIGURE 8: Power distribution of the DSP operations in an ASIC for metropolitan or inter data centers optical networks for a typical 64-QAM at 64 Gbaud transmission (760 Gbits/s gross) if a coherent signaling is employed [16]. *Tx shaping* is the filtering of the signal at the transmitter side (pulse-shaping or digital pre-emphasis, see Chapter 1). *CD comp* is the chromatic dispersion digital pre- or post-compensation. *Pol/PMD* is the digital polarization demultiplexing and compensation of the polarization mode dispersion. *CarrierRec* stands for carrier frequency and phase recovery at the receiver and *FEC* stands for forward error correction.

the DSP operations power consumption[5] is mainly due to the DAC and the ADC. These results are confirmed by authors in [16] who estimate that the DAC/ADC pair accounts for 40% of the overall power consumption for DSP operations, as shown in Fig.8.

The DAC and ADC power consumption increases with their sampling frequency and physical resolution [16–18]. For instance, a binary-weighted current steering architecture [10, 18], used for high-speed DAC, is considered and depicted in Fig.9. In that case the power consumption is comprised of two terms. The first one is a static component which scales with the resolution but is independent of the sampling frequency. The second is a dynamic component which scales linearly with both the resolution and the sampling frequency. The static component P_s is mainly due to the array of current sources and can be calculated by [18]:

$$P_s \approx \frac{1}{2} V_{dd} I_0 \left(2^{N_b} - 1\right) \tag{1}$$

with N_b the physical resolution, V_{dd} the supply voltage and I_0 the unit current source corresponding to the least significant bit. The dynamic component P_d occurs during the switching process between symbols (when a switch is being

[5] An Application-Specific Integrated Circuit is an integrated circuit designed for a particular use. In optical systems, it is designed for the DSP operations, including the DAC and the ADC [15].

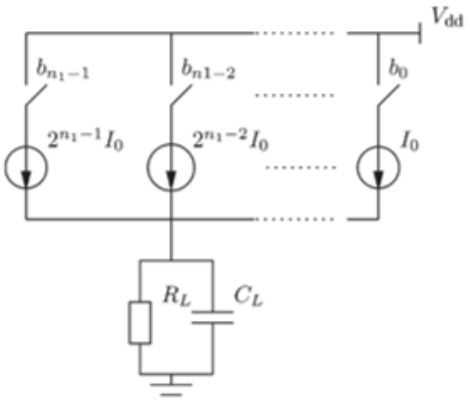

FIGURE 9: Binary-weighted current-steering architecture for high-speed DAC. Each amplitude sample is encoded into an N_b bits code b_n, N_b being the DAC physical resolution, and converted into a unique value of electrical current.

connected if the corresponding bit changes from 0 to 1). This power consumption depends on the parasite capacitance C_L of the current-steering architecture and is given by [18]:

$$P_d \approx \frac{1}{2} N_b C_L f_s V_{dd}^2 \tag{2}$$

Eq.(1) and Eq.(2) show that reducing the DAC physical resolution N_b is a promising solution for reducing the power consumption of the transmitter. Moreover, for metro networks, "lower cost hardware optimized for metro applications" have been identified as a top priority[6].

This manuscript

In that context, this manuscript assesses the possibility of using low-resolution DAC in metropolitan optical networks rather than the customarily used 8-bit DAC. I carried out my PhD under an industrial grant within Nokia Bell Labs (Nozay, France) and the *Laboratoire Charles Fabry* of the Institut d'Optique Graduate School (Palaiseau, France). This manuscript is organized in four chapters which present the work accomplished during these 3 years of research.

The first chapter describes the general architecture of an optical link. For the sake of generality, a coherent transmission is considered while the particular case of

[6]The IHS Markit Optical Network Strategies survey (released 31th January 2019), realized over 29 service providers over the world, indicates that ¡400 Gbit/s will represent 82% of the installed line ports while 400 Gbit/s and beyond transport solutions are available. Indeed, they place "lower cost hardware optimized for metro applications" at the top priority while "increased capacity per channel" comes only at the fourth priority. For long-haul systems, "increased capacity per channel" is the top priority, at any cost [19].

an intensity modulated with direct detection transmission is assessed in Chapter 4. After reviewing the basics elements of an optical link, the chapter offers a detailed description of an optical transmitter and focuses on the digital-to-analog converter, which is at the core of my work. It is an opportunity to explain how digital-to-analog converters allow the full exploitation of the coherent transmission potentialities. We also present the physical limitations of the digital-to-analog converters, especially in the case of a reduced physical resolution. Because of these limitations, the emitted signal suffers from detrimental distortions whose modeling and mitigation are reviewed based on state of the art solutions . Finally, the chapter introduces a performance model (mathematical tools, metrics) for the end-to-end optical link by considering the transmitter, the fiber and the receiver-induced distortions. It explains how the distortion coming from low-resolution digital-to-analog converters can be integrated into this model by treating it separately from the other distortions, rather than using the aggregated effective number of bits (ENOB) indicator.

The second chapter provides a detailed description of the distortions induced by low-resolution digital-to-analog converters i.e. the so-called *quantization noise* and *clipping noise* in order to establish a performance prediction model which aims at computing the optical link signal-to-noise ratio (SNR) when using low-resolution DAC and ADC. These two distortions are treated separately because of their different origins and influence on the system performance. After a review of the state of the art quantization noise theory, a statistical description of quantization noise is introduced and the assumptions to treat it as an additive noise uncorrelated with the signal are recalled. Regarding the clipping noise, a simple computation shows that it is correlated with the signal. However, this correlation is small enough when the amount of clipped values is optimized to maximize the low-resolution DAC performance such that it can be approximated as an additive noise. In addition, it is demonstrated both by numerical simulations and experiments that this model enables a prediction of an optical system performance using a low-resolution digital/analog converter in the practical situations. This model is necessary for our analysis of the performance optimization techniques presented in Chapter 3.

The third chapter reports on three optimization techniques to maximize the system SNR when using low-resolution DAC and ADC. First, a novel constellation phase rotation technique is presented. It aims at reducing the impact of the quantization noise when a pre-compensation of the chromatic dispersion is performed. The expected gains are verified experimentally. The two other techniques are borrowed

from the audio and radio domains. By exploiting the deterministic nature of the quantization, it becomes possible to filter the quantization noise such that its power spectral density within the signal bandwidth is strongly attenuated. This technique is known as noise shaping. A strategy to integrate it into an optical transmitter is presented and the achievable SNR gains when using a low-resolution DAC are demonstrated. The third technique, known as nonuniform quantization, consists in modifying the amplitude distribution of the quantization levels of the DAC, according to the input signal amplitude distribution. By a set of numerical simulations, we assess the achievable gains which are expected with this method when using a 4-bit DAC. Finally, a synthesis of these different methods is presented.

The fourth chapter presents two novel transceiver architectures adapted to short-reach or metropolitan optical networks. First, a innovative Faster-than-Nyquist (FTN) transceiver architecture is reported. In that case, the symbol rate is increased beyond the sampling frequency. It is demonstrated that 92 Gs/s high-speed DAC and ADC can generate up to 125 Gbaud signals without any precoding of the emitted signals, as it is customarily done in other FTN architectures. Second, a novel transparent transceiver architecture based on Sigma-Delta modulation (1-bit DAC) is presented. This transceiver aims at generating and demodulating signals which require a very high signal-to-noise ratio such as radio signals carried over optical fibers (Radio over Fiber). At the transmitter, it combines the use of a 1-bit DAC and the noise shaping technique presented in Chapter 3. At the receiver, rather than filtering the quantization noise resulting from the 1-bit quantization, we use it to recover the information signal in the limit of the signal-to-quantization noise ratio, possibly up to 60 dB.

Chapter 1

High speed optical communications

1.1 Motivations

In this chapter, we present the basics of high-speed optical communications. We review the latest research achievements both in short-haul or metro networks (<600 km) as well as in long-haul transmissions (>1000 km). Then, we focus on the transmitter which is one of the fundamental component of an optical link, and particularly on the DAC. We explain its role, its architecture and present an experimental procedure to highlight its physical limitations. Among them, we identify the *quantization noise* which becomes non-negligible when low-resolution DAC and symmetrically low-resolution ADC are used for cost or efficiency constraints in metro-networks. By low-resolution DAC/ADC, we refer to a quantizer for which the quantization noise is not negligible and must be considered when computing the optical link performance. We will see in section 1.3.4 that, in our case, this corresponds to a physical resolution of 5 bits or below. Finally, while the DAC and ADC distortions are usually aggregated, we explain why the resulting ENOB indicator is not the most relevant one in the context of low-resolution DAC and ADC and we propose an alternative way to model the distortions by isolating the quantization noise from the other physical limitations.

1.2 General design of an optical link

Any system of communication is composed of three fundamental elements that are specifically studied to act together and form a *link*, as depicted in Fig.1.1.

- the **transmitter** encodes the information, a sequence of 0 and 1, into a suitable signal that can be supported by the transmission channel. In optical communications, the transmitter is composed of a laser which can be directly or externally modulated by an electrical signal. In the first case the laser works in a non-continuous regime while in the second case the laser emits a continuous wave which is modulated by means of an external device (modulator). The binary data to be transmitted are transformed into digital waveforms which have specific characteristics, adapted to the transmission channel. This is performed with DSP operations. The DACs transform the digital waveforms into electrical signals which will feed the electro-optic modulator. See section 1.3 for more details.
- the **transmission channel** is the medium through which the information is carried from the transmitter to the receiver. In the case of optical networks the transmission channel is the optical fiber. To connect two points separated

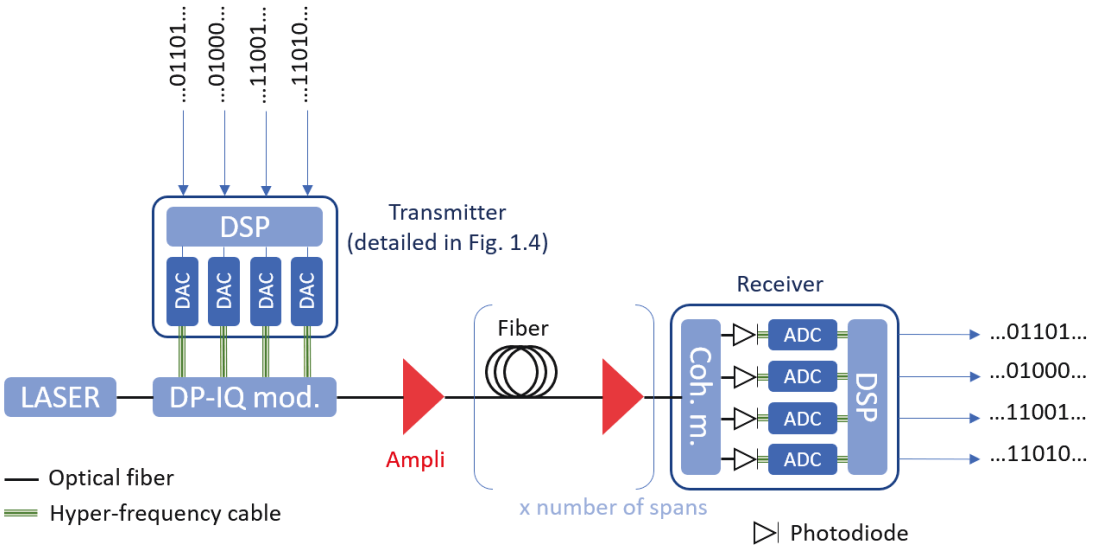

FIGURE 1.1: General optical link. DAC and ADC stands for digital to analog and analog to digital converter, respectively. DP-IQ-mod. stands for dual-polarization real and imaginary electro-optic modulator. Coh. m. is the coherent mixer which demultiplexes the real and imaginary components and the two polarizations of the optical field. DSP stands for digital signal processing.

by hundreds or thousands of kilometers, it is necessary to concatenate multiple optical fibers, each of them paired with an optical amplifier to compensate for the attenuation of the optical wave. The fiber between two amplifiers is called a span.

- the **receiver** transforms the optical signal into an electrical signal which is digitally processed. Modern optical systems transmit information on two orthogonal polarizations. At the receiver side, a coherent mixer enables the demultiplexing of the two polarizations as well as both their real and imaginary components. The four resulting optical fields are converted into electrical currents with photodiodes and then into digital waveforms with ADCs. Moreover, during its propagation the signal is deeply altered by various phenomena that take place in the transmission channel (attenuation, noise, distortion...). Hence, the receiver incorporates numerical algorithms that restore the initial shape of the signal and enable the retrieval of the transmitted information. In digital communications, such algorithms, collectively known as DSP, take place right after the conversion of the optical signal into an electrical signal by the photodiodes in optical receivers.

To cope with the ever-increasing demand in capacity, state of the art optical networks make use of the (only!) five *physical dimensions* available with optical electromagnetic waves, as shown in Fig.1.2:

- **time**. Originally, optical systems employed IM which consists in modulating the light intensity according to the 0 and 1 of the data stream. We then refer to on-off keying (OOK) modulation. When only two levels of intensity are allowed, the symbol rate is directly given by the modulation rate of the light intensity expressed in *Baud* or equivalently symbols per second. An evolution of OOK is to modulate the light intensity on four levels instead of two, carrying 2 bits per symbol and hence doubling the data rate (bits per second) at a constant symbol rate. This is the popular 4 levels pulse-amplitude modulation (PAM). The main interest of IM systems is the relatively low complexity, especially at the receiver side, because the measurement of the light intensity is achieved with a single photodiode, in a DD scheme[1]. The main drawback of IM/DD systems is that DD does not enable the electronic compensation for the chromatic dispersion (CD) because the optical field

[1]It must be noted that DD can be used together with amplitude and phase modulation through the implementation of a Kramers-Kronig receiver, which is a hot subject of research [20].

phase is lost with intensity measurement. This strongly limits both the achievable data rate and the propagation distance or requires the use of costly dispersion compensating fibers. However, with the booming of short-haul data traffic (see Introduction), tremendous efforts are made to increase the achievable data rates in IM/DD, leading to recent record-experiments with a data rate of up to 222 Gbaud OOK over 120 m [21], 204 GBaud OOK over 10 km [22] or 94 GBaud PAM-4 (186 Gb/s) over 2 km [23]. Along this line, this manuscript reports on a novel faster-than-Nyquist DSP technique for the next-generation 200 Gb/s IM/DD systems [24].

- **quadrature** (amplitude and phase). The renewal of the coherent receiver within this decade enables the recovery of the optical phase such that the modulation of the phase (and of the amplitude) has become a standard. In that case, each modulated symbol coincides with a given state in the complex plane, forming a *constellation*. Hence the data rate in bit/s scales with the number of accessible states, at constant symbol rate. For instance, quaternary phase-shit keying (QPSK) consists in modulating the optical field on four different states, generally $e^{i\frac{\pi}{4}}$, $e^{i\frac{3\pi}{4}}$, $e^{i\frac{5\pi}{4}}$ and $e^{i\frac{7\pi}{4}}$. The number of bits carried by each symbol is 2 and thus the data rate is twice the one of the OOK modulation at an equivalent symbol rate. By combining the modulation of both the phase and the amplitude, the number of states increases, for instance for the quaternary amplitude modulation (QAM) family. Commercial systems will employ up to 64-QAM at the symbol rate of 95 GBaud with a data rate of 400 Gb/s per polarization [25]. Although the QAM modulation is well-known, it has been revisited recently in the context

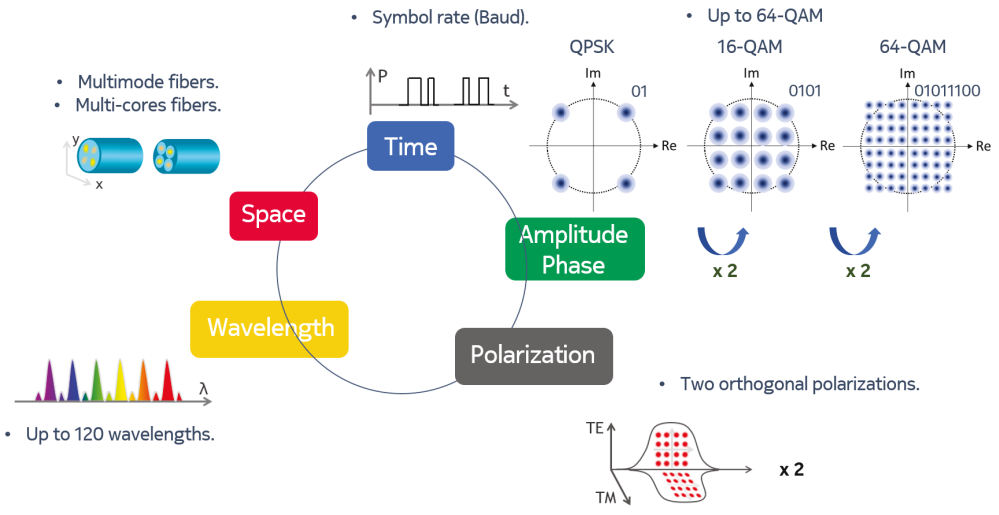

FIGURE 1.2: Properties of light used for modulation.

of long-haul transmissions. Indeed, it has been demonstrated (Shannon, 1949 [26]) that the fiber capacity under an additive white Gaussian noise (AWGN) can be maximized if the probability density function of the QAM symbols coincides with a Gaussian distribution. Thus, the binary data stream is mapped in the complex plane such that the symbols of low amplitude have a higher likelihood of appearing than the symbols of high amplitude. This process is called *probabilistic shaping* [27, 28] and helps reaching the Shannon limit in AWGN channels.

- **polarization**. Because the coherent receiver is also built to discriminate between polarization states, a phase and amplitude modulation is used jointly with a polarization division multiplexing (PDM). The optical field propagating in a fiber is characterized by a transverse electro-magnetic field[2]. The field can be decomposed in a basis of two orthogonal polarization states corresponding to the two orthogonal linear polarizations of the light. In practice, the light of a single laser source is separated into two paths that are independently modulated, creating a PDM signal. The two modulated optical fields are then recombined through a polarization beam splitter (PBS). At the receiver side the optical field is detected along two arbitrary polarization states with another PBS. These two polarizations are sampled and then processed by the DSP. However, one has to take into account that during the propagation, the injected polarization states rotate randomly during the propagation under mechanical stresses or other external perturbations applied to the fiber. Those perturbations are frequency-dependent such that the two polarizations experience polarization mode dispersion that must be recovered by the DSP. Moreover, at high power nonlinear effects introduce coupling between polarization states that propagate through the fiber, introducing an additional penalty [29]. Because PDM enables the doubling of the information rate for a given modulation format, with an affordable increase in DSP complexity, it has become a standard multiplexing technique combined with amplitude and phase modulation and it enables transmission of the order of the terabit per second (Tbit/s) [30].

- **wavelength**. Under a linear regime, two different wavelengths can propagate without interacting with each other. Thus, it is possible to carry different informations in different wavelengths (channels) inside the same optical fiber, as depicted in Fig.1.3. The different wavelengths, which are generated by different laser sources, are each modulated with a specific

[2]Under the weakly guiding assumption which is verified in all the situations of my thesis.

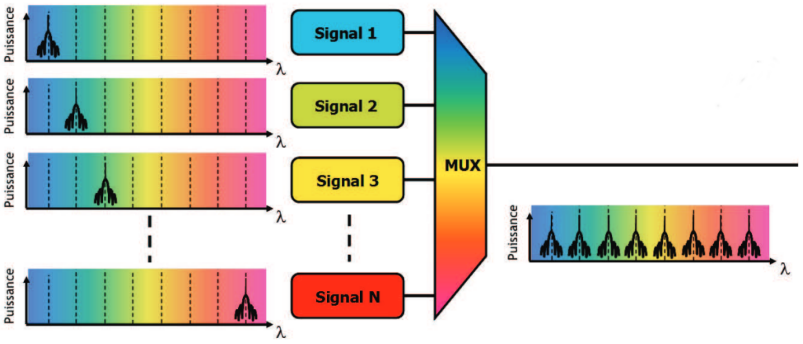

FIGURE 1.3: Principle of wavelength division multiplexing.

information, multiplexed at the input of the fiber and demultiplexed at its output (for instance by a diffraction grating). The initial data rate along the optical link is multiplied by the number of channels that co-propagate, typically between 80 and 120. When the nonlinear response of the fiber can no longer be neglected (under a high input power), channels interact with one another leading to signal distortions and to the degradation of the quality of the transmission. Thus the study of nonlinear effects is of huge importance in wavelength division multiplexing (WDM) optical networks. Because of the relatively broad low-absorption window of silica around 1550 nm as well as the existence of an efficient amplification technique such as the EDFA, WDM has become a standard technique and increases the fiber data rate up to a hundred Tbit/s when combined with the previously described modulation techniques [31, 32].

- **space**. The growth in the optical networks capacity has met the traffic demand in the past decade by taking advantage of all degrees of freedom available for light in single-mode fibers (SMFs): frequency, polarization, amplitude, and phase. To follow the increase in data traffic, further multiplicative growths must explore new degrees of freedom that do not exist in SMFs. The spatial division multiplexing (SDM) is one way to cope with the increasing data traffic. Many different approaches exist to propagate different spatial modes into the same optical fiber. With a multi-core fiber, each core carries a fundamental spatial mode while with a single-core fiber, different spatial modes propagate together within the same core. For more details on the SDM, one can refer to [33]. Recent research experiments indicate that the maximum number of cores in multi-core fibers for long-haul optical links is in the range 12-32 [34] while a record capacity of 159 Tbit/s has been reported for a 3-mode fiber (single core) over 1000 km

with 348 multiplexed wavelengths of 16-QAM modulated channels in each mode [35]. We observe that the scaling of the fiber capacity is not as high as expected compared to the single mode fiber. This is because of the very difficult integration of the multi-mode fiber into a fiber link, mainly due to mode multiplexing/demultiplexing difficulties and the huge DSP complexity required to mitigate for mode coupling, even in a linear regime of propagation [33].

1.3 The optical transmitter

1.3.1 Overview

The optical transmitter transforms a series of binary data (0 and 1) into a suitable signal that can be launched into the optical fiber. The general structure of an optical transmitter is shown in Fig.1.4 for the illustrative case of a single-channel PDM transmission (for WDM, all elements are repeated for each channel, all of them optically multiplexed at the transmitter output).

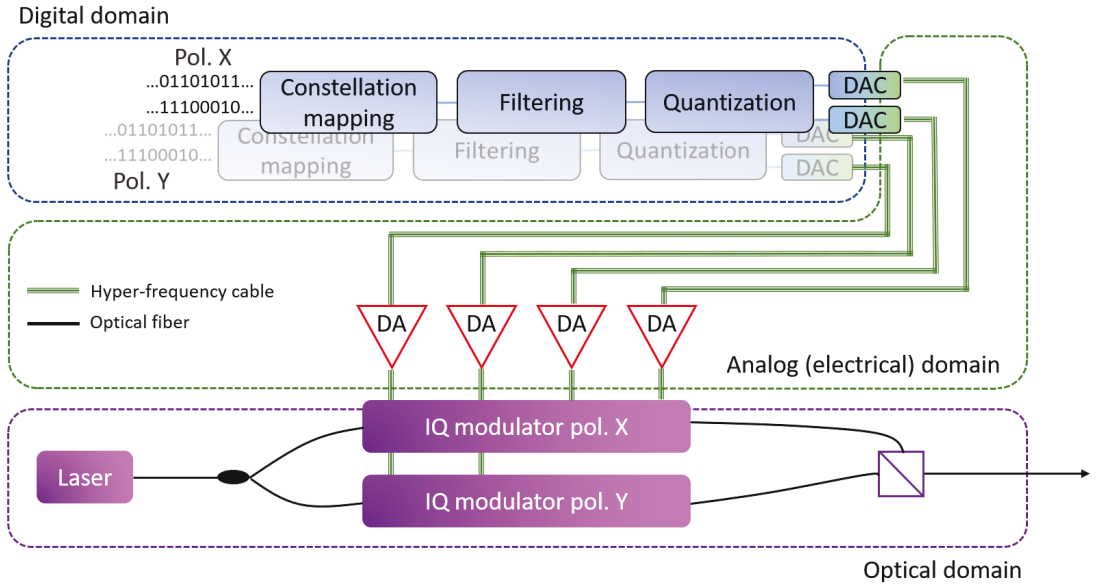

FIGURE 1.4: Optical transmitter for coherent single channel PDM transmission. For WDM the structure scales with the number of channels and they are optically multiplexed at the output of each transmitter. DA stands for driver amplifier and I/Q modulator for real and imaginary modulator.

In the digital domain, the binary data streams are mapped into points in the complex plane, according to the modulation format used for the transmission. This operation is called *constellation mapping*. For instance, when using 16-QAM, for each polarization each block of 4 bits is associated with one of the 16 possible states of the complex plane, as depicted in Fig.1.2. Each state is called a *symbol*. After the constellation mapping, the real and imaginary components of each polarization of the optical field are discrete multilevel signals. Unfortunately, these signals can not be suitably used in WDM transmissions because of the corresponding high spectral occupancy which limits the number of multiplexed channels. Indeed, the Fourier transform (FT) of a discrete symbol sequence follows a sinus cardinal like shape with a power spectral density (PSD) covering $2R$ Hz, with R the symbol rate[3]. We show in Fig.1.5 an example of binary symbols (-1 or 1) and the corresponding PSD with a sampling period fixed at 1/4 of the symbol period (4 samples per symbol). The width of the signal spectrum as well as the different lobes are particularly problematic when trying to multiplex several signals with different carrier frequencies. Hence, a filter which has a frequency response narrower than the one of the sinus cardinal is applied to the symbol sequence. For instance, if the symbol sequence is convoluted with a sinus cardinal, the resulting signal has a square-shaped PSD, as depicted in Fig.1.5, covering a fraction of R Hz of the optical spectrum. Hence, the spectral efficiency can be further improved by multiplexing more channels into a given spectral range with reduced cross-talk effects between them as side-lobes disappear. However, by doing this, the signal to be generated has a nearly continuous-amplitude such that a DAC is required for the conversion of the numerical waveform into electrical voltages.

1.3.2 The digital-to-analog converter (DAC) and the quantizer

The DAC aims at transforming digital series of data (a *digital waveform*) into the corresponding electrical voltages, suitable for the electro-optics modulators. Hence, it is a voltage generator. The digital waveforms represent the information to be carried into the fiber, which has been modified according to the link characteristics through the operations described before. For an IM/DD transmission, a single DAC is sufficient as the optical field is modulated along a single dimension (its amplitude). In coherent optical systems, the optical field is modulated along four dimensions (real and imaginary components of both polarization states) such that

[3]considering only the central lobe which contains more than 91% of the signal energy.

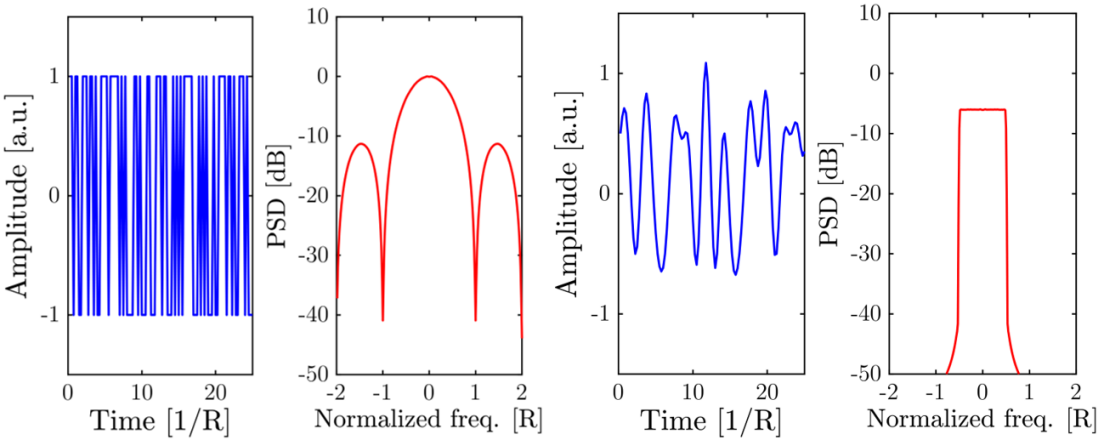

FIGURE 1.5: Numerical simulations. Temporal evolution and power spectral densities of a binary sequence at 4 samples per symbol without filtering (left curves) and with filtering (convolution with a sinus cardinal, right curves).

four DACs working in parallel are necessary. In this thesis, we used DACs produced by Socionext (formerly Futjitsu [36]) specifically designed for high speed optical communications. The electronic card consists in four identical DACs, sharing the same supply and clock circuitry. In all performed experiments, the clock reference was provided by an external synthesizer to reduce as much as possible the clock timing jitter influence (see subsection 1.3.4). The nominal physical resolution is 8 bits and the clock sampling frequency can be tuned between 88 and 100 Giga samples per second (GS/s). They have a memory size of 2^{18} samples, which are read and transformed continuously into analog voltages[4].

1.3.3 Physical limitations of the DAC

The electrical analog waveform at the DAC output always differs from its original digital version: the DAC introduces a *distortion* of the waveform, which arises from the following physical limitations [37]:

Bandwidth

The main limitation of the CMOS DAC used in optical communications is its electronic bandwidth. As shown in Fig.1.6, the bandwidth is of the order of

[4]In experiments, the memory length of the DAC fixes the minimum acquisition time needed to ensure that all the memory blocks are correctly read. At 88 GS/s, the 2^{18} samples correspond to 3 μs an acquisition length which is easily feasible with the employed oscilloscopes.

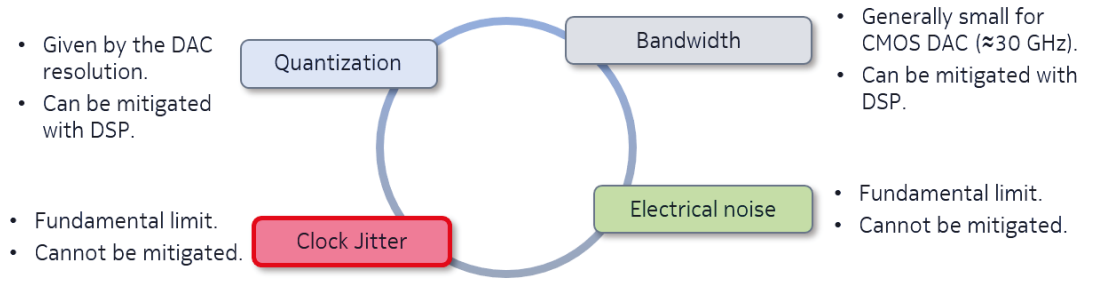

FIGURE 1.6: Physical limitations of a DAC (ADCs have the same limitation).

20 or 30 GHz (half-attenuation of the signal amplitude with respect to direct current frequency), limiting the spectral width of the generated signals and hence the achievable data rate. Moreover, the low-pass frequency response of the DAC can be aggravated by the low-pass frequency response of the driver amplifiers, the Mach-Zehnder modulator and also the receiver. Hence, without any specific compensation, the optical spectrum is strongly attenuated and modified at the output of the transmitter, resulting in a degradation of the quality of transmission. The problem of the limited bandwidth compensation has been widely assessed in 2014-2016 by Napoli et al. [38–41]. The limited bandwidth introduces a low-pass filtering of the signals, a linear operation represented in the digital domain by mean of finite impulse response digital filters. The principle of the bandwidth digital compensation, called *digital pre-emphasis*, consists in filtering the generated signals with a high-pass filter having a response as close as possible to the inverse of the total low-pass frequency response H_{DAC} of the DAC (and of the other transmitter elements if required). Customarily, it is a high-pass filter with a transfer function of the form [38]:

$$H_{pre}(f) = \frac{H_{desired}(f)}{H_{Tx\ total}(f) + c(f)} \tag{1.1}$$

where $H_{desired}(f)$ is the desired transfer function of the transmitter (the signal desired spectrum) and $c(f)$ an optimization constant[5] to avoid the divergence of the pre-emphasis filter when $H_{DAC}(f) \longrightarrow 0$. The pre-emphasis is done by a dedicated DSP block of the transmitter, as in Fig.1.4 and the effect on the emitted spectrum is shown in Fig.1.7. In [38], the authors report more than a doubling in reach when performing the digital pre-emphasis in commercial DACs for long-haul transmissions, confirming the algorithm efficiency to compensate

[5]One remarks that $H_{pre}(f)$ is the equivalent of the Wiener deconvolution filter in image processing [42], the constant $c(f)$ being the inverse of the signal-to-noise ratio at frequency f. When the signal to noise ratio tends to zero, $c(f) \longrightarrow \infty$ and the pre-emphasis is not applied on the emitted signal, as it would lead to a divergence of the signal power at the considered frequency.

for the transmitter-limited bandwidth. Hence, this technique is integrated in the DSP of many transmitters. We present in Fig.1.7 the frequency response of the DAC being used during my thesis as well as the corresponding pre-emphasis filter for which the constant $c(f) = 1/SNR(f)$ obtained from the characterization procedure described in section 1.3.4.

Electrical noise

The electrical noise refers to different distortions or noises, of electrical-device origin, which can be modeled as an additive white Gaussian noise. Indeed, even with a perfect mitigation of the DAC limited bandwidth and in absence of both the non-negligible quantization noise and the clock timing jitter, the SNR at the output of the DAC saturates. This persistent distortion originates from, for instance, the thermal noise of the electrical devices but also from the nonlinear distortion induced by the driver amplifiers and/or the Mach-Zehnder modulators [43]. The effect of these distortions is very similar to an AWGN [44] such that, for performance modeling, we can define a corresponding SNR: the signal-to-electrical noise ratio or SENR. When the output of the DAC is connected to an oscilloscope

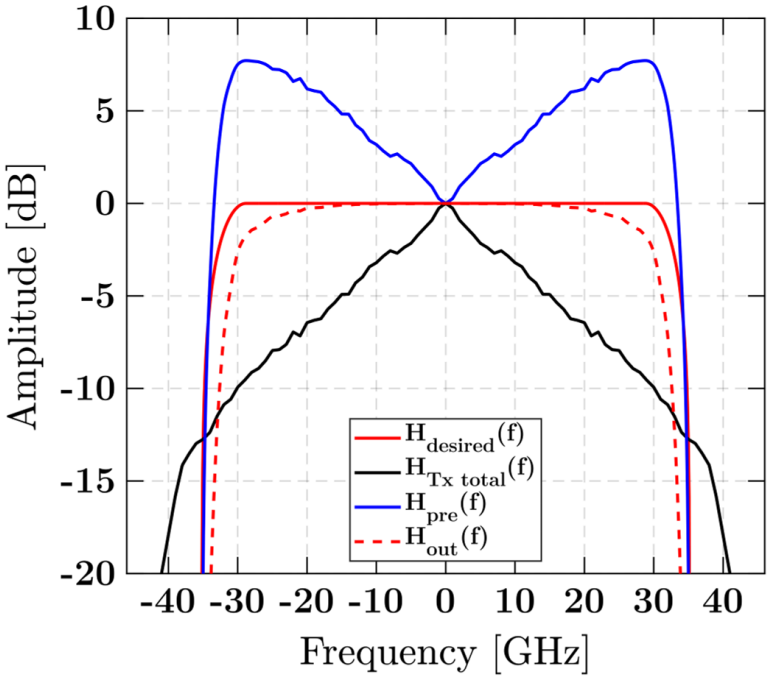

FIGURE 1.7: Effect of digital pre-emphasis on the spectrum of an emitted signal. The desired transfer function $H_{desired}$ is the signal ideal spectrum, here a 64 GBaud root-raised-cosine (RRC) filter with a roll-off factor of 0.1.

as in section 1.3.4, the electrical noise will correspond to the distortion observed in a sinusoid generated by the DAC at a very-low frequency ($H_{DAC} = 1$, clock timing jitter negligible) when the quantization noise is negligible (8 bit of physical resolution). In the present situation, this value is about 31 dB, measured in the experiment of section 1.3.4 (see Fig.1.14). Since in that case there is neither a driver amplifier nor a Mach-Zehnder modulator, this value corresponds to the internal noises of the DAC and the oscilloscope. In our optical back-to-back test-bed, the SENR rather saturates around 23 dB[6], as shown in Fig.1.8, such that the effects of the driver amplifiers, the Mach-Zehnder modulator and the coherent

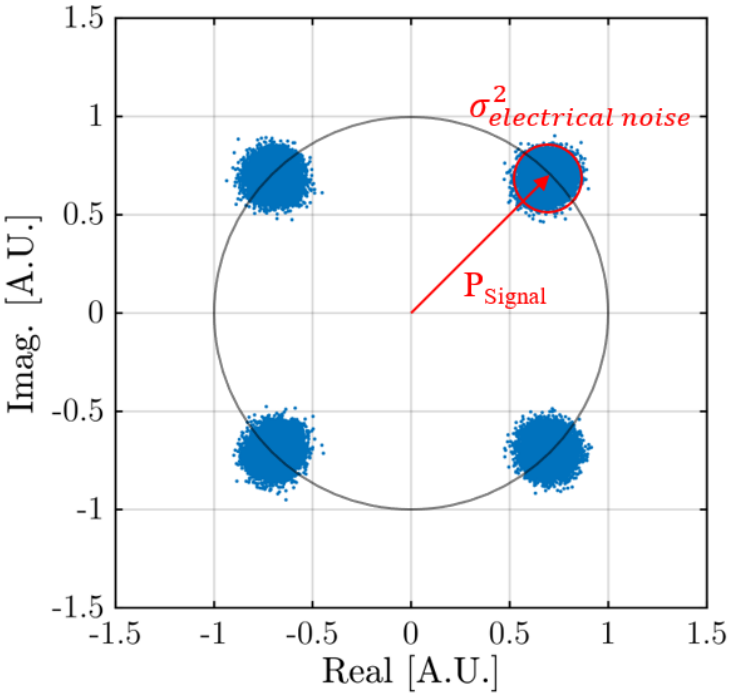

FIGURE 1.8: Experimental results. 32 GBaud QPSK signal after demodulation in an optical back-to-back test bed. The signal is filtered by a RRC filter with a roll-off factor of 0.2 and pre-emphasis as in section 1.3.3 efficiently compensate for both the transmitter and the receiver electrical bandwidth. The signal is quantized over 8 bits such that the quantization noise is negligible (see section 1.3.3) and the clock timing jitter is negligible (see section 1.3.3). Hence, the observed distortion coincides with the electrical noise of the transmitter and the receiver. The measured signal to electrical to noise ratio is ≈23 dB.

[6]This value depends on the data rate because of two effects. First, when the data rate increases, the equivalent bandwidth increases such that more noise is integrated for a constant signal power, hence reducing the SENR. Second, when the signal bandwidth increases, the pre-emphasis would not fully compensate for the limited bandwidth of the DAC, hence reducing the SENR.

receiver induce a decrease of the SNR by -6 dB, corresponding to an effective resolution of one bit.

Clock timing jitter

Another limitation is the clock timing jitter. Ideally, the samples at the output of a DAC are emitted at a regular time interval, kept equal to the inverse of the sampling frequency f_s. In practice, the sampling instant of each emitted sample follows a random distribution [45] because the clock circuitry of the converter is imperfect, especially in high speed electronic circuits operating around 100 GHz or beyond. Hence, the clock timing jitter is characterized by its *standard deviation*, which quantifies the random time drift with respect to the average sampling period. Back in 2017, authors in [46] showed that the effect of clock timing jitter can be accurately modeled by an additive noise whose variance depends on the signal derivative at the considered sampling instant. Same authors also showed its influence on the converter performance, especially at high frequencies [47]. This follows the intuition that, the more a signal fluctuates within a given time window, the more a drift in the sampling instant is detrimental. This can be explained by considering a sinusoid as a test signal:

$$s = A \cdot sin(2\pi f t_k + \phi_0) \tag{1.2}$$

with A the amplitude, f the frequency, ϕ_0 a constant phase and $t_k,\ k \in \mathbb{N}$ the ideal sampling instants. If the sampling instants are perturbed by a random variable ξ (each sample of this random variable being independent of the other) the resulting signal is:

$$s' = A \cdot sin(2\pi f(t_k + \xi(k)) + \phi_0) \tag{1.3}$$

which can be re-written:

$$s' = A \cdot sin(2\pi f t_k + \phi_0 + 2\pi f \xi(k)) \tag{1.4}$$

The effect of the clock timing jitter is then equivalent to a phase noise whose amplitude depends on the sinusoid frequency. For each emitted sample k, this phase noise translates into an amplitude noise $e(k)$ through the first order signal derivative:

$$e(k) = \frac{ds}{dt} \cdot \xi(k) = -A \cdot 2\pi f \cdot cos(2\pi f t_k + \phi_0) \cdot \xi(k) \tag{1.5}$$

whose variance is then:

$$\sigma_e^2 = \mathbb{E}\left[e(k)^2\right] - \mathbb{E}\left[e(k)\right]^2 \tag{1.6}$$

$$= \frac{A^2}{2} \cdot \pi^2 f^2 \cdot \mathbb{E}\left[\xi(k)^2\right] \tag{1.7}$$

This equation indicates that the variance of the amplitude noise due to the clock timing jitter is independent of the PDF of ξ but proportional to its variance[7] and grows quadratically with the signal frequency. We show in Fig.1.9 the effect of the clock timing jitter in a tone at different frequencies as well as the resulting amplitude noise, confirming the previous prediction. The independence of the amplitude noise with respect to the clock timing jitter PDF can be verified by a set of numerical simulations. The set-up reproduces a simplified optical back-to-back test bed where the receiver is assumed to be distortion free to only study

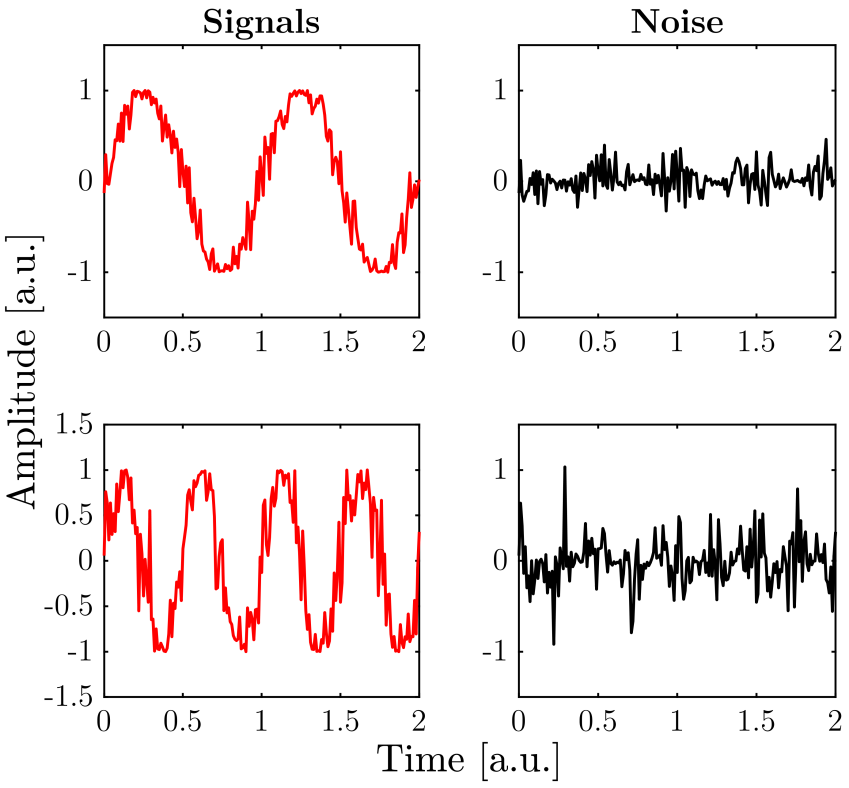

FIGURE 1.9: Representation of the clock timing jitter and its effect on a sinusoid with two different values of period T. The clock timing jitter standard deviation is fixed to 0.001 in the two cases such that it corresponds to 0.1% and 0.2% of T in the upper and bottom curves, respectively.

[7]To derive Eq.(1.7) we use the fact that the signal s is uncorrelated with the jitter noise ξ and that the jitter noise is of zero-mean.

transmitter impairments. The signal consists of a 64-QAM filtered by a RRC filter with a roll-off factor of 0.2 and generated at 2 samples per symbol, producing a data rate of 46 GBaud with a DAC clock frequency of 92 GS/s, to match with the experimental conditions. A pre-emphasis filter as described as in section 1.3.3 is applied to compensate for the measured frequency response of the DAC (see section 1.3.4). The amplitude noise due to the clock timing jitter can be retrieved from the output of the jitter emulator [37] which consists in the derivative model as in [46]. In Fig.1.10, we present the variance σ_e^2 of the amplitude noise as a function of the clock timing jitter standard deviation for a 64-QAM signal for two different clock timing jitter distributions (Uniform and Gaussian). These results clearly confirm that the clock timing jitter PDF has no influence on the resulting amplitude noise.

In [37], a systematic procedure to estimate[8] the clock timing jitter standard

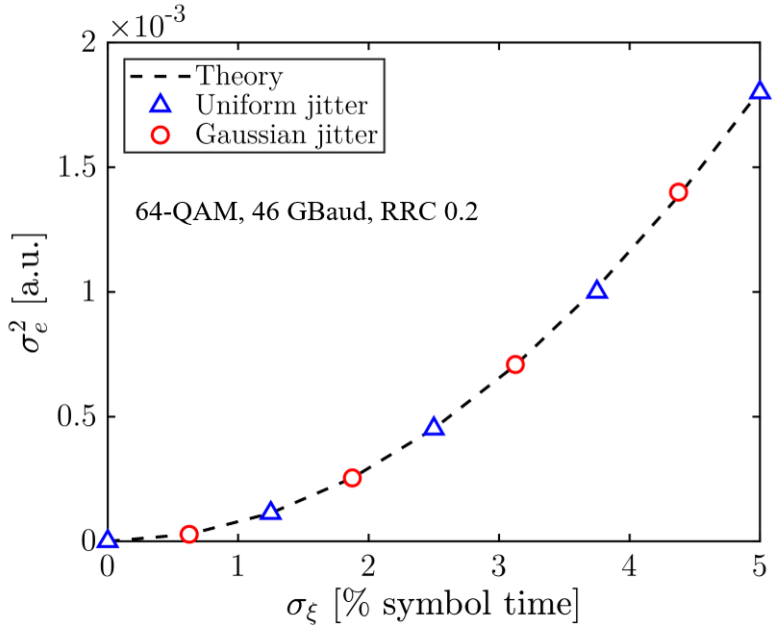

FIGURE 1.10: Numerical simulations from [37]. Variance σ_e^2 of the amplitude noise as a function of the clock timing jitter ξ standard deviation (in % of symbol time) for two different jitter probability density function (PDF): Uniform or Gaussian. The theoretical curve (black dashed line) is Eq.(1.5) in the form $\sigma_e^2 = \mathbb{E}\left[\left(\frac{ds}{dt}\right)^2\right] \cdot \mathbb{E}\left[\xi(k)^2\right]$.

[8] As we will see in section 1.3.4, we do not measure the clock timing jitter standard deviation following the *IEEE Standard for Terminology and Test Methods for Digital-to-Analog Converters* [48] but extract it from a measured effective number of bits (ENOB) versus frequency curve. While this method does not allow the measure of the clock timing jitter with precision, it helps to estimate its order of magnitude and to establish whether it is a limiting factor of performance for the link.

deviation is proposed (see section 1.3.4), and clock timing jitter requirements for 400 Gbit/s and beyond optical transceivers were established. We also showed that its influence on the overall system performance increases when the converter physical resolution is reduced, hence requiring a careful design of the clock for low-resolution DAC.

Physical resolution

A last limitation, which is at the core of my thesis work, is the physical resolution of the converter. Indeed, a DAC can generate only a limited number of electrical voltages such that a continuous-amplitude waveform cannot be exactly translated into its continuous-amplitude electrical representation, even in absence of any other distortions. The resulting distortion is the so-called *quantization noise* which sets an ultimate limit to the performance of DACs. The theoretical developments regarding the quantization noise have started in the late 1950's by Widrow [49] and continuous refinements have been undertaken up until the 1990's [50, 51]. In the context of optical communications, the quantization noise has not been an important subject of research until this decade, mainly because manufacturers of DAC proposed technical solutions with a sufficient resolution (8 bits) such that the quantization noise did not modify the overall system performance, as we will show in section 1.3.4. Theoretical and experimental works have been reported in the specific context of orthogonal frequency division multiplexing (OFDM) signals for which the Gaussian distribution of the emitted signals is an advantage to perform analytical studies, but at the cost of a loss in generality [52–54]. However, with the growing importance of metro networks (see Introduction), technical solutions to reduce the cost and power consumption of DAC are becoming of interest. Indeed, DAC (and ADC) represent up to 40 % of the DSP power consumption of a transceiver for metro networks [16] and one solution to cope with these tight constraints is to reduce their physical resolution [17]. However, the quantization noise contribution can no longer be neglected, impacting the system overall performance [55]. First, for instance, authors introduced in [56] an optimization technique to enhance the performance of low-resolution ADC. Second, the efforts focused on the transmitter side and 2018/2019 papers [57–59] report on optimization techniques to artificially enhance the performance of low-resolution DAC.

In the next section, we demonstrate that the quantization noise can be experimentally highlighted and discriminated from the other distortions. In Chapter 2, we will present an additive noise model which enables the quantitative prediction of

the quantization noise influence on the system performance when low-resolution DAC and/or ADC are used. This model is necessary to analyze the optimization techniques presented in Chapter 3.

1.3.4 Characterization of a DAC

The performance of a DAC is traditionally assessed by measuring the difference between a desired signal and the measured signal at the output of the converter. The test signal is a sinusoid whose frequency f is below the Nyquist frequency of the converter, i.e. $f_s/2$ with f_s the sampling frequency. The difference between the ideal sinusoid and the measured sinusoid reveals the distortion introduced by the converter at the considered frequency. A SNR at the converter output can then be defined as:

$$SNR(f) = \frac{P_{ideal\ sinusoid}(f)}{\sigma^2(f)} \tag{1.8}$$

with $\sigma^2(f)$ the variance of the distortion measured when the converter generates a sinusoid at a frequency f. The SNR is converted into an *effective resolution*, expressed in [bits], through the relation:

$$SNR(f)_{dB} = 6.02 \cdot ENOB(f) + 1.76 \tag{1.9}$$

where ENOB stands for *effective number of bits*. For instance, a converter with an ENOB of 2 bits at 46 GHz is able to generate a sinusoid at this frequency with a SNR of ≈13.8 dB. The definition of Eq.(1.9) finds its origin in the properties of the quantization noise. Indeed, as we will explain in Chapter 2, the quantization noise variance σ_q^2 of a converter is given by:

$$\sigma_q^2 = \frac{\Delta^2}{12} \tag{1.10}$$

where Δ is the quantization step. If the converter has a physical resolution of N_b bits, the sinusoid can have a peak-to-peak amplitude $N_b \cdot \Delta$ such that its average power is:

$$P_{ideal\ sinusoid} = \left(\frac{N_b \cdot \Delta}{2\sqrt{2}}\right)^2 \tag{1.11}$$

Combining Eq.(1.8) with Eq.(1.10) and Eq.(1.11) gives:

$$SNR_{dB} = 6.02 \cdot N_b + 1.76 \tag{1.12}$$

Hence, the ENOB at a given frequency f corresponds to the resolution of an ideal DAC, free of noise and distortions (except quantization), that would yield the same SNR as the DAC under test.

As an example, we perform the characterization of the Futjitsu DAC I used, following the experimental protocol defined in the IEEE Standard for DAC and ADC characterization [48]. This was presented in [37]. The memory buffer of one of the four DACs is loaded with a sinusoid of frequency f quantized over 8 bits (256 levels). To avoid any artifact at the beginning and at the end of the memory buffer, the frequencies of the sinusoid are such that the memory length (in time) of $2^{18} \cdot T_s = 2^{18}/f_s$ is an integer multiple n of the sinusoid period T:

$$n \cdot T = \frac{n}{f} = \frac{2^{18}}{f_s} \Longleftrightarrow f = \frac{n \cdot f_s}{2^{18}} \tag{1.13}$$

with n limited to 2^{17} such that $f < f_s/2$ to follow the Nyquist theorem. Hence, with a sampling frequency of 92 GS/s, the minimum frequency which can be generated is $92/2^{18}$ ≈350 kHz and the maximal one is 46 GHz. In what follows we vary the tone frequency between 1 GHz and 46 GHz. We consider that 1 GHz is the direct-current frequency (f≈0) because it is much lower than the cut-off frequency of the DAC. Also, to obtain the attenuation variation with frequency, we measure the attenuation of the other tones with respect to the amplitude at 1 GHz. To free ourselves from the driver amplifiers and the modulator distortions, we connect the output of the DAC directly to the electrical input of a real-time oscilloscope with 70 GHz electrical bandwidth and 200 GS/s sampling frequency. The performance of the oscilloscope has been characterized in previous experiments [60]. It exhibits a flat frequency response both in magnitude and in phase up to 70 GHz (a digital low-pass filter rejects any signal or noise above this frequency). Thus, we ensure that the signal attenuation comes from the DAC only. Moreover, to exclude the oscilloscope internal noise from the characterization, the variance of the noise is

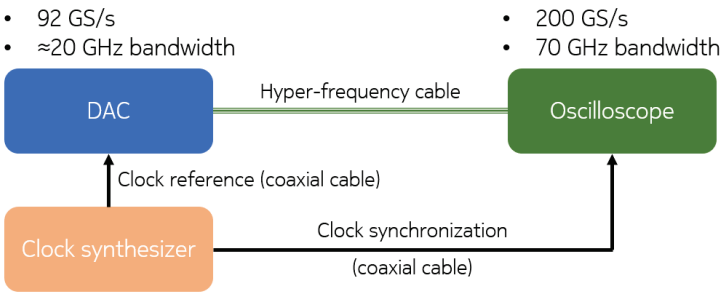

FIGURE 1.11: Experimental set-up for the ENOB measurement of a DAC.

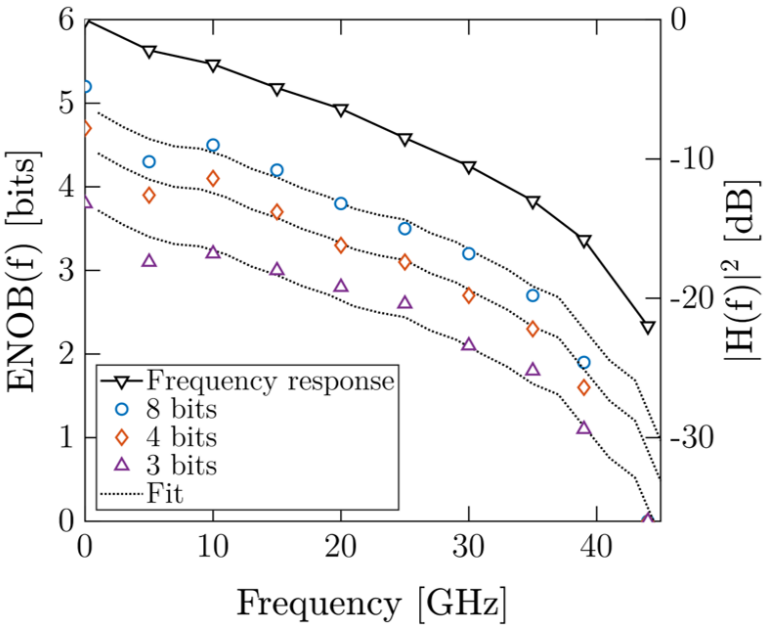

FIGURE 1.12: Experimental measurements. Evolution of the ENOB with frequency for various physical resolutions (symbols and dotted lines) and frequency response (symbols and solid line) of the DAC.

first measured in absence of any input signal and subtracted from the variance of the noise measured with the DAC. The experimental set-up is shown in Fig.1.11. Finally, to maximize the performance, an external synthesizer which acts as a clock reference for the DAC and the oscilloscope, which are thus simultaneously synchronized. By using a common external clock, we ensure that the DAC has a minimum clock timing jitter. Moreover, we do not need to perform a frequency estimation, i.e. a clock recovery algorithm, as the clock of the DAC and of the oscilloscope are synchronized. Hence, as the sinusoid is of known frequency, the recorded sinusoid is fitted with the 3-parameter method [61]. On the temporal trace, the variance of the distortion is the mean square error between the acquired signal and the fit.

The results of the characterization (ENOB and frequency response) are shown in Fig.1.12 for various physical resolutions. As proposed in [46], the ENOB versus frequency curves are fitted by a function of the form:

$$ENOB(f) = ENOB(f=0) + log_2(|H(f)|) - 0.5 \cdot log_2\left(1 + 6 \cdot \left(2^{ENOB(f=0)} \pi f \sigma_\xi\right)^2\right) \quad (1.14)$$

The term $ENOB(f = 0)$ gives the SNR for a sinusoid close to the zero

frequency and represents all the frequency-independent distortions. Indeed, as the oscilloscope does not attenuate the frequencies in the range of interest (0 to 46 GHz), the mean square error between the measured and the fitted sinusoid coincides with the overall distortion integrated over the whole Nyquist bandwidth of the DAC. In absence of a limited electrical bandwidth ($log_2(|H(f)|) = log_2(1) = 0$) and in absence of a clock timing jitter ($\sigma_\xi = 0$), the ENOB is frequency-independent. Indeed, the sinusoid variance at the DAC output is constant and the noise variance does not depend on the signal frequency.

The second term $log_2(|H(f)|)$ is the influence of the DAC frequency response. If the DAC distortions behave as a frequency-independent additive noise, a decrease of the signal power by a given factor corresponds to the same decrease of SNR. For instance, if the frequency response is $|H(f)| = 0.5$, the ENOB decreases by $log_2(0.5) = -1$ bit. This corresponds to a decrease in SNR by -6 dB because a division by a factor of 2 of the signal amplitude corresponds to a division by a factor of 4 of its variance such that the ENOB decreases by -1 bit, in accordance with Eq.(1.9). We remark that if the DAC is not perturbed by frequency-dependent distortions such as the clock timing jitter, the ENOB is proportional to the frequency response $|H(f)|$.

The last term of Eq.(1.14) accounts for the influence of the clock timing jitter, which can be modeled by a frequency-dependent additive noise. The complete derivation of this term can be found in [62]. It should be noted that the ENOB always decreases with the clock timing jitter and this effect is more pronounced at high frequencies. Then, when the effect of clock timing jitter is higher than the effect of the limited bandwidth, i.e. when $|log_2(|H(f)|)| \ll |log_2\left(1 + 6 \cdot \left(2^{ENOB(f=0)}\pi f \sigma_\xi\right)^2\right)|$, the ENOB decreases faster than the frequency response, as illustrated in the examples of Fig.1.13. In this figure, we show what would be the ENOB of our DAC for various clock timing jitter standard deviations, ranging from 0 to 500 femtoseconds (fs). This behavior is an indicator of the presence of a non-negligible clock-timing jitter. In our case, we observe that the curve of the ENOB versus the frequency follows the variations of those of the frequency response such that the clock timing jitter is negligible in this particular set-up, depicted in Fig.1.11, and for which an external synthesizer is employed to feed the clock circuitry of the DAC. This is consistent with the DAC datasheet which gives a typical clock timing jitter standard deviation of 50 fs (we recall that we only measure an order of magnitude with the presented procedure). This also indicates that the clock timing jitter of the oscilloscope is negligible as it

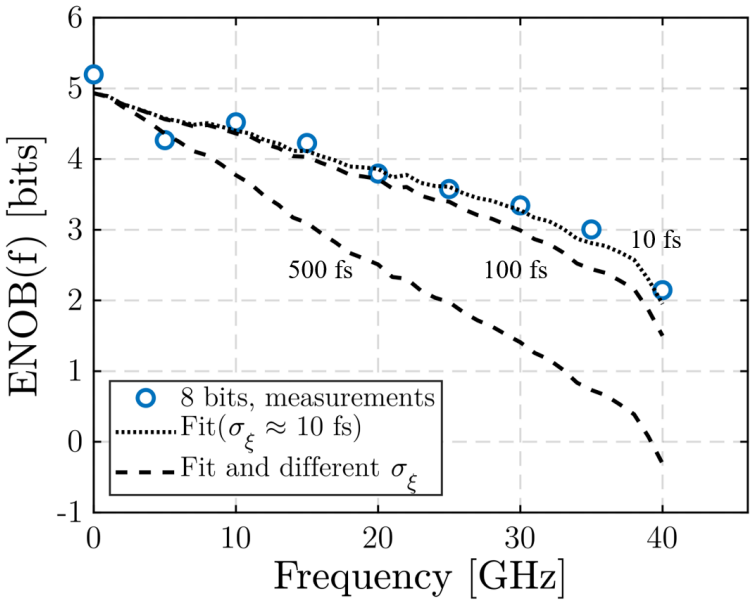

FIGURE 1.13: Experimental measurements and numerical exploration. Evolution of the ENOB versus frequency for a physical resolution of 8 bits and various clock timing jitter standard deviations. The dotted line corresponds to the results presented in Fig.1.12 for which the fit by Eq.(1.14) gives a clock timing jitter standard deviation $\sigma_\xi \approx 10$ femtosecond (fs). The dashed lines corresponds to different values of $\sigma_\xi = 100$ or 500 femtoseconds.

is included in our measurements (no discrimination between the DAC and the oscilloscope jitter).

Lastly, we also report in Fig.1.14 the ENOB evolution close to the zero frequency when varying the physical resolution between 3 and 8 bits. The physical resolution is modified by using only a reduced number of quantization levels (over the 255 available) during the offline quantization process. By doing so, we intentionally increase the variance of the quantization noise. Following the same procedure as previously, we fit the measured ENOB curves with Eq.(1.14) and extract the value of ENOB at $f = 0$. We first observe that the ENOB curves follow the same variations than those of the frequency response. This indicates that the quantization effect can be treated as an additive noise whose variance does not depend on the signal frequency. In Fig.(1.12), as expected, we observe that the ENOB decreases when the physical resolution of the DAC decreases. In addition, we observe that between 6 and 8 bits of physical resolution, the ENOB is constant and saturates. In such a regime, the distortions are mainly limited by the internal noise of the DAC, as our configuration minimizes clock jitter impairments. The SNR saturates around 31.5 dB, which corresponds to an ENOB of ≈4.96, according to Eq.(1.9). Since the quantization noise does not modify the performance of the

DAC resolution	ENOB(f=0) [bits]
3 bits	3.76
4 bits	4.46
5 bits	4.76
6 bits	4.96
7 bits	4.96
8 bits	4.96

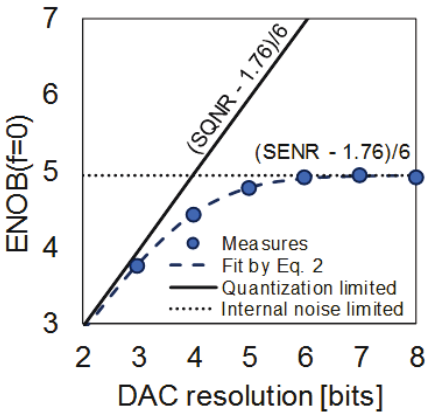

FIGURE 1.14: Experimental measurements. Evolution of the ENOB close to the zero frequency when reducing the DAC physical resolution.

DAC between 6 and 8 bits, those are considered high-resolution DACs. Conversely, for physical resolutions below 6 bits, the ENOB decreases with the physical resolution indicating that the quantization noise is not negligible. Those DACs are then considered low-resolution DACs. When the quantization noise strongly dominates, the ENOB evolves linearly with the physical resolution with a slope of +1 effective bit per physical bit. Finally, we observe that for a resolution of 4 bits the ENOB decreases by -0.5 bits corresponding to a -3 dB SNR reduction such that the quantization noise and the electrical noise are of same variance. In order to determine their respective contributions, the ENOB at $f = 0$ is fitted by a function of the form:

$$\frac{1}{6.02 \cdot ENOB(f=0) + 1.76 + C} = \frac{1}{SQNR} + \frac{1}{SENR} \tag{1.15}$$

with signal-to-quantization noise ratio (SQNR), the signal-to-quantization noise ratio for a sinusoid (Eq.(1.12)), which is known, and $SENR$ the signal-to-electrical noise ratio arising from the electrical noise of the DAC. We observe a very good agreement between the fit curve given by Eq.(1.15) and the measurements of Fig.1.14 allowing to find the value of $C = 0.96$ bits. This value corresponds to the *process gain* of the DAC. The process gain is the increase in performance due to the filtering of the noises by the low-pass transfer function of the DAC itself. It can be computed through the relation:

$$C = -\frac{1}{2} \cdot log_2 \left(\frac{2}{f_s} \int_0^{\frac{f_s}{2}} |H(f)|^2 df \right) \tag{1.16}$$

This effect explains why the ENOB can be greater than the physical resolution,

as in the present case. Finally, the agreement between the measurements and the fit expression in Eq.(1.15) shows that the quantization noise is uncorrelated with the electrical noise such that its contribution can be summed with the other distortions.

1.3.5 Comments on the ENOB indicator

As presented before, the ENOB contains all the useful information to characterize a DAC (or symmetrically an ADC). It allows the measure of the DAC transfer function and the estimation of the clock timing jitter standard deviation. Moreover, if the ENOB measurement is performed for various physical resolutions, it is possible to discriminate the influence of the two identified frequency-independent distortions: namely the quantization and the electrical noises. However, the ENOB indicator has several drawbacks which make it unappropriated for the performance prediction:

- the ENOB is frequency-dependent. Hence, a DAC or an ADC cannot be specified by a unique ENOB value but rather by an entire set of ENOB versus frequency values. This frequency dependence makes it difficult to use the ENOB as a performance indicator since the signal deviates from a sinusoid, having a broader spectrum. For instance, following the Fig.1.12 and assuming a signal spectrum that extends from 0 to 46 GHz, what is the ENOB that must be considered to predict the SNR? Or equivalently, how do the values of ENOB at different frequencies must be combined to produce a relevant value of SNR? These questions remain unanswered, to the best of the author's knowledge, and are let for further works.
- the ENOB of a DAC can depend on the DSP at the transmitter side. As we presented in section 1.3.3, a digital pre-emphasis can be applied to the emitted signal to counteract the effect of the low-pass frequency response. In that case, it is clear that the ENOB curve obtained with a sinusoid will not be representative of the system performance as the pre-emphasis improves the SNR at high frequencies. Another example is the noise shaping technique to be presented in Chapter 3. In that case the ENOB versus frequency distribution is deliberately modified in order to increase the SNR in a given part of the spectrum, while reducing it in another part.

This limits the use of the ENOB as a metric in a performance prediction tool.

1.4 Conclusion

In this chapter, we presented the basics of optical communications, with a system point of view, useful for the next chapters. Starting from the most recent state of the art, we highlighted the fact that all recent breakthroughs and record experiments involve the use of digital-to-analog and analog-to-digital converters since they enable the intensive use of the digital signal processing.

We then described the optical transmitter and focused on the digital-to-analog converter. We explained its role and described its physical limitations in terms of limited bandwidth, electrical noise, clock timing jitter and finally quantization noise. They act as distortions on the signal at the converter output. They can be highlighted and characterized through an experimental procedure which consists in measuring the signal-to-noise ratio, or equivalently the effective number of bits, following the generation of a sinusoid at various frequencies. We proposed to complete this procedure by adding a supplemental step which consists in varying the digital-to-analog converter physical resolution. Hence, it becomes possible to isolate the quantization noise from the other distortions. It was shown could be described by a frequency-independent additive noise. We further showed that, for our digital-to-analog converter, the quantization noise variance is equal to the variance of the other distortions when the physical resolution is equal to 4 bits. In that case, the signal-to-noise ratio decreases by -3 dB and the effective resolution decreases by -0.5 bit with respect to 8 bits physical resolution.

We also pointed out that the effective number of bits indicator cannot be used for the performance prediction because of its frequency dependence and because it aggregates distortions that arise from fundamentally different sources. This is the reason why we propose and develop, in the next chapter, a novel performance prediction model for optical systems employing low-resolution DACs and ADCs.

Chapter 2

Performance model for low-resolution DAC/ADC

2.1 Motivations

In this chapter, an additive noise performance model for end-to-end optical systems employing low-resolution DAC and ADC is developed [63]. The building of a precise, general and fast performance prediction model answers two objectives. First, to drive the design of optical systems employing low-resolution DACs and ADCs, it is necessary to know what are the maximum capabilities of any optical link in presence of low-resolution induced distortions (maximum modulation format, data rate, reach). Second, in the context of automated and re-configurable optical networks (elastic networking), the performance of the optical link must be computed almost instantaneously (1-100 ms) depending on the transmitter and receiver characteristics and configurations. If low-resolution DACs and ADCs are used, their effects on the end-to-end performance have to be taken into account with a fast and simple model . This is the purpose of this chapter. Hereafter, the transceiver induced distortions are modeled by an additive white Gaussian noise uncorrelated with the signal [64]. σ^2_{TRx} is denoted as the variance of this noise. Its contribution to the overall system performance can be added to the other contributions, since they are all assumed to be uncorrelated with one another:

$$\sigma^2_{tot} = \sigma^2_{ASE} + \sigma^2_{Kerr} + \sigma^2_{TRx} \tag{2.1}$$

with σ^2_{ASE} the noise variance induced by the amplified spontaneous emission generated by the EDFA and σ^2_{Kerr} the noise variance resulting from the accumulated

nonlinear distortions during propagation, under the assumptions of the Gaussian Noise model [65, 66]. The decorrelation hypothesis between the noises and the signal enables the definition of the SNR at symbol decision gate:

$$SNR \triangleq \frac{P_{Signal}}{\sigma^2_{tot}} \tag{2.2}$$

with P_{Signal} the power of the digital signal at the end of the receiver after the DSP operations and σ^2_{tot} the total variance of the noises within the signal bandwidth. Following the normalization of P_{Signal}, Eq.(2.2) yields:

$$\frac{1}{SNR} = \frac{1}{\mu}\left(\frac{1}{SNR_{ASE}} + \frac{1}{SNR_{Kerr}} + \frac{1}{SNR_{TRx}}\right) \tag{2.3}$$

with μ a parameter $0 \leq \mu \leq 1$ which accounts for the discrepancy between the system and its ideal representation. When $\mu < 1$, the SNR may differ from the direct accumulation of the contributed noise variances σ^2_{tot}. This difference originates from non-ideal filtering functions distributed along the transmission, notably at the receiver side [66]. In what follows, the transmitter and the receiver distortions are considered to be two uncorrelated noise sources[1]:

$$\sigma^2_{TRx} = \sigma^2_{Tx} + \sigma^2_{Rx} \tag{2.4}$$

Hereafter, I will highlight my contribution in extending this model to account for the distortions arising with the use of low-resolution DAC/ADC, i.e. when the so-called quantization noise becomes non negligible and modifies σ^2_{Tx} and/or σ^2_{Rx}.

2.2 Experimental observations

An experimental way of measuring σ^2_{TRx} is to set up an optical back-to-back (B2B) test bed. The optical transmitter is connected to the coherent receiver through a variable optical attenuator (VOA) followed by an EDFA, as depicted in Fig.2.1. Because the propagation length is very small compared to the nonlinear length we can safely assume that $\sigma^2_{Kerr} = 0$. The VOA enables the variation of the optical power at the entrance of the EDFA, which sets the optical power to feed the photodiodes of the coherent receiver. The lower the EDFA input power is, the more σ^2_{ASE} increases. The σ^2_{ASE} is estimated through the measured optical

[1] Actually, we assume that they are independent and hence uncorrelated (the reciprocal is false). However, as the uncorrelation is the only hypothesis needed to write equations of the form of Eq.(2.1) or Eq.(2.4), we only consider this sufficient condition.

signal-to-noise ratio (OSNR) by:

$$SNR_{ASE} = \frac{1}{\sigma^2_{ASE}} = \xi OSNR_{0.1nm} \tag{2.5}$$

The OSNR within an optical bandwidth of 0.1 nm (12.5 GHz) is measured with an optical spectrum analyzer through the method described in [64] and $\xi = 12.5/R$ is the conversion factor between the signal bandwidth R (in GHz) and the conventional amplified spontaneous emission (ASE) noise reference bandwidth of 12.5 GHz. As an example, we show in Fig.2.2 the measured SNR for a 16-QAM at 44 GBaud in the constellation at symbol decision for different σ^2_{ASE}. To highlight the effect of the quantization noise, the DAC physical resolution has been varied by using only a reduced number of quantization levels (over the set of 255 available) during the signal offline generation.

Under ASE dominant regime (left side of Fig.2.2) the SNR grows linearly with $1/\sigma^2_{ASE}$ and does not depend on the DAC physical resolution. Following Eq.(2.2), as the ASE contribution is reduced, the SNR saturates towards a value which increases with the DAC physical resolution. In the latter regime, transmitter and receiver distortions dominate over the σ^2_{ASE}. This result emphasizes the impact of the quantization noise on the SNR as the the DAC resolution is reduced (σ^2_{Rx} remains constant because the ADC physical resolution remained unchanged). Moreover, between 8 bits and 6 bits of physical resolution, we do not observe a significant variation of SNR_{TRx}. This is consistent with the experimental characterization of the DAC presented in Chapter 1 section 1.3.4, which shows a constant ENOB, and hence a constant SNR, when the resolution is comprised between 6 and 8 bits.

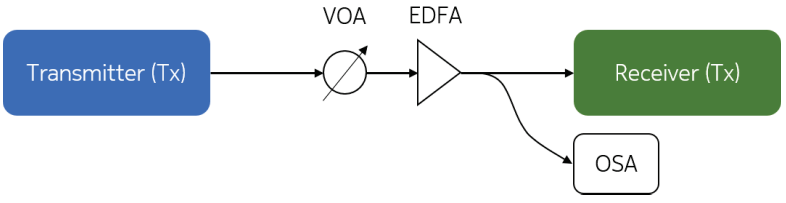

FIGURE 2.1: Optical back-to-back (B2B) set-up. The optical transmitter is connected to a variable optical attenuator (VOA) followed by an EDFA which delivers a constant optical power to feed the photodiodes of the coherent receiver.

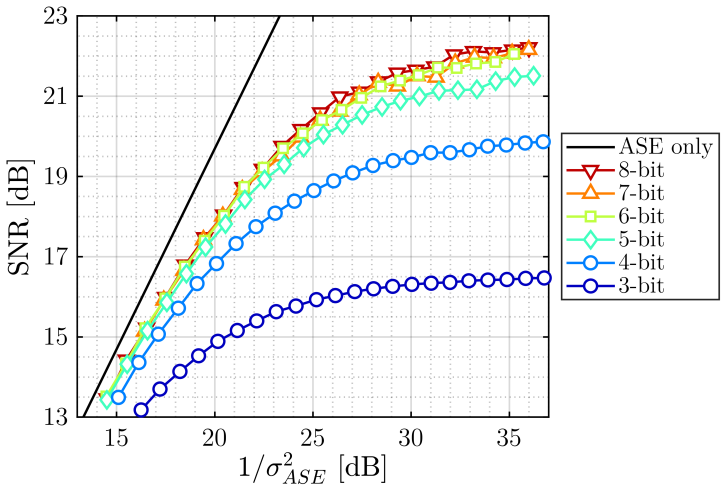

FIGURE 2.2: Experimental results. SNR evolution with $1/\sigma^2_{ASE}$ for different DAC physical resolutions. This signal is a dual-polarization 16-QAM at 44 GBaud RRC filtered with a roll-off factor of 0.02.

In the following, we intend to develop a consistent model for the transceiver distortions. To do so, we start by deriving σ^2_{TRx} as:

$$\sigma^2_{TRx} = \sigma^2_{Tx} + \sigma^2_{Rx} = \sigma^2_{DAC} + \sigma^2_{ADC} + \sigma^2_{TRx'} \tag{2.6}$$

where σ^2_{DAC} and σ^2_{ADC} are the variance of the distortions arising from the physical low-resolution of the DAC and the ADC, respectively, and $\sigma^2_{TRx'}$ the variance accounting for all the other distortions on the transmitter and the receiver sides[2].

2.3 Additive noise model for the quantizer

In this section, we introduce the notions of quantization and clipping as well as their corresponding noise contributions. A closed form expression of the SNR at the quantizer output will be derived, which can support both quantization and clipping effects[3]. In what follows, the quantizer is composed of a limited number of equally spaced quantization levels (uniform quantizer) coinciding with the possible level voltages at the DAC output. Each sample amplitude level is associated with the nearest available quantization level. The relation between the input signal

[2]It should be noted that $\sigma^2_{TRx'}$ in Eq.(2.6) corresponds to σ^2_{TRx} in the model developed in [64] where σ^2_{DAC} and σ^2_{ADC} were negligible because 8-bit DAC and ADC were employed.

[3]Sometimes, both quantization and clipping are grouped into the same term *quantization*. Here we discriminate the two noises and the reason will become clear hereinafter.

and the quantized output levels in a quantizer is shown in Fig. 2.3. When the amplitude of the input signal lies into the DAC dynamics, each sample is subject to rounding, i.e. *quantization*. On the other hand, when the sample amplitude is outside the DAC dynamic range, clipping occurs and the distortion induced in that case has other properties than the quantization noise. Note that we consider a unidimensional amplitude signal while coherent optical fields are composed of four amplitude signals (real and imaginary components of both polarization states). Indeed, all results obtained in these sections are valid for each component of the optical field, as they can be considered statistically independent and as the four signal components follow the same statistical properties.

2.3.1 Quantization noise, model and hypotheses

Signals are represented in digital computers or DSP machinery by sequences of finite bit-length numbers. In *Matlab*, numbers in double-precision floating-point

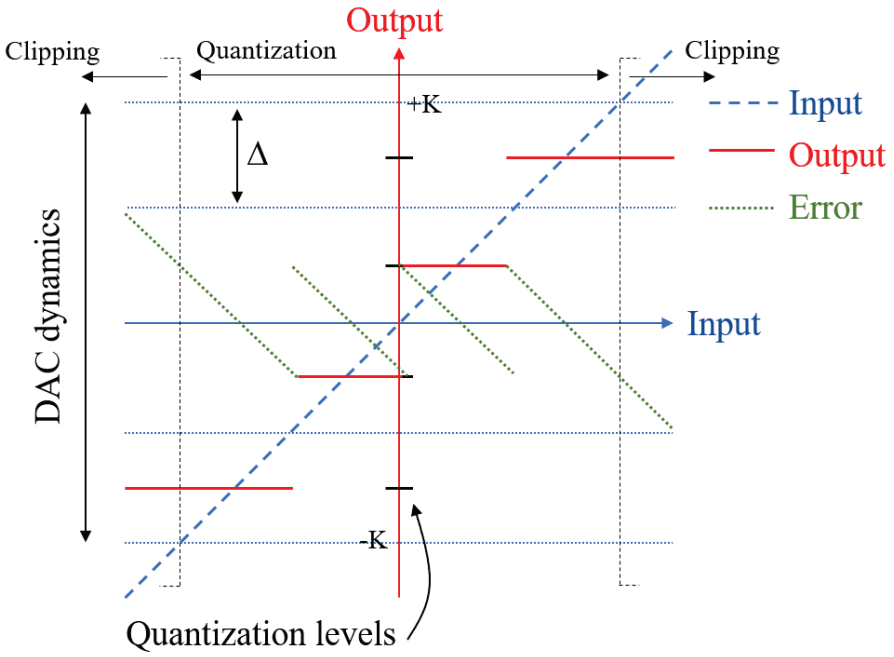

FIGURE 2.3: Schematic of the uniform quantizer. For illustration, with a physical resolution of $N_b = 2$ bits (4 quantization levels). The DAC dynamic range is the interval $\left]-2^{N_b-1}\Delta, -2^{N_b-1}\Delta\right[$. Within this interval, each sample is rounded to the nearest quantization level and the quantization error is bounded between $-\Delta/2$ and $+\Delta/2$ (quantization). Outside this interval, each sample is rounded to the nearest outer quantization level and the error is unbounded (clipping). K is the clipping threshold (see section 2.3.4).

format have their significant digits (*mantissa*) encoded into 53 bits, such that the precision is $2^{-53} \approx 10^{-16}$. This granularity is far smaller than any noise-induced fluctuations observable in optical systems. Hence, in what follows, we consider that our *Matlab* vectors of data are continuous-amplitude signals. On the other hand, the DAC resolution range is typically between 12 bits and 3 bits. Consequently, the mapping of the continuous-amplitude signals within the DAC available amplitude levels introduces an *irreversible* loss of precision, due to the rounding. The difference between the quantized signal s_q and its original continuous-amplitude version s is the quantization error q:

$$q = s_q - s \tag{2.7}$$

A first consequence of this definition is that the quantization is deterministic. Indeed, for each sample of the input signal s, the nearest quantization level is known and hence the corresponding quantization error. However, the quantization error cannot be carried together with the signal[4], such that it must be treated as a noise, at least from the receiver point of view[5]. Moreover, it is impossible to recover the continuous-amplitude signal from its quantized version, because quantization is a non-bijective relation. A second consequence of Eq.(2.7) is that the quantization error q is bounded between $-\Delta/2$ and $\Delta/2$ where Δ is the interval between two consecutive output levels of the quantizer, namely the quantization step, as depicted in Fig. (2.3). Thus, the quantization error increases with the quantization step, as illustrated in Fig. 2.4.

Despite its deterministic nature, it has been demonstrated that the quantization error can be modeled by a uniformly distributed noise, uncorrelated[6] with the input signal, and of white spectrum. In that case, the quantization error refers to the *quantization noise*. To establish this result, the signal PDF is considered, as proposed by Widrow in [50]. Strikingly, it is possible to find a unique sufficient condition on the input signal PDF such as the hypotheses (uniform distribution, uncorrelation with the signal and white spectrum) are simultaneously verified [50, 51]. The demonstration has been performed in two distinct steps, for which the principal results are presented. First, considering the PDF $f_s(x)$ of the continuous signal s and its characteristic function (CF) $\widetilde{f}_s(\nu)$, the necessary and sufficient condition for the quantization error to be uniformly distributed and of white

[4]Actually, we present in Chapter 4 a novel transceiver architecture in which the quantization noise of the transmitter is used (indirectly) at the receiver to demodulate the signal.

[5]The deterministic nature of quantization will be used in Chapter 3 to modify the spectral properties of the quantization noise.

[6]It is clear that Eq.(2.7) ensures that, even if the error is uncorrelated with the signal, they are statistically dependent.

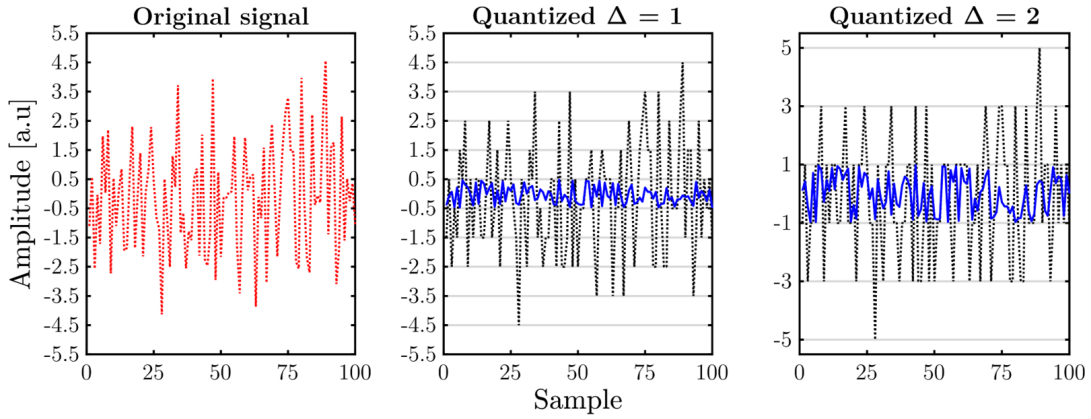

FIGURE 2.4: Numerical simulations. Left: Gaussian distributed random variable with $\sigma = 2$. Center and right: corresponding quantized waveforms (black dotted lines) and quantization errors (blue solid lines).

spectrum is[7]:

$$\widetilde{f_s}(\nu) = 0;\ \forall \nu = k\frac{1}{\Delta},\ k \in \mathbb{Z}^* \tag{2.8}$$

Equation (2.8) constitutes a *necessary* and *sufficient* condition for the quantization error to be modeled as an additive noise, uniformly distributed with a white spectrum. Second, the sufficient condition for the quantization error to be uncorrelated with the input signal is:

$$\frac{d\widetilde{f_s}(\nu)}{d\nu} = 0;\ \forall \nu = k\frac{1}{\Delta},\ k \in \mathbb{Z}^* \tag{2.9}$$

The demonstration can be found in [50, 51]. Thus, a *sufficient* condition for the quantization noise to be additive, uniformly distributed with a white spectrum, and uncorrelated with the input signal is:

$$\widetilde{f_s}(\nu) = 0;\ \forall \nu \geq \frac{1}{\Delta} \tag{2.10}$$

Consequently, if a signal has a bounded characteristic function in the range $]-1/\Delta; 1/\Delta[$, the quantization error is uniformly distributed, uncorrelated with the signal and of white spectrum. One remarks that the Eq.(2.10), known as Widrow quantizing theorem, looks like the Nyquist sampling theorem, but applied to the amplitude sampling rather than to the time sampling[8]. However, they are not

[7]The characteristic function is the Fourier transform of the density of probability $\widetilde{f_s}(\nu) = \int_{-\infty}^{+\infty} f_s(x)e^{2i\pi\nu x}dx$. Note that with the convention $\widetilde{f_s}(\nu) = \int_{-\infty}^{+\infty} f_s(x)e^{i\nu x}dx$ for the FT, $\frac{1}{\Delta}$ must be replaced by $\frac{2\pi}{\Delta}$ in Eq.(2.8) and Eq.(2.10).

[8]This results from the fact that quantization can be modeled as a sampling process of the signal PDF [50].

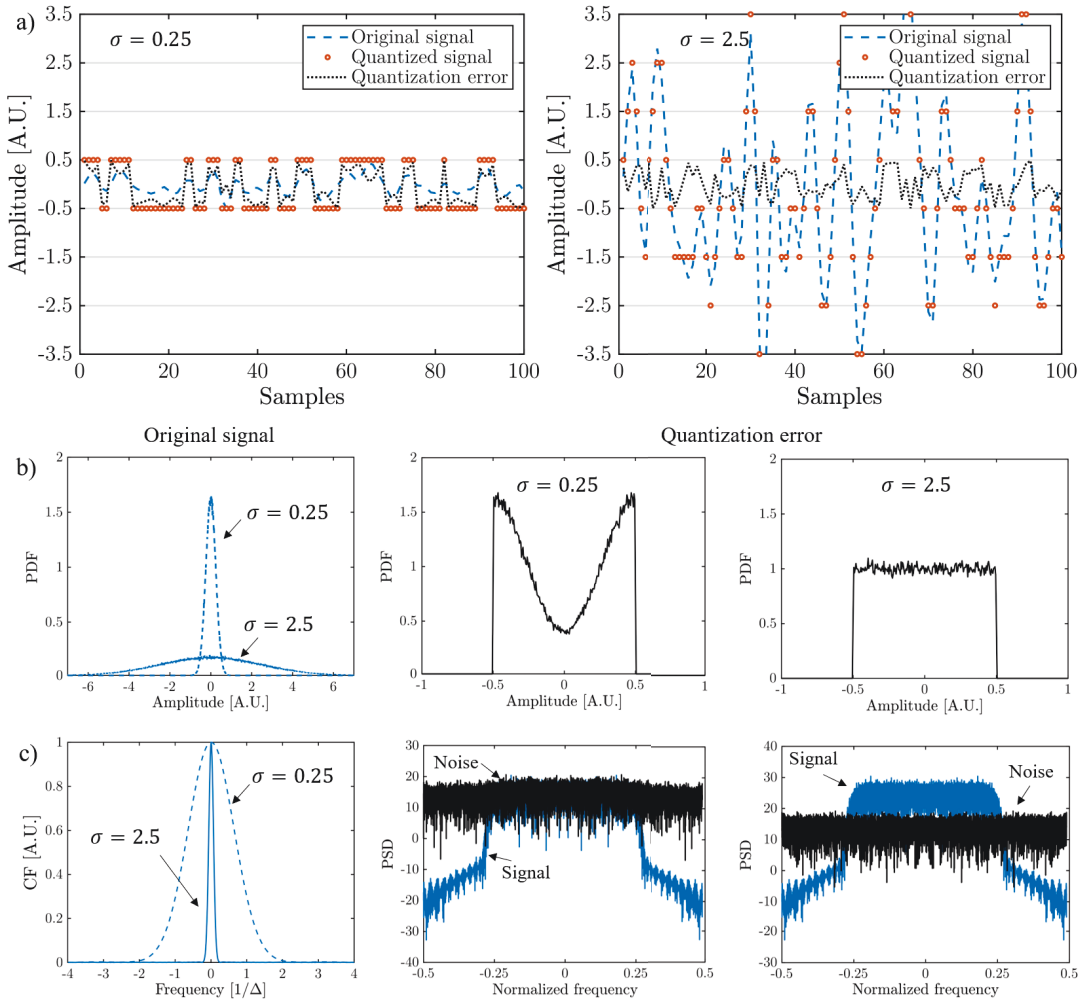

FIGURE 2.5: Numerical simulation. Quantization of a Gaussian random variable with two different ratios σ/Δ. a) Signals, quantized version and the corresponding quantization error. b) Left: PDF of the signal. Right: PDF of the quantization error. c) Left: characteristic function of the signal. Right: Signal and quantization noise spectra.

analogous since Eq.(2.10) indicates that the highest amplitude frequency in the signal CF can be up to the amplitude sampling frequency $1/\Delta$, and not half of it as for the Nyquist theorem.

The condition given by Eq.(2.10) can be understood by considering a simple but general example. Let us consider the quantization of a Gaussian distributed signal of arbitrary power spectral density whose variance is denoted σ^2. If the fluctuations of the signal are small or of the order of the quantization step Δ, i.e. $\sigma < \Delta$, the signal is quantized on a reduced number of quantization levels, as depicted on the left side of the Fig.2.5a. In that case, we remark that the quantization noise variations are similar to those of the signal, and does not seem uniformly

distributed, as plotted in the PDF reported in the central part of Fig.2.5b. Hence, the quantization noise spectrum might not be white, as the signal spectrum. This behavior was expected as the signal CF does not verify the Widrow condition given by Eq.(2.10) as $1/\sigma > 1/\Delta$ if $\sigma < \Delta$. As the signal variance increases, the quantization error becomes strongly different from the signal[9], as shown in the right plot of Fig.2.5a. In that case $\sigma > \Delta$ such that $1/\sigma < 1/\Delta$ and Eq.(2.10) holds with a good approximation. Moreover, and in such a case, the quantization error is uniformly distributed, as confirmed in the right plot of Fig.(2.5)c. Finally, when $\sigma \gg \Delta$, the fluctuations of the quantization error from one sample to its neighbors are uncorrelated such that it behaves like a white noise. This is the regime where Eq.(2.10) is verified. Finally, we report in Fig.2.5c the power spectral densities of the signal and the quantization error for the two investigated configurations. For $\sigma = 0.25\Delta$, Eq.(2.10) does not hold and the PSD of the quantization error is not white conversely to the case $\sigma = 2.5\Delta$ which verifies Eq.(2.10). Finally, the empirical correlation coefficient between the signal and the quantization noise is computed and found to be equal[10] to $\approx$0.45 for $\sigma = 0.25\Delta$ while it falls down to $\approx$0.0002 for $\sigma = 2.5\Delta$, confirming that the quantization noise is uncorrelated with the signal in the case where Eq.(2.10) holds with a good approximation.

When the Widrow quantizing theorem is verified, the variance of the quantization noise can be computed by:

$$\sigma_q^2 = \int_{-\Delta/2}^{+\Delta/2} x^2 f_s(x) dx = \frac{1}{\Delta} \int_{-\Delta/2}^{\Delta/2} x^2 dx = \frac{\Delta^2}{12} \tag{2.11}$$

2.3.2 Signal to quantization noise ratio

In section 2.3.1, we showed that, if the Widrow quantizing theorem holds, the quantization error can be modeled as an additive noise uniformly distributed. Following the previous derivation, a signal-to-noise ratio is computed from the quantization noise variance given by Eq.(2.11). As the quantization noise is uncorrelated with the signal, one can define the SQNR:

$$SQNR \propto \frac{P_{Signal}}{\sigma_q^2} \tag{2.12}$$

[9]Even if a Gaussian distribution cannot strictly fulfill Eq.(2.8) nor Eq.(2.10), the discrepancy is negligible in practice when $\sigma \geq \Delta$. For a detailed quantitative analysis, refer to [51].

[10]In average over 100 realizations of the Gaussian random variable.

As it will be clarified in section 2.3.3, Eq.(2.12) is only a proportional relation. Substituting the relation for σ_q^2, the relation for the SQNR in dB scale becomes:

$$\begin{aligned} SQNR_{\text{dB}} &\propto [P_{Signal}]_{\text{dB}} - 10 \cdot \log_{10}(\Delta^2) + 10 \cdot \log_{10}(12) && (2.13) \\ &\propto [P_{Signal}]_{\text{dB}} - 10 \cdot \log_{10}(2^{-2N_b}) + 10.79 && (2.14) \\ &\propto [P_{Signal}]_{\text{dB}} + 6.02 \cdot N_b + 10.79 && (2.15) \end{aligned}$$

in which the DAC or ADC dynamic range is normalized[11]: $2^{N_b}\Delta = 1$. Thus, the SQNR maximization consists in maximizing the signal power given its distribution and the available set of quantization levels. One solution consists in conditioning the input signal such that its maximum amplitude corresponds to the highest quantization level (amplitude normalization)[12]. In that case, it is convenient to write the signal power in terms of its peak-to-average power ratio (PAPR) defined by [67]:

$$PAPR(s(n)) = \frac{\max_n(|\, s(n)\,|^2)}{\mathbb{E}[s(n)^2]} \tag{2.16}$$

where $P_{Signal} = \mathbb{E}[s(n)^2] = \sigma_s^2$ because each signal (real and imaginary components of both polarization of the optical field) is of zero mean. Thus, Eq.(2.15) can be rewritten as:

$$SQNR_{\text{dB}} \propto 10 \cdot \log_{10}(\max_n(|\, s(n)\,|)^2) - 10 \cdot \log_{10}(PAPR) + 6.02 \cdot N_b + 10.79 \tag{2.17}$$

Because of the normalization $2^{N_b}\Delta = 1$, $\max_n(|\, s(n)\,|) = 0.5$ which finally leads to:

$$SQNR_{\text{dB}} \propto 6.02 \cdot N_b - PAPR_{\text{dB}} + 4.77 \tag{2.18}$$

The latter relation is a fundamental relation for the SQNR for a uniform quantizer with a normalized input signal. It underlines that the performance of the quantizer depends on both the quantizer resolution N_b and the PAPR of the input signal. It must be noted that if the signal is a sinusoid, then the PAPR is equal to 3.01 dB and Eq.(2.18) becomes:

$$SQNR_{\text{dB}} \propto 6.02 \cdot N_b + 1.76 \tag{2.19}$$

which is involved in the ENOB definition (see Chapter 1 section 1.3.4). The Eq.(2.19) must not be used if the signal is not a sinusoid.

[11] This arbitrary normalization explains why P_{Signal} is expressed in dB and not in dBm.

[12] As we will see in section 2.4, it is also possible to clip the signal but it requires to optimize the clipping factor.

To test the validity of Eq.(2.18), we need to perform the quantization of input signals with fixed PAPR. Moreover, the test signals must strictly follow Eq.(2.8) to avoid any approximation in the SQNR estimation. For this purpose, Bates random variables are used as test signals. They consist in the average of k identical and independent uniformly distributed random variables and they follow properties which are of interest for the verification of the quantization model. The first interesting property is that the PAPR of Bates random variables constantly increases with k:

$$PAPR(k)_{dB} = 4.77 + 10 \cdot \log_{10}(k) \tag{2.20}$$

The second interesting property is that the Bates random variables can strictly follow the validity condition for an additive noise model stated in Eq.(2.8)without any approximation. The demonstration of these properties is provided in Appendix A. The PAPR of different Bates distributions is illustrated in Fig.2.6, showing that the PAPR increases with the number of summed uniform random variables. The calculated PAPR is slightly smaller than expected (black dashed line) because of the finite length of the sequences. Indeed, if we increase the number of samples for each realization, the average PAPR increases and gets closer to Eq.(2.20), which assumes an infinite number of samples for each realization of the random variables[13].

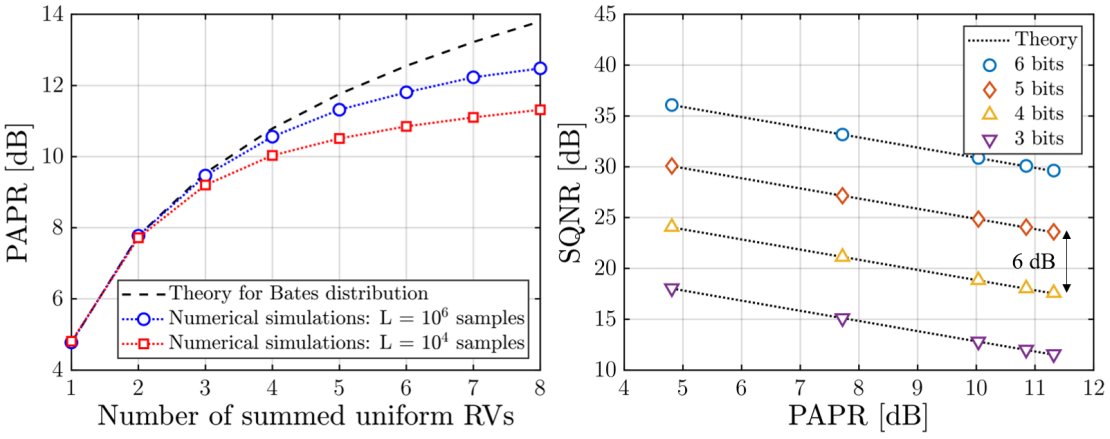

FIGURE 2.6: Numerical simulations. Left: PAPR (average over 100 realizations) of Bates distribution, consisting in the average of k identical and independent uniformly distributed random variables, with length $L = 10^4$ and $L = 10^6$ samples. Right: SQNR (average over 100 realizations of length $L = 10^4$ samples) evolution with the quantizer resolution N_b and the PAPR. In the right plot, the black dotted lines corresponds to the theoretical SQNR with Eq.2.18.

[13]This indicates that the PAPR must always be specified together with the number of samples considered in simulations or experiments

The evolution of the SQNR with the PAPR and the DAC resolution is highlighted through a set of numerical simulations. For each k value, 100 realizations of 10^6 samples are generated according to the Bates distribution. Each realization is normalized such that it occupies the full dynamic range of the DAC with 2^{N_b} equally spaced quantization levels. The quantization noise is extracted by applying Eq.(2.7) and enabling the computation of the (average) empirical SQNR through:

$$SQNR = \frac{\mathbb{E}[s]^2}{\mathbb{E}[s_q - s]^2} \tag{2.21}$$

We observe a complete agreement between Eq.(2.18) and the simulations. The curves highlight two fundamental trends: the SQNR is improved by +6 dB for one additional bit of resolution and follows a -1dB/dB slope with the input signal PAPR. The relation of proportionality in Eq.(2.18) corresponds to a vertical translation of the curves in Fig.2.6 and depends on the oversampling ratio, as shown in the next section.

2.3.3 Influence of the sampling frequency

Until now, we computed the SQNR by considering the variance of the quantization noise over the bandwidth defined by the sampling frequency of the DAC/ADC. However, the signal bandwidth is generally different such that the SQNR definition (or equivalently σ_q^2) must be corrected, implying a non strict equality for Eq.(2.18). When a quantization is performed on a signal recorded at the sampling frequency f_s, the quantization noise PSD is comprised between $-f_s/2$ to $+f_s/2$. On the other hand, if the signal spectrum occupies a bandwidth comprises between $-f_{Signal}$ to $+f_{Signal}$, with $f_{Signal} < f_s$, the out-of-band frequencies of the quantization noise will be rejected, at least by means of the receiver filtering. This situation is referred as *oversampling* in the literature.

Considering that Eq.(2.10) holds, the quantization distortion behaves as an additive white noise such that the effect of oversampling can be simply taken into account in Eq.(2.18). We consider that the signal is RRC filtered at the transmitter and RRC filtered at the receiver. Thus, the quantization noise of the DAC or the ADC is filtered by the receiver, as shown in Fig.2.7, such that the variance of the quantization noise $\sigma_q'^2$ to consider at symbol decision is:

$$\sigma_q'^2 = \int_{-\frac{f_s}{2}}^{+\frac{f_s}{2}} |\,\widetilde{\sigma_q}(\nu)\,|^2 |\,H_{rrc}(\nu)\,|^2 \, d\nu \tag{2.22}$$

with f_s the sampling frequency and $\mid \widetilde{\sigma_q}(\nu) \mid^2$ and $\mid H_{rrc}(\nu) \mid^2$ the PSD of the quantization noise and of the RRC filter, respectively. Because the quantization noise follows white spectrum within the bandwidth $\nu \in [-f_s/2, +f_s/2]$ we can re-write Eq.(2.22) in the form:

$$\sigma_q^{2'} = \frac{\sigma_q^2}{f_s} \cdot \int_{-\frac{f_s}{2}}^{+\frac{f_s}{2}} \mid H_{rrc}(\nu) \mid^2 d\nu \tag{2.23}$$

$$= \frac{\sigma_q^2}{f_s} \cdot \int_{-\frac{-R(1+\beta)}{2}}^{+\frac{R(1+\beta)}{2}} \mid H_{rrc}(\nu) \mid^2 d\nu \tag{2.24}$$

with β the roll-off factor of the RRC filter. A particularity of the RRC filter is that the integral of Eq.(2.24) is equal to R such that[14]:

$$\sigma_q^{2'} = \frac{\sigma_q^2}{f_s} \cdot R = \frac{\sigma_q^2}{SPS} \tag{2.25}$$

with SPS the number of *samples per symbol* of the DAC or the ADC. Injecting Eq.(2.25) into Eq.(2.11) leads to an extended version of Eq.(2.18):

$$SQNR_{\text{dB}} = 6.02 \cdot N_b - PAPR_{\text{dB}} + 4.77 + 10 \cdot \log_{10}(SPS) \tag{2.26}$$

which is now a strict equality and not a simple relation of proportionality. Customarily, the SQNR is expressed as:

$$SQNR_{\text{dB}} = 6.02 \cdot N_b - PAPR_{\text{dB}} + 4.77 + OSR_{\text{dB}} \tag{2.27}$$

where OSR_{dB}, the oversampling ratio (OSR) expressed in dB, is the ratio between the sampling frequency f_s and the noise equivalent bandwidth.

To test the validity of Eq.(2.26) a simulation has been launched following the block diagram depicted in Fig.2.7. The test signal s is a Gaussian distributed random variable which is oversampled and then filtered by a RRC filter with a roll-off $\beta = 0$ (convolution of the oversampled version s with a sinus cardinal impulse response). This step fixes the OSR. The signal is then processed through two dedicated paths. In path (1) the signal is quantized, followed by a RRC filtering, and down-sampled to its original sampling rate. Path (2) serves as a reference where the signal follows the same operations except the quantization step. By comparing the respected signals s_1 and s_2, we extract the quantization noise after filtering and down-sampling and compute the SQNR according to Eq.(2.26), for which

[14]It is equivalent to say that that the *noise equivalent bandwidth* of the RRC filter is R, the symbol rate.

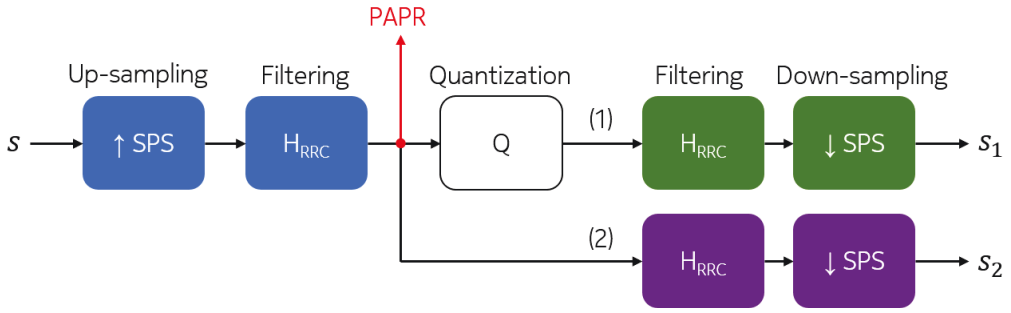

FIGURE 2.7: Numerical simulations set-up to highlight the effect of oversampling on quantization noise.

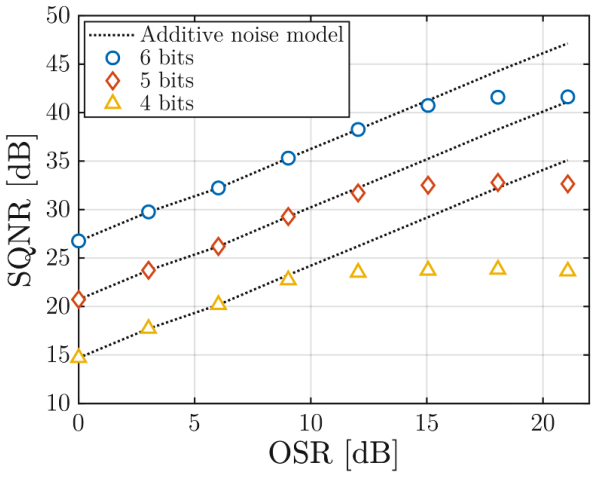

FIGURE 2.8: Numerical simulations. Evolution of the SQNR with the oversampling ratio and the quantizer resolution. The test signal is a vector of $L = 10^6$ samples following a Gaussian distribution of standard deviation $\sigma \gg \Delta$ such that Eq.(2.10) holds in a very good approximation and Eq.(2.26) can be used.

the PAPR is measured right before quantization. The results of the numerical simulations are shown in Fig.2.8 and analyzed as follows. For a small oversampling ratio (left side of the plot), the SQNR grows linearly with OSR, in accordance with Eq.(2.26). The increase by a factor of 4 (+6 dB) of the sampling frequency leads to a +6 dB improvement in SQNR. However, for high OSR values (>10 for 4-bit resolution), the SQNR saturates, which unveils a discrepancy with the model given by Eq.(2.26). This reveals a limitation of the statistical approach used to derive the SQNR formula, in which we ignored the time sampling process which occurs in conjunction with the quantization. Indeed, if the sampling frequency increases, a correlation between adjacent samples of the quantization error can appear, even if the Widrow theorem applies. In that case, the autocorrelation of the quantization

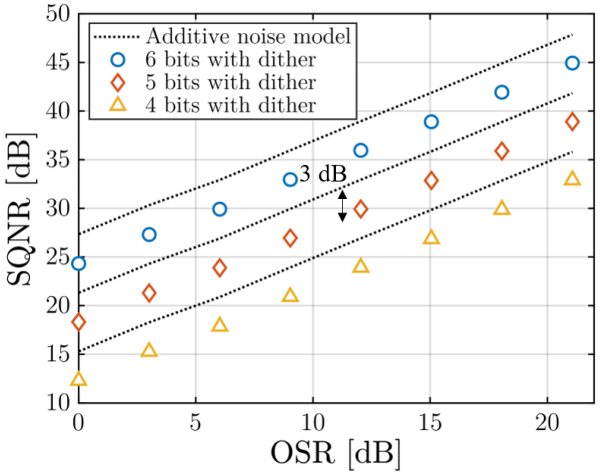

FIGURE 2.9: Numerical simulations. Evolution of the SQNR with the oversampling ratio and the quantizer resolution when dithering is applied. The test signal is a vector of $L = 10^6$ samples following a Gaussian distribution of standard deviation $\sigma \gg \Delta$ such that Eq.(2.10) holds in a very good approximation and Eq.(2.26) can be used.

noise differs from a Dirac delta and the PSD is not white. The discussion of this phenomenon can be found in [68] (Chapter 20) and the time-sampling condition for whiteness of the quantization noise (which adds to the Widrow theorem) is:

$$\frac{\sigma}{\Delta} > \frac{f_s}{5.3 f_N} \tag{2.28}$$

with σ the standard deviation of the signal input[15], f_s the sampling frequency and f_N the Nyquist frequency of the signal (highest frequency of its spectrum) with $f_N = 2B$, where B is the signal bandwidth. Hence, Eq.(2.28) can be re-written:

$$\frac{\sigma}{\Delta} > \frac{OSR}{10.6} \tag{2.29}$$

where $f_s/f_N = f_s/(2B) = OSR$ per definition. Thus, for each doubling in quantization step Δ (reduction by -1 bit of the physical resolution), the OSR for which Eq.(2.29) is verified is divided by 2 (or reduced by -3 dB), as confirmed by Fig.2.8.

To cope with this limitation, it is possible to force the input signal to have random variations of the order of the quantization step Δ. To do this, we add to the

[15]The derivation is done for a Gaussian input but we extend the result to other distributions, for clarity.

input signal an additive white noise uniformly distributed[16], of support Δ. Hence, the OSR equals 1 because the noise PSD covers the entire Nyquist band of the quantizer[17] and the right side of Eq.(2.29) is ≈ 0.1. Moreover, this noise has a standard deviation $\sigma = \Delta/\sqrt{12}$ such that $\sigma/\Delta \approx 0.3$. Thus, the time-sampling condition given by Eq.(2.29) is verified for any value of Δ and any OSR. In that situation, the SQNR grows linearly with the OSR, as confirmed by Fig.2.9, which depicts the SNR with noise addition at the quantizer input. One notes that, with respect to the quantizer without noise addition, the SQNR is reduced by -3 dB as a noise of same variance than the quantization noise is added at the quantizer. However the SQNR saturation disappears.

Within this thesis, we will either work with small OSR values (typically less than 5), because increasing the OSR will be further detrimental for the data rate, or either perform quantization with applying noise shaping (see Chapter 3, section 3.3). The later consists in re-injecting the quantization noise at the DAC input and hence implicitly performs dithering. Thus, Eq.(2.26) remains our basic formula for the SQNR performance prediction in absence of clipping. However, performing the quantization without any clipping generally does not maximize the quantizer performance. That is why clipping is generally applied to the input signal. Thus, a prediction model to account for this distortion needs to be developed, and this is the purpose of the next section.

[16]This process is called *dithering*, and one remarks that adding at the DAC input a uniform noise of support Δ forces the signal to follow the Widrow theorem. Indeed, adding two signals corresponds to the convolution of their PDF and to the multiplication of their CF. Hence, adding a uniform noise of support Δ at the entrance of the DAC makes both Eq.(2.8) and Eq.(2.10) verified.

[17]We refer here to the OSR for the signal plus the noise (DAC input), while the analysis in SQNR (DAC output) is still performed with respect to the OSR relative to the signal only, and reported in Fig.2.9.

2.3.4 Clipping noise

Previously, the signal PDF coincided with the quantizer dynamic range. However, as shown later in this chapter, this configuration does not maximize the SNR at the output of a low-resolution DAC/ADC. Indeed, it is possible to spread the signal PDF outside the quantizer dynamic range in order to optimize the SNR at the output of the low-resolution DAC/ADC. So, the digital signal power is artificially increased with respect to the quantization noise variance. However, the samples that fall outside of the quantizer dynamic range are "clipped" and the resulting distortion refers to the clipping noise, whose properties drastically differ from that of the quantization noise. The purpose of this section is to highlight the basic properties of the clipping noise and to include its influence on our performance model through the introduction of a signal to clipping noise ratio (SCNR).

For a signal s , the clipped signal s_c is expressed mathematically as follows:

$$s_c(i) = \begin{cases} s(i), \text{ if } |s(i)| \leq K \\ sign(s(i)) \cdot \left(K - \frac{\Delta}{2}\right), \text{ if } |s(i)| > K \end{cases} \tag{2.30}$$

Such that the clipping noise $c = s_c - s$ is:

$$c(i) = s_c(i) - s(i) = \begin{cases} 0, \text{ if } |s(i)| \leq K \\ sign(s(i)) \cdot \left(K - \frac{\Delta}{2}\right) - s(i), \text{ if } |s(i)| > K \end{cases} \tag{2.31}$$

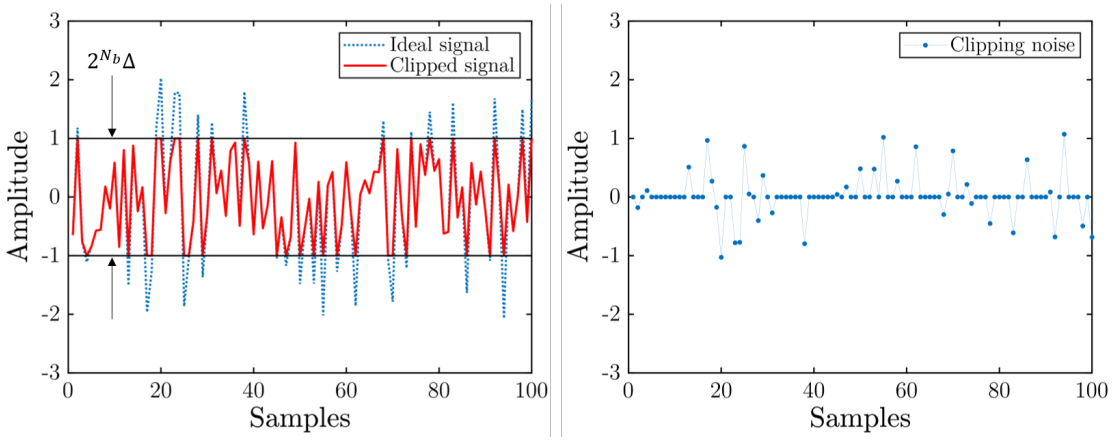

FIGURE 2.10: Numerical simulations. Clipping of a Gaussian random variable with the clipping factor $C = \sigma/(2^{N_b}\Delta) = 0.5$. Note that $2^{N_b}\Delta$ is the quantizer dynamic range and $\sigma = 1$ in this example.

One remarks that, with this definition, the samples subject to clipping are not subject to quantization because they are mapped to the nearest outer quantization level by the clipping. The clipping process is illustrated in Fig.2.10 for a Gaussian distributed signal with a standard deviation $\sigma = 1$ and $\Delta = 0$ (infinite resolution), for generality. In what follows, we define the clipping factor C:

$$C = \frac{\sigma}{2^{N_b}\Delta} \tag{2.32}$$

with $2^{N_b}\Delta$ the quantizer dynamic range (number of levels times quantization step). In practice, we choose to clip the signal before entering the quantizer such that the clipping noise and its variance σ_c^2 is extracted before quantization[18].

As for the quantization noise, we want to define a signal to clipping noise ratio from the clipping noise variance. This preliminary requires to demonstrate that the clipping noise is additive, uncorrelated with the signal and has a white spectrum (this last condition is not necessary to define the SNR but can greatly simplify the analysis). From the clipping noise definition given by Eq.(2.31), it is clear that

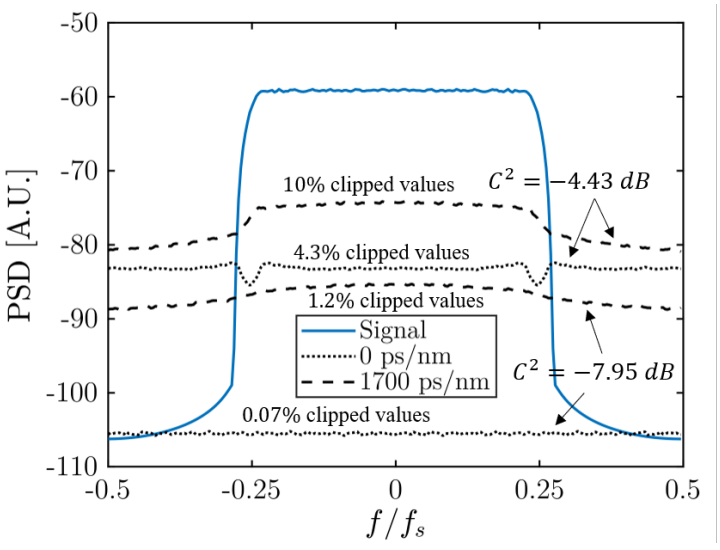

FIGURE 2.11: Numerical simulations. Spectra of the clipping noise, right after the clipping process. The test signal is a 16-QAM symbol sequence generated at 2 sample(s) per symbol (SPS) and RRC filtered with roll-off factor 0.1 and clipped according to Eq.(2.30).

[18]This is possible only at the transmitter side as the signal prior to clipping is known. At the ADC, the estimation of the clipping noise variance requires to estimate the signal PDF from its quantized version. This problem is let for further investigations. However, in the experiments reported after, the low-resolution ADC is emulated in the digital domain. The clipping is performed on the recorded waveform (without clipping) with 8-bit physical resolution and the clipping noise is computed digitally.

the clipping noise is additive. Regarding the spectral distribution of the clipping noise, Fig.2.11 reports the power spectral density of the ideal signal together with the PSD of the clipping noise for two different clipping factors. The test signal is a 16-QAM generated at 2 SPS and RRC filtered with a roll-off of 0.1. For each clipping factor, we also apply the chromatic dispersion operator to modify the signal PDF and emulate a typical ADC situation (Gaussian distribution at the quantizer input). For $C^2 = -7.95$ dB and without CD, the number of clipped values is about 0.07 % of the total number of samples. The corresponding clipping noise PSD is white. Actually, for very small clipping factors, only a very small number of clipped values occurs. The clipping noise can then be described as an impulsive noise. Thus, the clipping noise consists in a train of Dirac deltas, separated by long sequences of zeros, which in the spectral domain provides a white noise.

However, when the amount of clipped value increases (when the signal is dispersed at the quantizer input, black dashed lines in Fig.2.11, or when the clipping factor is increased to $C^2 = -4.43$ dB), the PSD of the clipping noise is colored. Hence, the clipping noise cannot be considered as an additive white noise in these situations. We understand this by analyzing the extreme case with a clipping threshold which tends to zero (almost all the signal samples clipped) and for which the clipping noise will be the opposite of the signal (see Eq.(2.31)). Hence, its PSD will possibly not be white.

However, for a small amount of clipped values (of the order of 1 % or below), we assume that the clipping noise is a white noise. We do not assess the question of its distribution in the complex plane as our analysis of the system performance restricts to the SNR. However, even under the white noise assumption, we still have to assess the problem of the correlation between the clipping noise and the signal. The correlation between the clipping noise and the quantization noise is also studied in order to be able to combine both the SQNR and the signal-to-clipping-noise ratio (SCNR). This is the purpose of the next subsection.

Correlation of the clipping distortion with the signal and the quantization noise

To treat the clipping distortion as an additive noise, we have to check whether the clipping noise is uncorrelated with the signal. From the definition of the clipping given by Eq.(2.31), it is clear that the clipping distortion is additive. However, Eq.(2.31) also indicates that the clipping distortion is correlated with the signal.

To confirm this, one can compute the empirical covariance between the clipping noise c and the signal s[19]. Explicitly, because the signal and the clipping noise are of zero mean[20], one can write the empirical estimation of the covariance for one realization of the signal and of the clipping noise[21]:

$$Cov(s,c) = \frac{1}{n}\sum_{i=1}^{n} s(i)\cdot c(i) \tag{2.33}$$

with $s = s(i)$ and $s_c = s_c(i)$ with $i = [1, 2, ..., n]$, a realization of the signal and its corresponding clipping distortion, respectively. From the previous equation, we can rewrite Eq.(2.33):

$$Cov(s,c) = \frac{1}{n}\sum_{i'} s(i')\cdot c(i') \tag{2.34}$$

where this new summation runs over the i' elements of i for which clipping occurs. Hence:

$$Cov(s,c) = \frac{1}{n}\sum_{i'} s(i')\cdot(sign(s(i'))\cdot\left(K-\frac{\Delta}{2}\right)-s(i')) \tag{2.35}$$

$$= \frac{1}{n}\sum_{i'} |\,s(i')\,|\cdot\left(K-\frac{\Delta}{2}\right)-\frac{1}{n}\sum_{i'} s(i')^2 \tag{2.36}$$

Because clipping occurs when $|\,s(i)\,| > K$ and hence $|\,s(i)\,| > \left(K-\frac{\Delta}{2}\right)$, the first sum of Eq.(2.36) is strictly bounded by the second sum:

$$\sum_{i'} |\,s(i')\,|\cdot\left(K-\frac{\Delta}{2}\right) < \sum_{i'} s(i')^2 \tag{2.37}$$

And finally:

$$Cov(s,c) < 0 \tag{2.38}$$

which shows that the clipping distortion (if it exists) is correlated with the signal. Note that the result of Eq.(2.38) is general because there is no assumption on the signal s. To check the consistency of Eq.(2.38) we can explore two extreme regimes of clipping. When $K \to \infty$ both sum of Eq.(2.36) tend to zero because the amount of clipped samples tends to zero. Conversely, if $K \to 0$ we have[22] $c = -s$ (the clipping distortion is the opposite of the signal because all the samples are clipped) and $Cov(s, s_c) = -\sigma_s^2$ with σ_s^2 the variance of the signal.

[19] It is considered that $n - 1 \approx n$ because the number of samples n is much greater than 1.

[20] Regarding the clipping noise, it is assumed of zero mean because of the signal PDF symmetry with respect to zero.

[21] We assume the signal and the clipping noise to be stationary and ergodic.

[22] In that case Δ also tends to zero.

Alternatively, we can use the correlation coefficient between the clipping noise and the signal through the relation:

$$Corr(s,c) = \frac{Cov(s,c)}{\sqrt{\sigma_s^2 \cdot \sigma_c^2}} \tag{2.39}$$

Regarding the covariance between the clipping distortion c and the quantization distortion q we write:

$$Cov(q,c) = \frac{1}{n}\sum_{i=1}^{n} q(i) \cdot c(i) = 0 \tag{2.40}$$

which is obtained by replacing s by s_q in Eq.(2.33) and use the fact that the quantization distortion is of zero mean. However, a sample can be either quantized or clipped, but not both, such that it is clear that all the products in the sum vanish. Hence, the clipping distortion and the quantization distortion are uncorrelated. The correlation coefficient between the clipping noise and the

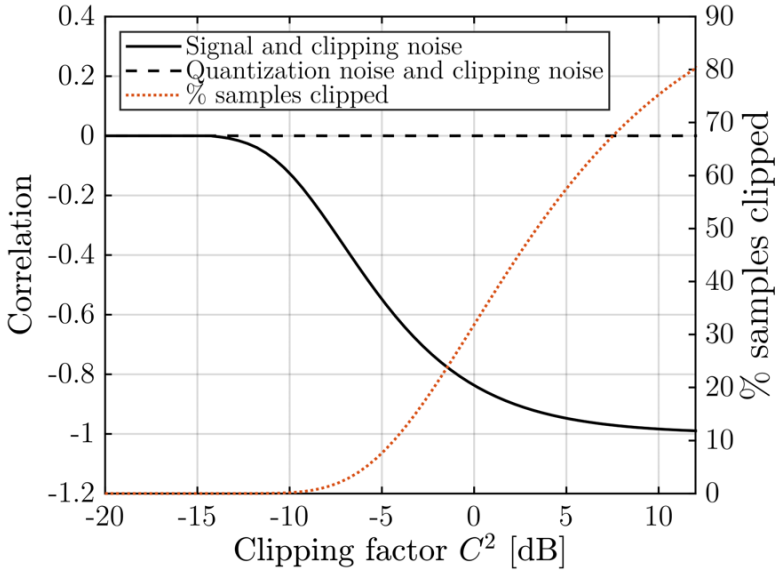

FIGURE 2.12: Numerical simulations. The test signals consist in 10 realizations of a Gaussian distributed random variables of 10^6 samples and standard deviation σ. Evolution of the correlation coefficient (average over 10 realizations) between the clipping noise and the ideal signal (black line) and between the clipping noise and the quantization noise (black dashed line) with the clipping factor $C^2 = \frac{\sigma^2}{(2^{N_b}\Delta)^2}$. The corresponding amount of clipped values (average over 10 realizations) is reported in the orange dotted line.

quantization noise is:

$$Corr(s, s_q) = \frac{Cov(s, s_q)}{\sqrt{\sigma_q^2 \cdot \sigma_c^2}} \tag{2.41}$$

which should be equal to zero.

We verify these assertions by a set of numerical simulations. The quantizer resolution is fixed to 4 bits and the test signals consist in 10 realizations of Gaussian distributed random variables for which the standard deviation σ is modified at the quantizer input. The number of samples for each realization is fixed to $L = 10^6$. The overall distortion (quantization and possibly clipping) is extracted at the quantizer output through the relation:

$$SQNR = \frac{\mathbb{E}[s]^2}{\mathbb{E}[s_q - s]^2} \tag{2.42}$$

where s_q denotes the quantized and possibly clipped signal at the quantizer output. The clipping noise variance can be extracted by clipping the signal before it enters the quantizer. The simulation results are shown in Fig.2.12 and confirm the predictions. For small amount of clipped values (small clipping factor), the correlation between the clipping distortion and the signal is zero. However, it continuously increases, in absolute value, with the clipping factor and finally reaches -1, in accordance by Eq.(2.36) with $K = 0$. These results also show that the correlation between the clipping distortion and the quantization distortion is always zero, in accordance with Eq.(2.40).

2.3.5 Combination of quantization and clipping: a general formula for the quantizer performance

We have seen that the total distortion at the output of a quantizer is, in general, a mixture of quantization noise and clipping noise. Regarding quantization and assuming that the Widrow theorem holds, the quantization error can be modeled as an additive white noise, uncorrelated with the signal and of variance σ_q^2. The corresponding signal to quantization noise ratio is:

$$SQNR = 6.02 \cdot N_b - PAPR_{\text{dB}} + 4.77 + OSR_{dB} \tag{2.43}$$

with N_b the DAC resolution in bits, $PAPR$ the peak-to-average power ratio of the signal being quantized and OSR the oversampling ratio (ratio of the signal noise equivalent bandwidth over the DAC sampling frequency).

Regarding clipping, we showed in the previous sections that the clipping error is an additive distortion, uncorrelated with the quantization noise but correlated with the signal (Eq.(2.40) and Eq.(2.38), respectively). When the number of clipped values is small (typically 1% or less), we showed that the clipping noise is of white spectrum and its correlation with the signal is negligible. Within the domain of validity of these assumptions we can define a signal-to-clipping noise ratio in the form:

$$SCNR = \frac{P_{Signal}}{\sigma_c^2} \tag{2.44}$$

with σ_c^2 the variance of the clipping noise within the signal bandwidth at symbol decision gate. By combining with the SQNR:

$$SNR = \left(\frac{1}{SQNR} + \frac{1}{SCNR} \right)^{-1} \tag{2.45}$$

with the following definition for the $SCNR$:

$$SCNR = \frac{P_{Signal}}{\int_{\Omega_S} PSD_c(\nu) d\nu} \tag{2.46}$$

which means that we integrate the clipping noise PSD within the signal bandwidth[23]. The Equation (2.45) is an approximation because the clipping noise is correlated with the signal. However, both numerical simulations and experiments will show that the approximation enables the correct prediction of the clipping factor which maximizes the SNR in Equation (2.45). However, in a regime dominated by the clipping noise (clipping factor greater than its optimal value), the quantizer perfomance, and hence the overall system performance, will differ from the prediction given by Eq.(2.45).

2.3.6 Precision of the model

The purpose of this section is to compute the uncertainty (precision) of the model given by Eq.(2.45). Regarding the clipping noise, its variance is extracted by clipping the signal before it enters the quantizer. Thus, considering the additive model for the clipping noise, no uncertainty comes with the SCNR. Regarding the quantization noise, the variance has been previously estimated equal to $\sigma_q^2 = \frac{\Delta^2}{12}$.

[23] We could also use the OSR similarly to the quantization noise if we consider that the clipping noise PSD is flat within the whole Nyquist frequency range of the DAC. By using Eq.2.46 instead, we assess the case in which the clipping noise PSD is not white.

But in practice, $\sigma_q^2 = \frac{\Delta^2}{12}$ is an estimation of the empirical variance S_n [69] of the quantization noise for each signal realization:

$$S_n^2 = \frac{1}{n}\sum_{i=1}^{n}(X_i - m)^2 \tag{2.47}$$

where n is the number of samples, X_i is the quantization noise value of sample i for each signal realization and m is the average value of the quantization noise. Taking into account that $m = 0$ once the additive noise model applies, one can easily check that S_n is an unbiased estimation[24]:

$$\mathbb{E}[S_n^2] = \mathbb{E}\left[\frac{1}{n}\sum_{i=1}^{n}(X_i - m)^2\right] = \frac{1}{n}\sum_{i=1}^{n}(X_i)^2 - m^2 = \sigma_q^2 \tag{2.48}$$

The variance of the estimation is:

$$\begin{aligned}\mathrm{Var}\left(S_n^2\right) &= \frac{1}{n}\sum_{i=1}^{n} Var\left((X_i - m)^2\right) \\ &= \frac{1}{n}\left(\mathbb{E}\left[(X-m)^4\right] - \mathbb{E}\left[(X-m)^2\right]^2\right) \\ &= \frac{1}{n}\left(\mu_4 - \sigma_q^4\right)\end{aligned} \tag{2.49}$$

where $\mu_4 = \mathbb{E}[(X-m)^4]$ is the fourth order centered moment of X. In the regime of validity of the additive noise model for quantization, the random variable X is uniformly distributed between $-\Delta/2$ and $\Delta/2$ such that:

$$\mu_4 = \int_{-\Delta/2}^{+\Delta/2} x^4 \frac{1}{\Delta} dx = \frac{\Delta^4}{80} \tag{2.50}$$

while:

$$\left(\sigma_q^2\right)^2 = \frac{\Delta^4}{144} \tag{2.51}$$

The comparison between Eq.(2.50) and Eq.(2.51) indicates that $\mu_4 = 1.8\sigma_q^4$. Moreover, assuming that the random variable S_n^2 is Gaussian distributed, the confidence interval at 99.7% on the estimation of the quantization noise variance is:

[24]For any value of n , an unbiased estimator for the variance is $S_n^2 = \frac{1}{n-1}\sum_{i=1}^{n-1}(X_i - m)^2$. However, to simplify the computation we consider that $n \approx n-1$ because we use values of n greater than 100

$$\delta\sigma^2 = 3 \times \sqrt{\frac{\mu_4 - \sigma_q^4}{n}} = 3 \times \sqrt{\frac{0.8\sigma^4}{n}} = 3\sigma_q^2 \times \sqrt{\frac{0.8}{n}}. \tag{2.52}$$

One remarks that the precision depends on the quantization noise variance itself. One solution to remove this dependency is to express the uncertainty in logarithmic scale:

$$\begin{aligned}\left(\delta\sigma^2\right)_{dB} &= 10 \times \log_{10}\left(\frac{\sigma^2 \pm 3\sigma_q^2 \times \sqrt{\frac{0.8}{n}}}{\sigma_q^2}\right) \\ &= 10 \times \log_{10}\left(1 \pm 3 \times \sqrt{\frac{0.8}{n}}\right)\end{aligned} \tag{2.53}$$

To validate this model, a set of numerical simulations has been launched, which consists in quantifying $N = 100$ Gaussian distributed random variables of standard deviation $\sigma = 50$ which ensure a minimum σ/Δ ratio of 6.25 with $\Delta = 8$ such that the additive noise model for quantization is verified. The simulation is repeated for different number of samples of each random variables realization, from 100 to 10^6, and different level of quantization noise by varying Δ. For each of them, the uncertainty at the confidence level of 99.7% is reported in Fig.2.13.

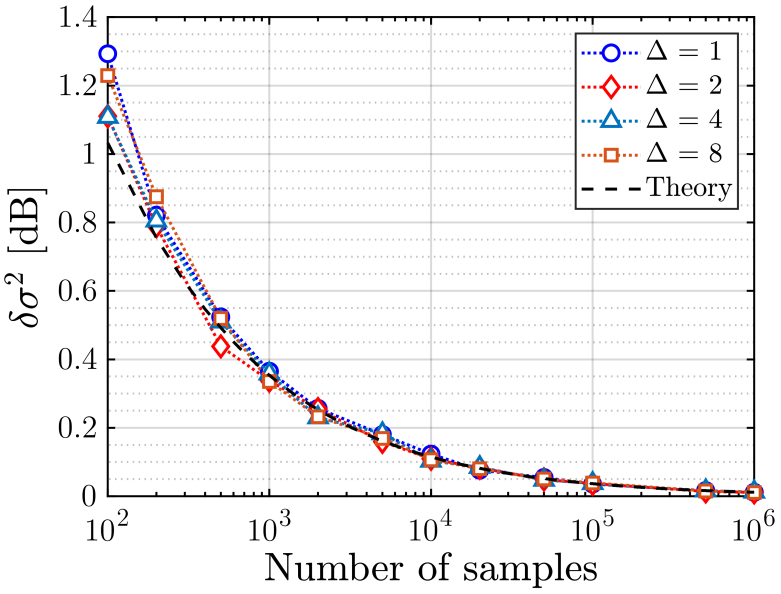

FIGURE 2.13: Uncertainty (confidence level 99.7%) on the estimation of the quantization noise variance under the assumption of the additive noise model for quantization. Dotted lines correspond to the theory for a uniformly distributed noise given by Eq.(2.53).

In practice, the waveforms have a number of samples of $2^{18} = 262144$ (memory length of the DAC used in experiment) such that the uncertainty on the quantization noise variance is below 0.05 dB. Hence, during numerical simulations or experiments, if the predicted SNR differs from the measured SNR, this may be not due to the finite length of the signals.

2.4 Numerical simulations

To test our additive noise model for the quantizer, we first perform an extensive set of numerical simulations. For conciseness, the presented results include the configurations which will be exploited for the experimental verification (see section 2.5). The test signals consist in random symbol sequences mapped on 16-QAM modulation format. The waveform are filtered with a RRC filter with roll-off factor 0.1 and the DAC sampling frequency is 92 GS/s, to match with experiments. Different data rates are investigated: 23 and 46 GBaud (OSR = 4 and 2 dB, respectively) to highlight the influence of oversampling on the performance of low-resolution DAC. Note that a relative delay between the real and imaginary components of each polarization is applied to emulate the electronic compensation of the skew between each component inside the Mach-Zehnder modulator. The performance prediction is done according to the following procedure:

- Re-scaling of the signal at the targeted clipping factor $C^2 = \sigma^2 / \left(2^{N_b} \cdot \Delta\right)^2$. This fixes the variance σ^2 of the digital signal.
- Computation of the $SQNR = \sigma^2 / \left(\sigma_q^2 \cdot SPS\right)$.
- Clipping of the signal, extraction of the clipping noise and computation of its variance σ_c^2.
- Computation of the $SCNR = \sigma^2 / \left(\sigma_c^2 \int_{\Omega_S} PSD_c(\nu) d\nu\right)$.
- Computation of the $SNR = (1/SQNR + 1/SCNR)^{-1}$.

At the receiver side, DSP consists in match filtering, down sampling to 1 SPS and constellation analysis to extract the SNR as in [64]. For the analysis, the predicted SNR and the measured SNR are averaged over the 10 realizations of symbol sequences.

The different parameters of interest for the simulation are reported in the Table 2.1 and the simulations results are shown in Fig.2.14 where the SNR evolution with

Parameter	Value
Modulation format	16-QAM
Number of symbols	2^{17}
Number of SPS	2
DAC resolution	4 and 3 bits

TABLE 2.1: Numerical simulations. Parameters of the signal and of the quantizers.

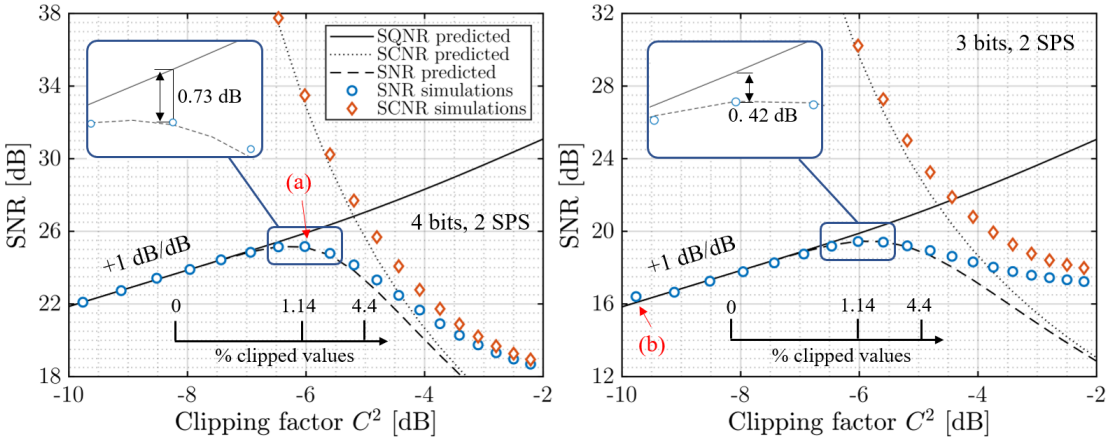

FIGURE 2.14: Numerical simulations. Evolution of the SNR at symbol decision with the DAC physical resolution and the clipping factor. The SNR is the average over 10 realizations of the symbol sequence. The test signal is a 16-QAM RRC filtered with roll-off 0.1 at 2 SPS. The blue points are the average SNR when both quantization and clipping occur. The orange diamonds are the average of the measured SNR when only clipping occurs. The black lines correspond to the predicted SNR: with only quantization only (SQNR), with only clipping (SCNR, Eq.(2.46)) and with both quantization and clipping (SNR, Eq.(2.45)).

the clipping factor are depicted for two DAC resolution. Note that in Fig.2.14, the vertical axes of the right plot is shifted by -6 dB with respect to the vertical axes of the left plot, to ease the comparison between 4 bits and 3 bits physical resolution. For low clipping factors (left side of the plots, small values of C^2), the system SNR is proportional to the SQNR and increases by +1 dB for +1 dB increase of signal variance σ^2 (or equivalently the clipping factor $C^2 = \sigma^2/(2^{N_b}\Delta)^2$). This is consistent with the additive noise model for quantization[25]. For both 4 bits and

[25]One remarks the analogy of the Fig.2.14 with the so-called Bell curve for performance of optical systems under the influence of linear (ASE) or nonlinear (Kerr effect) noises. However, here, both quantization and clipping are nonlinear distortions but the quantization noise behaves as an additive noise whose variance is signal independent.

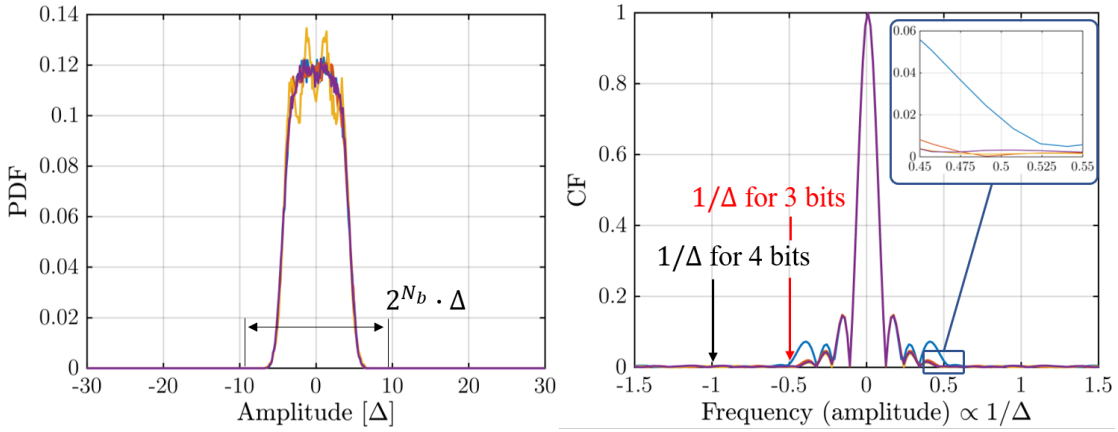

FIGURE 2.15: Numerical simulations. Probability density functions (left) and characteristic functions (right) of the real and imaginary components of each polarization of the test signal used for Fig.2.14.

3 bits physical resolution, clipping starts to occur for $C^2 \approx -8$ dB. This value only depends on the signal distribution and not on the DAC physical resolution as the clipping only depends on the clipping threshold K. As the clipping factor increases such that the amount of clipped values is kept small, the system SNR increases, following the SQNR increase with the clipping factor, while in that regime, the SCNR decreases but remains sufficiently high to be neglected in the system performance given by Eq.(2.45). The maximal system SNR is obtained for a given clipping factor, here $C^2 = -6$ dB, which is the optimal balance between quantization and clipping noises for this signal distribution. Regarding the maximum SNR, it is obtained for approximately 1% of clipped values in that case. Also, at the best SNR, the clipping noise variance is much smaller than the quantization noise variance and the maximum SNR remains very close to the SQNR, as shown in Fig.2.14: -0.73 dB for 4 bits and -0.42 dB for 3 bits. We also note that the maximum achievable SNR increases by +5.71 dB between 3 bits and 4 bits of physical resolution. This value is slightly smaller than Eq.(2.18) which is obtained by considering only the quantization noise, and not its mixture with the clipping noise. If the clipping factor further increases, the system SNR decreases because of the influence of the SCNR. We call this regime the "clipping noise limited regime".

Regarding the validity of the additive noise model of Eq.(2.45), the prediction and the simulation are in accordance in the quantization noise limited regime, except for the point denoted (b) for the 3-bit case (right plot), for which we observe a slight bias between the prediction and the simulation. This discrepancy can be explained with the signal probability density function and the corresponding

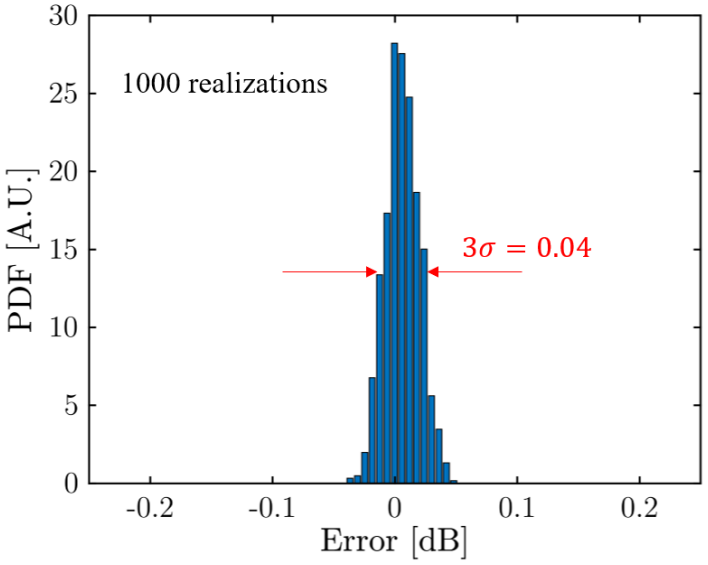

FIGURE 2.16: Numerical simulations. Histogram of the prediction error (difference between the SNR given by Eq.(2.45) and the SNR measured in the constellation as in [64]). The signal corresponds to the configuration (a) in the left plot of Fig.2.14. The number of samples of the generated signals is 2^{18} (2^{17} symbols at 2 SPS.

characteristic function for the clipping factor $C^2 = -9.76$ dB, reported in Fig.2.15. We observe that the signal CF does not vanish at $1/\Delta = 0.5$ (3-bit DAC, $\Delta = 2$) while it is the case for the 4-bit DAC for which $\Delta = 1$ is set to 1. However, when the clipping factor is increased, the discrepancy between the prediction and the simulation disappears rapidly. Indeed, as σ^2 increases, the signal PDF becomes broader and hence its CF vanishes more rapidly. Another interesting observation concerns the signal to clipping noise ratio. The Fig.2.14 reports the system SNR with considering only clipping effect (orange diamonds). As expected, the SCNR decreases with the clipping factor and the amount of clipping values (see black rulers). The deviation between the prediction under Eq.(2.46) and the simulation continuously increases with the clipping factor C^2 as the correlation between the clipping noise and the signal can not be neglected. However, around the optimal clipping factor, the discrepancy is sufficiently small (≈ 0.5 dB) such that the SNR prediction is done with enough accuracy (0.03 dB and <0.01 dB for the 4 and 3 bits resolution, respectively).

Finally, Fig.2.16 depicts the histogram of the error between the predicted performance and the measured SNR for 1000 realizations of the signal at the operating point (a) in the left plot of Fig.2.14 (clipping factor corresponding to the best SNR for 4-bit physical resolution). Note that the prediction error in dB

is the difference between the measured SNR and the predicted SNR expressed in dB:

$$error_{\text{dB}} = SNR_{\text{measured, dB}} - SNR_{\text{predicted, dB}} \tag{2.54}$$

We observe that the prediction error variability is about 0.04 dB at 3σ and we never observe a prediction error greater than 0.1 dB in absolute value. It should be noted that this variability is in accordance with the prediction error given by Eq.(2.53) in section 2.3.6: ≈ 0.04 dB for 2^{18} samples.

2.5 Experimental validation

To validate the additive noise model presented in this chapter, experiments on an optical back-to-back test bed [63] are carried. The transmitter uses a dual polarization coherent transmitter based on (four) 8-bit DAC, identical to the one characterized in Chapter 1 section 1.3.4. The DAC clock reference is provided by an external synthesizer to minimize clock timing jitter impairments and the clock sampling frequency is set to 92 GS/s. An optical attenuator placed right before an amplifier ensures a constant optical power into the coherent mixer and the OSNR is varied by ASE loading. At the receiver side, the photo-currents from the coherent mixer are sampled by a real-time oscilloscope with 70 GHz electrical bandwidth and 200 GS/s 8-bit ADCs.

Regarding quantization, a low physical resolution is emulated at the transmitter and receiver sides by using only a reduced number of quantization levels over the 255 available on the DAC and the ADC. At the transmitter, quantization is done during the offline generation of the signals in *Matlab*. At the receiver, the 8-bit digital signals are re-quantized over a reduced amount of quantization levels before entering the receiver DSP algorithms. In both cases, the clipping factor is adjusted following Eq.(2.32) to explore the system behavior in presence of different amount of clipping noise. Moreover, the high sampling frequency of the oscilloscope enables the decimation of the recorded signals such that it is possible to study the effect of the oversampling when employing low-resolution quantizers. The decimation consists in taking one sample out of two before re-quantization at the receiver side such that 100 GS/s ADCs are emulated. Note that the received spectrum has no frequency above 50 GHz (due to the DAC low pass frequency response measured in Chapter 1 section 1.3.4) such that decimation at 100 GS/s does not lead to aliasing.

The test signals consist in 16-QAM and 64-QAM at 64 GBaud, filtered by an RRC filter with roll-off factor 0.1 (same as in numerical simulations). An high pass frequency response is also applied to the waveforms in order to compensate for the low pass frequency response of the DAC (see Chapter 1 section 1.3.4). Regarding the receiver, the DSP routine consists in resampling at 2 SPS, polarization demultiplexing and equalization with a 17 taps multiple modulus algorithm, down sampling at 1 SPS, carrier frequency and carrier phase estimation and finally symbol detection. Note that the clock reference is shared between the transmitter and the receiver such that a clock recovery algorithm is not needed. The system SNR is measured on the constellation as in [64] over 10^6 symbols to get a (total) uncertainty on the quantization and other noises (all assumed to be Gaussian distributed, as justified after) variance below 0.05 dB (see section 2.3.6). The SNR is expressed by isolating the low-resolution DAC and ADC contributions according to our model:

$$\frac{1}{SNR} = \frac{1}{\mu}\left(\frac{1}{\xi OSNR} + \frac{1}{SNR_{TRx'}} + \frac{1}{SNR_{DAC}} + \frac{1}{SNR_{ADC}}\right) \tag{2.55}$$

One recalls that $SNR_{TRx'}$ sets the saturation level of SNR for high OSNR ($1/\xi OSNR$ negligible in Eq.(2.55)) and neglecting $1/SNR_{DAC}$ and $1/SNR_{ADC}$ (for instance with 8-bit DAC and ADC resolution).

Measurement of $SNR_{TRx'}$

To measure $SNR_{TRx'}$, the system SNR is measured when employing 8-bit resolution at DAC and ADC. The measured SNR versus OSNR is shown in Fig.2.17 (red squares). The test signal is a 16-QAM at 46 GBaud. At low OSNR (left side of the figure), the SNR tends to its theoretical value for a system impacted only by ASE noise (black dashed line), with a $1/\xi OSNR$ factor dominant in Eq.(2.55) in the ASE noise limited regime. In that regime, the system SNR grows linearly with the OSNR, in accordance with Eq.(2.55). However, the slope is slightly smaller than +1 dB/dB, represented by the black dashed line. The deviation between the SNR value and the OSNR is given by the μ factor in Eq.(2.55). At high OSNR, the system SNR saturates around 23 dB as in this regime the ASE noise becomes negligible. Since the DAC and ADC resolutions are equals to 8 bits, the value of $1/SNR_{DAC}$ and $1/SNR_{ADC}$ are also negligible in Eq.(2.55) and the saturation SNR provides $SNR_{TRx'}$. The values of μ and $SNR_{TRx'}$ are extracted by fitting

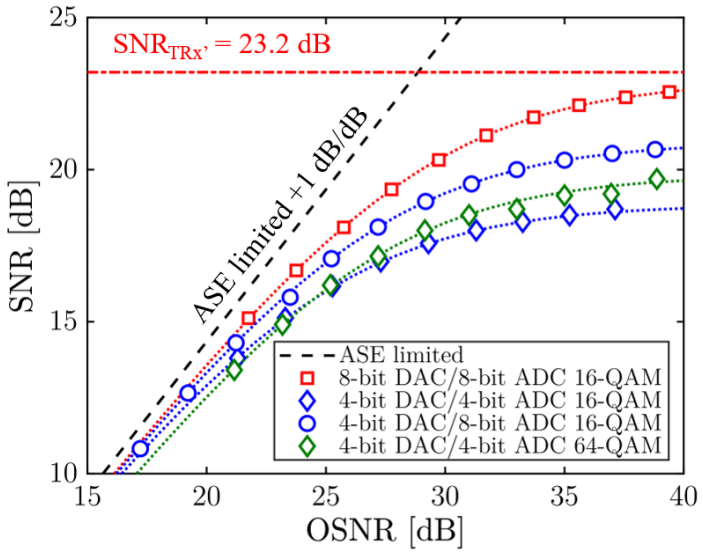

FIGURE 2.17: Experimental results. SNR versus OSNR in an optical back-to-back test bed employing low-resolution DAC and ADC. Symbols are measurements (average over 5 measurements for the same symbol sequence) and dotted lines are fits with a function of the form of Eq.(2.55).

Configuration	μ	SNR_{TRx} [dB]
8-bit DAC/8-bit ADC	0.95	23.2 ($=SNR_{TRx'}$)
4-bit DAC/8-bit ADC	0.94	21.1
4-bit DAC/4-bit ADC	0.96	19.4

TABLE 2.2: Experimental results. Extracted value of μ and SNR_{TRx} when fitting the measurements of Fig.2.17 with Eq.2.56.

the red squares measurements in Fig.2.17 by a function of the form:

$$\frac{1}{SNR} = \frac{1}{\mu}\left(\frac{1}{\xi OSNR} + \frac{1}{SNR_{TRx'}}\right) \tag{2.56}$$

The fitted curve is represented in red dotted points and shows a good agreement with the measurements. The extracted values of μ and $SNR_{TRx'}$ are given in Table 2.2. For the 8-bit DAC and 8-bit ADC, $\mu = 0.95$ and $SNR_{TRx'} = 23.2$ dB. Note that in the curves presented in Fig.2.17, the clipping factor for the DAC is $C^2 = -6.46$ dB and $C^2 = -7.95$ dB for the ADC when its resolution is reduced to 4 bits.

Influence of the DAC and/or ADC resolution

The same procedure is repeated for different configurations, i.e. by varying the DAC and/or the ADC physical resolution. The measurements are reported in Fig.2.17 and the fitted value of μ and SNR_{TRx} are reported in Table 2.2. We observe that the SNR_{TRx} decreases when the DAC and/or the ADC resolution decreases. Another observation is that the value of μ is independent of the DAC or ADC physical resolution. Thus, the system performance in the ASE noise limited regime is independent of the amount of quantization noise. This is a good indication that the quantization noise behaves as an additive noise. In order to confirm this, different configurations are explored. For each configuration, we compute offline the SNR_{DAC} and SNR_{ADC} terms and combine them with the $SNR_{TRx'}$ as follows:

$$\frac{1}{SNR} = \frac{1}{SNR_{TRx'}} + \frac{1}{SNR_{DAC}} + \frac{1}{SNR_{ADC}} \tag{2.57}$$

If our model is correct, the left term in Eq.(2.57) should corresponds to $1/SNR_{TRx}$. The comparison is reported in Table 2.3. In both situations, the predicted value SNR and the measured value SNR_{TRx} differ by less than 0.5 dB.

Also, for comparison with other experiments reported in the literature [58], the system performance for the 64-QAM at 46 GBaud employing a 4-bit DAC and a 8-bit ADC is reported in Fig.2.17. The saturation $SNR_{TRx} \approx 20$ dB and the corresponding bit error ratio (BER) is about 10^{-2}. It is interesting to note that this value is close to the one reported in [58] (which is slightly higher but obtained with

Config.	SNR_{DAC} [dB]	SNR_{ADC} [dB]	SNR_{TRx} [dB]	SNR [dB]
4-bit DAC/8-bit ADC	25.2	-	21.1	21.08
4-bit DAC/4-bit ADC	24.8	26.4	19.4	19.83

TABLE 2.3: Experimental results. Comparison between the predicted SNR when using low-resolution DAC/ADC. The system performance $SNR_{TRx'}$ in absence of quantization effect is measured and the SNR_{DAC} and SNR_{ADC} are extracted during the signal generation in *Matlab* or at the low-resolution quantization emulator at the entrance of the receiver DSP. The predicted SNR (right column) is compared to its measured value SNR_{TRx} obtained by fitting the measurements in Fig.2.17 by a function of the form of Eq.(2.55).

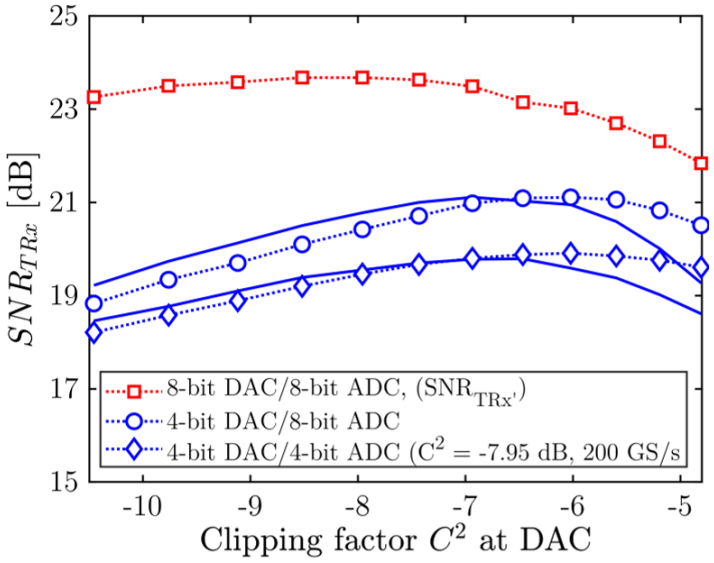

FIGURE 2.18: Experimental results. Evolution of the SNR_{TRx} with the DAC clipping factor $C^2 = \frac{\sigma^2}{(2^{N_b}\Delta)}$ for various DAC and ADC resolutions. Each point corresponds to the saturation SNR_{TRx} extracted by fitting an $SNR = f(OSNR)$ curve with a function of the form of Eq.(2.56) as done with the results presented in Fig.2.17.

propagation and not in back-to-back). Indeed, as the quantization and clipping noises result from distortions arising in the digital domain, the comparison between different optical set-ups is relevant, as long as the quantizer characteristics are identical.

Then, the same procedure is repeated for various clipping factors at the DAC and the results are presented in Fig.2.18. Note that for each clipping factor, the $SNR_{TRx'}$ is also measured because, even in absence of quantization effects, the clipping at the transmitter modifies the signal power at the DAC output such that the system performance can be modified. In Fig.2.18, a difference between the predicted SNR (solid lines) and its measured value (symbols) is visible and attributed to the possible modifications of the quantization noise characteristics (spectrum) which can arise between the transmitter and the receiver. Indeed, our model assumes that the quantization noise has white spectrum. However, because quantization occurs in the digital domain, the quantization noise suffers from attenuation of its high frequencies due to the low-pass transfer function of the DAC (see Chapter 1 section 1.3.4) such that it enters the receiver DSP with a non-flat PSD such that the SNR cannot be inferred directly with an additive white noise model. However, the discrepancy is such that, if the system operates at the

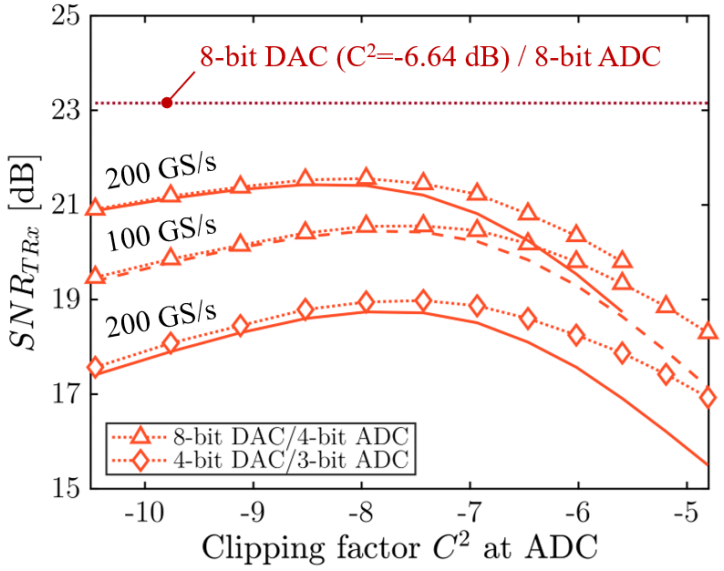

FIGURE 2.19: Experimental results. Evolution of the SNR_{TRx} with the ADC clipping factor $C^2 = \frac{\sigma^2}{(2^{N_b}\Delta)}$ for various DAC and ADC resolutions. Each point corresponds to the saturation SNR_{TRx} extracted by fitting an $SNR = f(OSNR)$ curve with a function of the form of Eq.(2.56) as done with the results presented in Fig.2.17.

clipping ratio which gives the best predicted SNR, the measured SNR differs by less than 0.5 dB.

Influence of the ADC sampling frequency

The measured system SNR for two different ADC sampling frequencies (200 or 100 GS/s) is reported in Fig.2.19. The DAC clipping factor is kept constant and the $SNR_{TRx'} = 23.2$ dB serves as calibration value (red dotted lines in Fig.2.19) to predict the SNR. As predicted by the additive noise model for quantization, the system performance is smaller if the ADC sampling frequency is 100 GS/s rather than 200 GS/s, as the $SQNR_{ADC}$ (and thus the SNR_{ADC}) decreases by -3 dB when the sampling frequency is divided by 2, as predicted by Eq.(2.26). At the best clipping ratio, the prediction and the measurement differ by less than 0.5 dB.

2.6 Resolution requirements for next generation optical transceivers

The performance prediction model presented in this chapter is used to establish the physical resolution requirements for the next generation of optical transceivers [63]. The analysis consists in computing the maximum SNR which can be obtained for a given DAC or ADC physical resolution, assuming a Gaussian distributed input signal, for generality. However, this analysis can be performed for any signal distribution if it follows the Widrow theorem and since the clipping noise can be safely assumed uncorrelated with the signal. With the predicted maximum achievable SNR, we compute the corresponding BER, targeting 10^{-3} for a practical limit of feasibility. This threshold is smaller than the one generally employed in literature [58, 70] to take a reasonable margin in BER and account for additional sources of noises and distortions in addition to quantization and clipping noises considered here.

The physical resolution requirements are reported in Fig.2.20 [63] for 3 different cases: 1) The DAC or the ADC physical resolution is reduced; 2) The DAC and the ADC physical resolutions are reduced; 3) The DAC physical resolution is reduced and a digital resolution enhancer (DRE) is used [59], providing 1 bit of resolution increase. These results show that the maximum data rate can be increased if the DAC and/or ADC resolution is increased or when the sampling frequency is increased. When both the DAC and the ADC physical resolutions are reduced (case 2), the physical resolution requirement increases by +0.5bit with respect to case 1 because the low-resolution induced performance $(1/SNR_{DAC} + 1/SNR_{ADC})^{-1}$ decreases by -3dB. In case 3, with respect to case 1, the resolution requirements are reduced accordingly to the DRE gain.

The requirements reported in Fig.2.20 can be compared to recent experiments in the literature. For instance, authors in [70] demonstrate the feasibility of 600 Gbit/s net (64-QAM at 64 GBaud, 770 Gbit/s gross) with 1.6 SPS and 3 bits of physical resolution by employing the digital resolution enhancer (DRE) introduced in [58], which provides slightly more than +1 dB of physical resolution enhancement. This result is close to the requirement presented in Fig.2.20 for 1.44 SPS and 4 bits of physical resolution without DRE (640 Gbit/s gross). Alternatively, they also demonstrate the feasibility of 460 Gbit/s with the same physical resolution and the same DRE architecture but with an higher oversampling factor of ≈ 2.4. This configuration is also close to the requirements

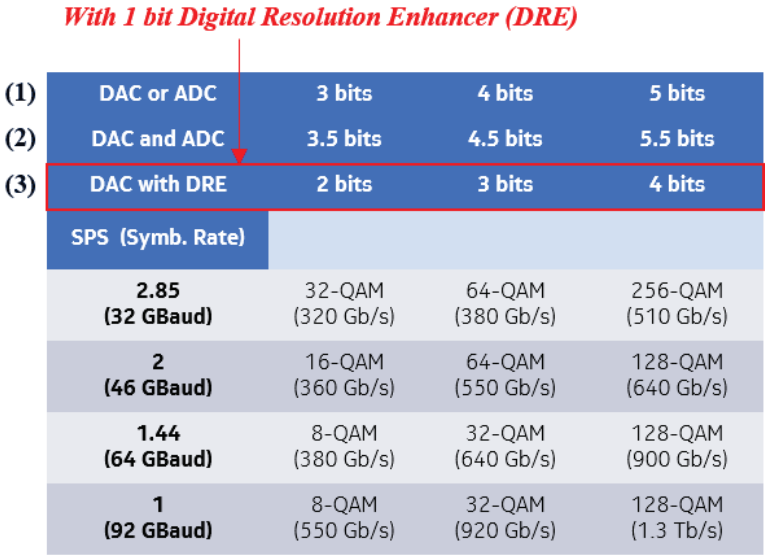

(1)	DAC or ADC	3 bits	4 bits	5 bits
(2)	DAC and ADC	3.5 bits	4.5 bits	5.5 bits
(3)	DAC with DRE	2 bits	3 bits	4 bits
	SPS (Symb. Rate)			
	2.85 (32 GBaud)	32-QAM (320 Gb/s)	64-QAM (380 Gb/s)	256-QAM (510 Gb/s)
	2 (46 GBaud)	16-QAM (360 Gb/s)	64-QAM (550 Gb/s)	128-QAM (640 Gb/s)
	1.44 (64 GBaud)	8-QAM (380 Gb/s)	32-QAM (640 Gb/s)	128-QAM (900 Gb/s)
	1 (92 GBaud)	8-QAM (550 Gb/s)	32-QAM (920 Gb/s)	128-QAM (1.3 Tb/s)

FIGURE 2.20: Numerical simulations. Physical resolution requirements targeting 10^{-3} BER for three different cases: 1) The DAC or the ADC physical resolution is reduced; 2) The DAC and the ADC physical resolutions are reduced; 3) The DAC physical resolution is reduced and a digital resolution enhancer (DRE) is used, providing 1 bit of resolution increase. Data rates are gross values, including FEC overhead.

for 4 bits without DRE and 2 SPS, at a comparable gross data rate (550 Gbit/s versus 590 Gbit/s in [70]).

2.7 Conclusion

In this chapter, we proposed an additive noise model for optical systems employing low-resolution DAC and/or ADC in the form:

$$\sigma^2 = \sigma^2_{ASE} + \sigma^2_{Kerr} + \sigma^2_{TRx'} + \sigma^2_{DAC} + \sigma^2_{ADC} \tag{2.58}$$

with σ^2_{ASE} the variance of the ASE, σ^2_{Kerr} the variance of the nonlinear distortions (non investigated in this work), $\sigma^2_{TRx'}$ the variance of the transmitter and receiver noise excluding low-resolution effects and finally σ^2_{DAC} and σ^2_{ADC} the variance of the quantization and clipping noise of the DAC and the ADC, respectively. We converted these variances in system SNR through the relation:

$$\frac{1}{SNR} \propto \left(\frac{1}{\xi OSNR} + \frac{1}{SNR_{TRx'}} + \frac{1}{SNR_{DAC}} + \frac{1}{SNR_{ADC}} \right) \tag{2.59}$$

which is an extension of the model presented in [64] to optical system employing low-resolution DAC and ADC. In this model, SNR_{DAC} and SNR_{ADC} take the form:

$$\frac{1}{SNR_{DAC,ADC}} = \frac{1}{SQNR_{DAC,ADC}} + \frac{1}{SCNR_{DAC,ADC}} \tag{2.60}$$

which are the signal-to-quantization noise ratio and the signal-to-clipping-noise ratio, respectively.

Regarding the quantization error, the theory in [50, 51] derives a *sufficient* condition for the quantization error to be modeled as an additive noise, uniformly distributed, uncorrelated with the signal and of white spectrum such that it is possible to compute the SQNR with the quantization noise variance. The condition of validity of this model is that the signal characteristic function (CF) (Fourier transform of its probability density function) identically vanishes for frequencies (in the Fourier domain corresponding to the signal amplitude) greater or equal to $1/\Delta$, with Δ the quantization step. We showed that when the signal standard deviation σ is greater than the quantization step Δ, the condition is verified in a good approximation. However, reducing the quantizer resolution requires to carefully verify its validity for performance prediction because Δ increases at constant signal standard deviation σ. If the model applies, σ_q^2 can be converted in a signal-to-quantization noise ratio which depends on the quantizer resolution, the signal PAPR and the oversampling ratio or the number of SPS at signal generation.

Regarding the clipping, it is necessary to maximize the $SNR_{DAC,ADC}$ at the output of the quantizer and hence the system SNR. We showed that it is an additive distortion but, rigorously, it is also correlated with the signal and of colored spectrum. However, when the amount of clipping is such that the quantizer performance is maximum, there is only small amount of clipped values and the clipping noise is of white spectrum (impulsive noise). Moreover, in that case, the correlation between the clipping noise is small enough (but not null) such that a signal-to-clipping noise ration (SCNR) can be derived from the clipping noise variance σ_c^2, which is extracted by clipping the signal prior to quantization.

We showed by numerical simulations and experiments that the system SNR can be predicted from $SNR_{DAC,ADC}$ by first measuring $SNR_{TRx'}$, the performance in absence of quantization effects. Both simulation and experiments showed a prediction error below 0.5 dB, when the amount of clipped values is optimized to maximize the system SNR. The next step will be to translate the system SNR prediction into a bit error ratio (BER) prediction, more useful to conclude on the feasibility of the optical systems by employing low-resolution DAC and ADC.

This will require to study the statistical distribution of the quantization noise and clipping noise in the constellation plane at symbol decision.

It should be noted that the effect of quantization and clipping with low-resolution DAC and ADC has been previously assessed in the context of optical communications. For instance, authors in [54] report an extensive (but not complete) theoretical and experimental study for Gaussian distributed signals (case of orthogonal frequency division multiplexing) by treating quantization and clipping as an unique distortion, and without assessing the effect of oversampling. In this work, supplementary steps in the analysis are reported. First, there is no restriction to specific signal distributions. Indeed, based on the statistical theory for quantization established by Widrow and Sripad [50, 51], if the additive noise model for quantization applies, the quantization noise variance does not depend on the signal. Moreover, by explicitly separating the quantization and the clipping noises, we highlight their different properties and different effects in the optical system performance. It has been clearly established that, conversely to the quantization noise, the clipping noise is correlated with the signal. Finally, we showed that the effect of oversampling during quantization can be taken into account through the noise equivalent bandwidth of the signal. In case of RRC pulse-shaping, the OSR coincides with the number of SPS at the DAC or ADC.

This model has been used to establish physical resolution requirements for optical transceivers employing low-resolution DAC and/or ADC, and compared with recent experiments.

Chapter 3

Digitally enhanced DAC: DSP techniques for low-resolution optical transmitters

3.1 Motivations

Low-resolution DACs are a promising solution to meet the tight constraints of metropolitan optical networks in terms of hardware complexity, power consumption and cost [16, 17]. However, we have seen in Chapter 2 that reducing the DAC physical resolution has strong implications on the system performance and design [63]. This is because the quantization noise becomes non-negligible, and its variance is multiplied by a factor of 4 (6 dB) each time the physical resolution is reduced by -1 bit. Hence, with a physical resolution of 5 bits or below [37], the quantization noise becomes a limiting factor of performance, constraining the achievable data rate or reach of the optical link, particularly for metropolitan distances [71]. However, it is possible to act on the signal, the quantization noise or on the quantizer itself, to maximize the SQNR. While many techniques already exist to maximize the SQNR such as clipping (see Chapter 2), quantization noise shaping (see this chapter), Sigma-Delta modulation (see next chapter), companding [72] or nonuniform quantization (see this chapter), they have not been extensively studied in the context of optical communications. This is because optical transceivers employ high resolution DACs (8 bits) such that the quantization noise is negligible with respect to the other distortions. However, the recent interest for low-resolution DACs led to a renewed interest in SQNR-optimization methods.

In this chapter, we present and study three optimization techniques which enable an increase in the performance, i.e. SQNR, of low-resolution DAC. We focus on the DAC rather than on the ADC because, at the transmitter side, we can take advantage of the deterministic nature of quantization as the signal is known prior to quantization. At the receiver side, the quantization noise remains undetermined, reducing the possible optimization techniques without hardware implementation[1]. In a first section, we present a novel signal-optimization technique to maximize the SQNR in optical transmitters. The prerequisite for this technique is that the optical transmitters must perform a pre-compensation of the chromatic dispersion. In a second section, the benefits for a quantization noise optimization technique, namely noise shaping, are presented. Its implementation in the digital domain into an optical transmitter is proposed. Among different possibilities [59, 73, 74], we develop one strategy to perform a quantization noise shaping and to demonstrate the achievable performance gains. Finally, we assess the question of using a nonuniform quantization rather than an uniform quantization and we numerically establish the expected performance gains in the context of optical communications [75].

[1]But it is still possible to exploit the possible correlation between the quantization noise and the signal, see for instance [56].

3.2 Constellation rotation to reduce transmitter noise in metro links

Metropolitan optical networks are heterogeneous, i.e., made of legacy 10 Gb/s channels with dispersion managed (DM) optical links, mixed with higher capacity coherent channels (e.g. 100 Gb/s). The latter can additionally go through dispersion unmanaged (DU) links [64]. Moreover, in metro networks, coherent transmitters can digitally apply a chromatic dispersion pre-compensation to optimize the link performance. Regarding the evolution of the DAC/ADC performance, C. Xie showed in [76] that the signal PAPR is minimized when the accumulated chromatic dispersion (CD) is zero. Thus, if a low-resolution ADC is employed, it may be beneficial to pre-compensate for the CD at the transmitter, such that the accumulated CD at the receiver is zero, hence minimizing the PAPR and maximizing the SQNR of the ADC (see Chapter 2). However, this may create an additional penalty at the transmitter because of the PAPR increase due to the digital CD pre-compensation. Additionally, we also observe that for small CD pre-compensation values (typically less than 500 ps/nm), the digital complex

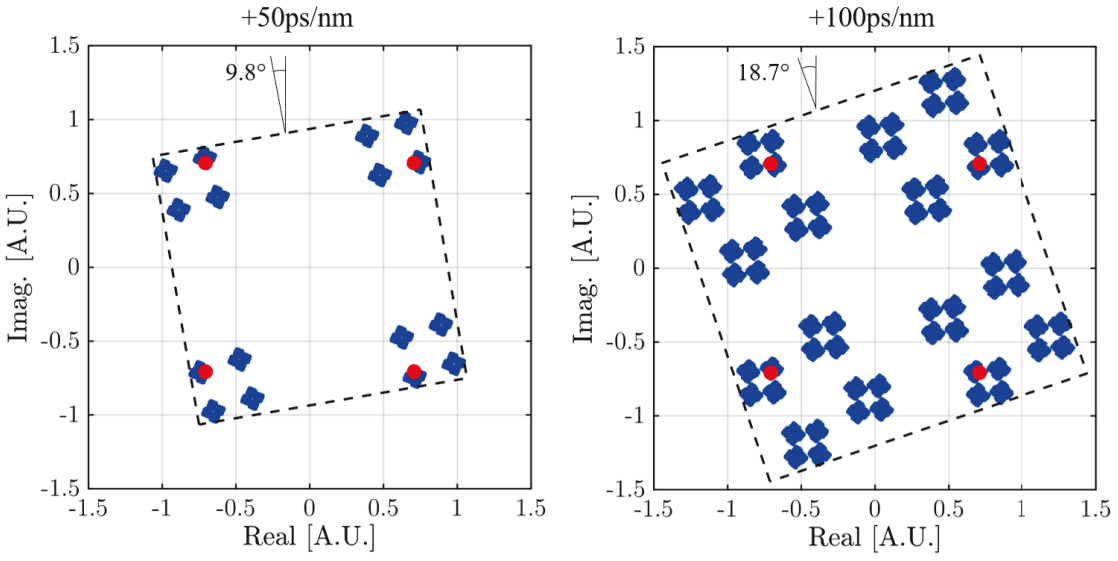

FIGURE 3.1: Numerical simulations. Digital complex field corresponding to a non return QPSK sequence at 2 samples per symbol without and with application of the chromatic dispersion operator. The red points correspond to the QPSK without chromatic dispersion and serve as reference. The blue dots correspond to the digital complex field when a chromatic dispersion of +50 ps/nm or +100 ps/nm is applied on the digital sequence. The black dashed line is the oriented minimum area bounding box of the complex field.

field entering the DAC at the transmitter side presents a tilt with respect to the real and imaginary axes of the constellation plane, as illustrated in Fig.3.1, and previously observed in [64].

The Fig.3.1 is analyzed as follows. The test signal is a non-return-to-zero QPSK at 2 SPS. Thus, in absence of a CD pre-compensation, the possible values of the complex digital field on each polarization coincides with the QPSK mapping in the constellation plane axes. These points are represented by red dots in the two plots of Fig.3.1. With CD pre-compensation, we observe that each QPSK state divides into several states, as a result of the inter symbol interference (ISI) due to the temporal spreading of each symbol. For instance, for a very small value of CD pre-compensation (+50 ps/nm), we observe that each QPSK symbol divides into four different symbols. We explain this as the result of the ISI between each possible group of two adjacent (in the temporal domain) symbols. For an higher value of CD pre-compensation (+100 ps/nm), the temporal spreading of each symbol increases such that ISI occurs between each group of three adjacent symbols. Hence, each original QPSK symbol divides into 16 possible states in the complex plane, as shown in the right plot of Fig.3.1.

The ISI due to the small amount of CD pre-compensation tilt the complex field with respect to the real and imaginary axes of the constellation plane. Unfortunately, generating such signals with a low resolution DAC is not optimal because the PAPR of the real and imaginary components of the tilted field is higher than in absence of tilt, such that the SQNR decreases. In what follows, we define the tilt of the complex field as the angle between the oriented minimum area bounding box (OMBB) and the constellation plane axes. One remarks that the orientation of the OMBB which minimizes the PAPR is precisely the one for which the faces of the OMBB coincides with the real and imaginary axes of the constellation plane. This is because the PAPR minimization consists in minimizing the maximum value of the real and imaginary part of each component of the complex field, as the field variance is left unchanged by the rotation. This is illustrated in Fig.3.2. We observe that, if the complex field is rotated such that the OMBB faces coincides with the constellation plane axes, the distribution of the amplitude along the real or imaginary component is more concentrated and hence of lower PAPR.

Using this observation, we report on a method, called the constellation phase rotation method (CPRM), to minimize the DAC induced penalty in presence of CD pre-compensation. The method applies for moderate CD pre-compensation (typically <500 ps/nm) which corresponds roughly to 30 km of SMF fiber or

125 km of LEAF fiber, at 1550 nm, and takes advantage of the possible non-Gaussian distribution of the emitted signal in this regime[2]. The method consists in computing the OMBB of the complex field and applying a rotation to make the OMBB faces coincide with the real and imaginary axes of the constellation plane. In what follows, we first perform a extensive set of numerical simulations to measure the achievable PAPR reduction and the corresponding $SQNR_{DAC}$ when employing the CPRM. We then run a set of experiments to measure the system SNR increase due to the $SQNR_{DAC}$ increase for various DAC physical resolutions. We observe that when a 4-bit DAC is employed, i.e. when the quantization noise dominates with respect to the other impairments, as shown in Chapter 1, the CPRM enables a system SNR gain of up to +1.1 dB for a 16-QAM signal.

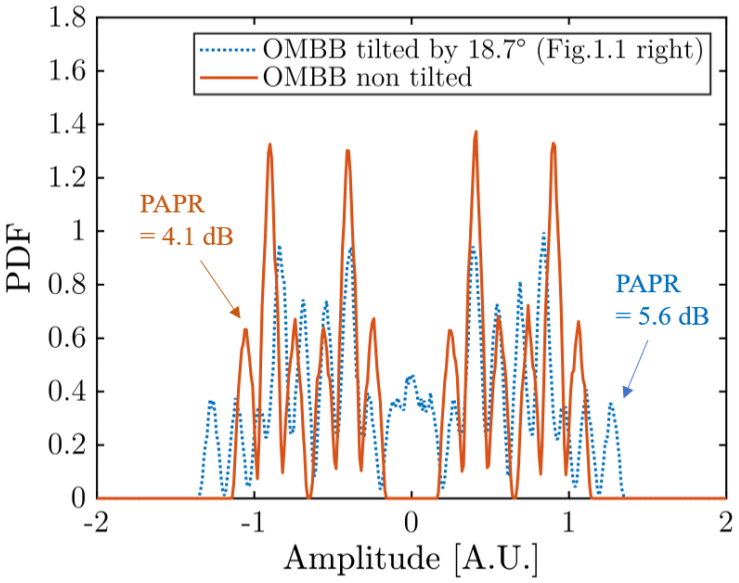

FIGURE 3.2: Numerical simulations. Probability density function of the real or imaginary component of the non return to zero QPSK with +100 ps/nm CD pre-compensation. The blue dotted line corresponds to the complex field of the right plot of Fig.3.1 (PAPR = 5.6 dB). The orange line is with application of a rotation such that the oriented minimum bounding box of the complex field is aligned with the real and imaginary axes of the constellation plane (PAPR = 4.1 dB). The rotation angle in that case is 18.7° clockwise.

[2]In this study, we arbitrarily apply positive CD pre-compensation values, but all the results apply for negative CD pre-compensation.

3.2.1 Principle and system model

The system model for the analysis of the CPRM is shown in Fig.3.3. For the sake of simplicity, only a single polarization transmission is represented as the CPRM applies independently to each polarization. Two independent DACs convert the real and imaginary components of the optical field. The DAC quantization penalty is specified by the signal-to-quantization noise ratio at the quantizer output (see Chapter 2). Formally, for the real or the imaginary components of the digital field, we can write:

$$SQNR_{\{\mathbb{R},\mathbb{I}\}} = \frac{P_{\{\mathbb{R},\mathbb{I}\}}}{\sigma_q^2} \tag{3.1}$$

with $SQNR_{\mathbb{R}}$ and $SQNR_{\mathbb{I}}$ the SQNR of the DAC converting the real or imaginary components of the digital field, respectively, and $P_{\mathbb{R}}$ or $P_{\mathbb{I}}$ the powers (or variance as we consider zero mean signals) of the real and imaginary components, respectively. Finally, $\sigma_q^2 = \Delta^2/12$ is the variance of the quantization noise introduced by each DAC of same resolutions. The Eq.(3.1) is developed as follows:

$$SQNR_{DAC} = \left(\frac{\sigma_q^2}{P_{\mathbb{R}}} + \frac{\sigma_q^2}{P_{\mathbb{I}}}\right)^{-1} \tag{3.2}$$

At this stage, it is convenient to simplify the analysis since the real and imaginary components of optical communication signals generally follow the same statistical properties, with the same variance (power), same probability density function and almost the same maximum absolute value. Indeed, the initial mapping of the constellation set in the complex plane leads to an invariance by inversion of the real and imaginary components[3]. Thus, the PAPR can be safely assumed equal for each component and the optimization problem resumes in maximizing Eq.(3.3) for one component, as the two terms in the right side of Eq.(3.2) are equal. Finally, each component is normalized at the DAC input such that its maximum absolute value coincides with the maximum DAC output amplitude (no clipping) such that the SQNR is given by (see Chapter 2):

$$SQNR_{DAC,\mathrm{dB}} = 6.02 \cdot N_b - PAPR_{\mathrm{dB}} + 4.77 \tag{3.3}$$

where $SQNR_{DAC}$ now denotes the SQNR of the real or imaginary component of the digital field.

However, in practice, the SNR at the transmitter output, SNR_{Tx}, is smaller than the $SQNR_{DAC}$ because of the DAC limited bandwidth, the nonlinearities of the

[3]It is only true at the waveform level if we omit the bit streams encoded into each symbol.

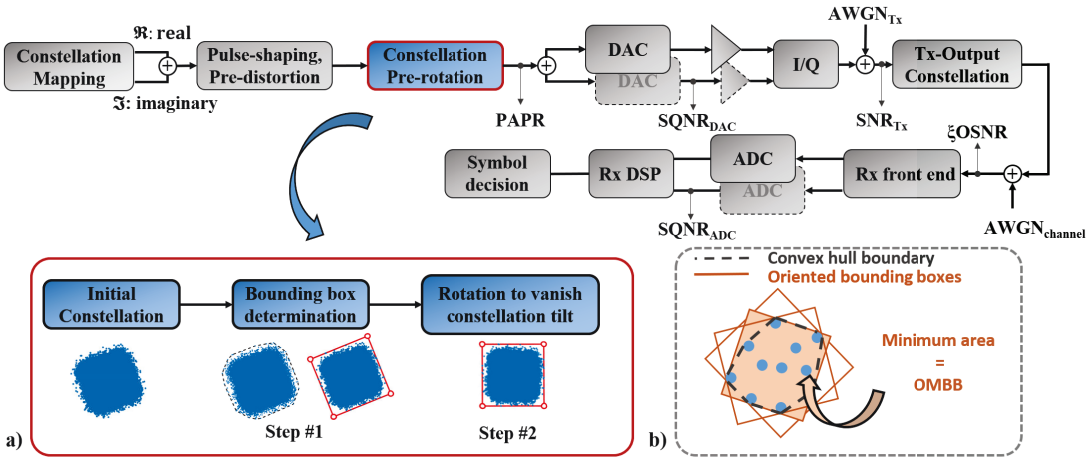

FIGURE 3.3: System model for the implementation and the analysis of the constellation phase rotation method (CPRM). Inset (a) illustrates the constellation phase rotation method with a 64-QAM root-raised-cosine (RRC) constellation with rolloff factor $\beta = 0.4$ and a chromatic dispersion pre-compensation of +100 ps/nm at 32.5 GBaud. Inset (b) shows step n°1 in more details.

driver amplifiers and Mach-Zehnder modulators as well as the thermal noise such as amplifier noises. To emulate this, the transmitter in Fig.3.3 also contains an additive white Gaussian noise ($AWGN_{Tx}$) term, assuming the limited bandwidth to be electronically pre-compensated [41]. Thus, as detailed in Chapter 2, we model the transmitter output SNR_{Tx} as:

$$SNR_{Tx} = \left(\frac{1}{SQNR_{DAC}} + \frac{1}{SNR_{Tx'}} \right)^{-1} \tag{3.4}$$

with $SNR_{Tx'}$ the signal-to-electrical noise ratio resulting from the noise and distortions of the transmitter, excluding the quantization noise, i.e. $SNR_{Tx'} = P_{Signal}/\sigma^2_{AWGN_{Tx}}$. Following, the channel AWGN drives the optical-signal-to-noise-ratio (OSNR) and contributes to the overall SNR linearly with $\xi OSNR$ where $\xi = 12.5/R$ is the conversion factor from the signal noise equivalent bandwidth R (in GHz) to the conventional 0.1 nm OSNR bandwidth (12.5 GHz). The receiver is modeled by a front-end block (coherent mixer and photodiodes) followed by two ADCs (one for each polarization). Similarly to the transmitter, the ADCs quantization penalty is given by $SQNR_{Rx}$ and other imperfections are modeled by an $AWGN_{Rx}$. The SNR at symbol decision is expressed as in [64] by discriminating

the transmitter and the receiver noises:

$$SNR = \left(\frac{1}{SQNR_{DAC}} + \frac{1}{SNR_{Tx'}} + \frac{1}{\xi OSNR} + \frac{1}{SNR_{Rx'}} + \frac{1}{SQNR_{ADC}} \right)^{-1} \tag{3.5}$$

The constellation phase rotation method

In metro optical links employing CD pre-compensation and low resolution DACs, we propose to apply a constellation phase rotation method to minimize the PAPR at the DAC input. The proposed CPRM aims at reducing the PAPR increase due to small CD pre-compensation, which leads to complex signals of the kind of Fig.3.1. However, the CPRM can be extended to pre-distortions that would induce a tilt of the constellation before the DAC. As shown in Fig.3.3, the CPRM block must be inserted just before the DACs. Restricting to the case in which the constellation mapping is square-shaped, I propose the following two-step procedure, namely constellation phase rotation method (CPRM), to align the signal's distribution with the constellation plane axes:

- Step n°1: compute the oriented minimum bounding box (OMBB) of the set of point forming the complex waveform. The OMBB is the square of minimum area which encloses all the points of the complex waveform.
- Step n°2: apply a global phase shift (rotation in the complex plane) to the complex waveform by an angle exactly opposed to the orientation of the OMBB.

The proposed CPRM uses the fact that the OMBB is rotated with respect to the constellation planes axes by an angle which is the rotation angle that minimizes the PAPR. Indeed, the variance of the real and imaginary components of the square constellations are independent of their orientation because of the unitary nature of the rotation operator. To perform fast computations of the OMBB in step n°1, we first compute the convex hull of the constellation points as illustrated in Fig.3.3. Indeed, it was demonstrated that one of the edges of the convex hull necessarily contains one face of the OMBB [77], thus reducing computational complexity. Second, we compute, for each face of the convex hull, the corresponding bounding box and keep the one of minimum area (OMBB).

In term of power consumption and implementation complexity, the CPRM additional power consumption is one complex multiplication per polarization,

which is very limited. Moreover, the ideal rotation angle can be pre-calculated for a given configuration, avoiding for real time implementation of the algorithm into the optical transmitter.

3.2.2 Numerical simulations

The purpose of this section is to assess by numerical simulations the SQNR gain induced by the PAPR minimization when applying the CPRM. The simulation set-up reproduces the system of Fig.3.3. The input data are random symbol sequences of length 2^{16} generated by Matlab and mapped on QPSK, 8 QAM, 16-QAM and 64-QAM at 32.5 GBaud. The waveforms are filtered by a root-raised-cosine (RRC) filter of rolloff factor β and a filter with linear slope +0.3 dB/GHz to compensate for the linear DAC frequency response (see Chapter 1). Note that the PAPR gain is not related to the DAC resolution, as per Eq.(3.3), such that these results apply to any quantizer for which Eq.(3.3) holds (see Chapter 2). To show only the CPRM effect on $SQNR_{Tx}$, we set $SNR_{Tx'}$, $OSNR$, $SNR_{Rx'}$ and $SQNR_{ADC}$ to infinity (quantization limited transmitter, no in-line noise loading and distortion free receiver).

In Fig.3.4, we plot the average PAPR gain ($\Delta PAPR$) with the CPRM over 1000 realizations of the random data sequences and the optimal rotation given by the CPRM. The PAPR gain is defined by the difference of PAPR without and

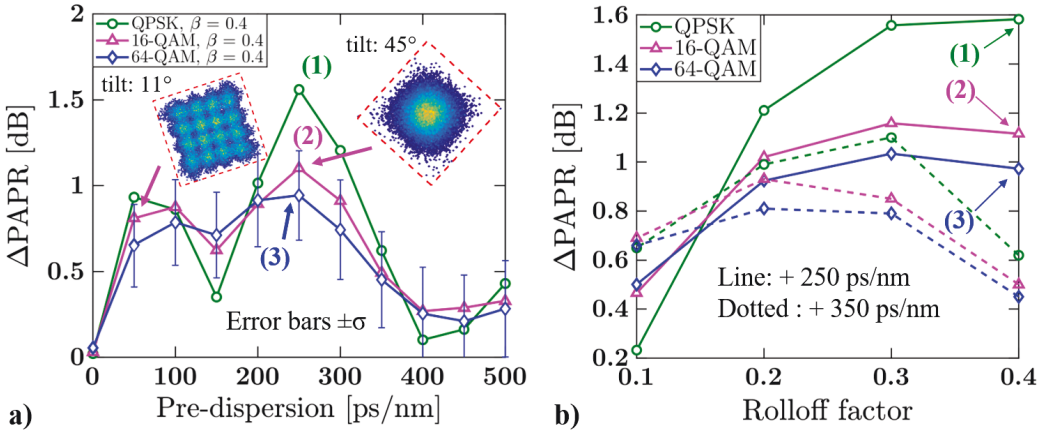

FIGURE 3.4: Numerical simulations. Average PAPR gain ($\Delta PAPR$) over 1000 realizations with CPRM for (a) QPSK, 16-QAM and 64-QAM filtered by a RRC filter of rolloff factor $\beta = 0.4$. (c) Evolution of $\Delta PAPR$ with the rolloff factor for two different CD pre-compensation values. As per Eq.(3.3), the $\Delta PAPR$ gain coincides with the SQNR gain.

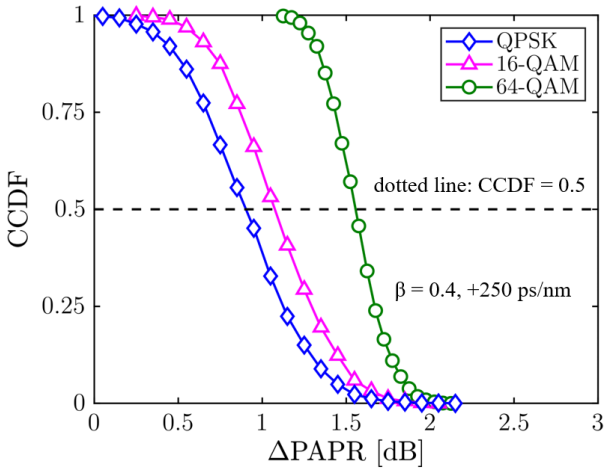

FIGURE 3.5: Numerical simulations. Complementary cumulative density functions (CCDFs) of $\Delta PAPR$ over 1000 realizations with the constellation phase rotation method: QPSK, 16-QAM and 64-QAM with RRC filter $\beta = 0.4$ and +250 ps/nm CD pre-compensation.

with CPRM. It corresponds to the SQNR gain. The PAPR gain depends on the modulation format, the CD pre-compensation and the RRC rolloff factor as these parameters modify the signal distribution. Fig.3.4 shows the PAPR gain and its variation with the CD pre-compensation for different modulation formats. It should be noted that the fluctuations in $\Delta PAPR$ is solely due to change in the symbol sequences because other parameters are kept constant. The CD pre-compensation is limited to 500 ps/nm because above this value the constellation reaches a circular shape and does not benefit from the CPRM. For a CD-pre-compensation of 0 ps/nm, $\Delta PAPR$ is null because the RRC filter itself does not rotate the constellation. When the CD pre-compensation value increases, the $\Delta PAPR$ becomes more important until it reaches a maximum value of +1.6 dB for QPSK, +1.1 dB for 16-QAM and +0.95 dB for 64-QAM at +250 ps/nm for $\beta = 0.4$ which corresponds to a rotation angle of 45°. The optimal rotation is plotted for the 16QAM format, but it is also valid for QPSK and 64QAM as the optimal rotation values are very close and curves would be superimposed. In Fig.3.4 we show the $\Delta PAPR$ as a function of the RRC rolloff factor. We observe that $\Delta PAPR$ gain depends both on the CD pre-compensation, the rolloff factor and the modulation format. At a given rolloff factor the maximum achievable $\Delta PAPR$ depends on the CD pre-compensation. For instance, the best $\Delta PAPR$ is obtained at + 250 ps/nm for $\beta = 0.4$ and + 350 ps/nm for $\beta = 0.1$ These values of CD pre-compensation are chosen because they correspond to the maximum achievable $\Delta PAPR$ in both situations. In any case the $\Delta PAPR$ decreases when

the constellation becomes more circular. We observe that the $\Delta PAPR$ remains up to +0.65 dB for 16-QAM and 64-QAM signals with $\beta = 0.1$ at + 350 ps/nm of CD pre-compensation. Moreover, to have order of magnitude of the variability of $\Delta PAPR$ with the sequence realization, we report in Fig.3.5 the complementary cumulative density functions (CCDF) of $\Delta PAPR$ for +250 ps/nm. The spreading of $\Delta PAPR$ increases with the modulation order (larger CCDF) due to the increasing fluctuations of the constellation with the modulation order. Note that the mean value of the CCDF (i.e. CCDF = 0.5) matches the PAPR gain reported in Fig.3.4.

For illustration, we report on a specific case for which the constellation mapping in absence of the CD pre-compensation does not minimize the PAPR and hence is not optimal for optical networks employing low resolution DAC. For instance, in the context of flexible optical networks, the 8-QAM constellation (3 bits per symbol and per polarization) has been proposed because it offers a good trade off between data rate (higher than QPSK but smaller than 16-QAM) and optical reach (smaller than QPSK but higher than 16-QAM). Different 8-QAM constellations have been proposed such as the 4-4 Star-QAM (or cross 8-QAM), the rectangular 8-QAM or the Circular 8-QAM [78]. Due to its simplicity of implementation with I/Q modulators, the 4-4 Star-QAM is widely use in optical communication systems. Its constellation mapping is shown in Fig.3.6 in the way it is customarily implemented.

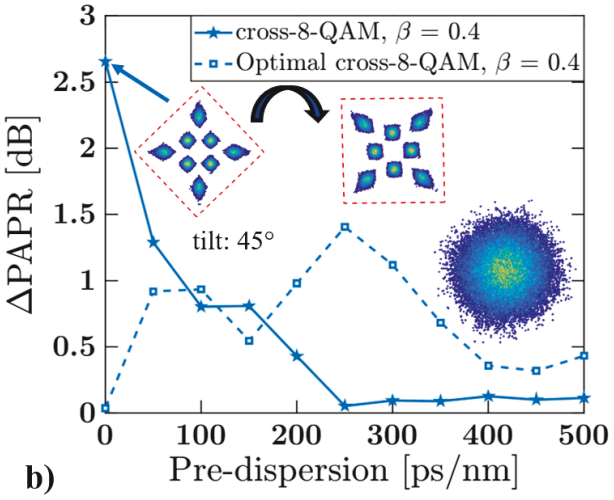

FIGURE 3.6: Numerical simulations. Average PAPR gain ($\Delta PAPR$) over 1000 realizations with CPRM for the 4-4 Star-QAM (or cross 8-QAM) filtered by a RRC filter of rolloff factor $\beta = 0.4$(c). Evolution of $\Delta PAPR$ with the rolloff factor for two different CD pre-compensation values. As per Eq.(3.3), the $\Delta PAPR$ gain coincides with the SQNR gain.

In absence of CD pre-compensation, this cross 8-QAM has a minimum PAPR when it is rotated by an angle of 45°, resulting in a $\Delta PAPR$ of +2.7 dB. Then, if CD pre-compensation is applied, we observe that both the PAPR and the benefits of the CPRM $\Delta PAPR$ decrease because the ISI due to the CD pre-compensation makes the complex digital field aligned with the constellation plane axes. However, when the cross 8-QAM is rotated by a fixed angle of 45° in absence of CD pre-compensation, the behavior of $\Delta PAPR$ is like the square constellations.

Finally, we note that both In Fig.3.4 and Fig.3.6, a high CD pre-compensation value makes the signals more circular, and a suitable rotation angle that yields a meaningful improvement does not exist, as shown in Fig.3.4 above 400 ps/nm.

3.2.3 Experimental demonstration

To demonstrate the efficiency of the CPRM on a practical system in which the quantization induced by the low resolution DAC is not the unique impairment, we assess by experiments the system SNR gain resulting from the $SQNR_{DAC}$ increase when applying the CPRM. We set up an optical back-to-back experiment as in [64] employing an 8-bit DAC operating at 81.28 GS/s with $\approx$ 20 GHz bandwidth (-3 dB in amplitude, see Chapter 1 section 1.3.4). An optical attenuator associated with an amplifier ensures a constant optical power at the entrance of the coherent mixer and we vary the OSNR value by ASE loading. The photocurrents from the coherent mixer are sampled at 200 GS/s by a real-time oscilloscope with 70 GHz electrical bandwidth. With the CPRM, the DSP is unchanged and consists in CD compensation, channel equalization and resampling at 1 sample per symbol with a constant modulus algorithm (17 taps and 1/6000 convergence speed), carrier phase estimation (CPE) and constellation analysis [64] to extract the SNR. Note that CPE recovers the rotation induced by the CPRM. To address metro networks, we investigate the effect of degrading the DAC physical resolution by using only a reduced number of equally spaced quantization levels over the set of 255 available. As we employ a low-resolution DAC but an 8-bit ADC, we can neglect quantization noise at the Rx side, i.e., in Eq.(3.5) we assume $1/SQNR_{ADC} = 0$. We carry experiments with sequences having a $\Delta PAPR$ equal to the average one shown in Fig.3.5.

The Fig.3.7 depicts the measured SNR as a function of the OSNR for QPSK, 8-QAM and 16-QAM signals with rolloff $\beta = 0.4$. The CD pre-compensation is +250 ps/nm for 16-QAM and +0 ps/nm for 8-QAM, initially in the worst

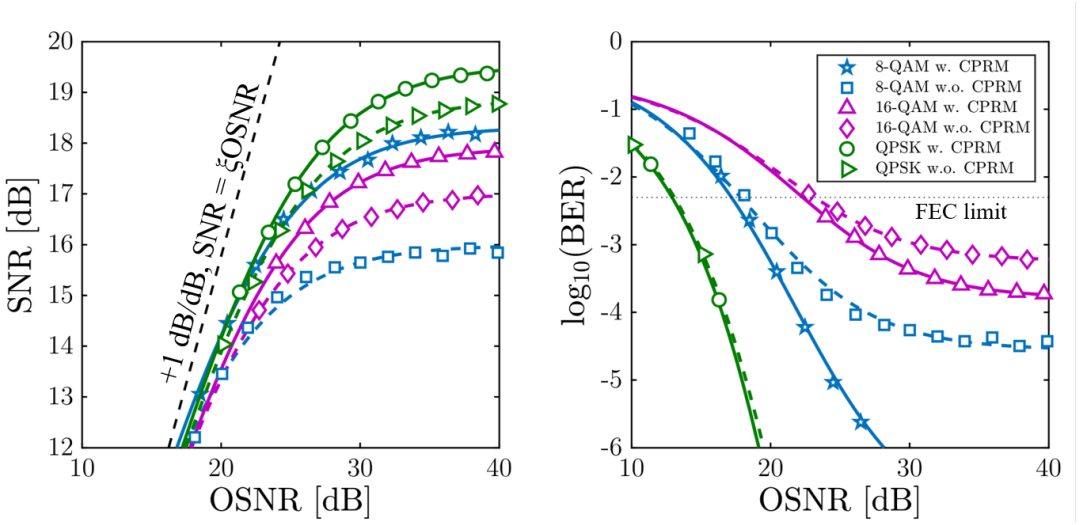

FIGURE 3.7: Experimental results. Left: SNR vs. OSNR for the QPSK, 16-QAM and 8-QAM filtered by a RRC filter of rolloff factor 0.4 and a CD pre-compensation of +250 ps/nm (+0 ps/nm for 8-QAM) with and without CPRM. The DAC physical resolution is 4 bits. Right: BER vs. OSNR for the same signals.

orientation. We used 16 quantization levels over the 255 available to emulate a 4-bit DAC. We observe two regimes. First, for low OSNR, the SNR is proportional to the OSNR (growing at +1 dB/dB) as $1/\xi OSNR$ is the dominant term, as suggested by Eq.(3.5). Second, when the OSNR increases, the SNR achieves an upper-limit given by the terms $SQNR_{DAC}$, $SNR_{Tx'}$ and $SNR_{Rx'}$. With the CPRM, we can improve the $SQNR_{DAC}$, resulting in a SNR gain of +0.65 dB for QPSK, +1.1 dB for 16-QAM and +2.3 dB for 8-QAM, initially in the worst orientation. The SNR gain (defined as the delta between the absolute SNR with and without CPRM) with 16QAM matches the simulations of Fig. 2(a), whereas with QPSK and 8-QAM the SNR gain is slightly lower in experiments than in simulations. We explain this difference by the contribution of $SNR_{Tx'}$ and $SNR_{Rx'}$ in Eq.(3.5). In Fig.3.7, we plot the corresponding BER confirming the performance improvement with CPRM. The pre-FEC BER limit is $2.3.10^{-2}$ corresponding to a FEC overhead of 20%. Note that for QPSK, we cannot measure experimentally a BER below 10^{-6}.

Finally, the Fig.3.8 shows the SNR gain versus the DAC physical resolution. When we increase the DAC resolution (+6 dB for each bit of physical resolution), we increase the absolute value of $SQNR_{DAC}$ while the effect of the CPRM is kept identical because it does not depend on the resolution, as per Eq.3.3. However, the CPRM effect on the overall system SNR decreases with the DAC resolution.

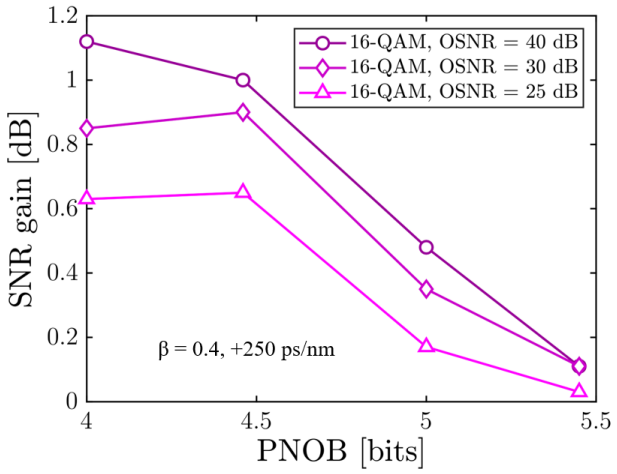

FIGURE 3.8: Experimental results. ΔSNR vs. PNOB for the 16-QAM case of Fig.3.7.

This is because the influence of $SQNR_{DAC}$ in Eq.(3.5) decreases. With a low-resolution DAC (5 bits or below, as shown in Chapter 1), the DAC quantization noise becomes the limiting factor in Eq.(3.5), thus significantly impacting the SNR from 24 dB for 5 bits to 18 dB for 4 bits, measured as in [64] for 16-QAM with CPRM at +250 ps/nm. At 40 dB OSNR, the SNR gain is +1.0 dB (resp. +1.1 dB) with a physical resolution of 4.5 bits (resp. 4 bits) and rapidly decreases when the physical resolution is equal or above 5 bits. Similarly, for a constant DAC resolution, if we increase the amount of ASE noise such that the OSNR decreases, we observe the CPRM effect on the overall system SNR decreases, as expected in Eq.(3.5). However, as the CPRM is efficient for small CD pre-compensation values, thus for small propagation distances, the OSNR influence is expected to be small or negligible in the application cases.

3.2.4 Conclusion

We proposed a novel constellation phase rotation method to reduce the quantization noise penalty induced by low resolution DACs in metro networks in which an electrical pre-compensation of the chromatic dispersion can be employed. We observed that an electrical chromatic dispersion pre-compensation can create a digital complex field which orientation in the complex plane does not minimize the real and imaginary components' PAPR. This leads to a SQNR decrease at the transmitter side if a low resolution DAC is employed. Our constellation phase rotation method aims at finding and applying the optimal phase rotation angle such that the PAPR is minimized and the SQNR as well as the system SNR

are maximized. We assessed by numerical simulations the proposed CPRM in various conditions (modulation formats, RRC rolloff, CD pre-compensation). We experimentally demonstrated up to +1.1 dB system SNR gain for a 4-bit DAC resolution with a 16-QAM signal, well-aligned with simulation, for a CD pre-compensation of 250 ps/nm.

3.3 Noise shaping for optical transmitters

3.3.1 Principle

We have seen in Chapter 2 (section 2.3.3) that the SQNR at the DAC output grows with the oversampling factor, or the number of SPS, at signal quantization, through the relation:

$$SQNR_{\text{dB}} = 6.02 \cdot N_b - PAPR_{\text{dB}} + 4.77 + 10 \cdot \log_{10}(SPS) \tag{3.6}$$

$$= 6.02 \cdot N_b - PAPR_{\text{dB}} + 4.77 + OSR_{\text{dB}} \tag{3.7}$$

Equation (3.7) indicates that the SQNR is proportional to the oversampling factor. Although the advantage of oversampling is clear, increasing the SQNR comes at the expense of an important increase of the DAC sampling frequency, which raises severe technological difficulties. For instance, maintaing the same SQNR when reducing the physical resolution by -1 bit requires to oversample by a factor of 4 (6 dB). However, oversampling has the advantage to create an unused band of frequencies in the spectrum of the signal being quantized, as depicted

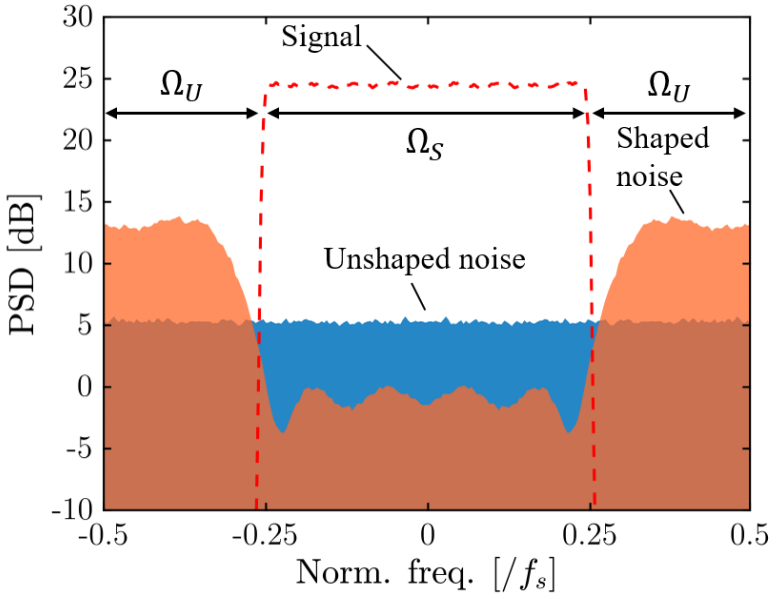

FIGURE 3.9: Numerical simulations. Spectral analysis of the quantization noise shaping. The signal spectrum is a RRC with rolloff factor 0.02 at 2 samples per symbol (red dashed line). The noise shaping filter has 7 taps computed with the weighted least square method and provides a SQNR gain of 6 dB (see subsection 3.3.2). Ω_S denotes the signal bandwidth and Ω_U the unused bandwidth.

in Fig.3.9. The principle of quantization *noise shaping* is to modify the PSD of the quantization noise such that it increases in the unused bandwidth while it decreases in the signal bandwidth, as depicted in Fig.3.9. This further enhances the SQNR gain due to oversampling, as we will show later.

To modify the PSD of the quantization error, noise shaping takes advantage of the deterministic nature of quantization. For a signal $s(n)$, the corresponding quantization noise $q(n)$ can be computed, stored and processed. The digital implementation of noise shaping consists in filtering the quantization noise and re-inject it at the DAC input, as shown in Fig.3.10. We can express the quantizer output $s_q(n)$ as a function of the input $s(n)$, the quantization noise $q(n)$ and the filter taps h:

$$s_q(n) = s(n) + q(n) - \sum_{k=1}^{M} h(n-k) \cdot q(n-k) \tag{3.8}$$

Such that the total error $e(n)$ between the ideal signal $s(n)$ and its quantized version $s_q(n)$ is:

$$e(n) = s_q(n) - s(n) = q(n) - \sum_{k=1}^{M} h(n-k) \cdot q(n-k) \tag{3.9}$$

It should be noted that, whereas the properties of the quantization noise $q(n)$ remain unchanged, an additive uniform white noise, the total error $e(n)$ is spectrally shaped.

To derive the transfer function of the feedback loop of the system in Fig.3.10, it is

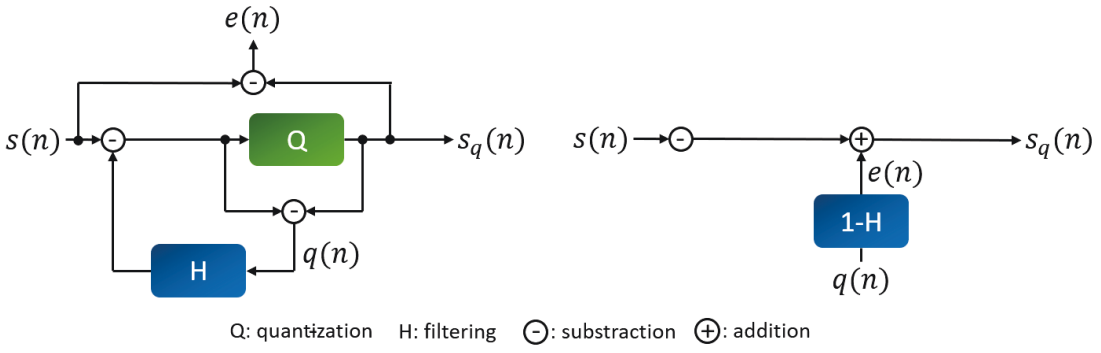

FIGURE 3.10: Left: block diagram of quantization with noise shaping. The quantization error $q(n)$ is filtered by H and subtracted to the incoming signal. Right: corresponding linear system. Noise shaping can be modeled as an additive noise $e(n)$ which is a filtered version of $q(n)$. In both, the block H is a M-taps finite impulse response (FIR) filter.

convenient to introduce the z-transform as we work with discrete time sequences. The z-transform of a sequence $s(n)$ is defined by:

$$S(z) = Z\left[s(n)\right] = \sum_{n=0}^{N} s(n) z^{-n} \tag{3.10}$$

with z a complex number and N the number of samples of the sequence. By choosing $z = e^{2i\pi f}$, Eq.(3.10) coincides with the discrete Fourier transform (DFT). One important property of Eq.(3.10) is that the z-transform of the convolution of two discrete sequences is the product of their z-transform (convolution theorem). As linear filtering is a convolution with the filter impulse response, one can write in the z-domain:

$$s_q(n) = s(n) + q(n) - h(n) * q(n) \iff S_q(z) = S(z) + Q(z) - H(z) \cdot Q(z) \tag{3.11}$$

where $*$ denotes the convolution product and $S_q(z)$, $S(z)$, $Q(z)$ and $H(z)$ are the z-transform of the quantized signal, ideal signal, quantization noise and noise shaping filter, respectively. From Eq.(3.11), we identify the z-transform of the total error $E(z)$:

$$E(z) = (1 - H(z)) \cdot Q(z) \tag{3.12}$$

with:

$$H(z) = h_1 z^{-1} + h_2 z^{-2} + ... + h_M z^{-M} \tag{3.13}$$

the z-transform of the noise shaping filter impulse response. The noise transfer function (NTF) in the spectral Fourier domain is obtained by taking $z = e^{2i\pi f}$:

$$NTF = \frac{E(e^{2i\pi f})}{Q(e^{2i\pi f})} = 1 - H(e^{2i\pi f}) \tag{3.14}$$

In practice, the DFTs involved in Eq.(3.11) are computed by the Fast Fourier Transform (FFT) algorithm. Thus, we define a time vector associated to the signal as:

$$t(n) = \left[0, \frac{1}{f_s}, \frac{2}{f_s}, ..., \frac{N-1}{f_s}\right] \tag{3.15}$$

with f_s the sampling frequency, N the sequence length and $n \in [1, N]$. Hence, the discrete frequencies f are given by[4]:

$$f(n) = \left[-\frac{f_s}{2}, -\frac{f_s}{2} + \frac{f_s}{N}, ..., \frac{f_s}{2} - \frac{f_s}{N}\right] \tag{3.16}$$

[4]For clarity, we directly define the vector f through its shifted version with the zero frequency in the middle, whereas the FFT algorithm uses the non shifted version of f, with the zero frequency in first position

Equation (3.16) car be re-written:

$$f(n) = \left[-\frac{f_s}{2}, -\frac{f_s}{2} + \frac{1}{T}, ..., \frac{f_s}{2} - \frac{1}{T}\right] \tag{3.17}$$

where $T = \frac{N}{f_s}$ is the temporal length of the discrete sequence $t(n)$. The purpose of noise shaping is to minimize the NTF within the signal bandwidth.

3.3.2 Design of the noise shaping filter

The design of the noise shaping filter consists in computing the set of taps $[h_1, h_2, ..., h_M]$ such that the corresponding NTF is minimal within the signal bandwidth, denoted Ω_S. Several approaches have been reported in the literature. In [73], the author proposed a method based on the Hilbert transform of the targeted transfer function's log-magnitude. This method is of interest if a specific noise transfer function, and not simply a minimization within the signal bandwidth, is targeted. In [74], author proposed a weighted least square approach based on the signal spectrum only. More recently, authors in [58, 59] proposed a dynamic algorithm which performs quantization with noise shaping based on a 2-step procedure. In this thesis, we choose to consider the general weighted least square approach of [74] for different reasons. First, this approach is based on a matrix formalism, hence simplifying the numerical implementation and the computation of the noise shaping filter taps. Second, assuming that the filter taps have been pre-computed, its complexity of implementation coincides with one of a linear filter with a reduced number of taps (≈20 in the worst cases). Such an additional complexity is not expected to vanish, in terms of power consumption, the benefits of the physical resolution reduction.

Mathematical formalism

Formally, the noise transfer function (NTF) minimization within the signal bandwidth Ω_S is written [74]:

$$\min_{h_1,h_2,...,h_M} \int_{\Omega_S} |1 - H(e^{2i\pi f})|^2 df \tag{3.18}$$

Which becomes with the discretization in the frequency domain:

$$\min_{h_1,h_2,...,h_M} \sum_{i=1}^{N'} |1 - H(e^{2i\pi f_i})|^2 df \tag{3.19}$$

with i the indexes of the $N' < N$ frequencies comprised within the signal bandwidth Ω_S. The Eq.(3.19) can be written into a matrix form:

$$1 - H(e^{2i\pi f_i}) = \begin{bmatrix} 1 \\ 1 \\ \vdots \\ 1 \end{bmatrix} - \begin{bmatrix} e^{-2i\pi f_1} & e^{-2i\cdot 2\cdot \pi f_1} & \dots & e^{-2i\cdot M\cdot \pi f_1} \\ e^{-2i\pi f_2} & e^{-2i\cdot 2\cdot \pi f_2} & \dots & e^{-2i\cdot M\cdot \pi f_2} \\ \vdots & \vdots & \ddots & \vdots \\ e^{-2i\pi f_M} & e^{-2i\cdot 2\cdot \pi f_M} & \dots & e^{-2i\cdot M\cdot \pi f_M} \end{bmatrix} \begin{bmatrix} h_1 \\ h_2 \\ \vdots \\ h_M \end{bmatrix} \tag{3.20}$$

Which can be rewritten:

$$\min_{\mathbf{h}} ||\mathbf{1} - \mathbf{A}\mathbf{h}||^2 \tag{3.21}$$

with $\mathbf{1} = [1; 1; ...; 1]$, $\mathbf{h} = [h_1; h_2; ...; h_M]$ and:

$$\mathbf{A} = \begin{bmatrix} e^{-2i\pi f_1} & e^{-2i\cdot 2\cdot \pi f_1} & \dots & e^{-2i\cdot M\cdot \pi f_1} \\ e^{-2i\pi f_2} & e^{-2i\cdot 2\cdot \pi f_2} & \dots & e^{-2i\cdot M\cdot \pi f_2} \\ \vdots & \vdots & \ddots & \vdots \\ e^{-2i\pi f_S} & e^{-2i\cdot 2\cdot \pi f_S} & \dots & e^{-2i\cdot M\cdot \pi f_S} \end{bmatrix} \tag{3.22}$$

Note that $\mathbf{h}$ is constrained to be real valued and $\mathbf{A}$ is complex valued. We can stack the real $\mathbf{A_r}$ and imaginary $\mathbf{A_i}$ part of $\mathbf{A}$ and define a new vector $\mathbf{0}$ of same size of $\mathbf{1}$ such that the minimization problem becomes:

$$\min_{\mathbf{h}} || \begin{bmatrix} \mathbf{1} \\ \mathbf{0} \end{bmatrix} - \begin{bmatrix} \mathbf{A_r} \\ \mathbf{A_i} \end{bmatrix} \mathbf{h}||^2 \tag{3.23}$$

For which a real solution is:

$$\mathbf{h}_{opt} = + \begin{bmatrix} \mathbf{A_r} \\ \mathbf{A_i} \end{bmatrix}^{\dagger} \begin{bmatrix} \mathbf{1} \\ \mathbf{0} \end{bmatrix} \tag{3.24}$$

where † denotes the *pseudoinverse* of matrix $\mathbf{A}$.

Equation (3.24) minimizes the NTF within the signal bandwidth without additional constraints within the unused bandwidth Ω_U. Hence, it is possible that the NTF becomes too large in the unused bandwidth, generating excessive values of the filtered error and saturation of the quantizer. To resolve this limitation, author in [74] proposes to modify the matrix $\mathbf{A}$ such that it includes also the frequencies

of the unused bandwidth Ω_U:

$$\mathbf{A} = \begin{bmatrix} e^{-2i\pi f_1} & e^{-2i\cdot 2\cdot \pi f_1} & \dots & e^{-2i\cdot M\cdot \pi f_1} \\ e^{-2i\pi f_2} & e^{-2i\cdot 2\cdot \pi f_2} & \dots & e^{-2i\cdot M\cdot \pi f_2} \\ \vdots & \vdots & \ddots & \vdots \\ e^{-2i\pi f_{S+U}} & e^{-2i\cdot 2\cdot \pi f_{S+U}} & \dots & e^{-2i\cdot M\cdot \pi f_{S+U}} \end{bmatrix} \tag{3.25}$$

Moreover, the trade-off between attenuation of the quantization noise within the signal bandwidth and amplification in the unused bandwidth is assessed by introducing a weighting matrix $\mathbf{W} = diag(W_1, W_2, ..., W_{S+U})$ where the weights give more or less importance to the optimization at the corresponding frequency. For instance, if $W_i, f_i \in \Omega_S > W_j, f_j \in \Omega_U$, the optimization gives more importance to the attenuation of the quantization noise within the signal bandwidth while if $W_i, f_i \in \Omega_S < W_j, f_j \in \Omega_U$, the optimization tends to maintain a small amplification of the quantization noise in the unused bandwidth (more stable feedback).

With the weighting matrix the optimization problem becomes:

$$\min_{\mathbf{h}} ||\mathbf{W}'(\mathbf{1} - \mathbf{A}\mathbf{h})||^2 \tag{3.26}$$

where the matrix:

$$\mathbf{W}' = \begin{bmatrix} \mathbf{W} & 0 \\ 0 & \mathbf{W} \end{bmatrix} \tag{3.27}$$

accounts for the extension of the matrix $\mathbf{A}$ into its real and imaginary parts. The new solution of the optimization problem is:

$$\mathbf{h}_{opt} = + \begin{bmatrix} \mathbf{W}' \begin{bmatrix} \mathbf{A_r} \\ \mathbf{A_i} \end{bmatrix} \end{bmatrix}^{\dagger} \mathbf{W}' \begin{bmatrix} \mathbf{1} \\ \mathbf{0} \end{bmatrix} \tag{3.28}$$

Strategy for the filter design

To design the noise shaping filter, we choose a square-shaped weighting function of the form:

$$W_i = a, f_i \in \Omega_S \text{ and } W_j = b, f_j \in \Omega_U \tag{3.29}$$

The square form of the weighting function aims at imitate a RRC spectra with small rolloff, a standard configuration in optical communications, as depicted in Fig.3.11. Moreover, it simplifies the design as the only parameters is the ratio a/b and the number of SPS, as shown in Fig.3.11. Once the weighting function is

chosen, we select a given number of taps for the noise shaping filter (length of the vector $\mathbf{h}$) and we apply Eq.(3.28). This computation is done for several ratios a/b and we finally choose the taps which give the best $\Delta SQNR$ gain:

$$\Delta SQNR_{\text{dB}} = 10 \cdot \log_{10} \left(\int_{\Omega_S} |1 - H\left(e^{-2i\pi f}\right)|^2 \right) \tag{3.30}$$

Hence, with quantization noise shaping, the SQNR becomes:

$$SQNR_{\text{dB}} = 6.02 \cdot N_b - PAPR_{\text{dB}} + 4.77 + OSR_{\text{dB}} + \Delta SQNR_{\text{dB}} \tag{3.31}$$

In what follows, we define $\Delta SQNR'_{\text{dB}} = OSR_{\text{dB}} + \Delta SQNR_{\text{dB}}$ the overall SQNR gain with oversampling and noise shaping.

The procedure for the noise shaping filter design can be summarized as follows:

- 1) Choose the number of SPS or OSR.
- 2) Choose the ratio a/b of the square weighting function.
- 3) Choose the number M of taps of the noise shaping filter and compute the filter's taps with Eq.(3.28).
- 4) Compute the SQNR gain by numerical integration of the noise-transfer function, through Eq.(3.30)
- 4bis) Repeat 2), 3) and 4) to find the filter which maximizes the SQNR gain, at a given OSR, with respect to the ration a/b and the number of taps M.

An example of weighting function for 2 SPS (the signal bandwidth is half the Nyquist bandwidth of the DAC, corresponding to the example of Fig.3.9) is shown in Fig.3.11. The computed NTF with a filter length of 7 taps and $a/b = 15$ dB is represented and clearly makes appear the NTF attenuation within the signal bandwidth Ω_S.

Now, for each OSR value, the noise shaping filter is determined to provide the best SQNR gain by an extensive set of numerical computations. We apply the filter design procedure for various values of number of taps M and different ratios a/b. These results are presented in Fig.3.12 in the form of a surface plot $SQNR = f(M, a/b)$ for different OSR values.

These results are analyzed as follows. We observe that for moderate and high OSR values (2 SPS and above) there is a ratio a/b which enables to maximize

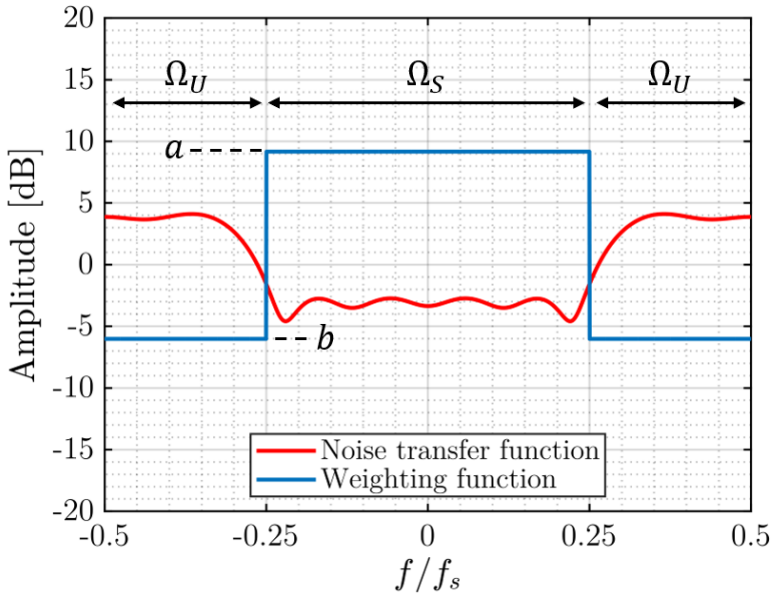

FIGURE 3.11: Numerical simulations. Example of the magnitude of the noise shaping transfer function with a square weighting function with ration $a/b =$ 15 dB and designed for operations at 2 samples per symbol.

the SQNR gain. On the other hand, the number of taps M has only a small influence on the $SQNR$ gain such that it can be chosen relatively small, which is beneficial in terms of complexity. For instance, with 4, 2.5 and 2 SPS, increasing M above ≈ 7 has no significative influence on the noise shaping filter's performance. However, for small OSR values (2 SPS and below) the behaviour is different because the SQNR gain depends more on the number of taps M than in the ratio a/b, and it can be interesting to increases M above 10, as we can see on the right bottom graph of Fig.3.12. For a better visualization of these trends, we show in Fig.3.13 the evolution of the SQNR gain at constant M or ratio a/b while varying the ratio a/b or the value of M, respectively. The Fig.3.13 confirms the qualitative observation of Fig.3.12. Finally, a fundamental observation is that the maximum achievable SQNR decreases with the OSR. This is because the smaller is the unused bandwidth Ω_U, the smaller is the amount of quantization noise which can be rejected outside the signal bandwidth Ω_S. Equivalently, obtaining a given SQNR gain when reducing the OSR requires a greater amplification of the quantization noise in the unused bandwidth, an amplification which is limited by the weighting process to avoid instability of the feedback path. Finally, we report in Fig.3.14, the maximum $\Delta SQNR'$ gain as a function of the OSR, confirming that quantization noise shaping enables to strongly increase the SQNR gain obtained by oversampling alone.

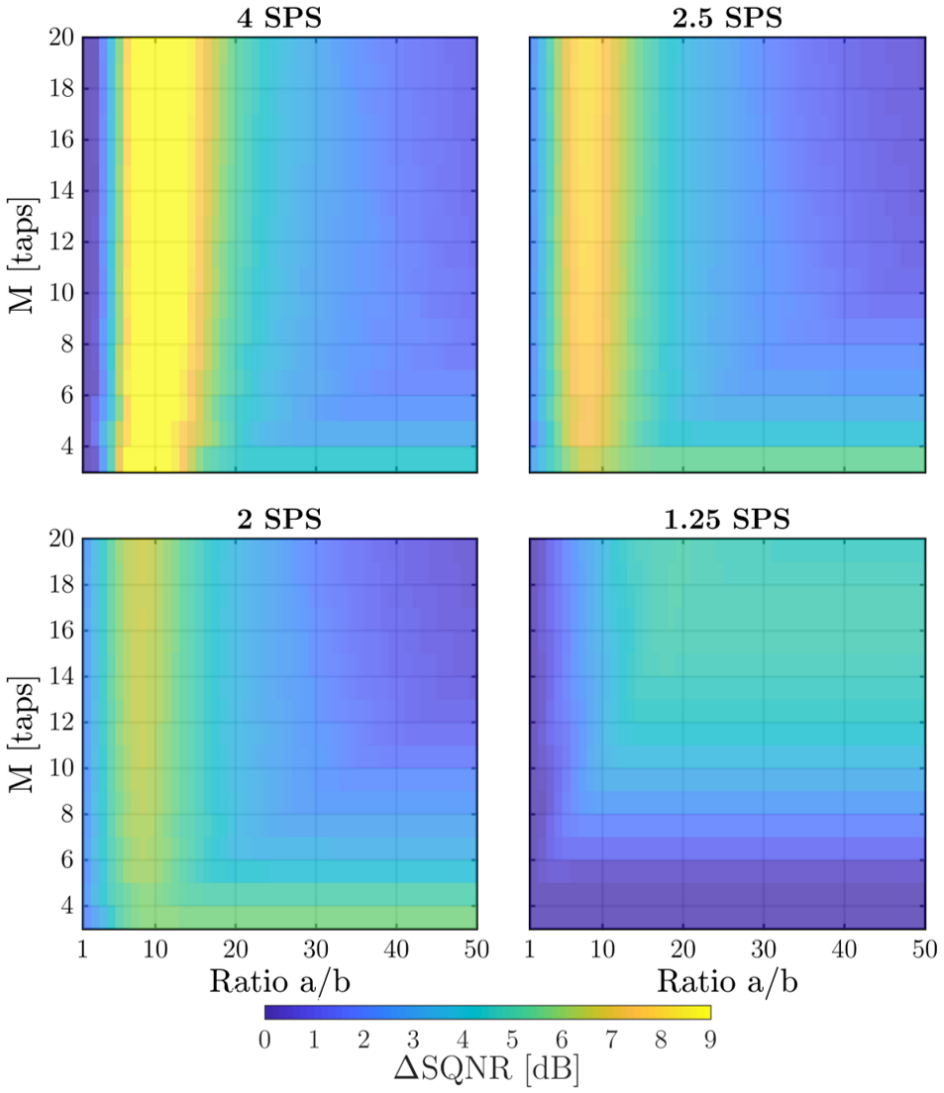

FIGURE 3.12: Numerical simulations. Signal to quantization noise ratio gain for different oversampling ratios as a function of the noise shaping filter number of taps M and weighting function ratio a/b.

3.3.3 Experimental demonstration

To demonstrate the efficiency of the noise shaping technique based on a weighted least-square computation of the filter taps, we set up an optical back-to-back (B2B) test-bed, as shown in Fig.3.15, and perform two distinct sets of experiments. First, a detailed performance gain analysis by employing 16-QAM modulation format at various data rates and with decreasing the DAC physical resolution down to 3 bits is performed. By doing this, we quantify the achievable performance gains with noise shaping in various configurations and compare our results with the expected values provided by the model of Eq.(3.31). In a second set of experiments, we

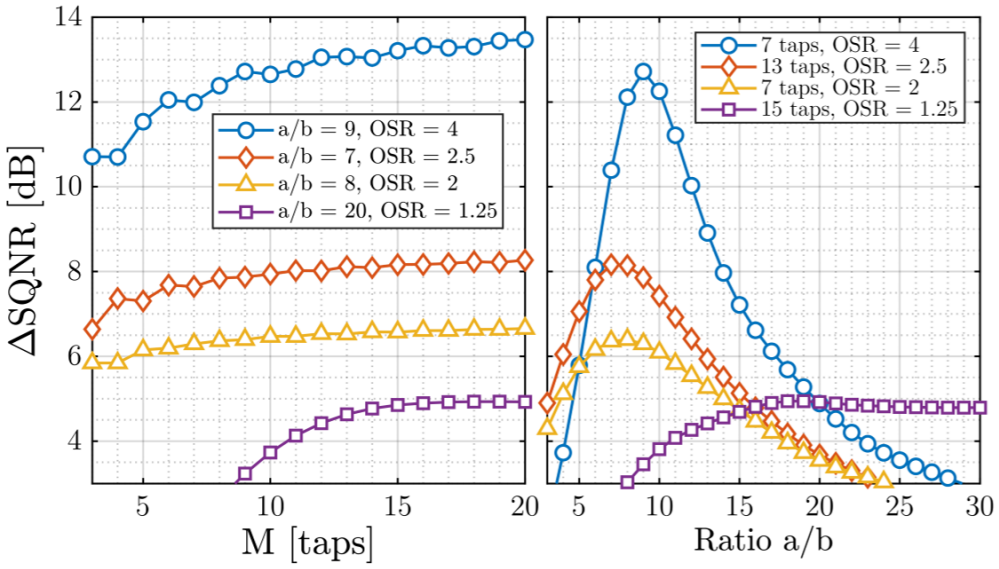

FIGURE 3.13: Numerical simulations. Signal to quantization noise ratio gain for different oversampling ratios as a function of the noise shaping filter number of taps M (left) and weighting function ration a/b (right).

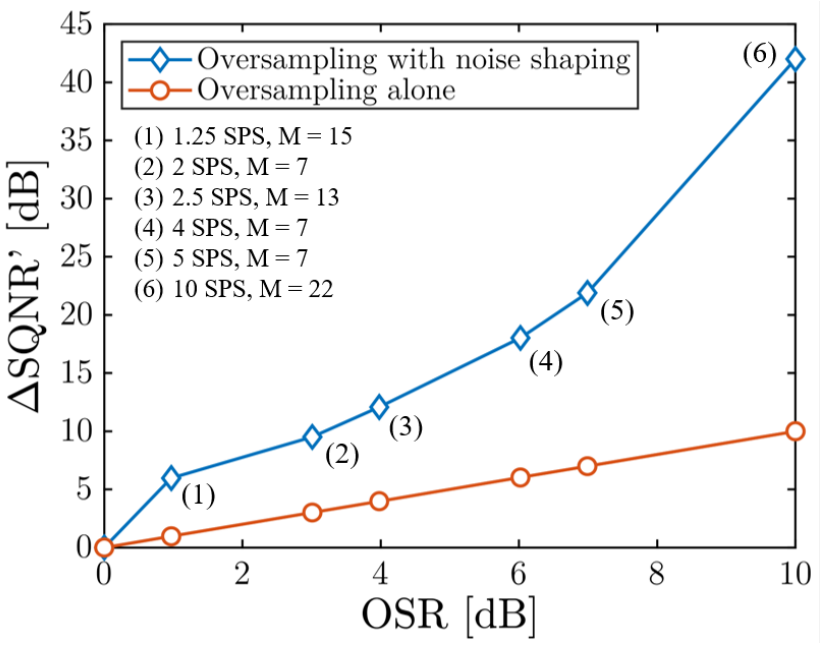

FIGURE 3.14: Numerical simulations. Maximum achievable $\Delta SQNR'$ gain with oversampling and noise shaping by using the weighted least square method for the filter design. For each OSR value, the considered $\Delta SQNR'$ is the greatest over the explored values of the ratio a/b and the number of taps M is chosen arbitrarily as low as possible.

demonstrate the feasibility of 16-QAM and 64-QAM transmission at 44 GBaud (352 and 528 Gbit/s) combining low resolution (2 and 3 bits) with quantization noise shaping and derive the expected achievable optical reach in case of low-resolution DAC.

1^{st} experiments: performance analysis

The coherent transmitter employs the same DAC as in Chapter 1, with a sampling frequency fixed at 81.28 GS/s. The clock reference is an external synthesizer operating at 2.54 GHz. As shown in Chapter 1, employing an external synthetizer enables the minimization of the clock timing jitter such that we focus on the quantization noise induced penalty only. Between the transmitter and the receiver (see Fig.3.15), a first VOA associated with an EDFA enables the variation of the OSNR. A second VOA enables the adjustment of the optical power at the entrance of the coherent mixer without modifying the OSNR. Hence, we can control the signal dynamic range at the ADCs. In all the measurements, the signal's dynamic range is adjusted to the entire ADCs dynamic range such that we force the $SQNR_{ADC}$ to be much greater than the other distortions, as the ADC physical resolution is 8-bit.

At the transmitter side, the signal consists in a Debruijn sequence of 2^{15} symbols, mapped on a 16-QAM constellation at 5, 4, 2.5 and 2 SPS (or OSR), hence producing the data rates of 16, 20, 32 and 40 GBaud. They are filtered with a RRC filter with rolloff factor 0.02. A high-pass filter with linear slope in frequency (+4 dB/GHz)[5] serves to compensate for the low-pass frequency response of the DAC (see Chapter 1). The waveforms are quantified over a set of 16 to 255 equally spaced quantization levels (4 to 8 bits uniform quantizer) without and with noise

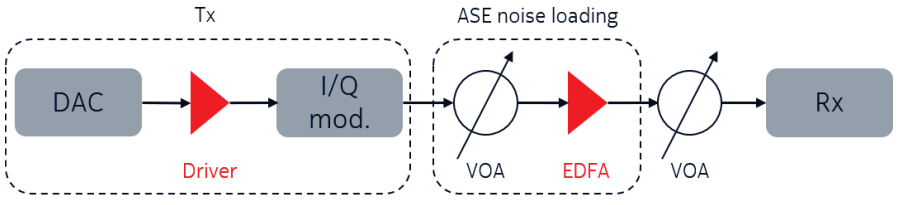

FIGURE 3.15: Experimental optical-back-to-back set-up for the noise shaping experiments.

[5]This value is slightly higher than the linear slope of the DAC frequency response, ≈-2.5 dB/GHz, as we have to include the frequency response of the driver amplifiers and of the electro-optics modulators.

Parameters	Value	Comment
DAC physical resolution	4 to 8 bits	Uniform quantizer
DAC sampling rate	81.28 GS/s	
Modulation format	16-QAM	RRC 0.02
Data rate [GBaud]	16, 20, 32, 40	5, 4, 2.5, 2 SPS
Weighting function a/b	10, 8, 8, 6	To maximize SQNR
Number of taps M	7, 7, 13, 7	To minimize complexity
ΔSQNR [dB]	+14.9, +12, +8.1, +6.1	

TABLE 3.1: Experimental configurations.

shaping. For each configuration, the noise shaping filter gives the best possible SQNR gain, respectively +14.9, +12, +8.1 and +6.1 dB, determined following the methodology presented in the previous section. The investigated configurations and the corresponding filter taps are shown in Table 3.1 and Fig.3.16, respectively. The alternance of positive and negative tap values is characteristic of an high-pass transfer function, as required to reject the quantization outside the signal bandwidth. The PSD of the signal and of the quantization noise with and without noise shaping are shown in Fig.3.17.

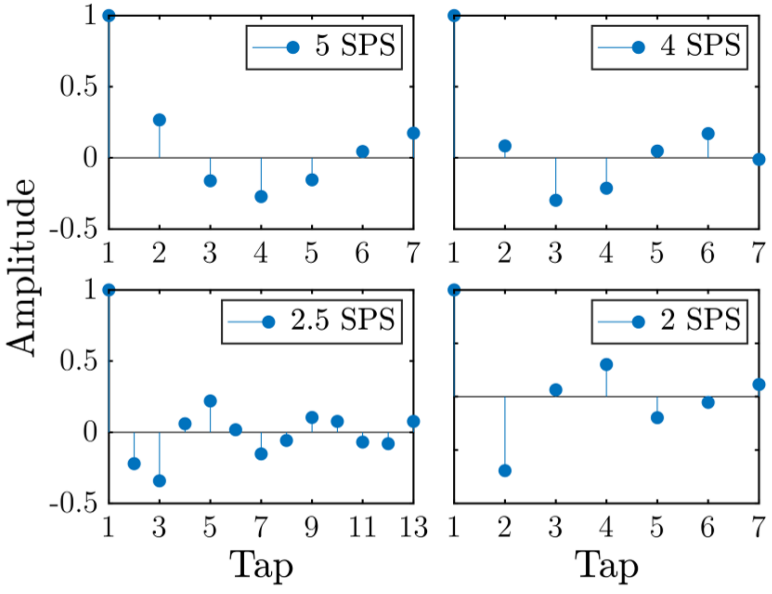

FIGURE 3.16: Experiments. Taps of the noise shaping filters for the configurations reported in Table 3.1.

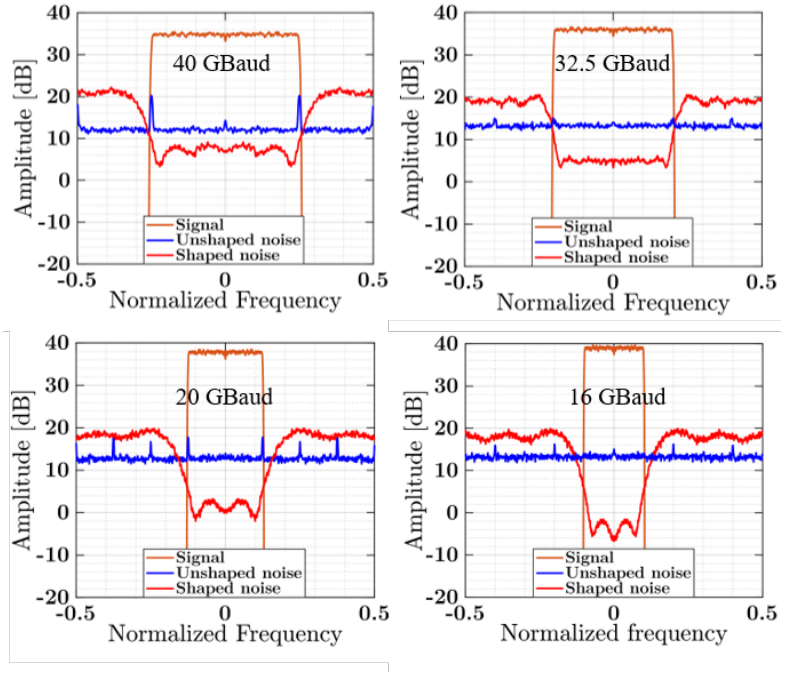

FIGURE 3.17: Experiments. Spectra of: the quantized signal (orange line), the quantization noise without noise shaping (blue curve) and the quantization noise with noise shaping (red curve). Each noise transfer function corresponds to the filter taps of Fig.3.16. The signal quantized with noise shaping (orange and red spectra) is loaded into the DAC memory.

At the receiver, the photo-currents issued from the coherent mixer are sampled by a 40 GS/s oscilloscope employing 8-bit ADCs. The receiver DSP consists in matched filter, resampling at 2 SPS, equalization with a 25 taps multi-modulus-algorithm and down-sampling at 1 SPS, frequency and phase recovery and finally a post-equalizer to compensate for a possible skew (time delay) between the real and imaginary components of each polarization. The electrical bandwidth of the oscilloscope is about 20 GHz (-3 dB) in amplitude such that it contributes to the filtering of the out-of-band quantization noise.

We report in Fig.3.18 the measured SNR (as in [64]) as a function of $1/\sigma^2_{ASE}$ for the different OSR. For the sake of visibility, these graphs only show the SNR curves for the 8-bit DAC, as reference, and for the 4-bit DAC without and with noise shaping to demonstrate the efficiency of the method. These results are analyzed as follows. First, the SNR evolution for the 8-bit DAC serves as a reference to extract the system behavior without quantization noise. As the ASE noise becomes negligible with respect to the transceiver noise, i.e. $\sigma^2_{ASE} \ll \sigma^2_{TRx}$ (right side fo the graphs), the measured SNR tends toward the limit set by $SNR_{TRx'}$, whose increases when the data rate decreases (red triangle symbols in Fig.3.18). However, the achievable

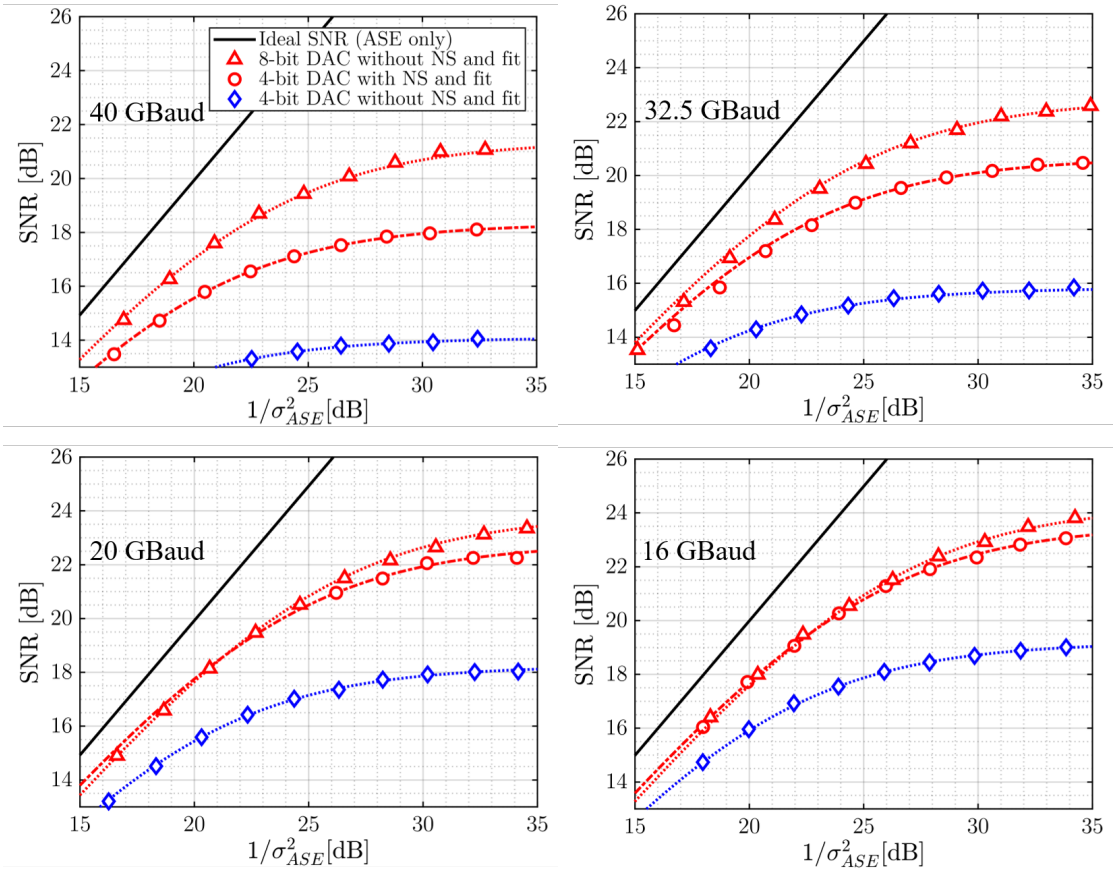

FIGURE 3.18: Experimental results. SNR as a function of $1/\sigma^2_{ASE}$ at four different data rates (40, 32.5, 20 and 16 GBaud) corresponding to 2, 2.5, 4 and 5 samples per symbol, respectively. Black line is the ideal system with ASE noise only. Symbols are measurements, curves are fit with Eq.(3.32).

OSNR in the experiments is not sufficient to observe the complete saturation of the SNR when $\sigma^2_{ASE} \to 0$. To overcome this limitation, we fit the measurements with a function of the form:

$$SNR = \frac{1}{\mu}\left(\frac{1}{SNR_{TRx'}} + \frac{1}{\xi OSNR}\right)^{-1} \tag{3.32}$$

where $\xi OSNR = 1/\sigma^2_{ASE}$ and $\xi = R/12.5$ is the conversion factor from the signal bandwidth (expressed in GHz) to the conventional bandwidth for the OSNR in 0.1 nm (12.5 GHz). The results are presented in Table 3.2 and confirm that the $SNR_{TRx'}$ decreases, following the widening of the equivalent noise bandwidth as the data rate increases, hence integrating more ASE noise from the EDFA. However, while the measurements are in accordance with Eq.3.32, the evolution of SNR_{TRx} with the data rate slightly differs from values expected for an additive white noise. Indeed, when dividing the signal bandwidth by a factor of 2 the

Data rate [GBaud]	μ	$SNR_{TRx'}$ [dB]
40	0.77	22.6
32	0.75	23.4
20	0.77	25
16	0.73	25.7

TABLE 3.2: Experimental results. Extracted μ and $SNR_{TRx'}$ with a fit by a function of the form of Eq.(3.32) on the measurements presented in Fig.3.18, when employing the 8-bit DAC. $SNR_{TRx'}$ is the SNR due to the transmitter and receiver noises in absence of quantization noise (see Chapter 2 for definition).

DAC resolution [bits]	SNR_{TRx} with NS [dB]	SNR_{TRx} without NS [dB]
8	22.5/23.8/25.4/25.7	22.6/23.8/25.0/25.7
7	22.3/23.7/24.9/25.8	21.8/23.6/24.7/25.4
6	22.0/23.7/24.8/25.4	21.6/22.9/24.4/24.9
5	21.6/23.3/24.6/25.0	19.5/21.1/22.7/24.0
4	19.4/21.7/23.3/24.5	15.4/17.2/19.5/20.5

TABLE 3.3: Experimental results. Extracted SNR_{TRx} by fitting the SNR versus σ^2_{ASE} measurements with a function of the form of Eq.(3.32) for different DAC resolution. The results are presented with and without quantization noise shaping and for different data rates: 40 GBaud (red values), 32.5 GBaud (orange values), 20 GBaud (green values) and 16 GBaud (black values), ordered from left to right in each column. SNR_{TRx} is the SNR due to the transmitter and receiver noises, including quantization noise (see Chapter 2 for definition).

$SNR_{TRx'}$ increases by less than +3 dB. We attribute this deviation from the additive noise model to the filtering of the signal by the oscilloscope[6], and to the possible effect of non-ideal signal equalization at the receiver side. However, at a given data rate, these effects, combined with the AWGN of the transceiver, can be modeled by an AWGN, as suggested by Eq.3.32.

Then, we analyze the results when the DAC resolution is 4 bits. As expected from the DAC characterization in Chapter 1, the quantization noise with 4-bit resolution is non negligible, and it explains the SNR decrease (see blue diamond symbols in the Fig.3.18). However, when applying quantization noise shaping, the SNR_{TRx} increases by several dB's, confirming the efficiency of the noise shaping for low-resolutions DAC (see red circle symbols). To analyze quantitatively the efficiency of the noise shaping we proceed as follows. The experiment is repeated

[6]And not to the limited bandwidth of the DAC as we perform digital pre-emphasis.

with different DAC resolutions (from 4 to 8 bits), with and without noise shaping, and the measurements are fitted by a function of the form of Eq.(3.32). The results are reported in Table 3.3 and the new saturation value is noted SNR_{TRx} to differentiate it from the 8-bit DAC configuration (see Chapter 2 for definition). For the 4-bit DAC without noise shaping, the SNR variation with data rate is consistent with the assumption of an additive noise as limiting factor. Indeed, from 40 to 20 GBaud or from 32 to 16 GBaud the SNR_{TRx} increases by ≈+3 dB: 15.4 to 19.5 dB and 17.2 to 20.5 dB, respectively. Indeed, with the 4-bit DAC without noise shaping, the quantization noise is the dominating distortion in this experimental set-up. With noise shaping, the performance improvement is of the order of +4 dB for all the data rates (we analyze below why this value is the same for all the data rates), a value which is particularly important as it corresponds to +0.7 bit. It should be noted that this value overcomes the SQNR gain which can be obtained by the other optimization methods, as summarized in section 3.5.

Finally, we demonstrate that the influence of the quantization noise can be separated from the other transceiver noises and distortions. To do so, we plot in Fig.3.19 the SNR_{TRx} as a function of the DAC resolution, with and without noise shaping. For the sake of conciseness, the results of the analysis are presented for 32.5 Gbaud only, in Fig.3.19. The values of SNR_{TRx} are fitted with a function of the form:

$$SNR_{TRx} = \left(\frac{1}{SNR_{TRx'}} + \frac{1}{SQNR_{DAC}} \right)^{-1} \tag{3.33}$$

with $SNR_{TRx'}$ the fitted SNR saturation value for 8-bit resolution and $SQNR_{DAC}$ the signal to quantization noise ratio of the emitted waveform given by:

$$SQNR_{DAC,\mathrm{dB}} = 6.02 \cdot N - PAPR_{\mathrm{dB}} + 4.77 + OSR_{\mathrm{dB}} + C_{\mathrm{dB}} \tag{3.34}$$

Because the PAPR and the OSR are known (we extract the PAPR on the waveforms before quantization in *Matlab*), the value of the constant C_{dB} should be close to zero without noise shaping and close to the noise shaping filter gain given by Eq.3.30 with noise shaping. The fits and the measurements for the different DAC resolutions are shown in Fig.3.19, and very well agree. For reference, we plot (red dotted line) the $SNR_{TRx'}$ when employing the 8-bit DAC, around +23.5 dB. The key result is the +4.5 dB of system SNR gain when employing the noise shaping with the 4-bit DAC at 2.5 SPS (pink arrow). Indeed, without noise shaping, the SNR_{TRx} for the 4-bit DAC is 17.2 dB while it becomes 21.7 dB with noise shaping. Regarding the other values of physical resolution, the noise shaping SNR gain decreases with the resolution. This is because quantization noise is negligible when the physical resolution is equal or higher to 7 bits in the present

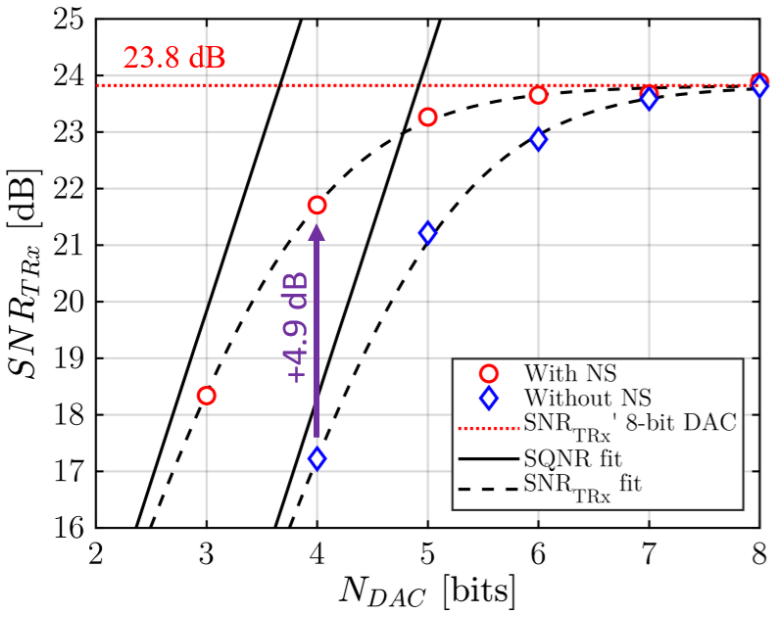

FIGURE 3.19: Experimental results. Evolution of the SNR_{TRx} with the DAC physical resolution, with and without noise shaping for 32.5 GBaud (2.5 SPS). In the two cases, the measures are fitted with a function of the form of Eq.(3.33) and Eq.(3.34).

configuration, such that noise shaping does not lead to performance improvement, in line with the characterization of Chapter 1.

From the fitted values of SNR_{TRx} with and without noise shaping, the $\Delta SQNR$ gain is extracted and compared with its expected value given by Eq.(3.30). The results are summarized in Table 3.4. For 2 SPS, the $\Delta SQNR$ gain with noise shaping coincides with its expected value while for the higher number of SPS, the measured gain is always smaller than the expected value. This can be explained as follows. When the DAC resolution is low (4 bits) and the number of SPS is small ($\leq$2), the quantization noise is the predominant noise both with and without noise shaping. Indeed, with a small number of SPS, the gain in SQNR due to noise shaping is not sufficient to neglect the quantization noise respectively to the other transceiver noises. Then, as the system performance is driven by the quantization noise, the evolution of the SNR coincides with the evolution of the SQNR. On the other hand, if the number of SPS is high (>2), the $\Delta SQNR$ gain is such that the quantization noise is less important with respect to the other noises of the transceiver and SNR_{TRx} saturates and coincides with $SNR_{TRx'}$ for the 8-bit resolution. The fitted values of C_{dB} for the different OSR values, with and without noise shaping, as well as the corresponding $\Delta SQNR$ with noise shaping, in comparison with its expected value given by Eq.(3.30), are reported in Table

OSR/data rate	C_{dB} (with NS)	C_{dB} (without NS)	$\Delta SQNR_{DAC,dB}/Eq.(3.30)$
5/ 16 GBaud	8.64	0.05	8.6/14.9
4/ 20 GBaud	7.46	0.04	7.5/11.5
2.5/32 GBaud	7.07	-0.5	7.12/8.1
2/40 GBaud	5.12	-1.08	6.2/6.2

TABLE 3.4: Experimental results. Extracted $SQNR$ and noise shaping $\Delta SQNR$ gain from the fitted SNR_{TRx} values.

3.4. In Table 3.4, we observe that the value of C_{dB} is very close to zero without noise shaping, except for 32 and 40 GBaud for which C_{dB} is negative such that the observed performance is actually worst than the one given by the expected SQNR value (Eq.(3.34) without C). We associate this behavior to the effect of the limited frequency response of the oscilloscope, which is not compensated by the digital pre-emphasis of the signal at the transmitter side, and introduces an additional penalty such that the system performance is worst than expected in presence of additive noise only.

2^{nd} experiments: demonstration of 64-QAM with 3 bits of physical resolution

In this second set of experiments, we employ the same set-up as in Fig.3.15 with minor modifications with respect to the previous experiments. The external clock synthesizer frequency is increased to 2.75 GHz such that the DAC sampling frequency is 88 GS/s, enabling to slightly increase the OSR and to operate at 44 Gbaud with 2 SPS. Additively, the driver amplifiers has been replaced by an upgraded version specifically designed for 64 GBaud in order to target maximal performance. The other elements of the set-up are unchanged. Regarding the signals, they consist in a 2^{16}-long random sequence mapped on 16-QAM and 64-QAM. The waveforms are resampled at 2 SPS and filtered with a RRC impulse response with rolloff factor 0.02. A high-pass filter with linear slope in frequency (+2.5 dB/GHz) is applied. The slope value is slightly smaller than in the previous set-up because of the frequency response improvement of the new driver amplifiers. Regarding noise shaping, we use the 7 taps filter for which design parameters for operations at 2 SPS are given in Table.3.1. As previously, quantization is performed on a set of equally spaced quantization levels and the clipping factor is optimized for each configuration. At the receiver, as proof of feasibility for commercial optical systems, we measure the BER before forward error correction

(FEC) after demodulation of the signal. Assuming hard-decision FEC and 7% overhead for 16-QAM and 25% for 64-QAM, the maximum acceptable BER before error correction (pre-FEC BER) are $4.9.10^{-3}$ and $3.4.10^{-2}$, respectively.

We report in Fig.3.20 and Fig.3.21 the measured BER as a function of $1/\sigma^2_{ASE}$ (or equivalently the OSNR). In both cases, we first report the performance when employing the 8-bit DAC without noise shaping, as reference. We observe two different regimes. At low OSNR (left side of the plots), the BER tends to its theoretical value for the ASE-limited channel. In this regime, the ASE noise dominates with respect to the transceiver noises. For 16-QAM, we can observe that around 25 dB OSNR and below, the performance when employing the 4-bit DAC without and with noise shaping and the 3-bit DAC with noise shaping coincides with the 8-bit DAC performance. For 64-QAM, the performance when employing 4-bit resolution with noise shaping is very similar to 8-bit resolution without noise shaping. This confirms that, in this regime, the DAC quantization noise is negligible and does not act on the system performance[7]. On the other hand, for high OSNR values (right side of the plots), the BER strongly depends

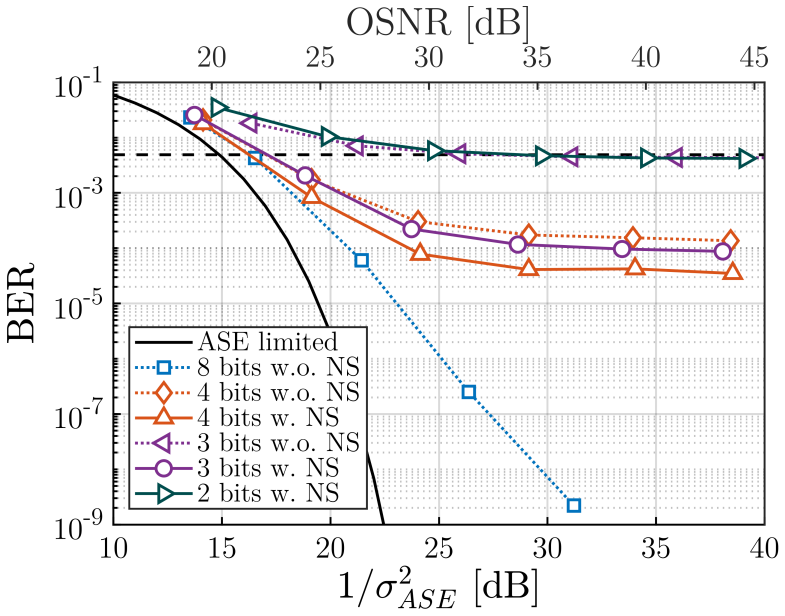

FIGURE 3.20: Experimental results for 16-QAM at 44 GBaud. Measured pre-FEC BER versus $1/\sigma^2_{ASE}$ (or OSNR) for various DAC physical resolutions without and with noise shaping. The acceptable pre-FEC BER is $4.9.10^{-3}$ (black dashed line) assuming hard decision and an overhead of 7%.

[7]We should not conclude that employing low-resolution DACs is transparent for long-haul propagation. Indeed, when specific DSP algorithms are employed to mitigate from nonlinear distortions, such as digital back propagation, their efficiency depends on the SNR_{TRx}, as shown in [79].

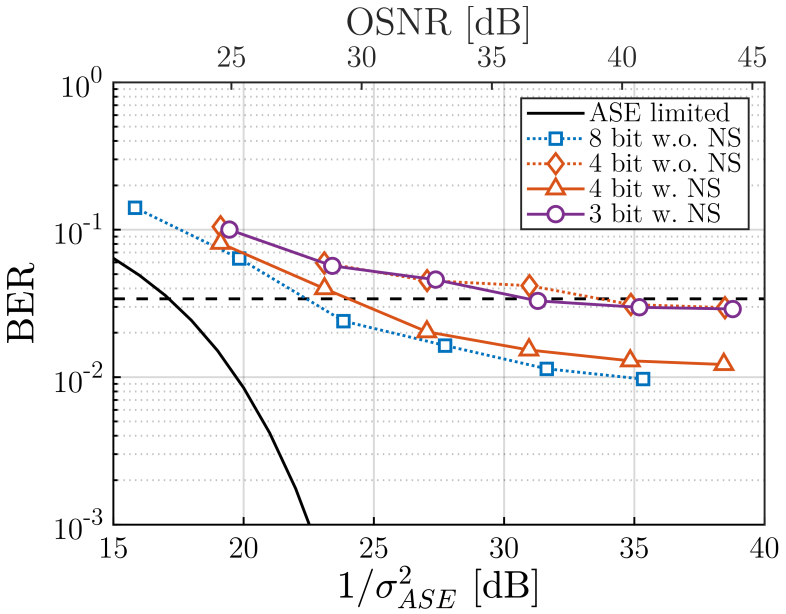

FIGURE 3.21: Experimental results for 64-QAM at 44 GBaud. Measured pre-FEC BER versus $1/\sigma^2_{ASE}$ (or OSNR) for various DAC physical resolutions without and with noise shaping. The acceptable pre-FEC BER is $3.4.10^{-2}$ (black dashed line) assuming hard decision and an overhead of 25%.

on the DAC resolution. This is because, in this regime, the ASE noise is negligible with respect to the transceiver noises, and particularly the quantization noise with low-resolution DAC. Both for 16-QAM and 64-QAM, we observe that the selected noise shaping filter enables a gain of +1 bit of effective resolution. Indeed, the BER with the 4-bit DAC without noise shaping coincides with the performance with the 3-bit DAC with noise shaping, and so on. This is because the implemented noise shaping filter provides +6 dB of $\Delta SQNR$ gain at 2 SPS. As an example, we visualize in Fig.3.22 the experimental 64-QAM demodulated constellation without and with noise shaping, showing the performance enhancement.

Regarding the feasibility for commercial optical systems, we perform the following analysis. For 16-QAM, we observe that for the 3-bit DAC with noise shaping or for higher resolutions, the performance around the pre-FEC limit are not impacted with respect to the 8-bit DAC. Thus, the same performance in terms of achievable optical reach is expected. However, for the 3-bit DAC without noise shaping and for lower resolutions, the lost in performance is such that, even in back-to-back, the BER margin with respect to the pre-FEC limit is reduced such that the tolerance to ASE noise is strongly reduced as well as the achievable reach, as discussed after. For 64-QAM, the analysis is qualitatively similar unless that 3-bit DAC resolution with noise shaping already places the system in its limit of operation

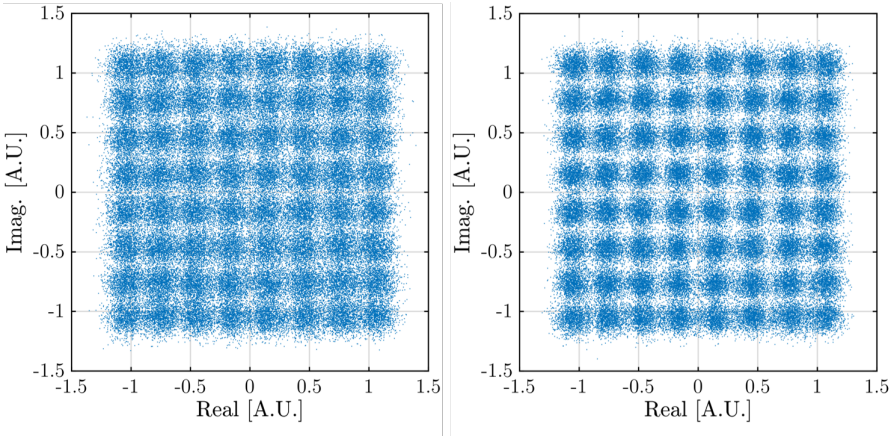

FIGURE 3.22: Experimental results. Constellation at 1 sample per symbol after receiver DSP at ≈43 dB of OSNR. The signal is a 64-QAM at 44 GBaud generated at 2 SPS and 4 bits of DAC physical resolution: without noise shaping (left) and with noise shaping (right). The noise shaping provides 6 dB of $\Delta SQNR$ gain.

in terms of pre-FEC BER. The propagation length (reach) which can be expected when reducing the transceiver performance can be analytically inferred. To do this, we consider a linear propagation (the Kerr effect is neglected) because of the relatively small optical input power in a metropolitan scenario. Hence, the optical link performance is modeled by:

$$SNR = \left(\frac{1}{SNR_{TRx}} + \frac{1}{\xi OSNR} \right)^{-1} \tag{3.35}$$

with SNR_{TRx} the saturated SNR when $\sigma^2_{ASE} \to 0$. The OSNR can be computed through the relation [80]:

$$OSNR_{0.1nm,\mathrm{dB}} = 58_{\mathrm{dBm}} + P_{in,\mathrm{dBm}} - L_{\mathrm{dB}} - NF_{\mathrm{dB}} - 10 \cdot \log_{10}(N) \tag{3.36}$$

with $P_{in,\mathrm{dBm}}$ the optical power (per channel) at the span entrance (we consider that, at each span, the EDFA counterbalances exactly the span losses), L_{dB} the span losses, NF_{dB} the noise factor of the EDFA and N the number of spans. For this study we choose $L_{\mathrm{dB}} = 20$ dB (100 km span with a loss of 0.2 dB/km) and $NF_{\mathrm{dB}} = 5$ dB. These values are typical for commercial optical systems. Note that N can be smaller than 1 to emulate propagation distances below 100 km. As an example, we choose $P_{in,\mathrm{dBm}} = 0$ dBm which corresponds to a linear regime of propagation, as shown in [64] with comparable conditions. The predicted evolution of the SNR with distance for the two investigated scenario is shown in Fig.3.23.

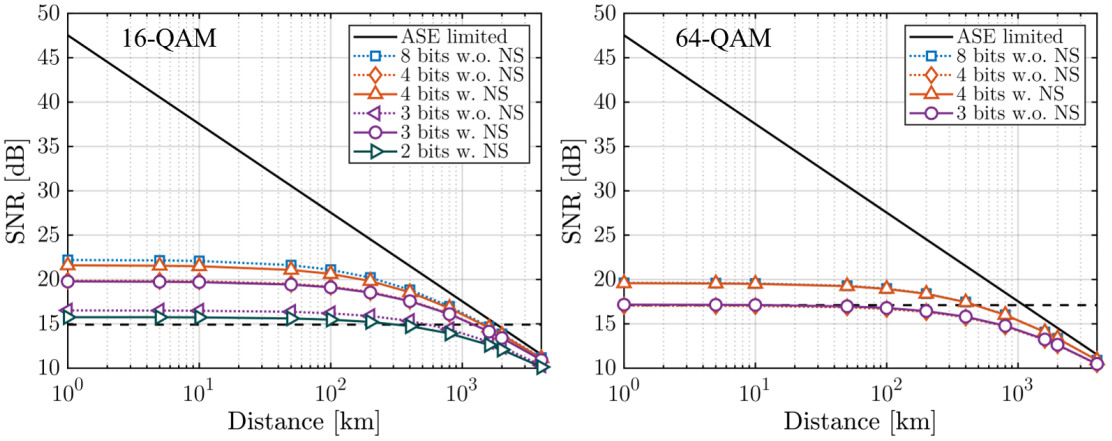

FIGURE 3.23: Numerical simulations. Evolution of the SNR along distance in the linear regime of propagation (the Kerr effect is neglected) when varying the transmitter physical resolution. The black solid lines is the performance which would be obtained with an infinite SNR_{TRx} (ideal transceiver), due to ASE noise only. The black dashed line corresponds to the SNR which gives a BER equal to the pre-FEC BER limits in each scenario. Left: 16-QAM at 44 GBaud. Right: 64-QAM at 44 GBaud. The SNR_{TRx} used for this simulation are extracted from the experiments presented in this section.

These curves are analyzed as follows. For very small propagation distances (<100 km), the performance is not impacted by propagation. This is because the ASE noise is negligible with respect to the transceiver noise and particularly the quantization noise of the transmitter. Between 100 and ≈1000 km, the SNR starts to decrease under the influence of the ASE noise, which becomes non-negligible. In this regime, the transceiver noise strongly impacts the achievable reach. Indeed, for 16-QAM, the SNR reaches the pre-FEC BER limit at ≈1500 km with 3-bit DAC with noise shaping and only ≈300 km with 2-bit DAC with noise shaping. For 64-QAM, the optical reach is ≈500 km with 4-bit resolution with noise shaping while it reduces to only ≈100 km with 3-bit resolution and noise shaping. Finally, above 1000 km, the SNR follows the ASE limitation and the transceiver influence on the system performance becomes negligible (all the curves collapse) but this regime concerns long-haul optical networks.

Thus, the 4-bit resolution is a good trade-off between low-resolution to decrease cost and power-consumption will it conserves a good performance in terms of propagation reach for metropolitan scenarios (<600 km).

3.3.4 Conclusion

We implemented into an optical transceiver a quantization noise shaping filter to increase the SQNR of low-resolution DAC. This implementation is fully digital and does not require hardware modification. To compute the noise shaping filter taps, we used the weighted least square method proposed in [74] and show that a filter length of maximum $\approx$ 20 taps is sufficient in most of the practical situations to obtain significant $SQNR$ gains. Moreover, such a design leads to a unique filter for each data rates and the taps computation can be done offline. We demonstrated that up to +6 dB of system SNR improvement can be obtained with noise shaping when a 4-bit low-resolution DAC is employed (second set of experiments). This translates into several interesting results. For 16-QAM at 44 GBaud, we demonstrated that noise shaping enables to maintain sufficient performance when switching from 8-bit to 4-bit physical resolution at the transmitter side. We also inferred that the same propagation reach can be obtained while the transmitter cost and power consumption is expected to decrease. If the resolution is further reduced to 2 bits, we inferred by numerical simulations that noise shaping enables to maintain up to $\approx$ 300 km of optical reach while it becomes impossible without noise shaping. For 64-QAM at 44 Gbaud, we also demonstrated that 4-bit resolution with noise shaping enables to maintain the performance of the 8-bit DAC while noise shaping also enables to operate with only 3-bit of physical resolution, at the cost of a reduced optical reach of about 100 km. This makes the 4-bit resolution an attractive candidate for low-resolution DAC. Finally, in terms of system performance modeling, we demonstrated that in presence of noise shaping, the SNR can still be predicted through the additive noise model for quantization by including the noise shaping filter gain in the SQNR formula.

3.4 Nonuniform quantization

Until now, the quantization levels of the DAC were equally spaced. In optical communications, such a restriction is justified because the commercial DAC are built to generate equally spaced voltages. However, in that case, it has been demonstrated that the quantizer is not optimal if the signal distribution is not uniform [81]. This is a common situation in optical communication. However, if the signal PDF is known, it is possible to find a different distribution of the quantization levels which maximizes the SQNR [81]. In that case, the quantization levels are not equally spaced and we refer to *nonuniform quantization*. The purpose of this section is to assess by numerical simulations the achievable gain in SQNR when employing nonuniform quantization rather than uniform quantization with optimized clipping ratio (see Chapter 2). Regarding the literature in the field of optical communications, this problem has been assessed in the case of the Gaussian distribution [82] (for the DAC) or at the ADC with extremely low resolution (down to 2 bits). In this case, the quantization noise is treated as a nonlinear distortion, and the receiver DSP includes supplemental algorithms to mitigate it. Here, we study nonuniform quantization at the DAC without restricting to the case of Gaussian distributions. For conciseness, we perform the study at the physical resolution of 4 bits only [75][8].

Conversely to the two previous optimization methods presented in this manuscript, nonuniform quantization requires to modify the quantization levels distribution of the DAC, an operation which is possible only by *hardware* modifications. Moreover, it means that the DAC will be designed for a unique signal distribution.

3.4.1 Principle

Given a signal s and its PDF $f_s(x)$, the design of the nonuniform quantizer consists in finding the position of the quantization levels s_q and of the decision boundaries b_q such that the mean square error σ_q^2 between the quantized signal and its original version is minimized:

$$\min_{x_q, b_q} \mathbb{E}\left[s_q(n) - s(n)\right]^2 \tag{3.37}$$

[8] At the opposite of the previous optimization methods, the SQNR gain resulting from the nonuniform quantization depends on the DAC resolution. The higher is the DAC resolution, the higher is the SQNR gain of nonuniform quantization versus uniform quantization with optimized clipping ratio. However, in an optical system, this will not translate into higher performance gain because above 4 bits of resolution the quantization noise influence becomes negligible. For more details, see [81].

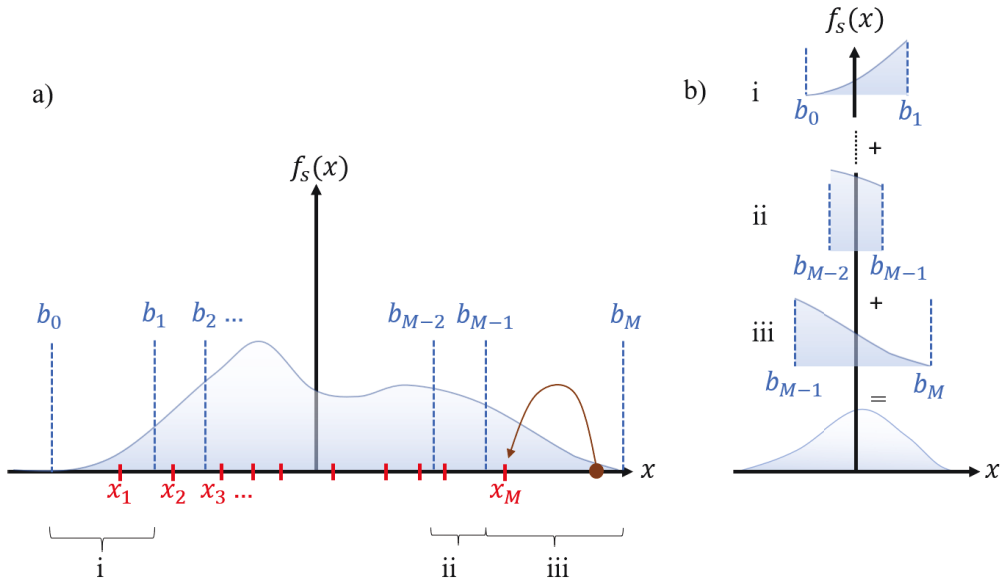

FIGURE 3.24: Nonuniform quantization (arbitrary illustration). (a) A signal PDF $f_s(x)$ together with a possible set of $M = 2^{N_b}$ quantization levels x_q (N_b being the DAC physical resolution) and a possible set of $M + 1$ decision boundaries b. Each sample whose amplitude is between b_q and b_{q-1} is quantized on the quantization levels x_q (see orange point as an example). (b) Graphical construction of the quantization noise PDF to understand Eq.(3.38).

with x_q the quantization levels and the possible values of the quantized signal s_q, s the original signal and $\mathbb{E}[\cdot]$ the expectation operator over samples. The index q runs in $[1, 2, ..., 2^{N_b}]$ with N_b the DAC resolution, while the decision boundaries are $[b_0, b_1, ..., b_M]$. The problem and its notations are illustrated in Fig.3.24a. For each quantization level x_q, the decision boundaries b_{q-1} and b_q define the limit within which a sample is quantized on the level x_q[9].

With these notations, we first write the quantization noise variance σ_q^2 (or mean square error) in the form:

$$\sigma_q^2 = \sum_{q=1}^{M} \int_{b_{q-1}}^{b_q} (x_q - x)^2 \, f_s(x) dx \tag{3.38}$$

Equation (3.38) can be understood by remarking that the PDF of the quantization error is the sum of the PDF of the signal within each interval inside pairs of decision

[9]For the uniform quantizer, the decision boundaries are equally spaced, separated by the quantization interval Δ, and are situated at same distance of their nearest neighbors quantization levels. This is a particular case in which quantization coincides with rounding.

boundaries, as illustrated in Fig.3.24a[10].

For a given quantization level x_q, we consider the following derivative:

$$\frac{\partial \sigma_q^2}{\partial x_q} = 2x_q \int_{b_{q-1}}^{b_q} f_s(x)dx - 2\int_{b_{q-1}}^{b_q} x f_s(x)dx \tag{3.39}$$

Setting Eq.(3.39) to zero in order to find a minimum of σ_q^2 leads to:

$$x_q = \frac{\int_{b_{q-1}}^{b_q} x f_s(x)dx}{\int_{b_{q-1}}^{b_q} f_s(x)dx} \tag{3.40}$$

Equation (3.40) indicates that the quantization level is the centroid of the mass probability between the decision boundaries. Another derivative is:

$$\frac{\partial \sigma_q^2}{\partial b_q} = (x_q - b_q)^2 p(b_q) - (x_{q+1} - b_q)^2 p(b_q) \tag{3.41}$$

For which setting to zero gives:

$$b_q = \frac{1}{2}(x_q + x_{q+1}) \tag{3.42}$$

Equation (3.42) indicates that the decision boundaries are at the middle of each pair of adjacent quantization levels.

Solving both Eq.(3.40) and Eq.(3.42) gives the nonuniform quantizer which minimizes σ_q^2 and thus maximizes the SQNR for a given signal PDF. However, to solve Eq.(3.40) we need b_q and b_{q-1}, while to solve Eq.(3.42) we need x_q and x_{q+1}. It is a vicious circle. However, it is possible to use an iterative procedure to solve Eq.(3.40) and Eq.(3.42), known as Lloyd's algorithm. The resulting nonuniform quantizer is called Lloyd quantizer.

3.4.2 Lloyd algorithm

The Lloyd algorithm is an iterative procedure to solve both Eq.(3.40) and Eq.(3.42) for a given signal PDF $f_s(x)$. Before entering the algorithm, we first remark that

[10] Also, in the particular case of the uniform quantizer, this can be understood by remarking that the quantization noise is proportional to the original signal modulo $\Delta/2$ and the construction process in Fig.3.24b will give a uniform PDF. For a nonuniform quantizer, the quantization step is variable such that the quantization noise PDF consists in the summation of sub-PDF with different support, producing possibly a non uniformly distributed quantization noise. For more details about this ways of constructing the quantization noise PDF, refer to [50].

the first and last boundaries are known and can be chosen as follows: $b_0 = -\infty$ and $b_M = +\infty$. The algorithm takes as input parameters the DAC resolution, which gives the number of quantization levels and of decision boundaries, and the signal, whose PDF can be computed numerically. The following steps are performed [81]:

- 1) Make a guess for the first quantization level x_1.
- 2) The index $q = 1$.
- 3) Plug x_q and b_{q-1} into Eq.(3.40) and find the value of b_q for which the equality is satisfied. This can be done by integrating the numerator and the denumerator forward from b_{q-1} and for increasing values of b_q.
- 4) Plug the computed value of b_q in the previous step into Eq.(3.42) to find the next quantization level x_{q+1}
- 5) Increment $q = q + 1$
- 6) Repeat steps 2 to 5 until $q = M$
- 7) When $q = M$, compute:

$$\epsilon = x_M - \frac{\int_{b_{M-1}}^{b_M} x f_s(x) dx}{\int_{b_{M-1}}^{b_M} f_s(x) dx} \tag{3.43}$$

- 8) Finish if $|\epsilon| < threshold$
- 9) Decrease the guess x_1 if $\epsilon > 0$ or increase x_1 if $\epsilon < 0$.
- 10) Start again from step 2

The algorithm can be summarized in three main operations. First, given the first boundary b_0 and the guessed x_1, compute the second boundary b_1 such that x_1 is the centroid of the probability mass in the interval $[b_o, b_1]$. Second, x_1 gives x_2 because of Eq.(3.42). Third, repeat until all the decision boundaries are computed. Now, the condition of success of the algorithm, i.e. step 8, can be understood as follows. If the guess x_1 is greater than its optimal value (unknown), the boundary b_1 is also greater than its optimal value and so on for all the quantization levels and decision boundaries. Hence, the last quantization level x_M, which is the centroid of the mass probability in the last interval from b_{M-1} to $b_M = +\infty$, will be greater than its optimal value (which vanishes ϵ). On the other hand, if x_1 is smaller than its actual value, all the quantization levels and decision boundaries will be smaller

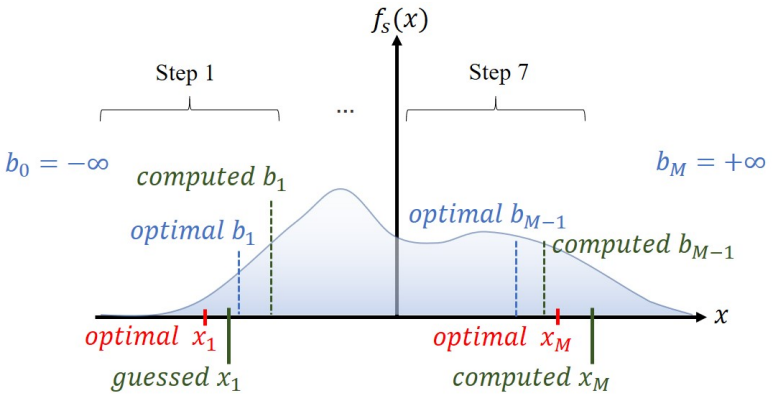

FIGURE 3.25: Illustration of the Lloyd algorithm in the case in which the guess of the first quantization level x_1 its greater than its optimal value. In that case the whole set of computed quantization levels and decision boundaries is off. The last quantization level x_M is also greater than its optimal value. If the absolute difference between x_M and its optimal value is greater than a given threshold, the algorithm is restarted with a new guess for x_1, smaller than the previous one.

than their optimal value. These observations are illustrated in Fig.3.25. Thus, the Lloyd algorithm consist in finding the optimal value of x_1 which corresponds to the true centroid of the mass probability in the interval $[b_0, b_1]$[11].

In what follows, we will use the Lloyd algorithm to determine the optimal nonuniform quantizer for a selected example of telecommunication signals.

3.4.3 Numerical simulations

In this section, the achievable gain when employing nonuniform quantization rather than uniform quantization with optimized clipping ratio are assessed. We choose as test signals the circular 64-QAM constellation with probabilistic shaping of the symbols. The circular mapping is chosen because it enhances the nonuniformity of the real and imaginary components of the digital complex field. Moreover, the probabilistic shaping enables the further modification of the signal distribution by simply tuning the shaping parameter ν, which sets the probability

[11]The algorithm performance is a whole study of research because its complexity and convergence speed towards the optimal nonuniform quantizer (which is never reached because of the non zero value of the threshold in step 8) depends on the error on the initial guess, the number of quantization levels, the threshold for the condition of success or even the quality of estimation of the signal PDF. Treating this these problems are out of scope as we do not consider to perform the optimization in real time in an optical transmitter.

distribution $P(a)$ to a symbol with amplitude a [83, 84]:

$$P(a) = e^{-\nu|a|^2} \tag{3.44}$$

which corresponds to a Maxwell-Boltzmann distribution. An illustration of the influence of the shaping parameter ν is shown in Fig.3.26 for the circular 64-QAM. The test signal consists in 2^{16} probabilistically shaped random symbols mapped on circular 64-QAM and filtered by an RRC with rolloff factor 0.1 at 2 SPS. The upper part of Fig.3.26 shows the symbol distribution and the bottom part shows the signal PDF before quantization for various parameters ν.

As the shaping parameter increases, the probability of the symbols close to the origin of the complex plane increases with respect to the probability of the symbol of amplitude a. This influences the distribution of the signal before quantization. Indeed, when ν increases, the signal PDF is more and more concentrated around zero, as shown in the bottom part of Fig.3.26. Hence, the PAPR of the signal

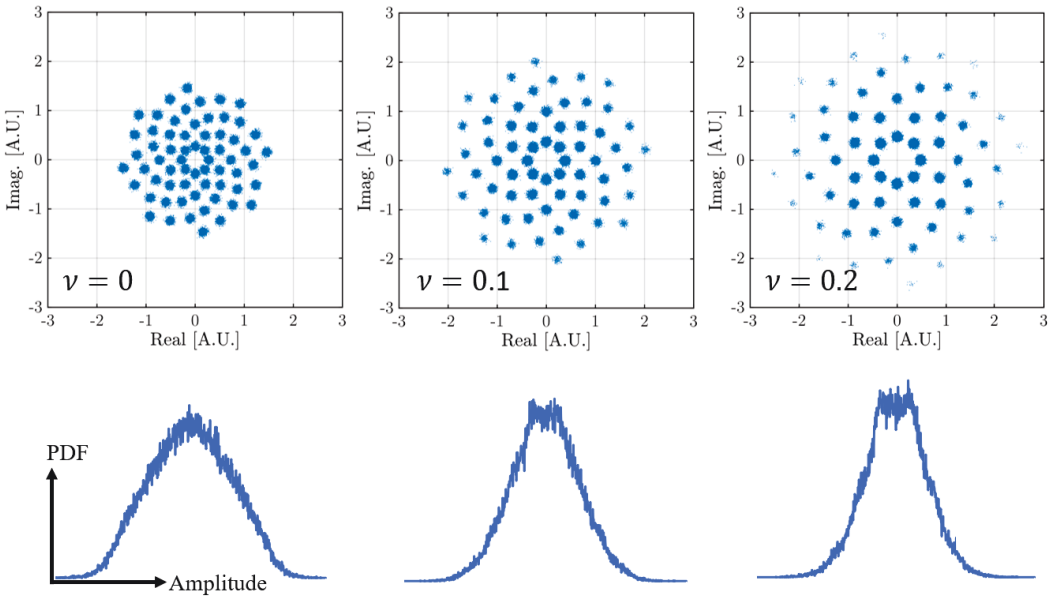

FIGURE 3.26: Numerical simulations. Up: Circular 64-QAM constellations with shaping parameter $\nu = 0, 0.1$ and 0.2 (from left to right). Gaussian noise is added to the symbols at the SNR of 22 dB to make appear the different symbol probabilities (in an optical system each shaping parameter value is adapted to a given SNR). Note: when increasing ν, the signal amplitude increases because the variance of the three constellations is normalized. Indeed, when ν increases, symbols of lower amplitude appear more likely such that it is necessary to increase the signal amplitude to have identical variance. Bottom: corresponding probability density functions after RRC filtering at the transmitter (this PDF are not the one of the demodulated signal shown above).

increases with ν such that we expect the SQNR to decrease with the uniform quantizer (see Chapter 2). In the same time, we expect an higher SQNR gain when employing the nonuniform quantizer because the signal distribution is more nonuniform for increasing values of ν. To verify these expectations, we perform an extensive set of numerical simulations. The test signals consist in 10 realizations of 2^{16} probabilistically shaped random symbols mapped on circular 64-QAM signals at 2 SPS and quantized with two different strategies (the considered SQNR is the average for the 10 realizations). In this study, for both uniform and nonuniform quantizations, the resolution is $N_b = 4$ bits. First, we employ the uniform quantizer at various clipping ratios. The SQNR at the best clipping ratio, for each value of ν, serves as reference for the comparison with the Lloyd quantizer. Second, for each value of ν, we use one realization of the signal to determine the nonuniform Lloyd quantizer[12]. The first boundary is set to $b_0 = -\infty$ and the waveform is not clipped. To initialize the Lloyd algorithm, we proceed as follows. We first scale the input signal such that its PDF occupies the full dynamic range of the uniform quantizer, whose first quantization level serves as initial guess x_1.

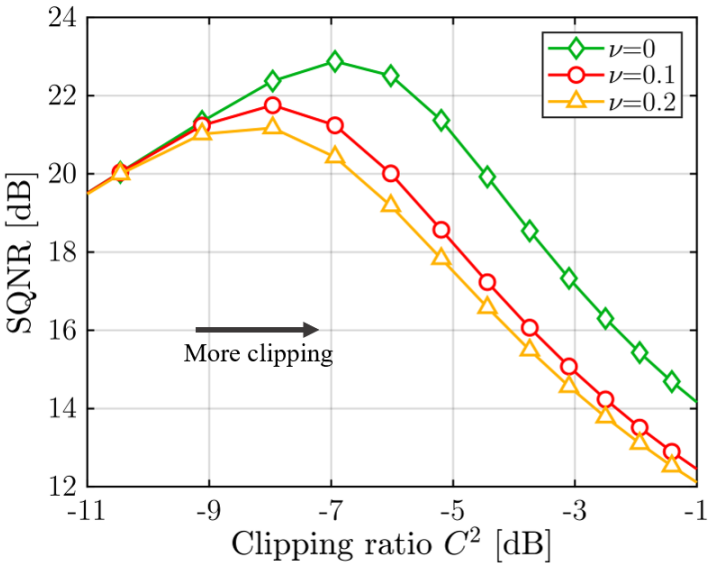

FIGURE 3.27: Numerical simulations. Evolution of the SQNR (average over 10 realizations) with the clipping ratio $C^2 = \frac{\sigma^2}{\left(2^{N_b} \cdot \Delta\right)^2}$, where σ^2 is the signal variance at the DAC input. The signal is a circular 64-QAM signal at 2 SPS filtered by a RRC with rolloff factor 0.1. Signal demodulation consists in match filtering and down sampling.

[12]We do not observe significant variations of the nonuniform quantization levels distribution between signals realizations.

The SQNR when employing the uniform quantizer for three different values of the shaping parameter ν are reported in Fig.3.27. The figure is analyzed as follows. For small clipping factor (typically $C^2 < -9$ dB), the SQNR is independent of the signal distribution, i.e. of the shaping factor ν. In this regime the clipping noise is negligible with respect to the quantization noise. Thus the SNR at the quantizer output is simply given by the ratio of the signal variance by the quantization noise variance. If the signal variance is expressed as a function of the clipping ratio and the quantizer dynamic range, the SQNR is:

$$SQNR = \frac{C^2 \cdot \left(2^{N_b} \cdot \Delta\right).^2}{\sigma_q^2} \tag{3.45}$$

which is constant for different signal distribution if they enter the quantizer with the same clipping ratio[13]. When the clipping ratio increases, the SQNR reaches it maximum value which decreases as the shaping parameter ν increases. Indeed, the more nonuniform is the signal PDF, the lower is the SQNR which can be achieved with the uniform quantizer. This is because, at a given clipping ratio (or equivalently at a given signal variance), the amount of clipping noise increases as the signal distribution differs from the uniform distribution. Thus, the signal to clipping noise ratio (SCNR) decreases with the shaping parameter ν, as shown in Fig.3.27, such that the maximum $SNR_{DAC} = (1/SQNR + 1/SCNR)^{-1}$ also decreases with the clipping ratio. For comparison with the Lloyd nonuniform quantizer, we consider the best SQNR for each ν ($C^2 = -7$ dB for $\nu = 0$ and $C^2 = -8$ dB for $\nu = 0.1$ and $\nu = 0.2$).

We perform the same simulation but the quantization is now performed by the Lloyd nonuniform quantizer computed with the Lloyd algorithm. We report in Fig.3.28 the SQNR obtained with the Lloyd quantizer together with the best SQNR which can be obtained with the uniform quantizer for various values of ν. These results show that the Lloyd quantizer always gives a higher SQNR than the uniform quantizer with optimized clipping ratio. It is because the signal PDF is nonuniform. For $\nu = 0$, the SQNR gain is +0.5 dB and it increases with ν because the signal PDF is more and more nonuniform. When $\nu = 0.2$ the SQNR gain reaches +1 dB. We also report in Fig.3.28 the SQNR when the Lloyd quantizer designed for $\nu = 0$ is used for the other values up to $\nu = 0.2$. In that case, apart from $\nu = 0$, the gain in SQNR is smaller than when the Lloyd quantizer is designed

[13]This is not in contradiction with the SQNR formula of Eq.(3.3) in section 3.2. Indeed, when the signal is scaled such that it occupies all the DAC dynamic range but without clipping, the PAPR depends on the clipping factor through the relation $C^2 = 2^{N_b-1} \cdot \Delta/(\sigma_q^2 \cdot PAPR)$. Thus, when the $PAPR$ increases, the clipping factor decreases as well as the SQNR, in accordance with Eq.(3.45).

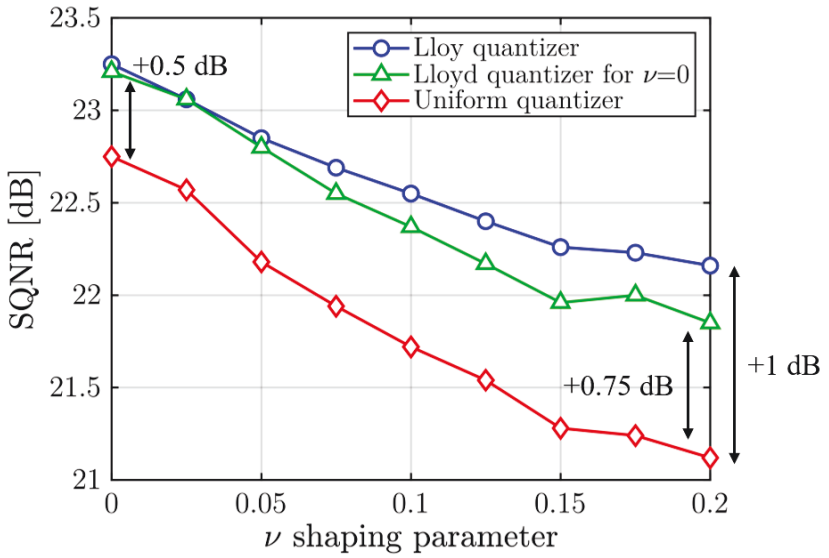

FIGURE 3.28: Numerical simulations. Evolution of the SQNR as a function of the shaping parameter ν when employing the Lloyd quantizer (computed for each value of ν), the Llyod quantizer computed for $\nu = 0$, or the uniform quantizer with optimized clipping ratio.

for each ν, but still outperforms the uniform quantizer. For $\nu = 0.2$, the SQNR gain with the Lloyd quantizer for $\nu = 0$ is +0.75 dB (-0.25 dB with respect to its value with the optimal nonuniform quantizer). This confirms that the Lloyd quantizer must be optimized for each different possible signal distribution. As an example, we report in Fig.3.29, the distribution of the quantization levels with the Lloyd quantizer and the uniform quantizer together with the signal distribution for $\nu = 0.2$.

To assess the system SNR gain resulting from the SQNR increase with nonuniform quantization, we plot in Fig.3.30 the SNR increase computed through the relation:

$$\Delta SNR = SNR_{Lloyd\,quantizer} - SNR_{uniform\,quantizer} \tag{3.46}$$

with:

$$SNR = \left(\frac{1}{SQNR} + \frac{1}{SNR_{opt}} \right)^{-1} \tag{3.47}$$

with SNR_{opt} the targeted SNR when employing probabilistic shaping with a given value of ν, and SQNR the signal to quantization noise ratio obtained with the Lloyd or the uniform quantizer with optimized clipping ratio.

Because of the influence of the in-line noise(s) (due to linear or nonlinear effects), we observe that the system SNR gain is smaller than the SQNR gain with

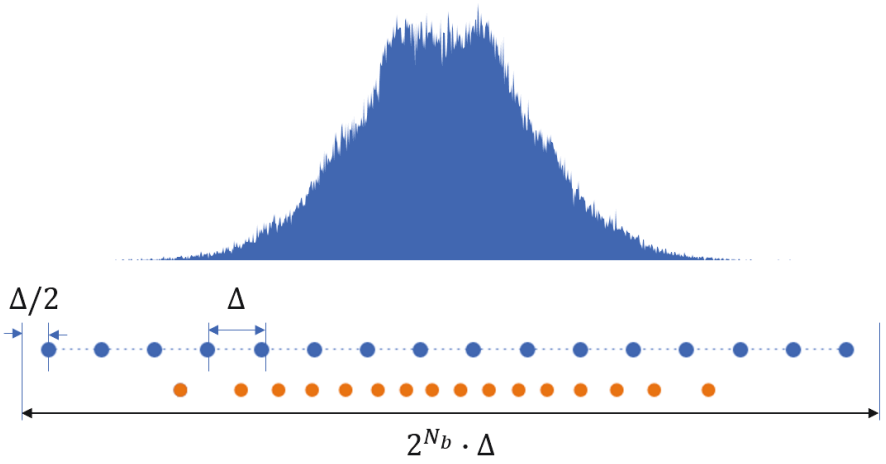

FIGURE 3.29: Numerical simulations. Signal distribution of a circular 64-QAM with shaping parameter $\nu = 0.2$ and RRC filtered with rolloff factor 0.1, generated at 2 SPS. The quantization levels of the uniform quantizer are shown in blue points and the Lloyd quantization levels are shown in orange points.

nonuniform quantization. For instance, for $\nu = 0.1$, the SQNR gain of +0.75 dB (see Fig.3.28) translates into +0.1 dB of system SNR gain. Indeed, the regime in which the efficiency of the nonuniform quantization increases (higher values of ν)

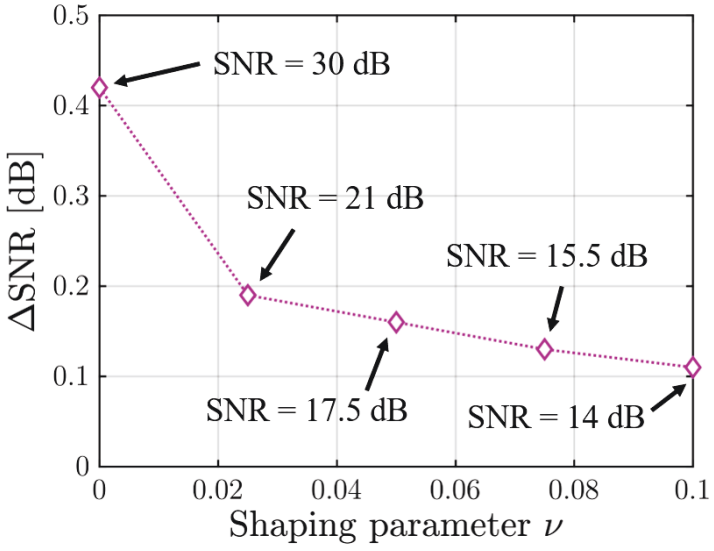

FIGURE 3.30: Numerical simulations. System SNR gain due to the SQNR increase when employing Lloyd nonuniform quantization rather than uniform quantization with optimized clipping ratio. We choose as operative SNR the one corresponding to each shaping parameter ν for which the link capacity is maximal. These results are obtained by injecting the value of SQNR with the Lloyd or the uniform quantizer into Eq.(3.47).

is also the regime in which the system SNR_{opt} decreases such that the influence of the quantization noise decreases and the benefit of nonuniform quantization is reduced. This observation is also valid for signal distributions obtained without probabilistic shaping, such that nonuniform quantization alone seems debatable, as it requires to modify the DAC and provide smaller gains than quantization noise shaping, for instance.

3.4.4 Conclusion

We assessed through numerical simulations the SQNR gain which can be expected when employing nonuniform quantization rather than uniform quantization with optimized clipping ratio. The study was performed on circular 64-QAM with probabilistic shaping of the symbols (without restriction because probabilistic shaping only aims at changing the signal distribution at all other parameters fixed). We chose these signals because they exhibit strong nonuniform distributions which can be easily modified by tuning the shaping parameter of the Maxwell distribution (Eq.(3.44)). The nonuniform quantizer for each signal distribution was computed through the Lloyd algorithm with a fixed physical resolution of 4 bits. The SQNR gain varies between +0.5 and +1 dB, and increases as the non-uniformity of the signal distribution at the DAC input increases. These values translate into up to +0.41 dB of system SNR gain, because of the influence of the other sources of noise.

3.5 Synthesis on the different optimization methods

In this section, we report the achievable SQNR gains obtained with the three investigated optimization methods. We also recall the domain of application of each method and establish a non-exhaustive list of advantages or drawbacks for each of them. This synthesis is given in Table 3.5.

The quantization with noise shaping is undoubtedly the optimization method which provides the highest SQNR gain with respect to CPRM or nonuniform quantization. Moreover, regarding the standard configurations in optical communication, it is the method that seems to have the wider range of application. Indeed, noise shaping only requires signal generation at more than 1 SPS. However,

Method	Application	SQNR gain (typical)	Pro and cons
Constellation Phase Rotation	CD pre-compensation	+1 dB	Easy implementation (one filter) but restricted use cases
Noise shaping	SPS >1	+4 dB	Easy implementation but requires oversampling
Nonuniform quantization	Nonuniform distribution	+1 dB	Require hardware modifications but apply for all communication signals

TABLE 3.5: Synthesis. Achievable SQNR gains with three different optimization methods as well at their domain of application and advantages and drawbacks. We consider a DAC resolution of 4 bits. Nota: the gains for the constellation phase rotation method and the noise shaping have been demonstrated experimentally. For nonuniform quantization, only numerical simulations have been performed.

as the three methods can be implemented all together because they act on independent parameters and are expected to provide at least additive gains, the CPRM and the nonuniform quantization can be used as add-on of the noise shaped quantizer. The very recent trends in the (published) literature regarding low-resolution DAC confirm this analysis, with 2018/2019 publications about digital resolution enhancer [57, 59].

3.6 Conclusion

In this chapter, we have investigated three digital signal processing techniques to maximize the signal to quantization noise ratio at the output of a quantizer: the constellation phase rotation method, the quantization noise shaping and the uniform quantization. We focused on the DAC rather than on the ADC to benefit from the knowledge of the quantization noise, extracted during the offline signal generation.

The constellation phase rotation technique consists in rotating the complex digital field such that the peak-to-average power ratio of both the real and imaginary components is minimized. This signal-based optimization technique applies to complex signals which do not exhibit a circular symmetry. This is for instance the case when a small amount of chromatic dispersion pre-compensation is applied before transmission (typically less than 500 ps/nm). The quantization noise shaping consists in filtering the quantization noise and re-inject it at the DAC entrance. By properly designing the filter, it is possible to reduce the quantization noise power within the signal bandwidth, hence increasing the signal to quantization noise ratio. It applies for any signal generated with at least one sample per symbol (oversampling). It is a quantization noise-based optimization technique which does not require hardware modification of the DAC. The nonuniform quantization consists in modifying the distribution of the quantization levels such that they are more concentrated for signal amplitudes which are more likely to appear. It is a quantizer-based optimization technique which applies to any signal having a nonuniform distribution, but requires hardware modification of the DAC. However, one can imagine selecting a reduced number of non-uniformly spaced quantization levels out of the 256 quantization levels of an 8-bit DAC.

The first two optimization techniques were implemented in an optical transmitter in which a low physical resolution DAC was emulated by limiting the number of quantization levels during the offline signal generation. By a set of numerical simulations, we extracted the achievable signal to quantization noise ratio gains obtained with these two techniques. Then, by experiments, we measured the resulting system signal to noise ratio improvement and the results are summarized in the previous section. The nonuniform quantization were only studied through numerical simulations.

Although the constellation phase rotation technique and the quantization noise shaping increases the signal to quantization noise ratio independently of the DAC physical resolution[14], the corresponding system SNR gain increases when the DAC resolution is reduced, because of the interplay between the quantization noise and the other sources of noises and distortions. For the constellation phase rotation method, the system SNR gain can be up to +1 dB in the case of dispersion pre-compensation on a 16-QAM signal. Regarding noise shaping, for the 4-bit DAC, we demonstrated up to +4.9 dB of system SNR gain when employing the noise shaping on a 16-QAM signal at 32.5 GBaud generated with a 81 GS/s DAC.

[14]Regarding the nonuniform quantization, the achievable SQNR gain increases with the physical resolution [81] but its benefit rapidly disappears because of the influence of the other sources of noises and distortions.

We also demonstrated the feasibility of 64-QAM at 44 GBaud with a 3-bit DAC running at 88 GS/s. Regarding the nonuniform quantization, the achievable signal to quantization noise ratio gain is about +1 dB at 4 bits of resolution, which translated into about +0.5 dB of system SNR increase. Thus, it appears that the quantization noise shaping is the most efficient technique for optimization of low resolution DAC in optical networks.

Chapter 4

Novel transceiver architectures for short-reach optical links

4.1 Motivations

The unrelenting growth in data traffic and the increasing diversity of optical links, especially in the metro and short-reach segments (<600 km and <100 km, respectively, see Introduction), challenges the communication industry to develop ever faster and flexible optical transceivers. In the previous chapters, the possibility of employing low-resolution DAC (typically 4-bit physical resolution) was introduced and demonstrated. In this chapter, rather than focusing on the DAC or on the ADC, a more general end-to-end system point of view is adopted, and two innovative transceiver architectures are proposed:

- in a first section, we present a novel sub-baudrate sampling transceiver architecture which enables the maximization of the symbol rate (and hence the data rate) at a fixed DAC sampling frequency. Indeed, if some errors in the transmitted data can be tolerated (before error correction), it is possible to transmit a signal at a symbol rate greater than the sampling frequency of the DAC (and of the ADC). Hence the reported architecture is a technique of Faster-than-Nyquist signaling. The demonstration is done in IM/DD optical links for intra-(1 km) or inter-(10 km) data centers.
- in a second section, a transceiver architecture employing Sigma-Delta (SD) modulation is reported and for which a novel demodulation scheme is proposed. The SD modulation [85] enables the generation of custom

signals with the lowest possible DAC resolution: 1-bit. Moreover, the SD modulation enables "transparency" at the transmitter side because a single point of operation is used for the whole electro-optics chain due to the 2-level statistics of the emitted SD stream. However, in standard systems employing SD modulation, the 2-level signal distribution is not used at the receiver. For instance, if a 64-QAM signal is SD modulated, the receiver equalizes a 64-QAM without using the 2-level nature of the SD stream. A process which is challenging in strongly noisy and bandwidth-limited environment. Conversely, the strategy of our architecture is to recover the 2-level SD signal in order to reconstruct the signal in a strongly noisy and bandwidth-limited environment. This new demodulation scheme also makes the receiver "transparent" because, for any input signal, it performs the demodulation of a 2-level SD stream. Together with the transparency at the transmitter side, we create a transparent transceiver. However, the SD modulation requires to oversample the signal in a large extent and thus, it is neither used to increase the data rate nor the spectral efficiency, but rather for applications requiring the transmission of high fidelity signals (high SNR) such as Radio over Fiber (RoF).

4.2 Sub-baudrate sampling

Data-center facilities become more and more meshed due to the new segmentation of optical networks (see Introduction) and significant research efforts focus on breaking the 100 GBaud barrier in short-reach optical link (<100 km). However, this regime of operation exceeds the capabilities of available commercial DAC/ADC, particularly those based on CMOS technology, both in terms of bandwidth (-3 dB bandwidth ≈30 GHz) and sampling rate (saturation around 100 GS/s). Regarding the transmitter and the DAC, the development of high-speed electronic circuits based on non-CMOS platforms have proven to be a good alternative. Indeed, recent experiments showed the feasibility of 200 Gbits/s per lane (at 200 GBaud) with transmitters based on InP (Indium Phosphide) devices [22]. Compare to CMOS technology, InP offers a higher electron mobility, which translates into a higher electronic bandwidth, and a higher energy band-gap, which translates into higher output power, facilitating its integration with the other electro-optics components.

However, InP technology suffers from serious limitations with respect to CMOS technology, such as a higher power consumption and much lower DSP capabilities because of the vertical resolution of the transmitter, limited to 1 or 2 bits. Hence, InP remains out-shined by CMOS technology. Under these present advantages, CMOS technology will probably remain, in the near future, the preferred solution for optical transceivers. Consequently, there is a need for technical or digital solutions alleviating CMOS limitations in terms of bandwidth and sampling speed. in this work, we explore the potential of operating high-speed optical transmission systems under 1 sample per symbol as a mean of operating at higher data rates while keeping a constant bandwidth, sampling speed and potentially power consumption (at least at the transmitter side in the presented architecture).

4.2.1 Faster-than-Nyquist signaling

The principle of Faster-than-Nyquist signaling (FTN) has been introduced in the late 1970's in the context of voice-band telephony [86]. It consists in transmitting symbols at a rate superior to what is permitted by the Nyquist criterion for *inter-symbol interference (ISI) free channel*, which can be expressed in the form:

$$h(nT) = \begin{cases} 1, & \text{if } n = 0 \\ 0, & \text{if } n \neq 0 \end{cases} \tag{4.1}$$

with h the impulse response of the channel, T the symbol period and n an integer. An example of impulse response following the ISI free condition is the sinus cardinal impulse response (or Nyquist pulse):

$$h(t) = \frac{sin(\pi t/T)}{(\pi t/T)} \tag{4.2}$$

A popular impulse response in optical communications, which also follows the ISI free condition, is the raised-cosine (RC) impulse response [87]. Alternatively, the root-raised-cosine impulse response (square root of the raised-cosine impulse response), can be applied on the signal at the transmitter and the receiver, and the overall impulse response is ISI free. Note that the RC and RRC coincide with the Nyquist pulse when their roll-off factor $\beta = 0$. The Nyquist pulse is shown in Fig.4.1 (blue solid line).

The relation between the Nyquist criterion for ISI free channel and the Nyquist theorem appears clearly when one tries to sample a signal at a frequency f_s smaller than twice the highest frequency f_{max} contained in the signal spectrum. Indeed, the sampling at frequency f_s first requires to filter the signal frequencies greater than $f_s/2$ in order to avoid aliasing. Thus, the anti-aliasing frequency response

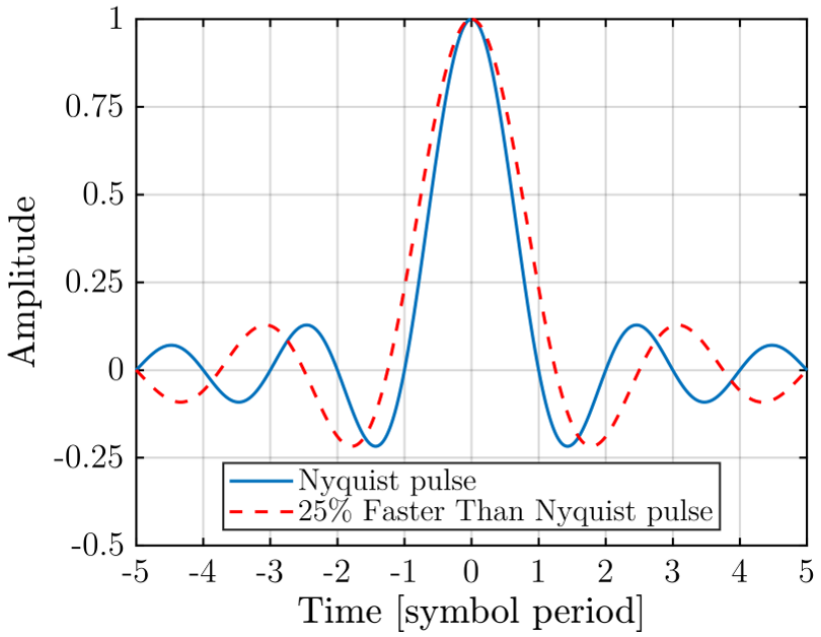

FIGURE 4.1: Illustration of Faster-than-Nyquist signaling in terms of impulse response of the communications channel.

$H(f)$ can be of the form:

$$H(f) = \begin{cases} 1, & \text{if } f < f_s/2 \\ 0, & \text{if } f \geq f_s/2 \end{cases} \tag{4.3}$$

for which the corresponding impulse response is:

$$h'(t) = \frac{sin(\pi t/T_s)}{(\pi t/T_s)} \tag{4.4}$$

with $T_s = 1/f_s$ the sampling period. It is clear that if $f_s < 2f_{max}$, the impulse response of the anti-aliasing filter introduces ISI because it does not vanish at each multiple nT. For instance, if the bandwidth of the anti-aliasing filter is 0.8 times f_{max}, the impulse response is 25% longer than the Nyquist pulse[1], as depicted in Fig.4.1.

Hence, the fundamental principle of Faster-than-Nyquist (FTN) signaling is to emit or receive a signal with a sampling frequency smaller than the one required by the Nyquist theorem. This introduces ISI, such that the transmitter and/or the receiver must integrate DSP algorithms to cancel the interference between the adjacent symbols. However, ISI mitigation by DSP is limited both by the amount of introduced ISI, and by the noise level in the communication channel. In presence of noise, the ISI cannot be totally compensated, resulting in additional errors (with respect to the errors introduced by the channel noise only) that occur at symbol decision. Equivalently, for a given amount of noise, the amount of ISI drives errors at symbol decision. These additional errors will potentially limit the system performance, in particular at the error correction stage. Hence, designing a FTN communication system consists in finding the correct amount of errors which can be tolerated when introducing ISI, given the DSP capabilities and the targeted bit error rate before the error correction stage.

4.2.2 Transceiver and receiver DSP architecture

In this work, built upon [24], we propose a novel FTN architecture and investigate the potential of commercial ≈30 GHz bandwidth CMOS DAC/ADC to run at more than 100 GBaud (> 200 Gbit/s with 4-PAM) with IM/DD modulation.

[1]It should be noted that respecting the Nyquist theorem, i.e. sampling at more than twice the highest signal frequency, does not ensure to respect the condition for ISI free channel. It occurs, for instance, if the RRC filter at the receiver side has a different roll-off factor than the RRC filter at the transmitter side.

We differentiate our architecture from recent works [23, 88] by locating all the additional DSP complexity required for signal recovery under aggressive ISI conditions at the receiver side. By doing this, we avoid any pre-coding of the emitted signal, drastically simplifying the FTN architecture. Concretely, at the transmitter, sub-baudrate sampling is achieved by filtering the signal such that the highest frequencies are removed (anti-aliasing filter) and then by resampling at less than 1 SPS to hit the target symbol rate, given the DAC clock sampling frequency. At the receiver, the ISI and low-pass limitations of the transmission elements are mitigated by a two-stage procedure. First, a feed-forward equalizer [87] aims at equalizing most of the ISI, mostly caused by the low-pass nature of the transceiver elements, whose bandwidth is much smaller than the bandwidth of the FTN signal (>50 GHz). Second, a maximum likelihood sequence detection (MLSD) [87] aims at resolving the residual duo-binary-type interference and recovering the emitted symbols. The general overview of our system is shown in Fig.4.2. In the next two subsections, we give more details about the transmitter and receiver architectures.

Transmitter

The OOK and 4-PAM modulation formats are chosen because of their strong sensitivity which enable to operate in the strong ISI conditions imposed by sub-baudrate sampling and low-pass frequency response of the transceiver elements. The transmitter architecture is described in Fig.4.2. First, the signal is generated according to the sampling frequency of the DAC. For non return to zero (NRZ) pulses, the signal is generated at 1 SPS such that the first lobe of the sinus cardinal spectrum occupies two times the entire Nyquist bandwidth of the DAC, which runs from $-f_s/2$ to $f_s/2$, as shown in step 1 of the transmitter inset of Fig.4.2. For RC filtering, the signal is generated at 2 SPS and the width of its spectrum is given by the roll-off factor β. Thus, in both cases, the signal spectrum is a smooth decay frequency profile as opposed to, for instance, the typical aggressive roll-off factors (close to 0) of systems operating close to 1 SPS[2]. Second, an anti-aliasing filter is applied, with a frequency response similar to Eq.(4.3). Its cut-off frequency f_c

[2]This is done to maximize the signal integrity for sub-baudrate operations. Indeed, as the anti-aliasing filter removes the highest frequencies of the signal spectrum (above the cutoff frequency $f_s/2$ with f_s the DAC sampling frequency), one tries to minimize the importance of these frequencies for the signal representation. With a small roll-off factor (close to zero) all the frequencies of the spectrum have the same importance (flat spectrum). However, with a smooth decay spectrum (NRZ for instance), the highest frequencies have less relevance in the signal representation, hence facilitating the recovery of the signal if an anti-aliasing filter is applied. In the different experiments, we thus explore signal generation with non return to zero (NRZ) and raised-cosine (RC) pulse shape with high roll-off factor ($\beta = 1$ or 0.6)

is chosen according to the targeted data rate R, or equivalently to the targeted number of SPS at the transmitter, through the relation:

$$f_c = SPS_{DAC} \cdot \frac{f_s(DAC)}{2} \tag{4.5}$$

with $SPS_{DAC} = f_s(DAC)/R$ a number smaller than 1 for sub-baudrate sampling and $f_s(DAC)$ the DAC sampling frequency. This is step 2 in the transmitter inset of Fig.4.2. Then, the filtered signal is up-sampled by a factor $1/SPS$ such that the highest frequency coincides with $f_s/2$ and the transmitter output data rate is:

$$R = \frac{f_s}{SPS_{DAC}} > f_s \tag{4.6}$$

This is step 3 in the transmitter inset of Fig.4.2. The sub-baudrate signal is then filtered with a high-pass filter of linear slope +0.25 dB/GHz to compensate for the low-pass frequency response of the DAC and of the electro-optical components. Finally, the waveform is quantized over a set of 256 (8 bits) equally spaced levels such that quantization noise is negligible (see Chapter 2). Finally, the signal is emitted by the DAC and suffers from its low-pass frequency response, as depicted in step 4. The signals parameters are summarized in the table of Fig.4.2.

Receiver

After propagation, the continuous-time and continuous-amplitude signal is sampled, possibly below the symbol rate, and quantized on 8-bit physical resolution. This is step 1 in the receiver inset of Fig.4.2. The number of SPS at the receiver can differ from the number of SPS at the transmitter, if the DAC and DAC sampling frequencies are different. It is given by:

$$SPS_{ADC} = SPS_{DAC} \cdot \frac{f_s(ADC)}{f_s(DAC)} \tag{4.7}$$

In all the presented experiments, the clock sampling frequency of the receiver is greater than the one of the transmitter. Hence, the anti-aliasing filter of the transmitter acts also as an anti-aliasing filter for the receiver. The digital waveform undergoes signal conditioning (possible offset removal and power normalization) and resampling at 2 SPS (step 2 of receiver inset of Fig.4.2). It must be noted that the clock of the transmitter and the receiver are synchronized such that a clock recovery algorithm is not needed[3].

[3]Further efforts are necessary to make possible clock recovery for sub-baudrate signals.

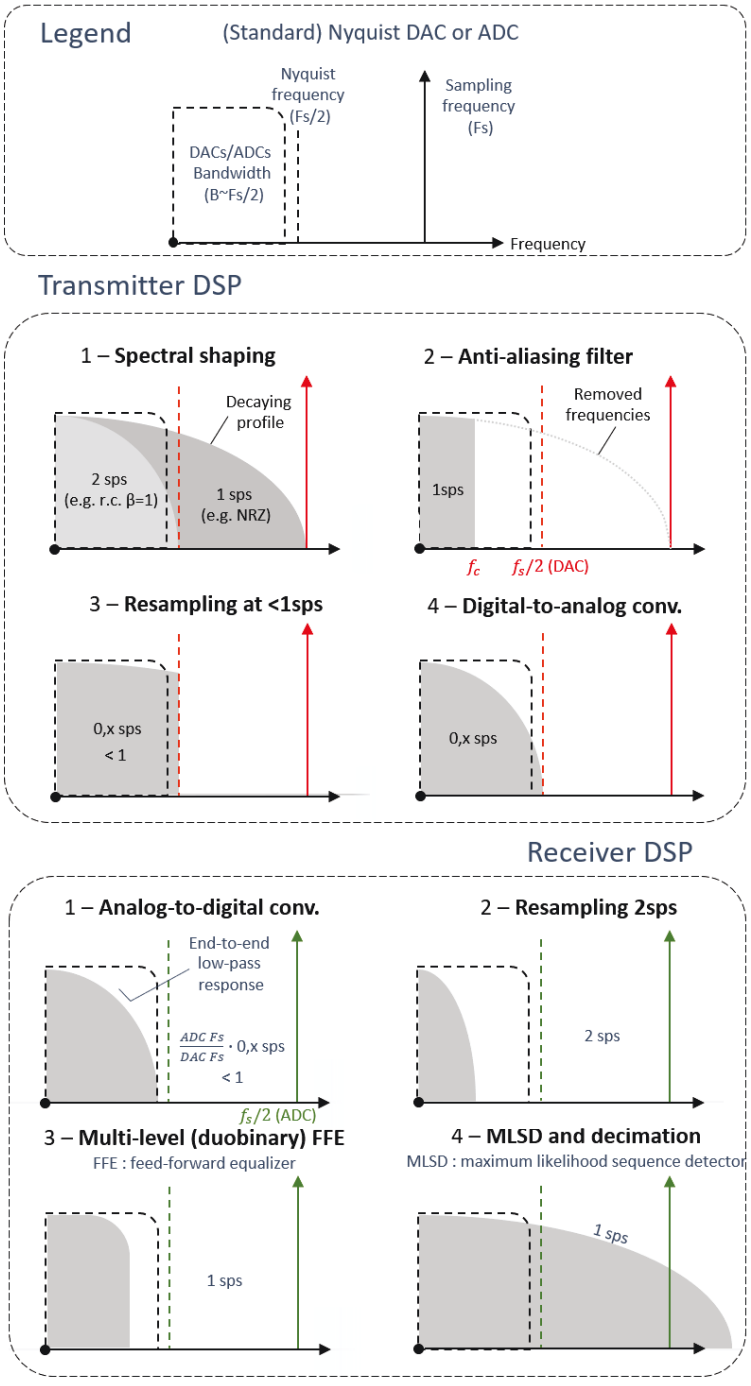

Mod. format	Pulse shaping	Spectral pre-emp. (dB/dec.)	Minimum samples per symbol	FFE taps	FFE target (levels)	MLSD taps
OOK	NRZ*, ** RC† (β=1)	2,5	~0,79*, **, 0.736†, 0.8†	31*, 91**,†	3	3**,†, 5*,†
PAM4	NRZ** RC† (β=0.6)	2,5	0.89**, 0.92†	91**, 105†	7	3

★ : PoC #1 ★★: PoC #2 † : Transmission

FIGURE 4.2: Top: Transceiver DSP architecture for sub-baudrate sampling at DAC and ADC. Bottom: some relevant signal parameters used in experiments.

Now the task is to compensate for the distortions and recover the ideal data stream with minimum errors. The first block is an adaptive linear feed forward equalizer (FFE), which is configured to converge to the duo-binary-equivalent multi-level amplitude signal of the target modulation format (OOK or 4-PAM). For OOK, the duo-binary-equivalent multi-level amplitude signal is a three-level signal while for 4-PAM, it is a seven-level signal. This can be understood as follows. A smooth low-pass filter of a discrete amplitude symbols (-1 and +1 for instance with OOK) can be represented by the convolution of the sequence with an impulse response of the form $h = [1, 1]$ (moving average). Thus, each group of 2 symbols of the initial sequence can result in three possible amplitudes: -1 and -1 gives -2, -1 and +1 gives 0 and +1 and +1 gives +2. The low-pass filtered OOK stream becomes a three-level signal. In presence of stronger filtering, i.e. impulse response of the form $h = [1, 1, 1]$, the OOK stream becomes a five-level signal, which of course is more challenging to equalize. For 4-PAM, smooth low-pass filtering transforms the four-level stream into a seven-level signal, and a stronger filtering transforms it into a nine-level signal. The reason for this duo-binary equalization is to avoid undesirable noise enhancement when trying to recover the nonexistent or excessively attenuated high frequencies spectral components of the signal, which are necessary to represent the OOK or 4-PAM signal. This first process compensates for the greatest portion of ISI, mostly caused by the anti-aliasing filter and the limiting response of the electro-optical components.

Then, a maximum-likelihood sequence detector (MLSD) implemented using the Viterbi algorithm [87] resolves the duo-binary-type interference and residual short-memory effects, also, without undesirable noise enhancement.

4.2.3 Proof of concept and transmission experiments

The experimental demonstration and evaluation is organized in two sub-sections describing two proofs of concept (PoC) in back-to-back (B2B), and then a transmission demonstration. In the first PoC experiment, we use sub-baudrate sampling at the transmitter and receiver (88 GS/s DAC and 92 GS/s ADC), proving successful detection of 112 GBaud OOK. In a second PoC, sub-baudrate sampling is performed only at the transmitter and the line rate is pushed up to 200 Gbits/s with 100 GBaud 4-PAM. In the last set of experiments, several C-band short-reach transmissions are performed employing sub-baudrate sampling at the transmitter and the receiver (92GS/s DAC and 100GS/s ADC). The scenarios include 1-km and 80-km standard single-mode fiber (SMF) where up to 100 GBaud

4-PAM and 125 GBaud OOK, respectively, are successfully transmitted. In all cases, the performance metric is the measured BER before forward error correction (FEC), considering a 7%-overhead hard-decision FEC with pre-FEC BER limit of $3.8 \cdot 10^{-3}$. The system configurations are shown in Fig.4.3 and detailed hereafter.

PoC in back-to-back

In PoC#1, we employ the 8-bit CMOS DAC operating at 88 GS/s to generate a 112 GBaud OOK signal. Note that in PoC#1 and PoC#2, the DAC uses its own internal clock synthesizer. The transmitter operates at 0.78 SPS. The emitted symbols are transformed into the corresponding NRZ waveforms such that the signal PSD occupies the frequency range +/-112 GHz (first lobe of the *sinc* spectrum). However, according to the Nyquist's sampling theorem, the DAC can only generate signals up to +/-44 GHz. Hence, the signal is filtered by an ideal rectangular window before quantization to avoid aliasing. Considering only the

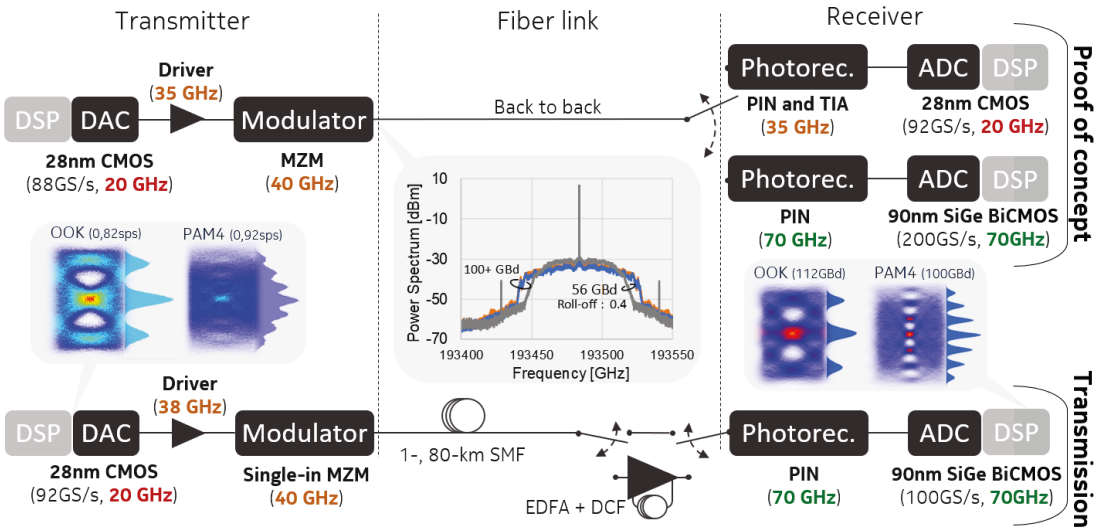

FIGURE 4.3: Experimental test beds for sub-baudrate sampling above 100 GBaud. We report the -3 dB bandwidth of each hardware component underneath the corresponding module. The two top chains correspond to the PoC in B2B. The bottom chain is the test bed used for transmissions. Insets: left, exemplary eye diagrams and associated histograms of sub-baudrate sampled OOK and 4-PAM aiming for 112 GBaud (0.82sps) and 100 GBaud (0.92sps), respectively, corresponding to the PoC#2. Middle, optical power spectrum at modulator output for 56 GBaud 40% roll-off 4-PAM, 112GBaud OOK, and 100 GBaud 4-PAM. Right, exemplary recovered experimental eye diagrams and histograms of 112 GBaud OOK, and 100 GBaud 4-PAM.

first lobe of the *sinc* spectrum, we observe that the anti-aliasing filter rejects about 60 % of the signal frequencies (from 44 to 112 GHz), but as explained previously, due to the decay profile of the spectrum, these frequencies are less relevant for the signal integrity[4]. At the receiver side, a PIN photodiode is followed by a trans-impedance amplifier (PIN-TIA) and a 28-nm CMOS 8-bit ADC at 92 GS/s. The recorded waveforms are post-processed as described in section 4.2.2, where the number of fractionally-spaced taps (2 SPS) for the FFE is fixed at 31, and 5 symbol-spaced taps for MLSD.

The results of the system characterization for PoC#1 are shown in Fig.4.4. It presents the BER as a function of the received power into the photoreceiver for 112 Gbaud OOK. The raised-cosine 56 GBaud (roll-off 0.4) 4-PAM without MLSD (the FFE equalizer directly targets 4 level as the channel frequency attenuation and ISI is moderate with respect to sub-baudrate situations) is reported in square symbols. This 4-PAM configuration delivers the same data rate than the 122 GBaud OOK but with more than 1 SPS at the transmitter and the receiver. The eye diagrams for both modulation formats around the sensitivity limit are also reported in Fig.4.3. For 4-PAM at 56 GBaud, the eye diagram is taken at the FFE output, targeting four levels, and clearly shows the efficiency of the entire receiver DSP chain, as the

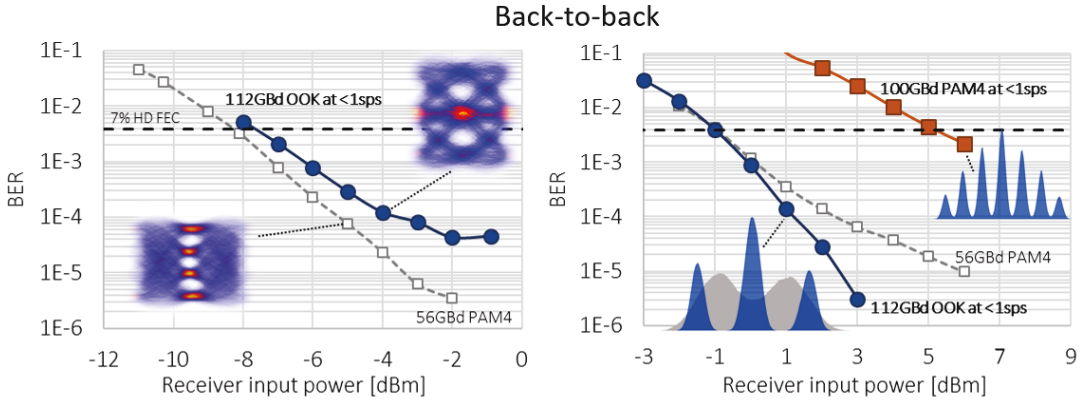

FIGURE 4.4: Experimental results. Proofs of Concept in back-to-back. BER as a function of received optical power. Left: PoC#1 sub-baudrate sampling of 112 GBaud OOK at both the transmitter (88 GS/s DAC) and the receiver (92 GS/s ADC) preceded by a PIN+TIA. Right: PoC#2 sub-baudrate sampling of 112 GBaud OOK and 100 GBaud 4-PAM at the transmitter (88.96 GS/s DAC) with a 70-GHz 200 GS/s ADC preceded by a 70-GHz PIN photodiode.

[4]One remarks that in amplitude, the -3 dB attenuation of the *sinc* function is ≈ 2/3 of the first lobe width, i.e. ≈ +/-74 GHz in our case. If we consider that only frequencies within the -3 dB attenuation window of the spectrum are of interest, the +/-44 GHz rectangular anti-aliasing filter conserves about 60% of the signal spectral components, which are the most relevant.

four levels are clearly distinguishable. For OOK and 4-PAM at 100 GBaud, the eye diagrams are extracted at the output of the FFE equalizer, which performance is inferred by the three or seven distinguishable levels of the duo-binary version of the OOK, or 4-PAM signal, respectively.

Regarding the PoC#1, we draw two conclusions. First, given the considered FEC, which requires less than $3.8 \cdot 10^{-3}$ BER after symbol detection and before error correction, the feasibility of the proposed sub-baudrate sampling architecture is demonstrated. Indeed, the required pre-FEC BER is reached with -7 dBm receiver input power, a customarily configuration in short-reach optical links. Second, for a same data rate, we observe that the performance of 4-PAM always outperforms the sub-baudrate OOK configuration. This is certainly contrary to what we could expect in an ideal situation. Indeed, considering that both signals occupy similar bandwidth (see inset of Fig.4.3), their SNRs at a given input power should be highly similar and a better performance is expected with sub-baudrate OOK as it contains less amplitude levels than 4-PAM. Nonetheless the system is not ideal, and hence we attribute the penalty (around 0.5dB at the sensitivity limit) to the excessive low-pass filtering on the entire receiver chain – i.e. photoreceiver and ADC. This leads to non-negligible noise enhancement at the FFE, despite targeting convergence to the equivalent 3-level partial response modulation. We then postulate that an improvement of the receiver specifications should compensate for the greatest part of the receiver impairments. This is the goal of PoC#2.

Compared to PoC#1, there are two modifications in the experimental set-up: we slightly increase the DAC sampling frequency (from 88 to 88.96 GS/s) seeking for resolution improvement while still employing the internal clock, and we also replace the dual-drive modulator by a single-ended zero-chirp LiNbO3 Mach-Zehnder modulator with identical bandwidth. The latter helped in facilitating the control of the skew, which was particularly challenging and detrimental for signals around 100 GBaud and beyond. In terms of digital signal generation, we now push the transmitter speed to 200 Gbits/s by using 4-PAM at 100 GBaud. Only B2B configuration is considered. With respect to PoC#1, the receiver in PoC#2 is replaced by a 200 GS/s real-time oscilloscope exhibiting an electrical bandwidth of the order of 70 GHz, above the bandwidth of the electrical signals after base band conversion, as shown in Fig.4.3, such that no bandwidth limitation is present at the receiver.

The Fig.4.4 (right) shows the BER results for the PoC#2. As a result of the hardware bandwidth improvements, 56 GBaud 4-PAM and 112 GBaud OOK exhibit very similar performances at the FEC limit. The frequency response of

the improved end-to-end system is inferred from the frequency response of the converged FFE taps shown in Fig.4.5, appearing flat up to 45 GHz for duo-binary equalization. Likewise, note the strong high-frequency enhancement with OOK as target constellation that certainly leads to additional artificial noise, justifying our choice of first targeting 3-level (respectively 7-level) instead of 2 (respectively 4) with OOK (respectively 4-PAM). These results prove once again the feasibility of high-speed data communication at below 1 SPS, underscoring the importance of bandwidth – and not the sampling rate, as well as the need to control noise enhancement to the largest possible extent during equalization.

Transmission experiments

We now switch from back-to-back to transmission experiments for intra (1 km) and inter data-center (80 km) experiments. To maximize the system performance, the set-up of PoC#2 is modified as follows. Regarding the DAC, we replace the internal clock by an external synthesizer. This configuration enables the maximization of the ENOB and ensures a negligible clock timing jitter (see Chapter 1). The clock sampling frequency is fixed at 92 GS/s, the frequency for which the DAC clock circuitry is designed. We further replace the electrical amplifier used in the PoC by a 38-GHz linear driver, slightly better than in the PoCs. The transmitter output is launched into the fiber at an optical power of

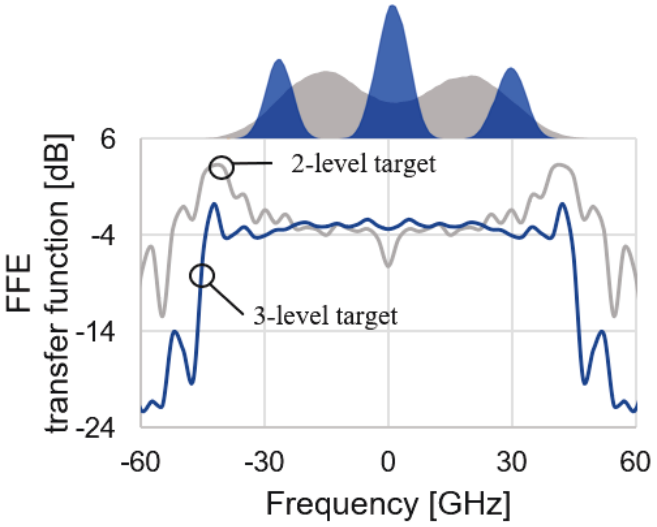

FIGURE 4.5: Experimental results. Power spectral response corresponding to the converged FFE taps (31) when the equalizer targets the OOK signal (gray 2-level histogram) or the duo-binary 3-level equivalent signal (blue histogram).

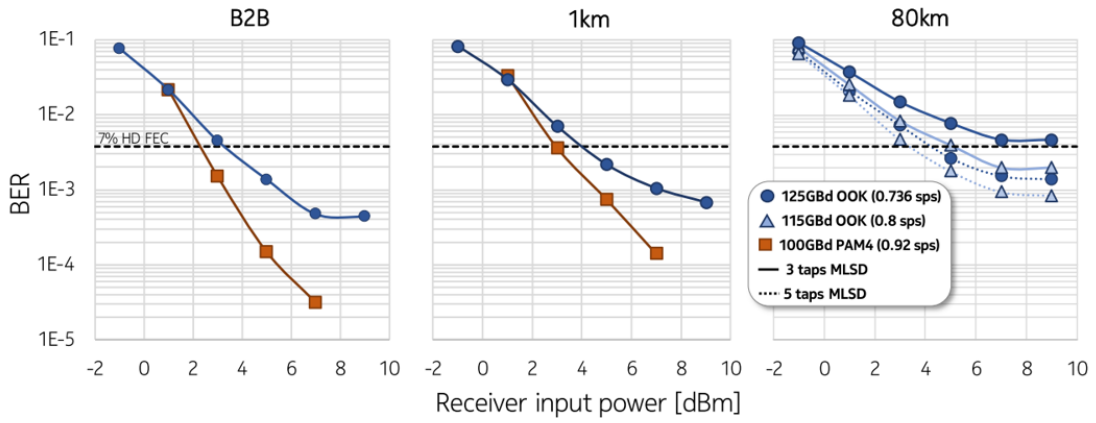

FIGURE 4.6: Experimental results. Transmission of 125 GBaud OOK and 100 GBaud 4-PAM, BER as a function of the received optical power. Sub-baudrate sampling is done both at the transmitter and the receiver for OOK and only at the transmitter for 4-PAM (92 GS/s DAC and 100 GS/s ADC. Left: back-to-back. Center: 1-km C-band uncompensated SMF transmission. Right: 80-km C-band compensated SMF transmission.

3 dBm, a value which has been chosen empirically to minimize the effect of the fiber nonlinearities while maintaining sufficient power at the span input. The receiver side is identical to PoC#2, that is, a 70-GHz PIN preceding a 8-bit 70-GHz ADC. For this test, although the ADC keeps running at 200 GS/s, one sample out of two can be removed on the stored traces to emulate an equivalent 70-GHz 100GS/s ADC and hence perform sub-baudrate sampling both at Tx and Rx. Regarding the transmitter DSP, the signals are RC filtered with roll-off 0.6 for 4-PAM and 1 for OOK. These values are empirically chosen to minimize the pre-FEC BER. For more details on the transmitter DSP, refer to the table in Fig.4.2.

The experimental results are reported in Fig.4.6. On the leftmost plot, the performance in back-to-back is reported for comparison with the PoC#2 in the case of 100 GBaud 4-PAM (filled squares). We observe that the required receiver input power at the sensitivity limit is 3 dB smaller than in PoC#2 (2 dBm against 5 dBm). This enhancement is attributed to two main factors. First, the PoC#2 was performed with 0.89 SPS at the transmitter side while it is 0.92 SPS in this transmission experiments. Moreover, in PoC#2, the 4-PAM signal was NRZ while it is RC filtered in experiments (roll-off 0.6, see table in Fig.4.2), thus slightly reducing the filtering penalty at the transmitter side. Note that the FFE number of taps has been also slightly increased from 91 to 105 taps. The leftmost plot also shows the feasibility of 125 GBaud OOK (blue filled circles), which translates into 0.736 SPS at the transmitter side and 0.8 SPS at the receiver.

Regarding the 1 km transmission, all the investigated configurations are successfully transmitted given the considered FEC limit. As in the PoCs, the FFE equalizer is configured to recover the 3-level duo-binary for OOK and 7-levels for 4-PAM with 91 and 105 taps, respectively, followed by the 3-tap MLSD algorithm. For 125 GBaud OOK, we measure 1 dBm transmission penalty (pre-FEC limit at 4 dBm instead of 3 dBm for B2B). This slight performance degradation is explained by the frequency fading of the first spectral notch of the chromatic dispersion equivalent power response, which falls within the signal modulation bandwidth [22]. Thus, 1-km propagation does not significantly reduce the performance of the considered OOK signal, as the severe low-pass frequency response drives the end-to-end optical set-up. By comparing these results with PoC#2 (which has similar receiver architecture), we observe that, for OOK: 10% of bit rate increase (112 to 125 GBaud or 0.79 to 0.736 SPS) translates into 4 dBm of penalty; and for 4-PAM at 100 GBaud, the receiver sensitivity is improved by 2 dB when switching from 0.89 to 0.92 SPS). Hence, operating beyond the range 100-115 GBaud may incur a sensibility penalty that will lead to uncontrolled reduction of the operation margins. For the 100 GBaud 4-PAM (200 Gbits/s), it is successfully transmitted over 1 km with considerable receiver sensitivity improvement (2 dBm) with respect to PoC#2, justifying the set-up improvement.

Now, we focus on the 80-km SMF scenario, for which the system reaches its practical operation limits. For 125 GBaud, 5-tap MLSD is necessary to successfully demodulate 125 GBaud while the regular 3-tap MLSD is sufficient for 115 Gbaud. This confirms that the sub-baudrate reliable range of operation is around 110-115 GBaud. Note that for 80-km propagation, potential misestimation of the link chromatic dispersion, noise of the EDFA at injection, as well as possible Kerr nonlinearities, due to the high input optical power (3 dBm) to overcome propagation loss (16 dB), are additional sources of distortions which explain the performance degradation with respect to previous results.

4.2.4 Conclusion

A novel transceiver architecture for Faster-than-Nyquist signaling is proposed, targeting 200 Gbits/s (and beyond) per lane for next generation high-speed transceivers. This technique demonstrates the feasibility of such data rates when employing bandwidth and sampling-speed-limited CMOS DAC/ADC. To do so, we proposed a DSP approach in which aggressive sub-baudrate sampling is performed at the transmitter using standard modulation techniques (symbol

mapping, pulse-shaping, anti-aliasing filter and down-sampling) and without the need for additional DSP complexity. The resulting severe inter-symbol interference is mitigated at the receiver by a two-step procedure. First, multi-level equalization recovers the duo-binary version of the emitted signal. Such a configuration prevents excessive noise enhancement. Second, a MLSD resolves the remaining ISI. As a demonstration, we successfully transmitted up to 125 Gbaud OOK at 0.736 SPS (resp. 100 GBaud 4-PAM at 0.92 SPS) on 80-km (resp. 1-km) SMF fiber, a particularly challenging configuration for IM/DD beyond 100 GBaud because of the chromatic dispersion. In these experiments, the DAC sampling frequency is 92 GS/s and the ADC sampling frequency is 100 GS/s such that these results demonstrate the feasibility of sub-baudrate for 100 GBaud and beyond IM/DD systems.

4.3 Sigma-Delta transparent transceiver

In this section, we present a novel transceiver architecture based on Sigma-Delta (SD) modulation [85]. The standard SD modulation/demodulation and the proposed demodulation scheme are depicted in Fig.4.7. The traditional SD modulation technique consists in oversampling a signal such that it can be quantized with 1-bit vertical resolution using noise shaping, as depicted in the upper inset of Fig.4.7. At the receiver, the low-pass filtered and noisy signal undergoes match filtering and traditional DSP, as depicted in Fig.4.7a. In this standard architecture, the 2-level statistics and the signal-dependent quantization noise are not used at the receiver. Conversely, in the proposed architecture, the 2-level SD stream is reconstructed by the 2-step procedure introduced for sub-baudrate sampling (see section 4.2): duo-binary equalization followed by MLSD to remove the remaining inter-symbol interference, which results from the low-pass filtering of the channel. The recovered 2-level SD stream is match filtered to recover the information impacted by the in-band quantization noise without supplementary DSP operation. Indeed, in case of coherent signaling, the polarization demultiplexing as well as the carrier frequency and phase estimation are performed during the equalization of the 2-level SD stream.

This technique can be used as an enabler for optical systems which may use SD modulation, such as Radio over Fiber (RoF) [89] or optical transmission for Hybrid Fiber Coaxial Networks (HFC) [90]. Indeed, these techniques require to transmit into an optical fiber very high cardinality signals, according to the standard used in radio networks or high-bandwidth internet over coaxial cables (for instance 256-QAM and 16384-QAM, respectively). The SD modulation is used in that context because it transforms these signals into a 1-bit stream, which is very resilient to hardware imperfections at the transmitter (especially the nonlinear response of the driver amplifiers and modulators). However, as it requires oversampling, a high sampling frequency is necessary. Moreover, the achievable data rate is then ultimately limited by the bandwidth of the electro-optics components. The bandwidth limitation is strong if the SD rate is pushed far beyond the electro-optics bandwidth limitations, as in our set-up where we have ≈ 100 GS sampling rate but only ≈ 30 GHz bandwidth. It should be noted that, with the standard SD modulation, which consists in filtering the out-of-band quantization noise (see Fig.4.7), it is still necessary to equalize high-order QAM signals, as for regular detection. This is very challenging in optical systems and

even impossible in presence of bandwidth and noise limitations. Our architecture, detailed hereinafter, overcomes this limitation[5].

4.3.1 Transmitter

The transmitter is based on a digital SD quantizer whose fundamental principle is to drastically increase the SQNR. The principle of SD quantization is to leverage oversampling and quantization with noise shaping to generate any signal with a limited 1-bit physical resolution, as depicted in Fig.4.9. It is a particular case of the digital noise shaping technique presented in Chapter 3 (section 3.3), because it requires a relatively high oversampling ratio (up to[6] 128) in order to reach a sufficient SQNR for this 1 bit physical resolution. We can identify at least three advantages for using the SD modulation. First, the ultra low-resolution of 1 bit enables the use of alternative components to CMOS 8-bit DAC that are presently limited to a sampling frequency of about 100 GS/s. For instance, we can plan to use ultra-fast 1-bit samplers, developed in the context of short-reach optical links as they can generate 1-bit streams beyond 200 GS/s [22, 91]. Second, the 2-level signal distribution strongly reduces the requirement on the electronics and electro-optics chain, as a single point of operation is maintained for any input signal, which is transformed into a 1-bit stream. This enables transparency at the transmitter. Third, 2-level signals offer better resilience to driver amplifier and Mach-Zehnder modulators nonlinear response than continuous-amplitude signals.

However, these advantages are obtained with an important oversampling ratio, such that application fields of SD transmitters are limited to optical systems in which transparency and low complexity is targeted, rather than data rate. Thus, they are very promising candidates in RoF transmitters because of the natural oversampling at the radio/optical interface, an interest confirmed in the literature [90, 92].

[5]We note that our work has been carried in parallel and independently of the work presented in [90], which seems closely related. However, while authors in [90] assess the problem of coherent transmission of SD signals, they do not investigate the regime in which the bandwidth is a strong limiting factor. Moreover, our work restricts to 1-bit SD quantization and employs a 1st order noise shaping filter (1 tap) to minimize complexity, while authors in [90] employ up to 2-bit DAC and fourth order noise shaping filter. We argue that our our strategy will benefit from the capability of transmitting 2-level signals at ultra high speed, while 4-level signals present much more limitations in terms of data rate (see section 4.2) and resilience to hardware nonlinear response and noises.

[6]This value is limited by the memory length of the DAC (2^{18}) in order to maintain a sufficient number of symbols in the data stream ($2^{18}/128 = 2048$), such that symbol error ratio or bit error ratio can still be estimated experimentally

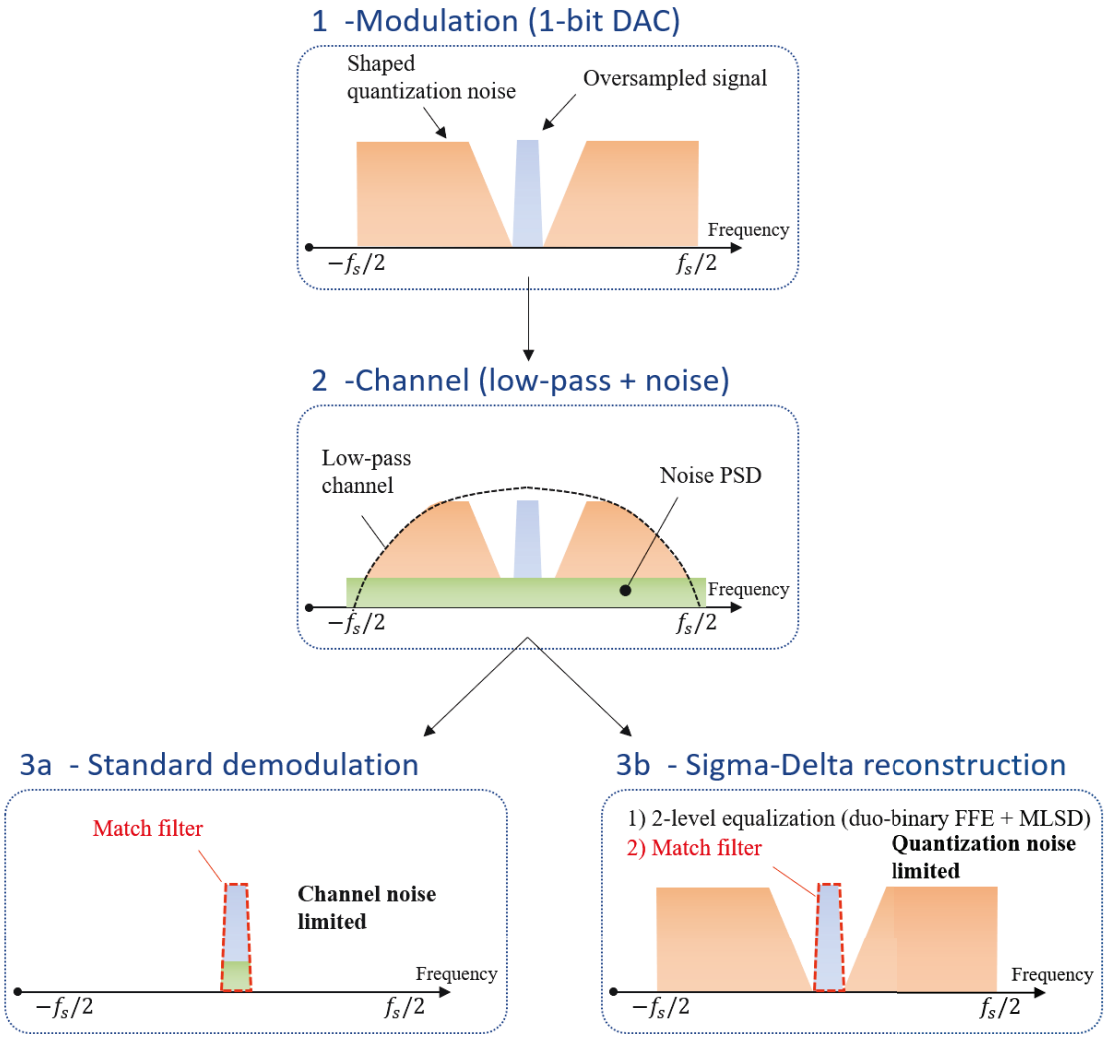

FIGURE 4.7: Principle of the Sigma-Delta (SD) modulation. Transmitter: a continuous-amplitude signal is oversampled and quantized on 1-bit vertical resolution with noise shaping. Channel: the 2-level SD stream is low-pass filtered by the channel and undergoes noise addition. It is then transformed into a continuous-amplitude signal. Receiver. Case 1: standard demodulation. The signal undergoes match filtering to remove the out-of-band quantization noise and follows traditional DSP. The channel noise limits the performance. Case 2: SD reconstruction. The 2-level SD stream is reconstructed in two steps. First, its duo-binary version is equalized with FFE. Second, a MLSD0 resolves the remaining inter-symbol interference. Then, the reconstructed SD stream is match filtered. The quantization noise within the signal bandwidth limits the performance while the channel noise is strongly attenuated during the SD reconstruction process.

To illustrate SD modulation, a continuous-amplitude signal together with the corresponding SD stream and quantization noise is shown in the left plot of Fig.4.8. The original signal is a 16-QAM RRC filtered with roll-off 0.02, generated at

32 SPS and quantized on 2 levels. The noise shaping is done with a 1 tap ($h_1 = -1$) filter (see section 3.3.2) whose transfer function is visible on the quantization noise PSD reported in the right plot of Fig.4.8 (black dashed line). The high pass nature of the noise shaping filter is confirmed by the temporal trace of the quantization noise (black dashed line in the left plot of Fig.4.8), which oscillates much faster than the original signal. A closer look also shows that the slowly varying envelope of the quantization noise corresponds to the original signal fluctuations. This property is used to recover the signal by low-pass filtering the SD stream in standard SD modulation. We note that, without noise shaping, the SQNR can be approximated[7] as follows:

$$SQNR_{\text{dB}} \approx 6.02 \cdot N_b - PAPR_{\text{dB}} + 4.77 + 10 \cdot \log_{10}(OSR) \tag{4.8}$$

which gives $SQNR \approx 17$ dB with $N_b = 1$, $OSR = 32$ and $PAPR_{\text{dB}} = 9.5$ dB (extracted before quantization). However, this SQNR is not sufficient, for instance, for radio signals carrying very high order QAM. Conversely, with noise shaping, we can see in the right plot of Fig.4.8 that the noise PSD is more than 30 dB bellow the signal PSD, anticipating a strong improvement in the transmission performance.

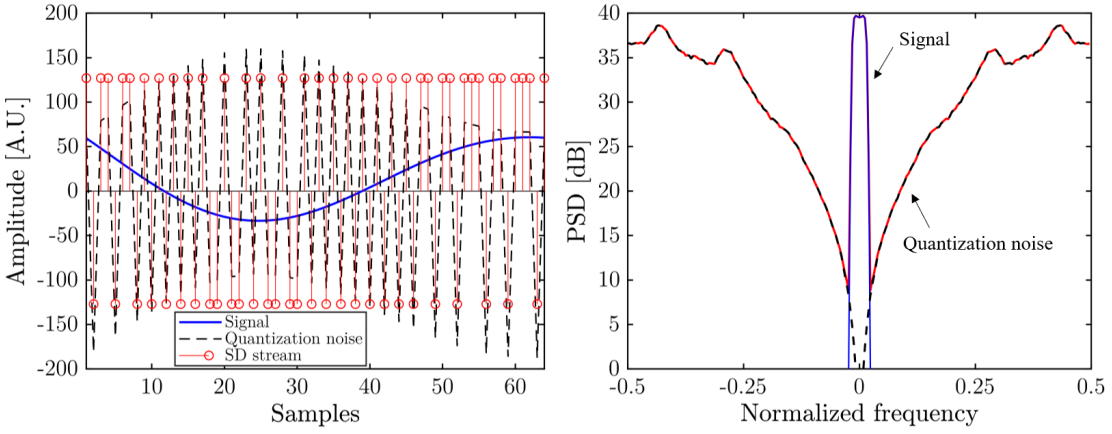

FIGURE 4.8: Numerical simulations. Sigma-Delta modulation of a 16-QAM RRC filtered with roll-off 0.02 and generated at 32 SPS (blue line). Left: corresponding SD stream (red points) and quantization noise (black dashed line). The observation window is 2 symbols (64 samples). Right: corresponding power spectral densities. The information signal spectrum is the blue line and the SD spectrum is the red line. The noise shaping filter is 1 tap $h_1 = -1$ and shapes the quantization noise PSD (black dashed line) toward high frequencies.

[7] the Widrow theorem for quantization does not apply in that case (see Chapter 2, section 2.3.1).

4.3.2 Receiver

In a traditional system employing SD modulation, the receiver architecture consists rejecting the out-of-band quantization noise with a match filter, such that the broadband data-dependent quantization distortion is not exploited at the receiver. In a coherent optical system, this requires performing regular DSP after match filter (polarization demultiplexing, carrier frequency and phase recovery), which is extremely challenging for high order QAM signals. Thus, optical systems employing the traditional SD modulation/demodulation are not tolerant to in-line linear or nonlinear distortions.

In this work, we overcome this limitation by proposing a novel receiver architecture, that takes advantage of SD streams specificities and exploits the SD quantization noise to perform signal demodulation. Instead of low-pass filtering the SD stream, we rather reconstruct the 2-level signal, strongly impaired by noise and bandwidth limitations, and then match filter it to recover the information signal. This new receiver architecture is depicted in Fig.4.9. The reconstruction of the SD stream is done in two steps. First, a linear impairment compensation FFE is performed (Sigma-Delta equalizer in Fig.4.9). To minimize the noise enhancement during the equalization process, the duo-binary version of the 2-level SD stream is targeted, which is either a 3-level signal (moderate low-pass filtering of the SD stream) or a 5-level signal (strong low-pass filtering of the SD stream).

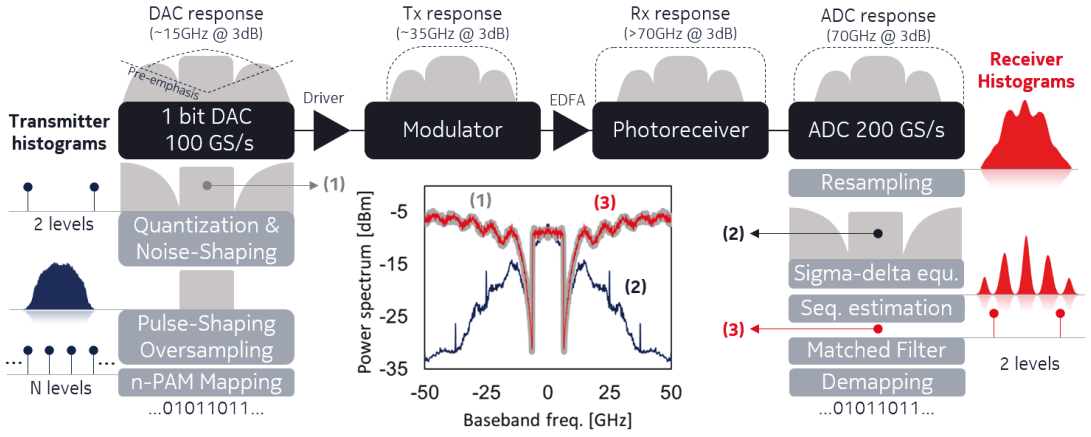

FIGURE 4.9: Schematic of the transparent Sigma-Delta transceiver, in the case of IM/DD signaling. For coherent, n-PAM is replaced by n-QAM. Inset: experimental spectra of (1) Sigma-Delta stream at 100 GS/s and oversampling of 8. (2) Spectrum after ADC and before entering the receiver DSP. The shape of the spectrum is driven by the DAC low-pass frequency response. (3) Spectrum after reconstruction of the 2-level Sigma-Delta stream.

Then, a MLSD block is in charge of retrieving the 2-level SD stream from its duo-binary version. It is fundamental to understand that the MLSD reconstructs the high frequencies of the SD stream. We note that this receiver structure is similar to the one used in section 4.2 but, to the best of our knowledge, it has never been used for SD signals. Following the reconstruction of the 2-level stream, a match filter is applied to recover the information signal. No supplementary equalization is needed. Indeed, if the SD stream is well reconstructed, after match filter, the signal is impaired only by the in-band quantization noise, such that the SNR coincides with the SQNR. Thus, as it is possible to recover the SD under severe noise and bandwidth conditions (receiver input SNR lower than the SQNR) because it is a 2-level signal, our demodulation scheme enables to recover the information with an effective SNR much greater than what could be expected with standard SD demodulation scheme. Finally, our new architecture also enables transparency at the receiver side, i.e. a unique point of operation of the whole electro-optics chain. Indeed, the DSP equalization always target a 2-level signal with fixed data rate (the sampling speed of the DAC), irrespectively of the signal characteristics.

4.3.3 Experimental demonstration

The novel concept of transparent SD transceiver is demonstrated on an optical back-to-back test bed thanks to two distinct sets of experiments. First, a proof of concept (PoC) by employing an intensity modulation and a direct detection is performed. Second, the very high resilience to bandwidth and noise limitations of our concept is confirmed by generating and demodulating up to 65536-QAM. In both cases, at the transmitter, the oversampled signals are quantized offline in *Matlab*. For each oversampling ratio (or number of SPS), the noise shaping filter is designed following the procedure described in section 3.3.2 such that the SQNR is maximized within the information signal bandwidth. The DAC sampling frequency is set to 100 GS/s.

IM/DD proof of concept

For the PoC, one electrical output of the DAC serves as intensity signal generator. The DAC frequency response is a severe low-pass transfer function with -3 dB attenuation (in amplitude) at 35 GHz (see Chapter 1 section 1.3.4). The DAC output is amplified by a 32 GHz driver feeding a 32 GHz push-pull $LiNbO_3$ Mach-Zehnder modulator. For noise loading, a variable optical attenuator is associated

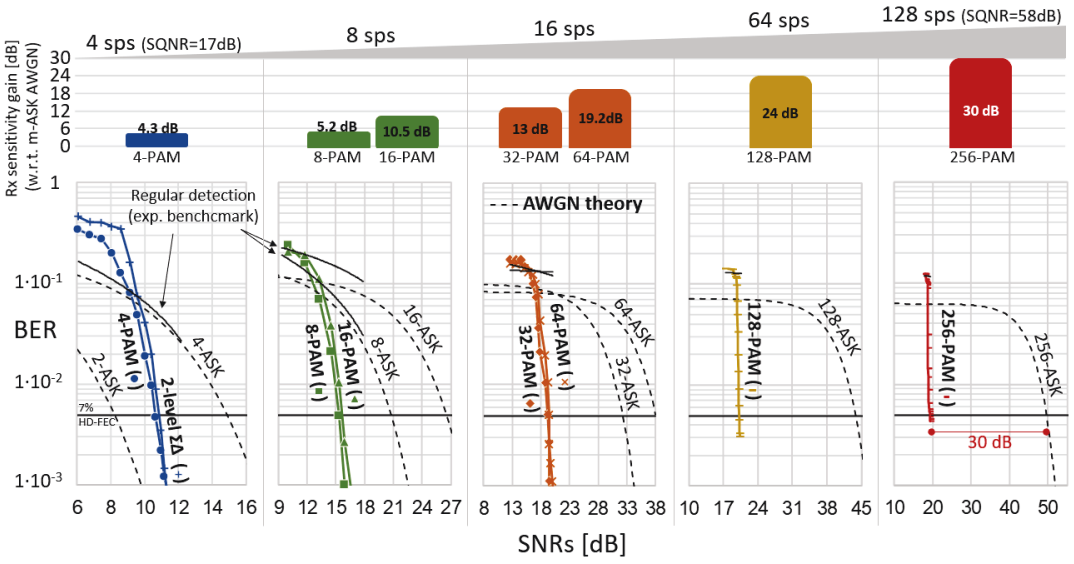

FIGURE 4.10: Experimental results. BER versus SNR for different n-PAM modulations and different OSR (number of SPS). Black dashed lines is the theory for AWGN channel. Black solid lines are the BER when SD modulation is used with match filter only at the receiver (standard demodulation). Symbols and colored solid lines is the BER when SD modulation is used together with reconstruction of the 2-level stream at the receiver (novel architecture). The sensitivity gain at the 7% HD-FEC BER limit ($4.9.10^{-3}$) is reported above.

to an EDFA. At the receiver side, the signal is recorded with a single photodiode whose output feeds a 200 GS/s real-time oscilloscope with 70 GHz electrical bandwidth. Hence, the DAC fixes the low-pass frequency limitations of the entire set-up. The end-to-end chain as well as the bandwidth of each element is depicted in Fig.4.9.

At the receiver, for the 2-level SD equalization, we use a 25-tap adaptive feed forward equalizer (FFE). Given the strong bandwidth limitation of the DAC, the equalization targets the 5-level duo-duo-binary version of the 2-level SD streams. The effectiveness of the FFE equalization can be inferred from the 5-level histogram at the output of the SD equalizer, as shown in Fig.4.9. Then, a 5-tap MLSD resolves the remaining inter-symbol interference to recover the 2-level SD stream.

In all plots of the Fig.4.10, the SNR (horizontal axis) has been measured on a demodulated 4-PAM signal after match filter and downsampling when using the SD standard demodulation at the receiver side, as depicted in Fig.4.7. Thus, this SNR gives the noise level in the information signal bandwidth. We note that the SNR increases by 3 dB per doubling the OSR, following the division by 2 of the

noise equivalent bandwidth of the information signal. However, for all OSR values, the SNR does not permit the transmission of high order modulation formats, as it saturates around $\approx$ 20 dB. As a sanity check, the system performance by using the standard SD architecture at the receiver is measured. At 4 SPS, the BER for the 4-PAM signal with regular demodulation (black solid line) is reported in the leftmost plot of Fig.4.10, and coincides with the AWGN theoretical performance (black dashed line). This confirms that the standard SD modulation/demodulation architecture does not under-perform, in terms of noise sensitivity and BER, with respect to traditional modulations/demodulations. However, the operative SNR conditions (around 12 dB), does not enable to successfully demodulate 4-PAM at 25 GBaud (50 Gbits/s) in compliance with the 7% hard-decision (HD) pre-FEC BER limit in a such drastically noisy and bandwidth-limited environment. Our new demodulation architecture aims at breaking this limitation. On the leftmost plot of Fig.4.10, the BER of the 4-PAM signal with $OSR = 4$ (blue circles) and the new architecture is reported. This curve shows that, with the reconstruction of the 2-level SD stream, the 4-PAM easily reaches the 7% HD-FEC limit, with an exceptional sensitivity with respect to AWGN theory (black dashed lines). The sensitivity gain at the HD-FEC limit is $\approx$4.3 dB.

Regarding the new architecture, the SD detection performance is given by the BER on the 100 GS/s 2-level stream (equivalent 100 Gbits/s) after MLSD. The BER on the 2-level SD stream is reported in Fig.4.10 at 4 SPS (leftmost plot, blue crosses). We observe that the BER of the 100 GS/s SD stream (blue crosses) is slightly worse than the AWGN channel theory for 100 GBaud OOK (leftmost black dashed curve). We attribute this to the different impact of the channel response on a SD stream, whose spectra differs from the one of a standard OOK signal. Indeed, with the SD modulation, most of the information to reconstruct the 2-level stream is on the high frequencies of the spectrum, and hence suffers more from the bandwidth-limited channel.

Then, the OSR is gradually increased to transmit higher PAM orders with the same noise and bandwidth limitations. In each case, we still estimate the SNR by demodulation of a 4-PAM with the standard SD architecture (match filter). We also report in Fig.4.10 the sensitivity gain for each configuration. At 16 SPS, the sensitivity gain enables the successful recovery of a 64-PAM signal with a BER of $4.5.10^{-3}$, in compliance with the 7% HD-FEC limit. The histogram of the 64-PAM signal at symbol decision is shown in Fig.4.11. The SNR in the information signal bandwidth, at the entrance of the receiver DSP, is 20 dB (see horizontal axis in Fig.4.10). Finally, we push the OSR to 128 and successfully

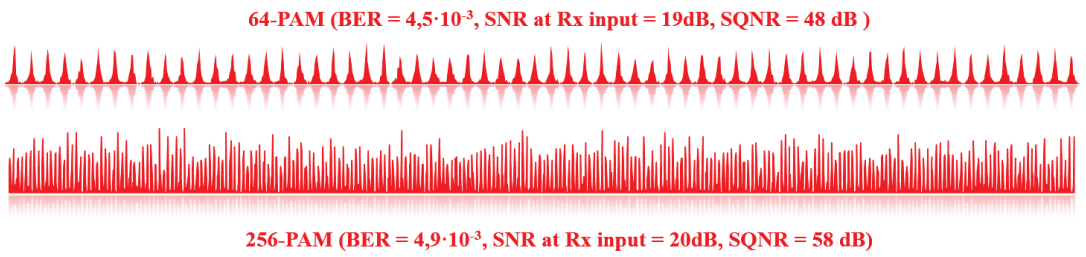

FIGURE 4.11: Experimental results. Histograms of 64-PAM and 256-PAM signals carried in a B2B optical set-up. The transmitter employs Sigma-Delta modulation with an oversampling ratio of 16 for 64-PAM and 128 for 256-PAM. The Sigma-Delta stream is generated with a 100 GS/s CMOS DAC having a 20 GHz -3 dB bandwidth. The signal-to-noise ratio in the information signal bandwidth (center of the SD spectrum) is about 20 dB. The new receiver architecture, which first reconstructs the filtered SD stream and then performs match filtering, enables the recovery of the information with an effective signal-to-noise ratio close to the signal-to-quantization-noise ratio.

generate and detect the first reported, to the author knowledge, 256-PAM signal carried in an optical channel. The corresponding histogram is shown in Fig.4.11. The BER reaches $4.9.10^{-3}$, which corresponds to an effective SNR of 50 dB, while the true SNR in the information signal bandwidth is $\approx$ 20 dB (estimated on a 4-PAM with standard SD demodulation). The sensitivity gain, obtained with the reconstruction of the SD stream at the receiver, is 30 dB with respect to AWGN theory for PAM modulation.

We insist on the fact that these results are obtained with important oversampling such that the maximum data rate with our architecture is 50 Gbits/s (4-PAM at 4 SPS) while the DAC operates at 100 GS/s. All the other configurations gives a smaller data rate. However, it becomes possible to transmit high cardinality modulation formats even in a strong noise and bandwidth-limited environment, and we extend our concept to coherent optical systems.

Coherent SD transceiver

We now switch to a coherent B2B optical set-up by replacing the modulator of the IM/DD experiment by a dual-polarization I/Q modulator designed to operate at 64-GBaud. However, the system end-to-end frequency response remains limited by the DAC limited bandwidth. Regarding the SD transmitter, the symbol sequences are oversampled and RRC filtered with a roll-off 0.02 and quantized on 2-level with noise shaping, as in the PoC for IM/DD. With coherent signaling, the output signal

is a dual-polarization QPSK at 100 GBaud (400 Gbits/s). At the receiver, the duo-binary version of the QPSK is equalized with a multi-modulus algorithm (MMA) configured for 9-QAM constellation. In all the presented results, the equalizer is a 115-tap radius directed equalizer (RDE) with a convergence parameter $\mu = 1/1000$. After equalization, the signal is down sampled to 1 SPS and undergoes carrier frequency and carrier phase estimation. For conciseness, we explore only two different OSR configurations. The recovered 9-QAM constellations for both polarizations at two OSR values (64 and 128) are shown in Fig.4.12.

From the 9-QAM constellation at 1 SPS, each component undergoes separately 3-tap MLSD in order to recover the real and imaginary components of both polarizations of the 100 GBaud QPSK signal. At the maximum SNR, the BER

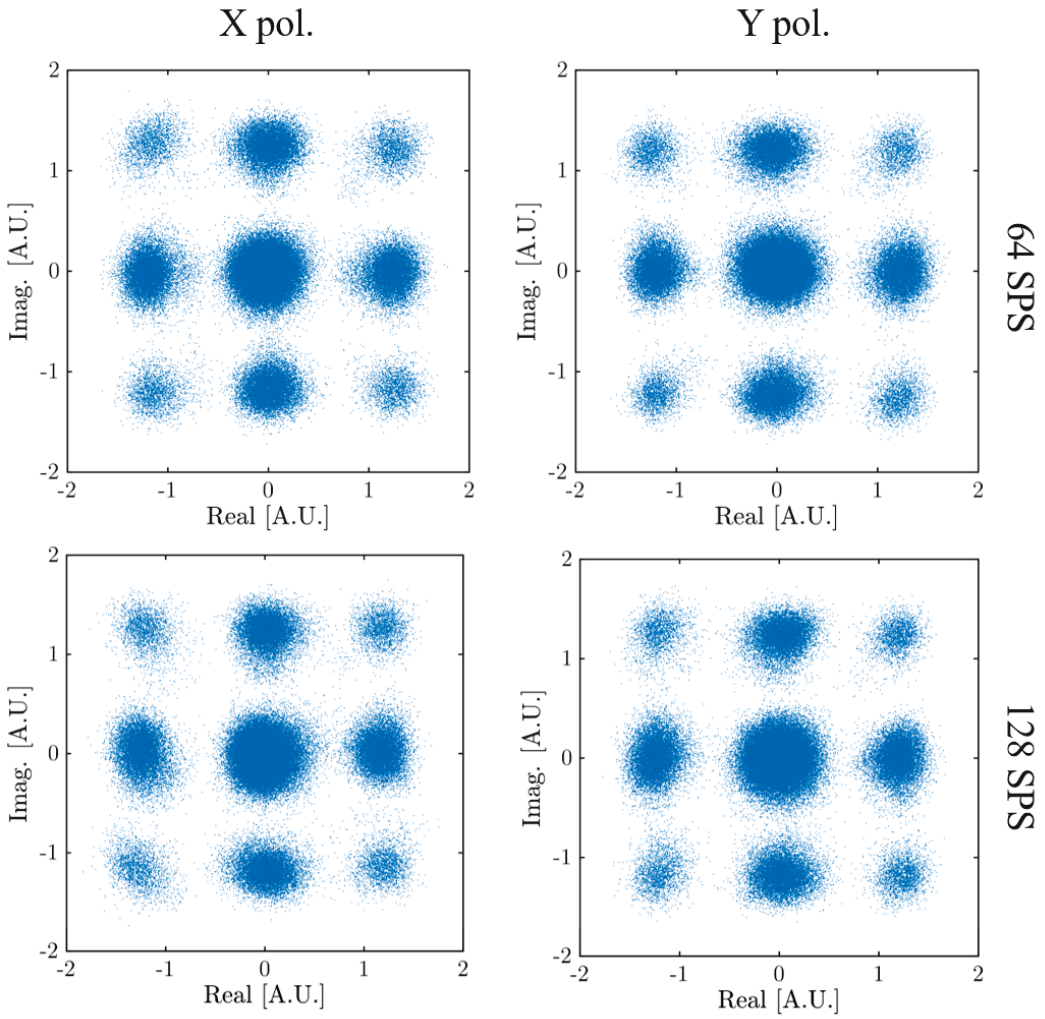

FIGURE 4.12: Experimental results. 100 GBaud 9-QAM constellations at the output of the equalizer targeting the duo-binary version of the 100 GBaud QPSK. Up: OSR=64 for 16384-QAM. Bottom: OSR=128 for 65536-QAM.

on the four demodulated SD streams is about 6.10^{-4} (average over the four tributaries). The BER is similar for the two OSR values because the QPSK signal properties (data rate and spectral shape) is let unchanged, confirming the transparency of our architecture at the receiver side. This is inferred in the 9-QAM constellations reported in Fig.4.12. Finally, the 2-level SD streams are match filtered to recover the information signal.

In Fig.4.13, we show a 16384-QAM at 64 SPS (1.6 GBaud, 45 Gbits/s), demodulated with a symbol error ratio of ≈ 0.02, which translates into a BER of $\approx 1.4.10^{-3}$ (with Gray coding)[8]. Also, note that, because of the finite length of the DAC memory buffer (2^{18} samples), we use a trick to represent the full constellation. We plot, for instance, the real component as a function of a time shifted version of the imaginary component (*circshift* function in *Matlab*) such that all the possible 16384 combinations appear. By doing so, the Fig.4.13 shows that the match filtered SD stream corresponds to 16384 different positions in the complex plane.

4.3.4 Conclusion

We presented a novel transceiver architecture for transmission of highly sensitive signals in strongly degraded noise and bandwidth conditions. At the transmitter, we employ Sigma-Delta modulation to transform any multilevel signals into a 2-level bit stream (for IM/DD) or non-return-to-zero QPSK for coherent signaling. This is obtained through aggressive oversampling and noise shaping, pushing the SQNR up to ≈ 60 dB. At the receiver, instead of match filtering the SD stream, as in standard SD demodulation, we rather reconstruct the 2-level (or QPSK) stream and then match filter it to recover the information signal. This is done through a multilevel equalization of the duo-binary version of the SD stream, concatenated with a maximum-likelihood-sequence detector for sequence retrieval. By reconstructing the SD stream, we put the system in the quantization-noise-limited regime and hence enable the transmission of highly sensitive modulation formats, such as 16384-QAM with 64 SPS, producing a bit rate of 44 Gbits/s, suitable for Radio-over-Fiber applications or optical transmission for Hybrid Fiber Coaxial Networks (HFC) [90]. For the sake of demonstration, we also successfully demodulate a 65536-QAM at 128 SPS. These results are obtained with a CMOS

[8]It must absolutely be noted that the constellation represented in Fig.4.13 or Fig.4.14 result from the plotting of the imaginary component versus the real component of the field right after match filter. There is no symbol decision which would tend to make the field to be concentrated on the ideal constellation symbols position.

DAC cadenced at 100 GS/s, but with only 20 GHz -3 dB bandwidth, while the system signal-to-noise ratio within the information signal spectrum is about 20 dB.

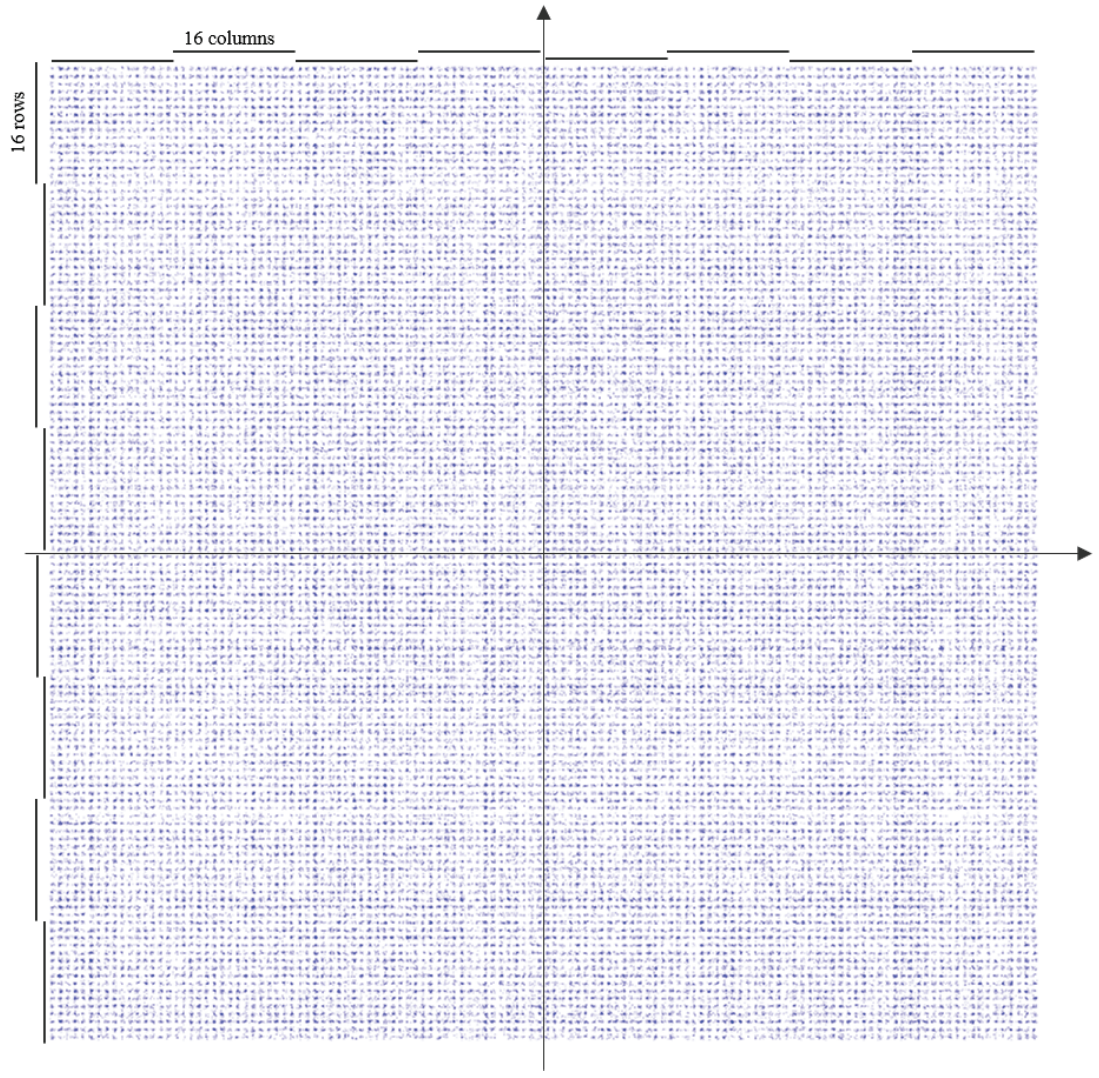

FIGURE 4.13: Experimental results. 16384-QAM constellation at 1.6 GBaud (43.75 Gbits/s in dual-polarization). The transmitter employs SD modulation at 64 SPS, producing a 100 GBaud QPSK signal. The transmitter -3 dB bandwidth is about 20 GHz. The SNR in the information signal bandwidth (center of the SD spectrum) is $\approx$ 20 dB. The receiver reconstructs the 2-level SD stream (with equalization of the duo-binary equivalent of the QPSK signal) and then perform match filtering to recover the information signal almost in the quantization noise-limited regime. The SER is $\approx 2.10^{-2}$ which corresponds to a BER of $1.4.10^{-3}$ (with Gray coding).

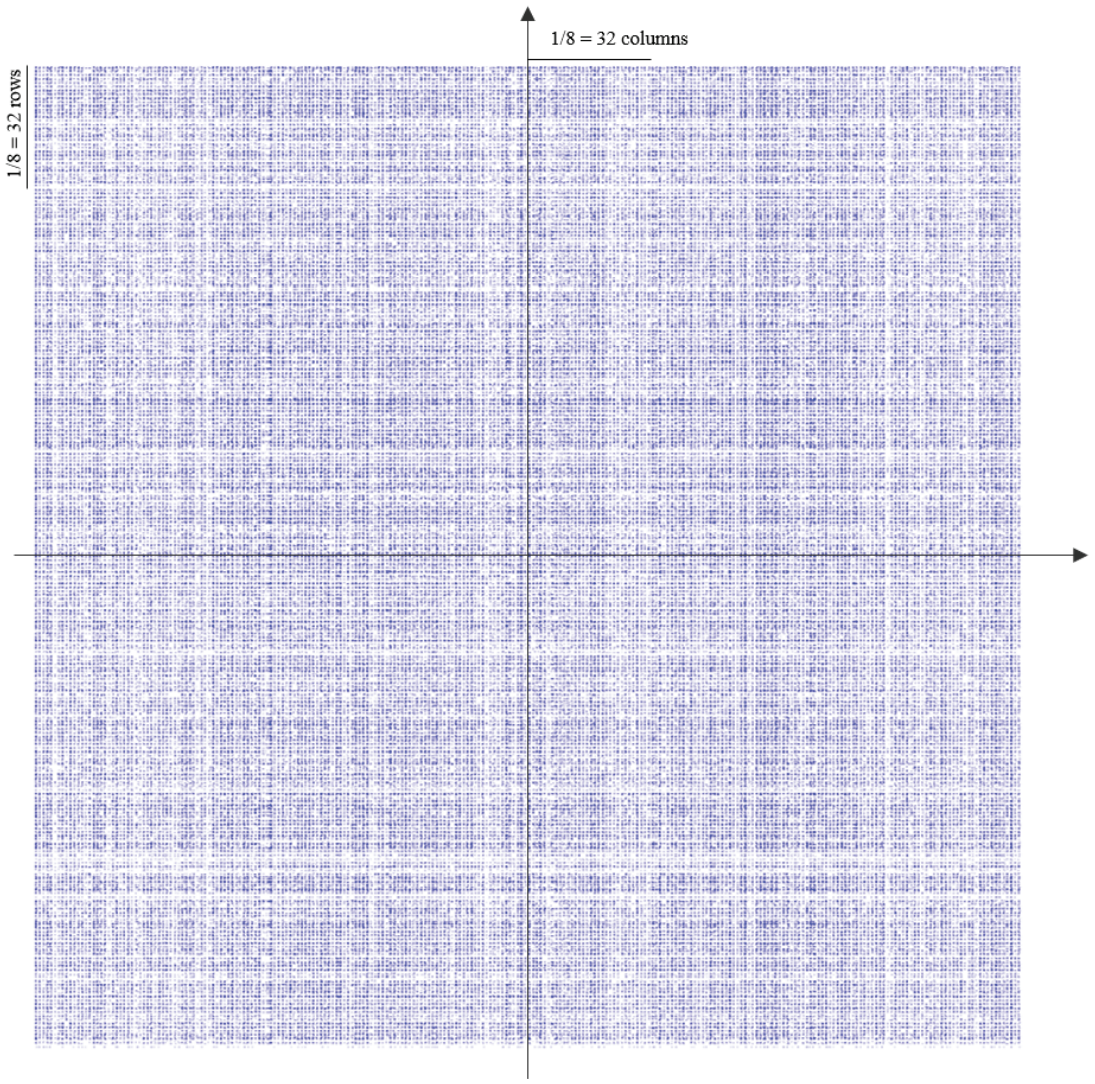

FIGURE 4.14: Experimental results. 65536-QAM constellation at 0.8 GBaud (25 Gbits/s in dual-polarization). The transmitter employs SD modulation at 128 SPS, producing a 100 GBaud non-return-to-zero QPSK signal. The transmitter -3 dB bandwidth is about 20 GHz. The SNR in the information signal bandwidth (center of the SD spectrum) is $\approx$ 20 dB. The receiver reconstructs the 2-level SD stream (with equalization of the duo-binary equivalent of the QPSK signal) and then perform match filtering to recover the information signal almost in the quantization noise-limited regime (SQNR around 58 dB). The SER is $\approx 2.10^{-2}$ which corresponds to a BER of $3.9.10^{-2}$ (with Gray coding).

4.4 Conclusion

In this chapter, we presented two novel transceiver architectures for short-reach optical links and based on high-speed CMOS DAC and ADC.

The first architecture, namely sub-baudrate sampling, is a new way of performing Faster-than-Nyquist signaling, i.e. to transmit at a symbol rate greater than the sampling frequency of the DAC and ADC. This enables the increase of the data rate at a fixed sampling frequency. Conversely to other existing Faster-than-Nyquist architectures, all the additional complexity to perform transmission below 1 sample per symbol is located at the receiver side, hence avoiding any pre-coding of the emitted signals. On an IM/DD optical system, we demonstrated the feasibility of this architecture with a 92 GS/s DAC and 100 GS/s ADC, pushing the symbol rate up to 125 GBaud with OOK and 100 GBaud for 4-PAM (200 Gbits/s), over respectively 80-km and 1-km of SMF fiber. This work paves the road for 200 Gbits/s and beyond IM/DD systems employing CMOS DAC and ADC.

The second architecture revisits the SD modulation and enables transmission of high cardinality signals in strongly noise and bandwidth-limited environments, as required in applications for which radio or electrical signals are transported through optical fibers, by means of electro-optics conversion. To do this, we proposed a new demodulation architecture for SD stream. Instead of match filtering the SD signal, it rather reconstructs the 2-level stream and then match filters it. By reconstructing the high frequencies of the SD stream, we showed that it is possible to use the quantization noise in order to increase the sensitivity at the receiver side. Indeed, with this new architecture, the SNR at symbol decision approaches the SQNR of the SD modulator, in general much higher than the SNR fixed by the in-line noises and distortions. With a 100 GS/s CMOS DAC, we demonstrated that a 16384-QAM signal can be transmitted with 1-bit vertical resolution at the symbol rate of 1.6 GBaud (64 SPS), giving 45 Gbits/s, in line with requirements for Hybrid Fiber Coaxial Networks (HFC) [90], for instance. The opportunity to use 200 GS/s 1-bit samplers [22] lets envision that much higher data rates are achievable in the near future.

Conclusion

Low-resolution digital-to-analog and analog-to-digital converters (DAC/ADC) are promising candidates for reducing the power consumption, the cost and the complexity of transmitters and receivers. In this thesis, we investigated the possibility to use low-resolution DAC in optical transmitters designed for metropolitan optical networks. However, when they are used, the quantization noise can no longer be neglected and may become one of the performance limiting factors. Thus, to efficiently make use of low-resolution DACs in optical networks, several questions need to be answered or assessed.

We highlighted the conditions in which the quantization noise is non negligible in an optical link. While today optical transceivers employ 8-bit DAC and ADC, for which the quantization noise is negligible with respect to the other noises and distortions, it has been demonstrated that reducing the physical resolution below 6 bits increases the effect of the quantization noise. Conversely, between a physical resolution of 8 and 6 bits, the ENOB of the converter is not modified because of the influence of the other noises and distortions, namely the electrical noise, the limited bandwidth and the clock timing jitter. Below a physical resolution of 6 bits, the optical system signal-to-noise ratio decreases by about -6 dB for each reduction of one bit of the physical resolution. In addition, it has been highlighted that the traditionally used ENOB indicator is not satisfying to predict the influence of low-resolution induced distortions for two reasons. First, it has been developed for sinusoidal signals whereas optical signals support wide spectra. Second, it aggregates all the physical limitations of the converter (limited bandwidth, electrical noise, clock timing jitter and quantization noise) and masks the specific properties of the quantization noise, such as its statistical dependency with the signal or the oversampling effect.

We developed a performance prediction model accounting for the low-resolution induced distortions by separating the quantization noise from the other distortions. We highlighted that low-resolution quantizers induce two different distortions:

the quantization noise and the clipping noise. By using a statistical theory of quantization, it has been demonstrated that the quantization can be treated as an additive noise uncorrelated with the signal. The assumptions underlying this model have been recalled and used to strictly bound the validity of this model. It has also been shown that the key parameters which govern the optical system performance in presence of the quantization noise are the physical resolution and the oversampling factor of the DAC or ADC. Moreover, we showed that the clipping is necessary to maximize the performance of low-resolution DAC/ADC, as it provides an increase in SNR of up to ≈2 dB. Although the clipping noise is correlated with the signal, it has been established that, with the amount of clipped values introduced to optimize the SNR, the correlation can be neglected. This model enables the correct prediction of the system SNR, with an experimental prediction error of less than 0.5 dB. We used our proposed model to derive the physical resolution requirements for next generations (>600 Gbit/s) optical systems. It has been inferred that a 4-bit DAC complies with the generation of 600 Gbit/s signals, in line with recent experiments.

We proposed several techniques to maximize low-resolution quantizers performance. Among different possibilities, it has been shown that modifying the power spectral density of the quantization noise is the most promising technique as it provides signal-to-quantization noise ratio (SQNR) gains of several dBs. Moreover, this technique applies to any signal generated with more than one sample per symbol. In a nutshell, we demonstrated the feasibility to generate a 64-QAM at 44 GBaud (528 Gbit/s gross) with a 3-bit physical resolution by employing a +6 dB (i.e. 1-bit) noise shaping filter, whose concept is adapted to optics from audio systems. This result is predicted by the model presented in Chapter 2. For an implementation in an optical transmitter, this technique has the strong advantage to be constituted by a linear filtering of the quantization noise, such that its implementation in a real-time transmitter should be possible. However, in that case, the performance in back-to-back only allows a limited reach (about 100 km). Thus, using a physical resolution of 4 bits should offer a greater reach (about 500 km), compliant with metropolitan networks. Two other optimization techniques are investigated. One is new and called "constellation phase rotation technique" and applies to complex signals which are not circular in the complex plane, in the case of a small pre-compensation of the chromatic dispersion for instance. Although this technique only applies in specific cases, the SQNR gain of the order of 1 dB and its simplicity of implementation (one rotation in the complex plane, i.e. a phase shift) illustrate its interest for digitally enhanced DACs. Finally,

the question of employing non-uniform quantization has been assessed. Any non-uniform distributed signal benefits from non-uniform quantization. For a 4 bit DAC, numerical simulations have shown that the SQNR gain is of the order of 1 dB, with respect to the uniform quantizer including clipping optimization. For a practical implementation, an 8-bit DAC can be transformed into a 4-bit non-uniform DAC by properly selecting the quantization levels. Such a solution is expected to reduce the power consumption according to the DAC architecture [10].

Finally, we designed two novel transceiver architectures. The first one consists in performing Faster-than-Nyquist (FTN) signaling, i.e. transmitting information at a symbol rate greater than the DAC and/or the ADC sampling frequency. This architecture differs from others FTN architectures as the additional complexity for the transmission below 1 sample per symbol (SPS) is located at the receiver side. Hence, it avoids performing any pre-coding of the emitted signals. At the receiver side, a 2-step strategy to demodulate signals impacted by a strong low-pass filtering and an important inter-symbol interference is proposed. The first step consists in equalizing the duo-binary version of the emitted signal rather than the original signal itself. The second step consists in a maximum likelihood sequence detection which resolves the remaining inter-symbol interference. For an intensity modulated (IM) and direct detection (DD) optical link for intra or inter data-center, we demonstrated the feasibility of transmitting 125 Gbaud OOK with no more than 92 GS/s DAC (0.736 SPS) and 100 GS/s ADC, both on 1-km and 80-km optical links, and 100 Gbaud 4-PAM (0.92 SPS at the receiver) on 1-km. This work paves the way for 200 Gbit/s and beyond IM/DD systems using CMOS DAC and ADC. The second architecture is a transparent transceiver which revisits the Sigma-Delta (SD) modulation and enables the transmission of high fidelity (high order QAM) optical signals in particularly noisy and bandwidth-limited environments, through a novel receiver architecture. The transmitter transforms any signal into a 2-level stream which provides a unique point of operation for the entire electro-optics chain. The receiver reconstructs the 2-level SD stream, whose properties are independent of the information. Hence, we called it a transparent transceiver. Applied to SD signals, the new concept is to use the quantization noise of the SD modulator in order to increase the receiver sensitivity and be able to demodulate signals which require high SNRs. This is done at the receiver side by reconstructing the 2-level SD stream, while in standard SD modulation it is match filtered such that the out-of-band quantization noise is removed and not used for the demodulation. As a proof of concept, we successfully demodulated

up to optical 256-PAM and 65536-QAM in an IM/DD and coherent test bed, respectively.

Prospects

While my work highlighted many aspects of low-resolution digital-to-analog conversion for optical networks, these three years of research pave the way for further investigations regarding their potential for short-reach and metropolitan optical networks. Regarding the modeling of the low-resolution distortions, our proposed model needs to be developed to predict other useful performance metrics such as the bit error ratio in addition to the SNR. To do so, it is necessary to perform a statistical study of the low-resolution distortions and clearly determine what is the corresponding noise distribution in the received constellation at symbol decision. For instance, given the definition of the clipping distortion, it may manifest differently than a 2-dimensional circular noise, making the conversion of the signal-to-noise ratio into a bit error ratio challenging.

Regarding the optimization techniques to maximize the performance of low-resolution digital-to-analog and analog-to-digital converters, it will be necessary to study the differences between the noise shaping technique presented in this manuscript and the digital resolution enhancer proposed recently in the literature. Indeed, even if they both perform quantization with noise shaping, they have deep differences in their conception. For instance, one can expect that for ultra low-resolution DAC and ADC (2-bit and below), when the quantization noise can be correlated with the signal, they have a different behavior on the system performance.

Regarding the novel transceiver architectures, and especially the Sigma-Delta transceiver, a proof of concept using a (at least) 200 GS/s 1-bit sampler will be a good step toward further experimental assessments. It will be done in close collaboration with Nokia III-V Laboratory which develops ultra high speed 1-bit samplers (>200 GS/S) component for Nokia. However, significant research and development efforts are necessary to interface the DSP for Sigma-Delta modulation with these components, which today only allow non pre-processed data at their input.

More generally, it should be noted that recent concepts of transmitters and receivers consist in interleaving (temporally or in the spectral domain) the output of different digital-to-analog converters to produce a unique signal. This enables the generation of signals having a bandwidth much greater than the bandwidth each DAC, taken separately, but requires a pre-processing of the signal by numerous DSP operations. In this new field of research, many modeling and optimization efforts can be pursued in order to maximize the potential of such new architectures and I also plan to collaborate with Nokia III-V Laboratory in the development of the ultra high speed interleavers and their interfacing with the transmitter DSP.

Also, recent advances in transverse fields such as machine learning pave the road for novel concepts in optical communications. For instance, recent experiments show that new reconstruction methods for the modulation/demodulation of low-resolution signals may be a good alternative towards a new generation of DAC and ADC.

Appendix A

Bates distribution

A Bates distribution is a probability distribution of the mean of statistically independent uniformly distributed random variables (r.v.) U_i:

$$X_k = \frac{1}{k}\sum_{i=1}^{k} U_i = \sum_{i=1}^{k} U_{i,k} \tag{A.1}$$

In what follows, the r.v. U_i are of zero-mean and of support $\left[-\frac{2^{N_b}\Delta}{2}, +\frac{2^{N_b}\Delta}{2}\right]$ and $U_{i,k}$ has support $(1/k)\left[-\frac{2^{N_b}\Delta}{2}, +\frac{2^{N_b}\Delta}{2}\right]$. In other words, the support of the r.v. X_k exactly coincides with the quantizer dynamic range $2^{N_b}\Delta$. The characteristic function of the r.v. X_k can be computed trough the characteristic function of the uniform r.v. $U_{i,k}$:

$$\widetilde{U}_{i,k}(\nu) = \int_{-\infty}^{+\infty} U_{i,k}(x) e^{2i\pi\nu x} dx = \int_{-\frac{2^{N_b}\Delta}{2k}}^{+\frac{2^{N_b}\Delta}{2k}} \left(\frac{k}{2^{N_b}\Delta}\right) e^{2i\pi\nu x} dx \tag{A.2}$$

$$= sinc\left(2\pi\nu\frac{2^{N_b}\Delta}{2k}\right) = sinc\left(\frac{2^{N_b}\Delta}{k}\pi\nu\right) \tag{A.3}$$

And per the properties of the FT, the characteristic function of X_k is:

$$\widetilde{X}_k(\nu) = \left[sinc\left(\pi\nu\frac{2^{N_b}\Delta}{k}\right)\right]^k \tag{A.4}$$

which vanishes for:

$$\frac{2^{N_b}\Delta}{k}\pi\nu = l\pi,\ l \in \mathbb{Z}^* \tag{A.5}$$

Such that:

$$\nu = \left(\frac{1}{\Delta}\right)\frac{kl}{2^{N_b}} \tag{A.6}$$

The Eq.(A.6) gives the set of ν for which the CF of the Bates distributions X_k vanishes.

Now, given a quantizer resolution N_b, one has to find the values of k that ensure that the fraction $kl/2^{N_b}$ generates an ensemble which contains $\mathbb{Z}^*$ to follow Eq.(2.8).

First, it is clear that for $k > 2^{N_b}$, the Eq.(A.6) cannot give all the integers multiple of $1/\Delta$. For instance, if $k = 2^{N_b} + \epsilon$, $\epsilon > 0$, the Eq.(A.6) becomes:

$$\nu = \left(\frac{1}{\Delta}\right) \cdot \left(1 + \frac{\epsilon}{2^{N_b}}\right) l \tag{A.7}$$

and in that case the Eq.(A.7) does not contains $1/\Delta$ and $-1/\Delta$ such that the Bates distributions with $k > 2^{N_b}$ do not follow the Widrow theorem. This is understood by the fact that, in that case, the r.v. $U_{i,k}$ has a support smaller than Δ such that the first zero of its characteristic function is greater than $1/\Delta$, as in Eq.(A.3).

Second, for $k = 2^{N_b}$, it is clear that Eq.(A.6) can give all the integer multiples of $1/\Delta$.

Third, if the fraction $kl/2^{N_b}$ must generate an ensemble which contains $\mathbb{Z}^*$, one notes that k must be a divider of 2^{N_b} as $l \in \mathbb{Z}^*$. This last condition is understood by the fact that if k is not a divider of 2^{N_b}, the support of $U_{i,k}$ is not an integer multiple of Δ such that its characteristic function does not vanish at integer multiples of $1/\Delta$.

Hence, for a quantizer with a physical resolution N_b bits, the family of Bates distributions X_k, $k \in \left[1, \frac{2^{N_b}}{2^{N_b-1}}, \frac{2^{N_b}}{2^{N_b-2}}, ..., 2^{N_b}\right]$ are good test distributions for Eq.(2.18) as they exactly follow the condition given by Eq.(2.8), without any approximation[1].

[1]Regarding the validity of Eq.(2.9) for the Bates distributions, we assume that it is verified even though a rigorous demonstration would be necessary, especially for $k = 1$.

Abbreviations

ADC analog-to-digital converter.

ASE amplified spontaneous emission.

AWGN additive white Gaussian noise.

BER bit error ratio.

CD chromatic dispersion.

CF characteristic function.

CPRM constellation phase rotation method.

DAC digital-to-analog converter.

DD direct detection.

DSP digital signal processing.

EDFA Erbium doped fiber amplifier.

ENOB effective number of bits.

FFE feed forward equalizer.

FT Fourier transform.

FTN Faster-than-Nyquist.

IM intensity modulation.

ISI inter-symbol interference.

MLSD maximum likelihood sequence detection.

NRZ non return to zero.

NTF noise transfer function.

OFDM orthogonal frequency division multiplexing.

OOK on-off keying.

OSNR optical signal-to-noise ratio.

OSR oversampling ratio.

PAM pulse-amplitude modulation.

PAPR peak-to-average power ratio.

PDF probability density function.

PDM polarization division multiplexing.

PSD power spectral density.

QAM quaternary amplitude modulation.

QPSK quaternary phase-shit keying.

RC raised-cosine.

RRC root-raised-cosine.

SCNR signal-to-clipping-noise ratio.

SD Sigma-Delta.

SNR signal-to-noise ratio.

SPS sample(s) per symbol.

SQNR signal-to-quantization noise ratio.

VOA variable optical attenuator.

WDM wavelength division multiplexing.

Bibliography

[1] M. K. Weldon, *The future X network, a Bell labs perspective*, 2016.

[2] Cisco, "Cisco Visual Networking Index : Forecast and Trends," Tech. Rep., 2018.

[3] L. Galdino, A. Edwards, M. Ionescu, J. James, W. Pelouch, E. Sillekens, D. Semrau, D. Lavery, R. I. Killey, S. Barnes, P. Bayvel, and S. Desbruslais, "120 Tbit/s Transmission over Single Mode Fibre using Continuous 91 nm Hybrid Raman-EDFA Amplification." [Online]. Available: https://arxiv.org/abs/1804.01845

[4] Mine Magazine, "Mining robots Rio Tinto doubles down on autonomous drilling," 2018. [Online]. Available: https://mine.nridigital.com/mine_aug18/issue_71

[5] K. Balachandran and K.C. Budka, *Future X for Industries: Mining - Exclusive chapter preview*. [Online]. Available: https://onestore.nokia.com/asset/205736

[6] Alcatel-Lucent Bell Labs, "Bell Labs Metro Network Traffic Growth: An Architecture Impact Study," Tech. Rep., 2013.

[7] AMS, "AMS-IX statistical data on connected networks," 2018. [Online]. Available: https://www.ams-ix.net/ams

[8] L. S. J. McNicol, M. O' Sullivan, K. Roberts, A. Comeau, D. McGhan, "Electrical Domain Compensation of Optical Dispersion," *Optical Fiber Communication Conference*, 2005.

[9] H. Sun, K.-t. Wu, and K. Roberts, "Real-time measurements of a 40 Gb/s coherent system," *Optics Express*, vol. 16, no. 2, pp. 873–879, 2008.

[10] C. Laperle and M. O. Sullivan, "Advances in High-Speed DACs, ADCs, and DSP for Optical Coherent Transceivers," *Journal of Lightwave Technology*, vol. 32, no. 4, pp. 629–643, 2014.

[11] T. Drenski and J. C. Rasmussen, "ADC and DAC - Technology Trends and Steps to Overcome Current Limitations," *Optical Fiber Communication Conference*, 2018.

[12] P. Layec, A. Dupas, D. Verch, K. Sparks, and S. Bigo, "Will Metro Networks Be the Playground for (True) Elastic Optical Networks ?" *Journal of Lightwave Technology*, vol. 35, no. 6, pp. 1260–1266, 2017.

[13] Nokia, "Maximize network capacity with Nokia Super Coherent Technologies," Tech. Rep., 2016.

[14] Nokia, "Nokia Photonic Service Engine 3: Taking light to the limit," Tech. Rep., 2018.

[15] T. Bo and H. Kim, "Coherent Versus Kramers-Kronig Transceivers in Metro Applications: A Power Consumption Perspective," in *Optical Fiber Communication Conference*, 2019.

[16] T. Kupfer, A. Bisplinghof, T. Duthel, C. Fludger, and S. Langenbach, "Optimizing Power Consumption of a Coherent DSP for Metro and Data Center Interconnects," in *Optical Fiber Communication Conference*, 2017.

[17] B. S. G. Pillai, B. Sedighi, K. Guan, N. P. Anthapadmanabhan, W. Shieh, K. J. Hinton, and R. S. Tucker, "End-to-End Energy Modeling and Analysis of Long-Haul Coherent Transmission Systems," *Journal of Lightwave Technology*, vol. 32, no. 18, pp. 3093–3111, 2014.

[18] S. Cui, A. J. Goldsmith, and A. Bahai, "Energy-constrained modulation optimization," *IEEE Transactions on Wireless Communications*, vol. 4, no. 5, pp. 2349–2360, 2005.

[19] H. Adams, "IHS Markit Technology: Optical Network Strategies, Service Provider Survey, Tech. Rep. January, 2019.

[20] A. Mecozzi, C. Antonelli, and M. Shtaif, "Kramers – Kronig coherent receiver," *Optica*, vol. 3, no. 11, pp. 1220–1226, 2016.

[21] H. Mardoyan, F. Jorge, B. Baeuerle, J. M. Estaran, A. Konczykowska, M. Riet, B. Duval, V. Nodjiadjim, M. G. J.-y. Dupuy, M. Destraz, C. Hoessbacher, H. Xu, D. Elder, L. Dalton, J. Leuthold, and S. Bigo, "222-GBaud On-Off Keying Transmitter Using Ultra-High-Seed 2 : 1-Selector And Plasmonic Modulator On Silicon Photonics," in *European Conference and Exhibition on Optical Communication*, 2019.

[22] J. M. Estarán, H. Mardoyan, P. Jorge, O. Ozolins, A. Udalcovs, A. Konczykowska, M. Riet, B. Duval, V. Nodjiadjim, J. Chen, S. Member, and S. Popov, "140/180/204-Gbaud OOK Transceiver for Inter- and Intra-Data Center Connectivity," *Journal of Lightwave Technology*, vol. 37, no. 1, pp. 178–187, 2019.

[23] Q. Hu, K. Schuh, M. Chagnon, F. Buchali, and H. Bülow, "Up to 94 GBd THP PAM-4 Transmission with 33 GHz Bandwidth Limitation," in *European Conference and Exhibition on Optical Communication*, 2018.

[24] J. M. Estarán, S. Almonacil, R. Rios-müller, H. Mardoyan, P. Jenneve, K. Benyahya, C. Simonneau, S. Bigo, J. Renaudier, and G. Charlet, "Sub-Baudrate Sampling at DAC and ADC : towards 200G per lane IM / DD Systems," *Journal of Lightwave Technology*, 2018.

[25] Ciena, "Building More Scalable and Programmable Networks with WaveLogic 5 Extreme," Tech. Rep., 2019.

[26] C. E. Shannon, "Communication in the presence of noise," *Proceedings of the Institute of Radio Engineers*, vol. 37, no. 1, pp. 10–21, 1949.

[27] F. Buchali, F. Steiner, B. Georg, L. Schmalen, P. Schulte, and W. Idler, "Rate Adaptation and Reach Increase by Probabilistically Shaped 64-QAM : An Experimental Demonstration," *Journal of Lightwave Technology*, vol. 34, no. 7, pp. 1599–1609, 2016.

[28] F. Buchali, W. Idler, L. Schmalen, and Q. Hu, "Flexible Optical Transmission close to the Shannon Limit by Probabilistically Shaped QAM," in *Optical Fiber Communication Conference*, 2017.

[29] G. Agrawal, *Nonlinear Fiber Optics, Third Edition (Optics and Photonics)*, A. Press, Ed., 2007.

[30] J. Renaudier, P. Brindel, H. Mardoyan, P. Jennevé, L. Schmalen, and G. Charlet, "1-Terabit/s Net Data-Rate Transceiver Based on Single-Carrier Nyquist-Shaped 124 GBaud PDM-32QAM," in *Optical Fiber Communication Conference*, 2015.

[31] J. Yu, K. Wang, J. Zhang, B. Zhu, S. Dzioba, and X. Li, "8 × 506-Gb/s 16QAM WDM Signal Coherent Transmission over 6000-km Enabled by PS and HB-CDM," in *Optical Fiber Communication Conference*, 2018.

[32] A. Ghazisaeidi, I. Fernandez, D. J. Ruiz, R. Rios-muller, L. Schmalen, P. Tran, P. Brindel, A. C. Meseguer, Q. Hu, F. Buchali, G. Charlet, and J. Renaudier, "65Tb/s Transoceanic Transmission Using Probabilistically- Shaped PDM-64QAM," in *European Conference and Exhibition on Optical Communication*, 2016.

[33] S. Almonacil, "Numerical Simulations of Space Division Multiplexed Optical Links in Linear and Nonlinear Regime," Università degli Studi di Parma, Institut d'Optique Graduate School, Tech. Rep., 2016.

[34] H. Takara, "Multi-core Fiber Transmission Technologies for Peta b/s per Fiber Capacity," in *European Conference and Exhibition on Optical Communication*, 2013.

[35] G. Rademacher, R. S. Lu, B. J. Puttnam, T. A. Eriksson, E. Agrell, R. Maruyama, K. Aikawa, Y. Awaji, and N. Wada, "159 Tbit/s C + L Band Transmission over 1045 km 3-Mode Graded-Index Few-Mode Fiber," in *Optical Fiber Communication Conference*, 2018.

[36] Futjitsu Semiconductor Europe, "OOLA Factsheet," Tech. Rep., 2013.

[37] S. Almonacil, P. Jennevé, P. Ramantanis, and P. Layec, "DAC Jitter Requirements for High Speed Optical Networks," in *European Conference and Exhibition on Optical Communication*, 2018.

[38] T. Rahman, D. Rafique, A. Napoli, E. de Man, M. Kuschnerov, B. Spinnler, M. Bohn, C. Okonkwo, and H. de Waardt, "Long-Haul Terabit Transmission (2272km) Employing Digitally Pre-distorted Quad-carrier PM-16QAM Super-channel," in *European Conference and Exhibition on Optical Communication*, 2014.

[39] D. Rafique, A. Napoli, S. Calabr, and B. Spinnler, "Digital Preemphasis in Optical Communication Systems : On the DAC Requirements for Terabit Transmission Applications," *Journal of Lightwave Technology*, vol. 32, no. 19, pp. 3247–3256, 2014.

[40] A. Napoli, M. M. Mezghanni, D. Rafique, V. A. J. M. Sleiffer, T. Rahman, B. Spinnler, and S. Calabr, "Novel DAC digital pre-emphasis algorithm for next-generation flexible optical transponders," in *Optical Fiber Communication Conference*, 2015.

[41] A. Napoli, M. M. Mezghanni, T. Rahman, S. Member, D. Rafique, R. Palmer, B. Spinnler, S. Calabr, C. Castro, M. Kuschnerov, and M. Bohn, "Digital Compensation of Bandwidth Limitations for High-Speed DACs and ADCs," *Journal of Lightwave Technology*, vol. 34, no. 13, pp. 3053–3064, 2016.

[42] S. V. Vaseghi, *Advanced Digital Signal Processing and Noise Reduction*, 2nd ed., J. W. and Sons, Ed., 2000.

[43] P. W. Berenguer, M. Nölle, L. Molle, T. Raman, A. Napoli, C. Schubert, and J. K. Fischer, "Nonlinear digital pre-distortion of transmitter components," *Journal of Lightwave Technology*, vol. 34, no. 8, pp. 1739–1745, 2016.

[44] R. Elschner, R. Emmerich, C. Schmidt-Langhorst, F. Frey, P. W. Berenguer, J. K. Fischer, H. Grießer, D. Rafique, J.-P. Elbers, and C. Schubert, "Improving Achievable Information Rates of 64-GBd PDM-64QAM by Nonlinear Transmitter Predistortion," in *Optical Fiber Communication Conference*, 2018.

[45] Tektronix, "Understanding and Characterizing Timing Jitter," Tech. Rep., 2003. [Online]. Available: www.tektronix.com/jitter

[46] S. Varughese, J. Langston, V. A. Thomas, S. Tibuleac, and S. E. Ralph, "Implementing DACs in High Speed Optical Link Simulations," in *Advanced Photonics Congress*, 2017.

[47] S. Varughese, J. Langston, V. A. Thomas, S. Tibuleac, and S. E. Ralph, "Frequency Dependent ENoB Requirements for M-QAM Optical Links : An Analysis Using an Improved Digital to Analog Converter Model," *Journal of Lightwave Technology*, vol. 36, no. 18, pp. 4082–4089, 2018.

[48] Instrumentation and Measurement Society, "IEEE Standard for Terminology and Test Methods for Analog-to-Digital IEEE, Tech. Rep. February, 2012. [Online]. Available: https://ieeexplore.ieee.org/stamp/stamp.jsp?tp=&arnumber=6152113

[49] B. Widrow, "A Study of Rough Amplitude Quantization by Means of Nyquist Sampling Theory," *IRE Transactions on Circuit Theory*, vol. 3, no. 4, pp. 266–276, 1956.

[50] B. Widrow, I. Kolll, and M.-c. Liu, "Statistical Theory of Quantization," *IEEE Transactions on Instrumentation and Measurement*, vol. 45, no. 2, pp. 353–361, 1996.

[51] A. Sripad and D. Snyder., "A Necessary and Sufficient Condition for Quantization Error to be Uniform and White," *IEEE Tran. On Acousric, Signal, and Speech Processing*, vol. 25, no. 5, pp. 442–448, 1997.

[52] N. Al-Dhahir and J. M. Cioffi, "On the Uniform ADC Bit Precision and Clip Level Computation for a Gaussian Signal," *IEEE Tran. On Acousric, Signal, and Speech Processing*, vol. 44, no. 2, pp. 434–438, 1996.

[53] D. Dardari, "Joint clip and quantization effects characterization in OFDM receivers," *IEEE Transactions on Circuits and Systems*, vol. 53, no. 8, pp. 1741–1748, 2006.

[54] C. R. Berger, Y. Benlachtar, R. I. Killey, and P. A. Milder, "Theoretical and experimental evaluation of clipping and quantization noise for optical OFDM," *Optics Express*, vol. 19, no. 18, pp. 17 713–17 728, 2011.

[55] X. Chen, S. Chandrasekhar, S. Randel, W. Gu, and P. Winzer, "Experimental Quantification of Implementation Penalties from Limited ADC Resolution for Nyquist Shaped Higher-Order QAM," in *Optical Fiber Communication Conference*, 2016.

[56] Y. Yoffe and D. Sadot, "Novel low resolution ADC-DSP optimization based on non-uniform quantization and MLSE for data centers interconnects," *Optics Express*, vol. 24, no. 5, p. 5346, 2016.

[57] Y. Yoffe, E. Wohlgemuth, and D. Sadot, "Digitally Enhanced DAC : Low-Resolution Digital Pre-Compensation for High Speed Optical Links," in *Optical Fiber Communication Conference*, 2018.

[58] G. Khanna, Y. Yoffe, E. de Man, E. Wohlgemuth, B. Spinnler, S. Calabro', A. Napoli, N. Hanik, and D. Sadot, "Experimental Verification of 400G 64QAM using 4 bits DACs Enabled by Digital Resolution Enhancer," in *European Conference and Exhibition on Optical Communication*, 2018.

[59] Y. Yoffe, G. Khanna, E. Wohlgemuth, E. de Man, B. Spinnler, N. Hanik, A. Napoli, and D. Sadot, "Low-Resolution Digital Pre-Compensation Enabled by Digital Resolution Enhancer," *Journal of Lightwave Technology*, vol. 37, no. 6, pp. 1543–1551, 2019.

[60] I. F. de Jauregui Ruiz, A. Ghazisaeidi, P. Brindel, R. Rios-Müller, A. Arnould, H. Mardoyan, O. A. Sab, J. Renaudier, and G. Charlet, "Record 560 Gb/s Single-Carrier and 850 Gb/s Dual-Carrier Transmission over Transoceanic Distances," in *Optical Fiber Communication Conference*, 2018.

[61] P. Händel, "Properties of the IEEE-STD-1057 four parameter sine wave fit algorithm," Tech. Rep., 2000.

[62] Planet-Analog, "Signal Chain Basics - Signal Chain Basics (Part 101) ENOB Degradation Analysis Over Frequency Due to Jitter," 2015. [Online]. Available: https://www.planetanalog.com/author.asp?section_id=483&doc_id=563962

[63] S. Almonacil, F. Von Kanel, F. Boitier, P. Jennevé, and P. Layec, "Performance Model and Design Rules for Optical Systems Employing Low-Resolution DAC/ADC," in *European Conference and Exhibition on Optical Communication*, 2019.

[64] P. Jennevé, P. Ramantanis, N. Dubreuil, F. Boitier, and P. Layec, "Measurement of Optical Nonlinear Distortions and Their Uncertainties in Coherent Systems," *Journal of Lightwave Technology*, vol. 35, no. 24, pp. 5432–5439, 2017.

[65] P. Poggiolini, "The GN Model of Non-Linear Propagation in Uncompensated Coherent Optical Systems," *Journal of Lightwave Technology*, vol. 30, no. 24, pp. 3857–3879, 2012.

[66] F. Vacondio, O. Rival, C. Simonneau, E. Grellier, A. Bononi, L. Lorcy, J.-c. Antona, and S. Bigo, "On nonlinear distortions of highly dispersive optical coherent systems," *Optics Express*, vol. 20, no. 2, pp. 1022–1032, 2012.

[67] S. Daumont, B. Rihawi, and Y. Lout, "Root-raised cosine filter influences on PAPR distribution of single carrier signals," in *International Symposium on Communications, Control, and Signal Processing*, 2008.

[68] B. Widrow and I. Kollár, *Quantization Noise: Roundoff Error in Digital Computation, Signal Processing, Control, and Communications*, C. University, Ed., 2008.

[69] F. Goudail, "Fundamental of estimation and detection in signals and images," Institut d'optique Graduate School, Tech. Rep., 2012. [Online]. Available: http://paristech.institutoptique.fr/site.php?id=146&fileid=6126

[70] M. van den Hout, S. van der Heide, and C. Okonkwo, "Experimental Validation Of Clipping Combined With Digital Resolution Enhancer," in *European Conference and Exhibition on Optical Communication*, 2019.

[71] L. Galdino, D. Semrau, M. Ionescu, A. Edwards, W. S. Pelouch, S. R. Desbruslais, J. James, E. Sillekens, D. Lavery, S. Barnes, R. I. Killey, and P. Bayvel, "Study on the Impact of Nonlinearity and Noise on the Performance of High-Capacity Broadband Hybrid Raman-EDFA Amplified System," *Journal of Lightwave Technology*, no. Early Access, 2019.

[72] B. Smith, "Instantaneous Companding of Quantized Signals," *Bell System Technical Journal*, vol. 36, no. 3, pp. 653–709, 1956. [Online]. Available: https://onlinelibrary.wiley.com/doi/abs/10.1002/j.1538-7305.1957.tb03858.x

[73] C. N. Christou, "Optimal Dither and Noise Shaping in Image Processing," University of Waterloo, Ontario, Canada, Tech. Rep., 2008.

[74] W. A. Ling, "Shaping quantization noise and clipping distortion in direct-detection discrete multitone," *Journal of Lightwave Technology*, vol. 32, no. 9, pp. 1750–1758, 2014.

[75] S. Almonacil, F. Jardel, P. Jennevé, and P. Layec, "Nonuniform DAC Design for Combined Geometrically and Probabilistically Shaped Circular QAM," in *Advanced Photonics Congress*, 2018.

[76] C. Xie, "Chromatic dispersion estimation for single-carrier coherent optical communications," *IEEE Photonics Technology Letters*, vol. 25, no. 10, pp. 992–995, 2013.

[77] H. Freeman and R. Shapira, "Determining the minimum-area encasing rectangle for an arbitrary closed curve," *Communications of the ACM*, vol. 18, no. 7, pp. 409–413, 1975.

[78] M. Nölle, F. Frey, R. Elschner, C. Schmidt-Langhorst, A. Napoli, and C. Schubert, "Performance comparison of different 8QAM constellations for the use in flexible optical networks," in *Optical Fiber Communication Conference*, 2014.

[79] L. Galdino, D. Semrau, D. Lavery, G. Saavedra, C. B. Czegledi, E. Agrell, R. I. Killey, and P. Bayvel, "On the limits of digital back-propagation in the presence of transceiver noise," *Optics Express*, vol. 25, no. 4, p. 4564, 2017.

[80] S. Bigo, "Communications optiques haut débit - Introduction et caractérisation," *Techniques de l'Ingénieur*, 2014.

[81] Y. You, *Audio coding: Theory and applications*, S. US, Ed., 2010.

[82] J. Peng, L. Han, Q. Zhu, C. Qiu, Y. Zhang, C. Tremblay, and Y. Su, "SQNR Improvement Enabled by Nonuniform DAC Output Levels for IM-DD OFDM Systems," *IEEE Photonics Journal*, vol. 9, no. 2, pp. 1–11, 2017.

[83] F. R. Kschischang and S. Pasupathy, "Optimal nonuniform signaling for gaussian channels," *IEEE Transactions on Information Theory*, vol. 39, no. 3, pp. 913–929, 1993.

[84] F. Jardel, T. A. Eriksson, C. Measson, A. Ghazisaeidi, F. Buchali, W. Idler, and J. J. Boutros, "Exploring and experimenting with shaping designs for next-generation optical communications," *Journal of Lightwave Technology*, vol. 36, no. 22, pp. 5298–5308, 2018.

[85] Renesas, "A Brief Introduction to Sigma Delta Conversion," Tech. Rep., 1995.

[86] J. Mazo, "Faster-Than-Nyquist Signaling," *The Bell System Technical Journal*, vol. 54, no. 8, pp. 1451–1462, 1975.

[87] J. Proakis, *Digital Communication*, 4th ed. McGraw-Hill, 2000.

[88] Y. Lu, Y. Yu, L. Liu, Y. Huang, X. Wang, and L. Li, "Faster-than-Nyquist Signal Generation of Single Carrier 483-Gb/s (120.75-GBaud) PDM-QPSK with 92-GSa/s DAC," in *Optical Fiber Communication Conference*, 2017.

[89] C. Lim, A. Nirmalathas, Y. Yang, and D. Novak, "Radio-over-Fiber systems," in *2009 Asia Communications and Photonics conference and Exhibition (ACP)*. IEEE, 2009.

[90] J. Wang, Z. Jia, L. A. Campos, L. Cheng, C. Knittle, and G. K. Chang, "Delta-Sigma Digitization and Optical Coherent Transmission of DOCSIS 3.1 Signals in Hybrid Fiber Coax Networks," *Journal of Lightwave Technology*, vol. 36, no. 2, pp. 568–579, 2018.

[91] A. Konczykowska, F. Jorge, M. Riet, V. Nodjiadjim, B. Duval, H. Mardoyan, J. M. Estaran, A. Adamiecki, G. Raybon, and J. Y. Dupuy, "212-Gbit/s 2:1 multiplexing selector realised in InP DHBT," *Electronics Letters*, vol. 55, no. 5, pp. 242–244, 2019.

[92] L. Breyne, G. Torfs, X. Yin, P. Demeester, and J. Bauwelinck, "Comparison Between Analog Radio-Over-Fiber and Sigma Delta Modulated Radio-Over-Fiber," *IEEE Photonics Technology Letters*, vol. 29, no. 21, pp. 1808–1811, 2017.

My publications

Conferences proceedings

[C1] **S. Almonacil**, F. Von Kanel, F. Boitier, P. Jennevé and P. Layec, "Performance Model and Design Rules for Optical Systems Employing Low-Resolution DAC/ADC," in *European Conference on Optical Communication*, 2019, p. Th.1.B.1. Presented orally.

[C2] **S. Almonacil**, P. Jennevé, P. Ramantanis, and P. Layec, "DAC Jitter Requirements for High Speed Optical Networks," in *European Conference on Optical Communication*, 2018, p. Th1D.4. Presented orally.

[C3] **S. Almonacil**, P. Jennevé, P. Ramantanis, and P.Layec, "Méthode de rotation de phase de la constellation afin de réduire le bruit du transmetteur dans les réseaux optiques," in *Optique Toulouse*, 2018. Presented orally.

[C4] **S. Almonacil**, F. Jardel, P. Jennevé, and P. Layec, "Nonuniform DAC Design for Combined Geometrically and Probabilistically Shaped Circular QAM," in *Advanced Photonics*, 2018, p. SpTu4G.5.

[C5] P. Serena, S. Musetti, **S. Almonacil**, S. Bigo, A. Bononi, P. Jennevé, N. Rossi, and P. Ramantanis, "The Gaussian Noise Model Extended to Polarization Depedent Loss and its Application to Outage Probability Estimation," in *European Conference on Optical Communication*, 2018, p. Tu4G4.

Journal publications

[J1] **S. Almonacil**, F. Boitier, P. Layec et al., "Performance model and Design Rules for Optical Systems Employing Low-Resolution DAC/ADC," extension of the ECOC 2019 paper, accepted for publication (Feb. 2020) in *IEEE Journal of Lightwave Technology*.

[J2] **S. Almonacil**, P. Jennevé, P. Ramantanis, and P. Layec, "A Novel Constellation Phase Rotation Method to Reduce Transmitter Noise in Metro Links," in *IEEE Photonics Technology Letters*, vol. 30, no 16, pp. 1459-1462, 2018.

[J3] J. M. Estarán, **S. Almonacil**, R. Rios-Muller, H. Mardoyan, P. Jennevé, K. Benyahya, C. Simonneau, S. Bigo, J. Renaudier, and G. Charlet, "Sub-Baudrate Sampling at DAC and ADC: Torwards 200G per Lane IM/DD Systems," in *IEEE Journal of Lightwave Technology*, vol. 37, no 6, pp. 1536-1542, 2019.

[J4] N. Rossi, S. Musetti, P. Ramantanis, and **S. Almonacil**, "The Impact of Kerr Nonlinearity on the SNR Variability Induced by Polarization Dependent Loss," in *IEEE Journal of Lightwave Technology*, vol. 37, no 19, pp. 5048-5055, 2019.

Patents

[P1] **S. Almonacil**, P. jennevé and P. Layec, "Method to reject the quantization noise outside the signal bandwidth", 2018.

[P2] **S. Almonacil**, and P. Layec, "Pre-Rotation Method To Enhance Transmitter Performance,", 2017.

université PARIS-SACLAY | ÉCOLE DOCTORALE Ondes et Matière (EDOM)

Titre : Modélisation et Conception de Convertisseurs Numérique-Analogique pour les Réseaux Optiques Métropolitains

Mots clés : Réseaux optiques fibrés ; Conversion numérique-analogique ; Traitement du signal

Résumé : Les transmetteurs et récepteurs utilisés dans les réseaux optiques sont basés sur des convertisseurs numérique/analogique et analogique/numérique (CNA/CAN) qui réalisent l'interface entre les domaines électrique et optique et permettent l'usage intensif d'opérations de traitement numérique pour la génération des signaux ou la compensation des distorsions (linéaires ou non-linéaires) dues à la propagation. Dans le contexte des transmissions courtes-distances ou métropolitaines (<600 km), le coût et la consommation des transmetteurs et récepteurs deviennent non négligeables pour le lien optique dans son ensemble (40% de l'énergie électrique utilisée dans les opérations de traitement du signal porte sur les CNA/CAN). Concernant les CAN/CNA, les deux paramètres qui influent sur leur complexité, leur coût et leur consommation sont la résolution et la fréquence d'échantillonnage. Les réduire est donc une solution prometteuse. Durant ma thèse, j'ai étudié la possibilite d'utiliser des CNA de faible résolution dans les réseaux optiques métropolitains. Un CNA de faible résolution (typiquement 4 bits ou moins) est un convertisseur pour lequel le bruit de quantification ne peut pas être négligé et limite donc la performance du lien optique ainsi que son débit ou sa portée. Tout d'abord, j'ai proposé un modèle de performance prenant en compte le bruit de quantification. Ensuite, j'ai proposé d'intégrer dans les transmetteurs optiques des algorithmes de traitement du signal, dont j'ai évalué la performance. Ils sont utilisés pour augmenter artificiellement la résolution et servent donc de base pour la conception des réseaux optiques métropolitains. En dernier lieu, j'ai proposé deux architectures innovantes de transmission optique qui permettent soit d'augmenter le débit d'information à fréquence d'échantillonnage fixe du CNA et du CAN ou alors d'utiliser la modulation Sigma-Delta (1 bit de résolution) dans un lien optique transparent de bout en bout.

Title : Model and Design Low-Resolution Digital-to-Analog Converters for Metropolitan Optical Networks

Keywords : Optical fiber networks; Digital to analog conversion; Digital signal processing

Abstract : Optical transceivers (transmitters and receivers) rely on digital-to-analog and analog-to-digital converters (DAC/ADC), for which the electrical and optical interfaces enable the use of digital signal processing operations (DSP) for arbitrary signal generation and mitigation of in-line propagation effects or transceiver imperfections. In the context of short-reach and metropolitan optical networks (regional to national scale), the propagation distance is reduced (<600 km) and the transceiver becomes a non-negligible contribution to cost and power consumption of the overall optical link (40% of electrical power used for digital signal processing operations is for the DAC/ADC). Regarding the DAC/ADC, the two factors that influence their complexity, cost and power consumption are the resolution and the sampling rate. Hence, decreasing the resolution or the sampling rate are promising solutions. During my PhD thesis, I studied the possibility to use low-resolution DAC in metropolitan networks. A low-resolution DAC (typically 4 or less bits) is a converter for which the quantization noise cannot be neglected, limiting the link performance, hence the data rate or reach. First, I proposed a performance prediction model accounting for the quantization noise. Then, I focused on the transmitter and proposed to integrate DSP algorithms that artificially increase the physical resolution of the DAC and maximize the link performance. The performance gains are assessed and serves as a basis for the design of optical networks employing low-resolution DAC/ADC. Last, I designed two innovative transceiver architectures: one enabling to increase the data rate at constant sampling rate and the second one enabling end-to-end transparency by employing Sigma-Delta modulation and a novel demodulation technique for signal with 1 bit of vertical resolution.

Université Paris-Saclay
Espace Technologique / Immeuble Discovery
Route de l'Orme aux Merisiers RD 128 / 91190 Saint-Aubin, France